Millimeter Emission From Protoplanetary Disks

Dust, Cold Gas, and Relativistic Electrons

Universiteit Leiden

Millimeter Emission From Protoplanetary Disks

Dust, Cold Gas, and Relativistic Electrons

PROEFSCHRIFT

ter verkrijging van
de graad van Doctor aan de Universiteit Leiden,
op gezag van de Rector Magnificus Prof. Mr. P. F. van der Heijden,
volgens besluit van het College voor Promoties
te verdedigen op donderdag 25 november 2010
klokke 11.15 uur

door

D. M. Salter

Promotiecommissie

Promotor:	Prof. Dr. E. F. van Dishoeck
Co-promotor:	Dr. M. R. Hogerheijde
Overige leden:	Prof. Dr. H. V. J. Linnartz (Leiden University / Vrije Universiteit Amsterdam) Prof. Dr. K. Kuijken (Leiden University) Prof. Dr. C. Dominik (University of Amsterdam / Radboud University Nijmegen) Prof. Dr. G. A. Blake (California Institute of Technology) Dr. L. Testi (European Southern Observatory)

Front Cover: An artist's rendering of the birth of a star. *Credit: NASA / JPL-Caltech / R. Hurt (SSC).*

Contents

Chapter 1

Introduction

In the 1700s, after noting how the planets appeared to orbit the Sun in one direction and in roughly the same plane, several European philosophers independently postulated that our Solar System must have formed from a flattened rotating disk (see Swedenborg 1734; Kant 1755; Laplace 1796). Two centuries later, particularly in the 1960s and 1970s, theoretical models linking the collapse of interstellar molecular clouds to star birth indicated that circumstellar disks, containing the raw materials for planetary systems, are both a natural and necessary consequence of the star formation process (e.g. Bok 1948; Hayashi 1961; Larson 1969; Shu 1977). With the development of infrared detectors in the 1980s, the first observational evidence for warm circumstellar material was discovered around several main-sequence stars (e.g. Aumann et al. 1984; Smith & Terrile 1984; Strom et al. 1989; Beckwith et al. 1990). However, only by the early 1990s had advances in millimeter interferometry provided definitive proof for the existence of protoplanetary disks around young forming stars, both in the form of resolved Solar System sized dusty disks (e.g. Simon & Guilloteau 1992; Koerner et al. 1993), as well as large gaseous disks exhibiting rotating Keplerian velocity structures (e.g. Sargent & Beckwith 1987; Weintraub et al. 1989; Dutrey et al. 1993; Kawabe et al. 1993). The ground-based millimeter measurements complemented space-based optical images taken by the then newly launched Hubble Space Telescope (HST), which revealed in silhouette several protoplanetary disks (or "proplyds") in the Orion star-forming region (see Figure 1.2, and O'dell et al. 1993); and just as the ubiquity of protoplanetary disks around young stars was established, the first indirect detections of planets orbiting around other main-sequence stars followed in 1995 (see Mayor & Queloz 1995; Marcy & Butler 1996; Butler & Marcy 1996). In the 15 years since then, hundreds of both confirmed and candidate planetary systems have been identified from radial-velocity measurements (e.g. Baranne et al. 1996; Queloz et al. 2000; Santos et al. 2001; Udry & Santos 2007), photometric transits (e.g. Charbonneau et al. 2000; Henry et al. 2000; Borucki et al. 2007; Barge et al. 2008; Léger et al. 2009), gravitational microlensing (e.g. Udalski et al. 1992, 2002; Bouchy et al. 2004), and most recently by direct imaging (e.g. Marois et al. 2008; Kalas et al. 2008; Lagrange et al. 2010). Most of these extra-solar planets (or "exoplanets") differ greatly from the planets in our own Solar System, and even defy traditional theories on planet formation. Now many of the fundamental questions in modern astronomy—and in this thesis—surround a desire to identify the specific physical and chemical processes that transform circumstellar disks into the variety of planetary systems that we observe today; including, why some disks apparently fail to produce planets at all.

1.1 Origins

Star and disk formation are intricately entwined, as is their evolution. Circumstellar disks are an essential outcome of stellar birth and the central star is responsible for many important drivers of the disk evolution. Accordingly, to place the subject of disk evolution and the formation of planetary systems into its proper context, it is necessary to first review the current theory for the formation of a low-mass ($\leq 2\,M_{\odot}$) Sun-like star.

1.1.1 The Formation of Sun-like Stars

For much of human history, stars were thought to be permanent fixtures in the night sky; but rather they, too, experience a life cycle of birth, ageing, and death. The earliest stages of star formation occur hidden from sight, deep within a cold and dark molecular cloud. These clouds are distributed throughout the galaxy and were first described as “holes in the heavens” by the British astronomer Sir Frederick William Herschel (see Herschel 1785). Once believed to be empty regions absent of light, they are now recognized as some of the densest concentrations of cold dust and molecular gas (see Bergin & Tafalla 2007, for a recent reveiw), which aptly block the optical light from the stars behind them (see Figure 1.1). These same dense conditions that shield our view into the cloud, are also critical to the success of star formation itself. To form a star, a large reservoir of dust and gas is needed. Molecular clouds spanning many parsecs possess the required ingredients, as well as an inhomogenous structure that, under the influence of gravity, becomes concentrated into separate, more massive, clumps of the order one parsec in diameter. Each clump is initially supported against further gravitational collapse by thermal gas pressure, magnetic pressure, and rotational pressure, in addition to turbulence. The balance begins to shift, however, when densities in the clumps start approaching 10^3–10^4 particles per cm^{-3}, or about a factor 100–1000 times denser than the surrounding interstellar medium, sometimes with the aid of shock fronts from nearby dying stars, or supernovae.

A denser concentration of material curtails the cloud-supporting mechanisms. Higher clump densities contribute to more effective shielding of the most embedded regions from external radiation sources and the corresponding heating effects; thereby reducing the internal gas pressure. Small micron-sized dust grains, in particular, form a protective layer against the interstellar UV field, which is otherwise an effective destroyer of all but the largest, or most strongly bound, molecular compounds. The surviving molecules, in turn, provide an effective pathway to radiate energy away from the clump. Unlike atomic matter, molecules can store (angular kinetic) energy through rotation about a molecular axis. When this energy is released via transitions to lower-energy rotational states, the emitted radiation is characterized by millimeter wavelengths that more easily escape the dense region; a property that will prove invaluable for the study of disks as well. Thus, as heat is generated by the slow condensation of the clump, this energy is quickly absorbed by the molecules during collisions, and then continuously radiated away via downward rotational transitions; thereby reducing further the thermal pressure, also from new internal heat sources. Other energy input sources, like cosmic ray heating, are not enough to compensate for an energy balance now skewed toward a net energy loss. The temperature throughout the clump drops to as low as 10 K ($-263.15\,^{\circ}$C). Neutral particles now drift freely past the magnetic field lines in a process called ambipolar diffusion, while simultaneously—and in a role reversal—collisionally corraling the ions along with them into a denser centralized core. Since the ions are tied to the magnetic field, the field lines become frozen to the large-scale movements of an impending collapse; thereby limiting any potential for magnetic braking. The gravitational attraction only intensifies as the clump becomes more centrally condensed while achieving characteristic densities of $\geq 10^5$ particles per cm^{-3}. Eventually, this concentration of material reaches a critical density, sometimes expressed as the Jeans mass, and runaway gravitational collapse ensues. This is time zero ($t = 0$) for star formation. From this point forward, the

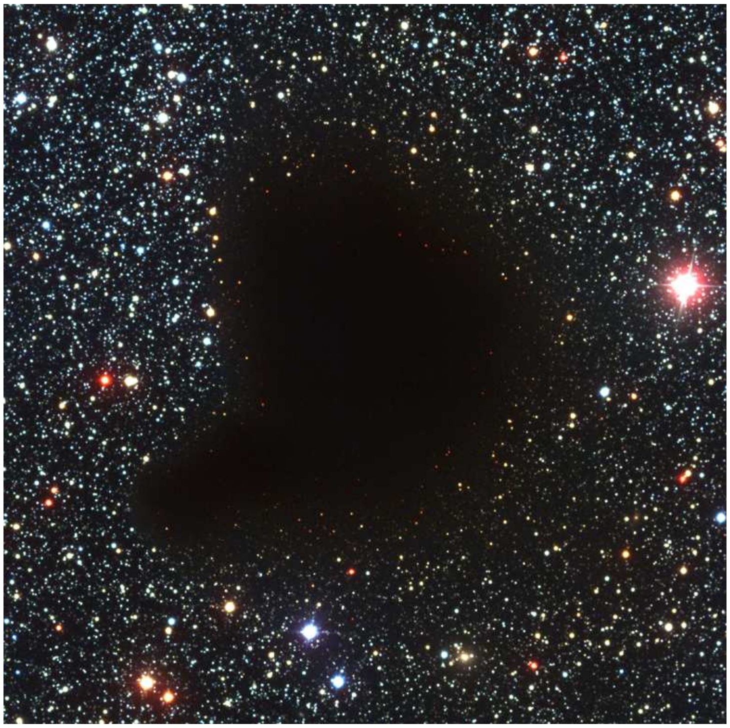

Figure 1.1 — A dark molecular cloud. An optical image of Barnard 68, a potential star formation site, as observed with the 8.2-meter VLT Antu at the Paranal Observatory in Chile. At a distance of 500 light-years from Earth, the cloud measures ∼0.5 light-years across. This image covers a $6.8' \times 6.8'$ region on the sky. (*Credit: ESO*)

central object will receive many names to describe its different evolutionary stages, but it may always be referred to as a young stellar object (YSO) while it is still forming.

The Four Classes of Young Stellar Objects

The dense structure is now a roughly spherical, gravitationally bound, isothermal cloud core of about 10,000 AU in size. This represents the Lada Class 0 deeply embedded phase of star formation (Lada & Wilking 1984; André et al. 1993). All of the necesary ingredients to form a star and a planetary system are presumed present (Krumholz et al. 2005), and this process that begins as an inside-out self-similar collapse of the core is expected to take 10^7 years or more to completely form a low-mass, main-sequence star similar to the Sun (Shu 1977).

In the beginning though, only a starless core exists. As material collapses in on itself from ever larger radii, the core begins to rotate in order to conserve angular momentum (Goodman et al. 1993), and the infalling envelope material slowly flattens along the direction of the rotation axis (Terebey et al. 1984; Basu 1998). Eventually a protostar forms at the center of the core, initially converting gravitational potential energy into accretion luminosity in what is sometimes known as the Kelvin-Helmholtz mechanism. Only recently have observational studies been able to reveal with some certainty the velocity field of a collapsing core, while looking to document the early conversion from an infall- to a rotationally-dominated structure (e.g. Hogerheijde 2001; Brinch et al. 2008, 2009). This velocity field transformation occurs when the initially inward free-falling material starts to collect in an accretion disk around the protostar, just outside the centrifugal radius where the rotational pressure dominates over gravity (see Cassen & Moosman 1981; Terebey et al. 1984; Yorke et al. 1993; Visser et al. 2009; Visser & Dullemond 2010). This radius moves outward over time as the disk grows and the protostar rotates faster.

The earliest evidence for a very deeply embedded Keplerian disk has now been detected in the Class I stage of the protostar development (e.g. Keene & Masson 1990; Sargent & Beckwith 1991; Chandler et al. 1994; Lommen et al. 2008; Jørgensen et al. 2009). In this second stage, the embedded source can be studied at shorter mid- to far-infrared (or micron) wavelengths due to warmed dust in the innermost regions close to the protostar. In addition, strong bipolar jets and outflows emerge to help relieve the build-up of angular momentum, and to aid the protostar in keeping a rotation rate below break-up speeds as material continues to accrete onto it. Within a period of about 10^4–10^5 years, the star begins converting deuterium for energy in its interior (Stahler 1983), strong pre-stellar winds disperse the thick envelope, the jets weaken as accretion slows, the outflow angles broaden over time, and the circumstellar disk flattens. When the central pre-main-sequence (PMS) star becomes optically visible, the low-mass source is called a classical T Tauri star (CTTS) and occupies Class II of the Lada evolutionary scheme. If a remnant envelope remains, the excess thermal emission originates primarily from the optically thick circumstellar disk ($M_{\rm disk} > M_{\rm env}$). This is the stage when we search for clues to planet formation; and thus, the main focus of the work presented in this thesis. Near the end of this stage, the PMS star may otherwise be known as a weak-line T Tauri star (WTTS) when it stops accreting material (Walter 1987). By the final Class III stage, the confirmed WTTS star is accompanied by a remnant disk, debris disk, planetary system, or nothing at all.

The final stages of star formation involve igniting nuclear fusion of hydrogen into helium within the stellar core, and then achieving hydrostatic equilibrium (or the balance between radiative pressure and gravitational contraction). When these two conditions have been satisfied, the central object has reached the zero-age main-sequence (Hayashi et al. 1962; Larson 2003). The star formation process is complete and a star is born. While the theory summarized here highlights singular low-mass star formation, we note that multiple-star systems also occur in large fractions, up to 65% of the stellar population in the middle of the main-sequence (Duquennoy & Mayor 1991), and may result from irregular fragmentation of the original cloud core (Dobbs et al. 2005; Krumholz et al. 2010). In addition, about 20% of all known exoplanets have been found in binary systems possessing stellar separations < 100 AU (Raghavan et al. 2006; Duchêne 2010). Since three of the studies presented in this thesis concern binary sources specifically, we will return periodically to their properties as well, including the challenges their stellar dynamics present to disk evolution. Finally, we remark how observations highlighting disk parameters around similarly aged PMS stars in the same cluster show significant variation (Muzerolle et al. 2000; Sicilia-Aguilar et al. 2006; Kessler-Silacci et al. 2006; Furlan et al. 2006), suggesting that the initial disk conditions resulting from this star formation process are neither consistent nor uniform (Alexander 2008), or that disk processing mechanisms vary significantly from disk to disk, or both.

In conclusion, the formation history of the star, its multiplicity, composition, mass, disk-dispersing winds, radiation field, and many other attributes, as discussed here, will all certainly impact the early circumstellar disk conditions and presumably the outcome of its evolution. However, for the purpose of the research presented in this thesis, we will focus our studies primarily on the current star and disk observables, and assume similar initial or environmental conditions to identify trends and draw conclusions about the *ongoing* disk processing, and what it means for future planets.

1.1.2 The Birth Sites of Planetary Systems

While circumstellar disks are an intrinsic consequence of the star formation process, planets are not necessarily. So when is a circumstellar disk also a protoplanetary disk? The latter term referring more specifically to a pre-cursor site for planet formation. The answers are still unclear, but ultimately, it is the direct competition between the disk dispersal timescales and the planet formation timescales that will determine the success rate for planetary systems. In this section, we discuss the general properties, trends, and major processes observed during the evolution of a circumstellar disk, with particular emphasis on

Figure 1.2 — Four protoplanetary disks in the Orion Nebula, shown in silhouette. At center, the largest disk is $\sim$800 AU in diameter. This image was taken in 1993 with the Wide Field and Planetary Camera 2 on board the Hubble Space Telescope, and measures 0.14 light-years across. (*Credit: C.R. O'Dell of Rice University / NASA*)

the disk dispersal mechanisms, planet formation theories, and the consequences both have for planets.

By far, the most stringent constraint on planet formation is the disk lifetime, and yet the relative impact of the main dissipation mechanisms is still not well understood. The primary dispersal mechanisms include: accretion onto the central star, viscous disk spreading, inner and outer disk truncation via stellar encounters, photoevaporation by stellar winds, the destructive stellar (UV and X-ray) radiation field, and the aggregation of material into orbiting planetary bodies (Hollenbach et al. 2000). The reservoir of circumstellar material initially present around a young T Tauri star is suspected to dissipate within 10^6 years on average, according to observations and stellar age tracks (Haisch et al. 2001; Bizzarro et al. 2005; Pascucci & Tachibana 2010), although there are also examples of disks possessing their primordial gas to ages beyond 10^7 years (see Favata et al. 1998); yet another indication that stellar age is not the primary determinant of the disk evolutionary state, as briefly hinted at in the last section. In fact, dusty disks around cooler (K and M type) PMS stars may live up to 2–3 times longer, meaning that dissipation mechanisms may not be as efficient in late-type stars (Sterzik et al. 2004; Carpenter et al. 2006; Lada et al. 2006), and that stellar properties other than age may still play a vital role in the disk lifetime.

When the envelope around a young forming star has dispersed, the revealed dust disk is usually several hundred AU in radius (Andrews et al. 2009; Isella et al. 2009; Ricci et al. 2010b). It is also about 5% of the mass of the central source (Andrews & Williams 2005; Fang et al. 2009; Greaves & Rice 2010), although a two-magnitude scatter in the derived disk masses ($\sim 0.1\,M_\odot$ to $\lesssim 0.001\,M_\odot$) has been observed around T Tauri stars (Beckwith et al. 1990). The ratio of the mass located in the disk versus the envelope can be used to distinguish between different YSO evolutionary stages (see Jørgensen et al. 2009), with this ratio increasing for more evolved systems. Thus, the disk masses observed likely represent the typical range possible from the time the disk is revealed until its disappearance. Another possibility is that some disks are more massive to begin with and as a result might easily survive longer, allowing more time for planet formation to occur (Andrews & Williams 2007). Indeed, some models show that a larger disk mass can result from a faster intrinsic rotation rate during the early disk accretion phase (see Visser & Dullemond 2010). And there is yet more evidence to support the idea that other initial conditions, like the composition of the disk, could also play a significant role in planet formation. For example, a higher disk metallicity to start out with (or roughly speaking, more dust to gas) may quicken the planet formation process. Exoplanet statistics exhibit a trend toward higher occurrences of gas giants around metal-rich stars (Santos et al. 2003). Computer simulations are able to show that the higher concentration of metals in the early disk allow for the build-up of planetary cores before dispersal of the gas reservoir is possible, making gas giants more likely (Ida & Lin 2004; Johansen et al. 2009; Ercolano & Clarke 2010). In contrast, lower metallicities in star-forming regions in the extreme outer Galaxy are believed to contribute to the relatively rapid dispersal of the circumstellar disks seen there, possibly caused by lower UV extinction from small dust grains (Yasui et al. 2009). For these reasons, there is a need to compare the evolution of the gas reservoir relative to the dust, which is one of the main motivating factors for part of the research presented in this thesis.

Separate Dust and Gas Dispersal Mechanisms

In general, the disk mass is comprised of one part sub-micron-sized (carbon and silicate) dust grains and ninety-nine parts cold gas (primarily H, H_2, and He); a standard ratio that also characterizes the interstellar medium. However, high-resolution observations together with modeling of large gaseous disks have shown that considerably different dust-to-gas ratios may also make for reasonable fits to the data for some sources (see Dutrey et al. 2003; Panić et al. 2008; Thi et al. 2010). In addition, the outer disk regions can exhibit larger dust depletion with respect to the inner radii (e.g. van Kempen et al. 2007; Isella et al. 2007; Panić et al. 2009). In some cases, modeling the outer disk density profile with a tapered edge can resolve this “observational discrepancy” (see Hughes et al. 2008). Thus, whether the different dust-to-gas ratios are a direct result of the initial conditions, an evolutionary outcome, or an observational effect often remains to be disentangled, but the true underlying amount of available gas is crucial to the ability to form gas giant planets like Jupiter, and worthy of investigation. Unfortunately, far less is known about the molecular gas reservoir because it is significantly more difficult to observe than the dust (see Section 1.2.3). As a result, current disk modeling methodologies usually assume that the gas structure accurately traces the dust structure, even though one of the big open questions in protoplanetary disk research today is whether the separate dust and gas components evolve simultaneously?

Recent progress is being made to identify relevant trends in the physical and chemical evolution of the gas disk (e.g. Dutrey et al. 1997; Qi 2001; Dutrey et al. 2007; Panić & Hogerheijde 2009; Bergin 2009; Öberg et al. 2010). The results are revealing disks with markedly different gas and dust structures. Some of these studies confirm separate outer dust and gas radii (e.g. van Kempen et al. 2007; Panić et al. 2009), or find that cleared inner dust gaps can still retain their gas component (e.g. Brown et al. 2008; Boden et al. 2009), or indicate that the gas temperature structure may be decoupled from that of the dust (e.g. Panić et al. 2008), or even that the gas disk can be flared while the dust disk is self-shadowed (see Fedele et al. 2008). Additional analyses of the gas component—the primary target of two of the observational studies presented in this thesis—can shed light on the processes relevant to both the dust and gas dispersal, and how they might be coupled. In the meantime, we continue reviewing the current disk evolutionary picture, acknowledging that much of our present knowledge is still based primarily on observations of the dust content in disks.

An Overview of Disk Evolution from Dust Observations

Disks come in many shapes and sizes, primarily reflecting different evolutionary stages. They usually start out flared as they funnel material from the spherical rotationally-flattened envelope down onto the central star. With a flared geometry, they intercept more of the stellar light, directly heating (and ionizing) the upper disk layers, which then re-radiate thermal energy into the deeper layers below, helping to maintain a warmer internal disk temperature and a larger pressure scale height. Over time, all disks evolve toward increasingly flatter geometries when: the envelope that feeds the disk dissipates and ceases to rain down on the disk; viscous spreading expands the disk material outward indefinitely while conserving angular momentum; the luminosity generated by the slowing accretion decreases, thus reducing the disk temperature and scale height; grain growth leads to a concentration of larger particles in the disk midplane; and, the disk evolves from a warm optically thick disk to a cold optically thin one (Dullemond & Dominik 2004a,b). During this flattening, disk clearing is likely to occur from the inside-out, initially forming an inner dust gap before dispersing the rest of the disk material via stellar photoevaporating winds, X-ray photoionization, UV photodissociation, and possibly via the process of planet formation itself (Strom et al. 1989; Skrutskie et al. 1990; Hollenbach et al. 2000).

By 3–8 Myr, only 10% of T Tauri stars still exhibit evidence for inner accretion disks (Hillenbrand 2005), a fact that may leave them more vulnerable to the stellar radiation field without the added veiling provided by accretion flows. From this point forward, the dissipation process appears to occur quite rapidly, within another 10^4–10^5 years by some estimates (Simon & Prato 1995; Wolk & Walter 1996), based on the fact that statistically fewer objects are observed in the transitional stage from CTTS to WTTS (Strom et al. 1989). However, the Spitzer Space Telescope (SST or Spitzer), launched in 2003, is quickly altering the field of transitional disks with observations at near- and mid-infrared wavelengths, and new analyses report that this transition period could be as long as 1 Myr (see Cieza et al. 2007; Currie & Kenyon 2009). In the meantime, a similar lack of statistical evidence for objects with an outer disk-in-transition suggests that the disk could be depleted throughout relatively simultaneously (Andrews & Williams 2005; Alexander & Armitage 2007; Alexander 2008). In further support, a recent study of grain growth signatures tracing both the inner and outer disk also revealed a parallel, albeit tentative, indication that the dust in disks might evolve concurrently at all radii (see Lommen et al. 2010). On the other hand, this initial finding stands in stark contrast to models that predict faster grain growth closer in to the forming star (Dullemond & Dominik 2004b; Natta et al. 2007), and follow-up studies have been unable to confirm the initial trend (Ricci et al. 2010a). In addition, several new observational studies are providing the first indications for a radial variation in the dust properties of individual sources (e.g. Isella et al. 2010; Banzatti et al. 2010). Consequently, a bi-modal interpretation of the observational data has been proposed (e.g. Strom et al. 1989; Cieza et al. 2007), contrasting transitional disks with inner holes versus those that are depleted homologously (see Cieza et al. 2007; Currie & Kenyon 2009; Ercolano et al. 2010; Merín et al. 2010). Therefore, it is important to determine whether two separate groups do exist and whether they might represent different outcomes for disk evolution or even different routes toward the same outcome, if we want to correctly place all disks into one evolutionary sequence.

Inner disk clearing, which may be followed by the rapid dispersal of the disk, can also be a sign of successful planet formation. There are currently two dominant theories for gas giant planet formation, known as the core accretion and the gravitational instability models. The core accretion model is currently the favored theory (see Safronov & Zvjagina 1969; Pollack et al. 1996); and the subject of a separate study in this thesis. The theory explains how sub-micron-sized dust grains in the disk initially collide and stick together quickly and efficiently due to surface adhesion, or specifically by van der Waals force (see Dominik & Tielens 1997; Poppe et al. 2000; Blum & Wurm 2008). In agreement with theory, laboratory studies have successfully reproduced the efficiency of collisional growth up to millimeter-sizes (Colwell & Taylor 1999; Blum et al. 2002; Colwell 2003; Love & Pettit 2004; Langkowski et al. 2008; Colwell et al. 2008). The collisions are caused by non-zero relative velocities due to turbulence and the differential coupling of the dust to the large-scale gas motions (Weidenschilling & Cuzzi 1993; Beckwith et al. 2000). When the growing dust agglomerate is massive enough ($\gtrsim 5$–$10\,M_\oplus$), a planetary core has formed and it is able to gravitationally accrete molecular gas. Runaway growth proceeds as the protoplanet sweeps up material in its orbital path until it has cleared a wide gap in the disk. At this point, several big challenges to the model appear during the intermediate growth stage. While collisional sticking is effective for small grains, and gravitational attraction works well for large boulders, the processes governing the growth of intermediate-sized grains (from millimeter sizes on up to kilometer sizes), remains an open investigation (see Blum 2010, for a recent review). Theory predicts that turbulence in disks and the weak molecular bonds mean that collisions of millimeter-sized aggregates are prone to particle fragmentation and semi-elastic (or re-bounding) collisions (Schäfer et al. 2007; Paszun & Dominik 2009). Now new microgravity experiments confer (Chapter 7, Salter et al. 2009; Heißelmann et al. 2010). Subsequently, collisional growth appears to be an incomplete solution thus far for planet formation (Blum 2010). Recently, streaming instabilities have been invoked to aid the core accretion process (Johansen et al. 2009). The theory describes how eddies in the rotating Keplerian velocity field of the gaseous component collect dust particles allowing them to aggregate to larger sizes in lower-velocity collisions more easily. In addition, when collisions do result in fragmentation, the fragmented material does not escape the eddy, but rather falls back onto the accreting core. These spiral streams are able to explain the spin rates and propensity for prograde rotation of the small bodies in the Solar System (Johansen & Lacerda 2010). However, the instabilites then also inherently stipulate that sufficient gas surface densities must be available to overcome destructive growth processes, even during the formation of small rocky Earth-like planets.

In the end, the requirements that must be met for a successful planetary outcome can be summarized as: a large reservoir of both dust and gas, a longer gas disk lifetime than the timescale needed for a planet to form, effective grain growth mechanisms, and eventually, stable planetary orbits. In this context, this thesis addresses research including: observations to identify gas-rich disks toward massive dust disks, studies to probe destructive gas processes in disks exhibiting preliminary grain growth, and experiments probing the effectiveness of collisional growth processes at intermediate grain sizes.

1.2 The Study of Protoplanetary Disks

The majority of the analyses and results presented in this thesis are based on observations combined with modeling. Because the evolutionary timescales for disks are very long, on the order of several Myr, we use statistical surveys of many circumstellar disks (at presumably different evolutionary stages) to piece together the complete evolutionary timeline for a typical disk. Observations are easiest to make of sources in the nearest low-mass star-forming regions. This includes the Taurus-Auriga complex (140 pc, Kenyon et al. 1994), the Orion Nebula (440 pc, Hirota et al. 2007), and ρ Ophiuchus (135 pc, Mamajek 2008). In this thesis, our source observation lists are comprised almost entirely of low-mass objects in Taurus. In general, we justify this selection criterium by the intent to establish a uniform sample, located in a roughly identical environment, and possessing similar initial conditions; the caveats of Section 1.1 notwithstanding. This can tell us a great deal about the T Tauri population in Taurus, but may require some caution when extrapolating the results to the general low-mass stellar population because Taurus has several distinguishing characteristics that set it apart from other regions, including an unusually high stellar multiplicity rate (∼75%), fewer high-mass stars, distributed (versus clustered) star formation, and a slightly higher disk fraction in general (Ghez et al. 1997; Luhman et al. 2010). Although some recent studies report that the dust properties seem to be independent of the star-forming region, suggesting that a more universal application of the results may also be possible (e.g. Lommen et al. 2010; Ricci et al. 2010a). In this section, we discuss our methods for studying the evolution of protoplanetary disks, including the telescope facilities used, the emission processes traced with observations, the disk (dust and gas) modeling, and finally, when we can study disk evolutionary processes in the laboratory.

1.2.1 Millimeter-wave Instrumentation

In Taurus, typical disk temperatures can range from 10 K in the midplane to 300 K in the surface layers. The importance of millimeter emission to probe such cold, dark and dense regions has been noted already, but making the transition to observations at longer wavelengths required new technological developments in millimeter-wave instrumentation. For one thing, larger telescopes are necessary because the angular resolution is inversely proportional to the observed wavelength ($\sim 1.2\,\lambda/D$). For example, the IRAM 30-meter telescope (in Chapter 6) is the second largest millimeter dish in the world, while (in Chapter 2) the James Clerk Maxwell Telescope (JCMT), located on Mauna Kea in Hawaii, possesses a 15-meter dish diameter. At wavelengths of 1–3 mm, where the bulk of the cold disk material emits thermal radiation, the angular resolution (or beam-size) of each telescope ranges from 8–25″ and 17–50″, respectively. In contrast, an average protoplanetary disk of radius 500 AU in Taurus has an angular size of 7″ and fills just 72–8% and 17–2% of the respective beams, assuming a face-on disk orientation. Thus, no disk is ever resolved, and building larger telescope dishes that are still maneuverable, is technologically challenging. As a result, single-dish millimeter data typically suffer from low-resolution, beam dilution, pointing errors, absolute flux calibration errors ($\sim$ 20%), and in crowded regions, confusion from nearby sources that also fall within the beam. The telescopes are, however, well suited for large surveys of protoplanetary disks, like those in Chapters 2 and 6 of this thesis. In doing so, separate offset observations are now made toward nearby "empty" patches of the star-forming cloud to quantify the external contribution from dust and molecules (see Figure 2.4) in the surrounding environment and along the line-of-sight to each source (e.g. Thi et al. 2001; van Kempen et al. 2007). Still, continuum fluxes can provide only a lower limit to the dust mass when $R_{\rm dust}$ (or the amount of beam dilution) is unknown. And while gas-line observations can help us to search for trends in the disk chemistry (see Chapter 2) and constrain some disk parameters including the gas disk size $R_{\rm gas}$ and inclination i (e.g. Panić et al. 2008), a lot of the kinematical information is still lost. Ultimately, our goal is to resolve the radial variations and evolution of the gas, particularly in light of the evidence for both inside-out and homologous dust dispersal processes. Thus, having identified suitable disks for follow-up studies, it is necessary to seek out solutions to bigger telescopes yet.

To achieve higher angular resolution, millimeter-wave instrumentation has borrowed on the principle of radio interferometry to link together multiple millimeter dishes (or antennas) to create a larger collecting area. Modern facilities include the Combined Array for Millimeter-wave Astronomy (CARMA) in eastern California, the IRAM Plateau de Bure Interferometer (PdBI) in the French Alps, the Submillimeter Array (SMA) on Mauna Kea in Hawaii, and the Nobeyama Millimeter Array (NMA) in Japan. The next-generation Atacama Large Millimeter / submillimeter Array (ALMA), the only dedicated millimeter interferometer to be located in the southern hemisphere, is currently in its commissioning phase (see Figure 1.3). In the meantime, the interferometers operating today feature baselines of several hundred meters in length and resolutions of $\sim$0.5″ (about 70 AU at the distance to Taurus); ALMA will extend this down to 0.02″ (or 3 AU) at the same wavelengths. Several non-trivial performance enhancements are achieved while using interferometry techniques: increased collecting area improves sensitivity and the ability to detect smaller column densities of molecular gas, in addition to smaller dust mass (also at larger radii); longer baselines increase the angular resolution allowing us to probe the radial and vertical structure on smaller scales; and, the interferometer is more sensitive to compact disk emission because it resolves out (or does not efficiently detect) the large-scale extended envelope and cloud contributions that contaminate (and sometimes dominate) the single-dish data. Interferometric observations of protoplanetary disks can be very time-consuming to achieve adequate signal-to-noise, often lasting the entire 8–9 hours that a source remains visible over an array. An entire 8–9 hour track is also recommended for better image fidelity, which is defined by a combination of the source brightness distribution on the sky, the details of the u,v-coverage (or collecting area) of the antennas, and the de-convolution algorithm used when re-constructing the image from a sparsely sampled u,v-plane (see Taylor et al. 1999, for a detailed introduction to interferometry techniques).

While an interferometer approximates a telescope the size of its longest baseline, the combined telescope has many "holes" in it, which results in lost source information. Thus, the more u,v-coverage, the fewer the holes. This can be achieved in two ways, through a higher density of antennas or a longer

Figure 1.3 — An artist's drawing of the original vision for the Atacama Large Millimeter / submillimeter Array (ALMA), now in its commissioning phase. Located at the Chajnantor plateau in the Atacama desert in Chile, early science is slated to begin in late 2011 when the first 16—of the planned 66—antennas are online. (*Credit: ESO*)

observation. The latter strategy is effective because the u,v-sampling changes as the Earth rotates, filling in the u,v-plane (see Figure 1.4 for an illustration of this effect); in addition, the u,v-plane is more symmetrically sampled (producing a more circular beam). This was the guiding principle when defining our CARMA observing strategy in Chapter 3. Rather than observing two sources per night for four consecutive hours each, we chose to rotate through all of our sources repeatedly over the course of five nights. The result was the anticipated, quiescent 5-night light curve for all sources, except one! This serendipitous discovery of atypical millimeter activity toward a T Tauri source is the subject of Chapter 4 of the thesis (Salter et al. 2008). In the follow-up observations of Chapter 5, we continued to use the increased sensitivity of the CARMA, IRAM PdBI, and SMA interferometers to detect the small- and large-scale flux variations in the active millimeter light curve (Salter et al. 2010).

1.2.2 The Dust

Although the gas content dominates the disk mass, it is the dust content that dominates the observed emission at millimeter wavelengths. In this section, we cover how we can derive the large-scale dust structure from continuum observations, and then we summarize the diagnostics available to "zoom-in" on the small-scale processes that constitute the first steps of planet formation.

Circumstellar dust irradiated by the central source emits at a characteristic wavelength corresponding to its temperature, size, and emissivity properties. The summation of this thermal emission from all of the small dust grains in the disk defines a spectrum of total flux per wavelength known as the dust continuum. This is just one component of the source's Spectral Energy Distribution (SED), which also includes the stellar blackbody spectrum. Ranging from the near-infrared to radio wavelengths, the dust continuum represents one of the easiest disk diagnostics to measure. In addition, if the stellar *input*

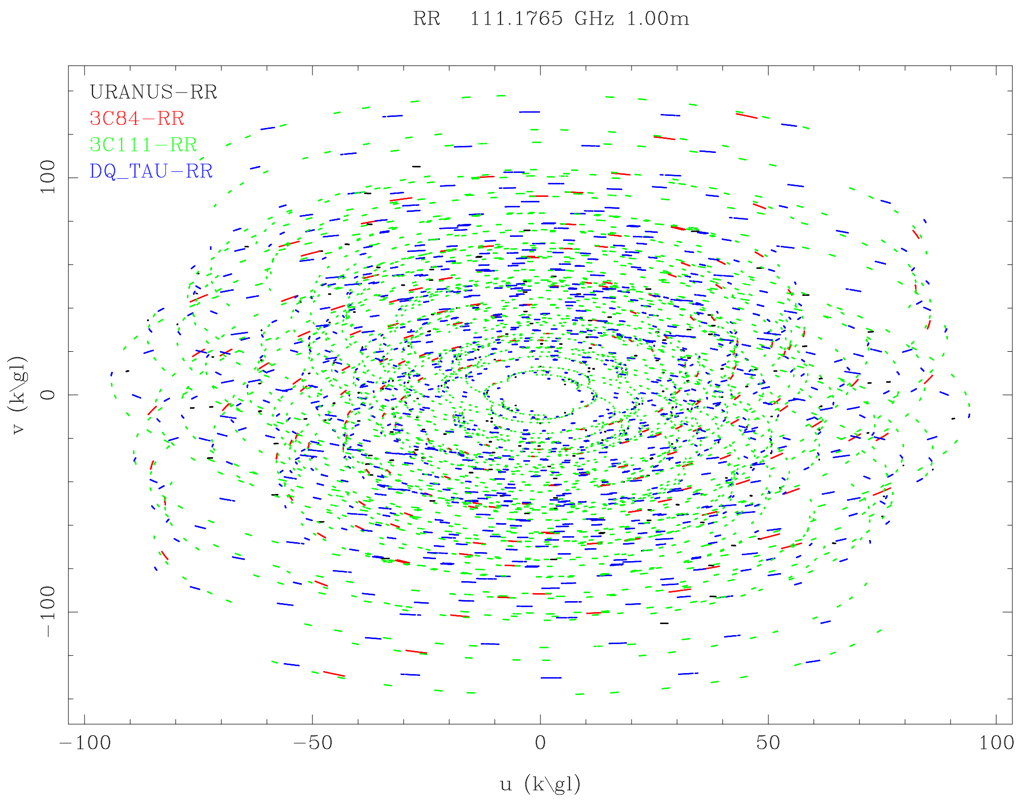

Figure 1.4 — The u, v-coverage for our CARMA C track on 2008 April 19 (see Chapter 2). The shorter (green) line segments represent the sampling for our 5-minute 3C 111 calibrator observations, while the longer (blue) segments are for each 12-minute DQ Tau on-source observation, and the longest (red) segments are the 3C 84 flux calibrator. Each grouping of nearly connected segments tracing out a curved path, represents one of the 120 baselines. For example, the arc running from $(-60, -110)$ to $(75, -110)$ shows that we observed 3C 111 fifteen times and DQ Tau five times throughout the track. The oval pattern in the coverage map is created by the rotation of the Earth during the course of a 8-hour track; each baseline will trace out an ellipse over the course of 24 hours.

radiation field (defined by $R_\star$, $L_\star$, and $T_\star$) is known, we can use dust radiative transfer calculations to reverse engineer the *output* SED and derive the temperature and density distribution of the circumstellar dust content (e.g. Dullemond & Turolla 2000). In Figure 1.5, we illustrate how four distinct SED shapes correspond to different circumstellar dust structures. In general, emission at shorter infrared wavelengths results from the warm surface layers and material closest to the star, whereas emission at longer radio wavelengths originates in the midplane and cold outer disk. As a result, when one or both of these regions is depleted of its dust, the corresponding emission is reduced, altering the SED shape. This process for deriving the large-scale dust structure is called SED modeling, and one of the biggest conclusions to be drawn from these analyses is, how the millimeter excess in particular is an important tracer of the disk structure information *and* therefore the total dust mass. With a few assumptions about the disk properties (i.e. radial size, mean dust temperature T, dust opacity κ_ν, and source distance D), a basic mass-flux relation ($S_\nu = 2\,k\,T\,\nu^2\,\kappa_\nu\,M_{\rm dust}\,/\,D^2\,c^2$) can be derived (see Beckwith et al. 1990; Dutrey et al. 1996).

SED modeling is not without its challenges, most notable of which is that the dust solutions are highly degenerate, meaning that many valid solutions exist for one SED profile. Additional constraints on the dust distribution can be made with millimeter interferometers when resolved observations detail the radial variation in the flux, in addition to the total integrated flux (e.g. Testi et al. 2001; Isella et al. 2009). In this respect, deriving the disk dust structure can be a very complicated and time-consuming

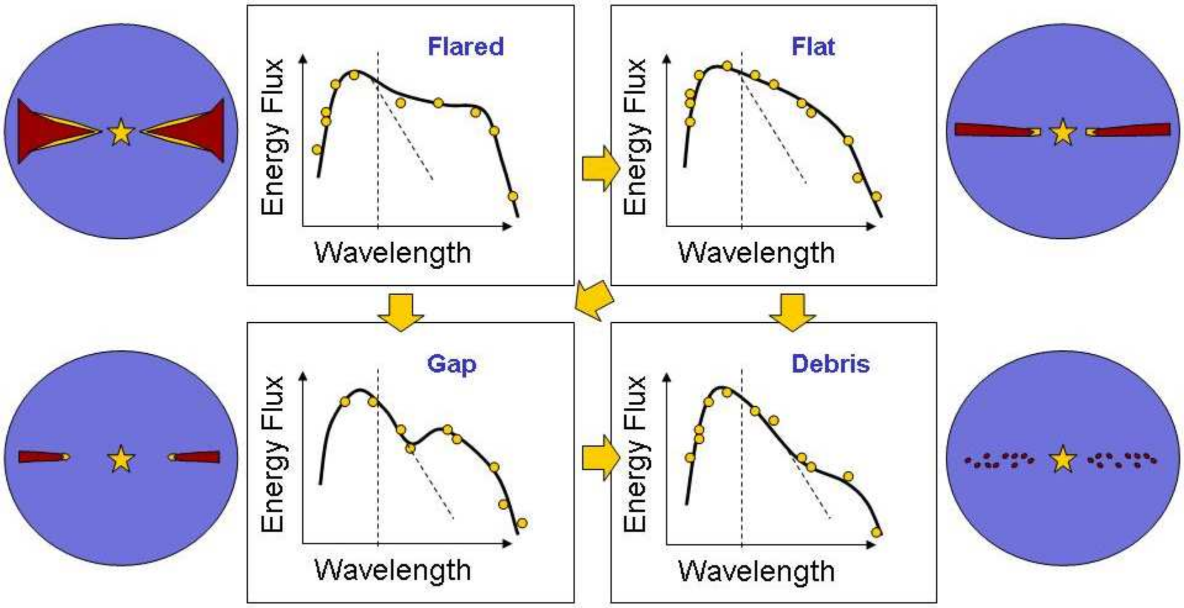

Figure 1.5 — A schematic illustrating how the spectral energy distribution (SED) of a source relates to the underlying dust structure. For example, disks with more mass, like the Flared or Flat disks, possess larger excesses at longer wavelengths. Whereas disks with inner holes, or the Gap disks, are characterized by dips at shorter wavelengths. Finally, we used arrows to indicate the potential routes for the evolution of one disk into another.

process involving many free parameters. Since there are many established dust models already available in the literature (e.g. Dullemond 2002; Dullemond et al. 2007; Robitaille et al. 2006), it is not our goal here to repeat the dust analysis. Instead, our motivation is to analyze the molecular gas content, and only then comment on the results within the context of the dust evolutionary state.

The SED profile is influenced most by the large-scale dust structure, but it can also reveal information about the current success of planet formation in the disk. One of the free parameters in the radiative transfer equations is the grain size. Larger particles intercept less radiation per unit volume, and therefore maintain colder core temperatures. Their peak thermal emission continues to shift toward longer wavelengths, until they have grown too large to efficiently radiate at millimeter wavelengths (Tanaka et al. 2005). When sufficient grain growth is occurring in the cold outer disk regions, the millimeter spectral slope will become shallower (Rodmann et al. 2006; Natta 2008; Lommen et al. 2010). Disentangling this effect due to growth from other evolutionary processes (e.g. mass loss) is trickier, but radio interferometry studies are able to confirm growth to at least a few centimeters in size (e.g. Wilner et al. 2000, 2005; Testi et al. 2001, 2003; Lommen et al. 2009), and in the case of TW Hya, predict that as much as $10^{-3}\,M_{\odot}$ could be hidden in large particles. At shorter wavelengths, the infrared regime allows us to probe grain growth in the warm surface regions of the disk. In recent years, the IRS instrument on board Spitzer has enabled astronomers to obtain the first mid-infrared spectra toward a large sample of PMS stars in Taurus (see Kessler-Silacci et al. 2006; Furlan et al. 2006). An analysis of the mid-infrared spectral slopes indicates again how shallower values are associated with grain growth and particularly dust settling. Just like in the cold outer disk regions, strong evidence for grain growth to centimeter sizes in the warm surface regions of the disk is found (e.g. Furlan et al. 2006). Finally, one additional diagnostic for grain growth in disks is the 10μm silicate emission feature. In those same Spitzer studies, strong evolutionary markers have been identified whereby the strength and shape of the 10μm silicate feature decreases with a depleting population of small sub-micron-sized grains.

In this section, we have identified four main diagnostics that we can use to describe the current dust evolutionary state in our disk samples. They include: millimeter flux as an indication of the total available dust mass; the millimeter spectral slope as a probe of grain growth at large radii; the infrared spectral slope to identify grain growth at smaller radii; and the 10μm (and 20μm) silicate emission feature as a tracer of dust settling in the upper disk layers. All these properties will affect the disk structure, opacity, and surface density, among other disk properties. Our goals now are to analyze the gas content for changes that are connected to this evolution in the dust content, which would suggest that the dust and gas evolve simultaneously.

1.2.3 Cold Gas

The gas in disks is significantly harder to observe than the dust continuum, but as already iterated, the gas represents the bulk of the circumstellar material and it is a critical ingredient in the formation of gas giants. In this section, we focus on the processes responsible for the gas-phase emission lines, the disk properties that they trace, and our modeling methods to derive the underlying chemical abundances.

The most abundant molecule in disks, and in the universe, is molecular hydrogen (H_2). Its symmetric structure, however, means that it lacks a permanent electric dipole moment and the corresponding rotational spectra, making it one of the most difficult molecules to observe (cf. Thi et al. 2001; Lahuis et al. 2007; Bitner et al. 2008). Instead, carbon monoxide (CO) is a logical alternative tracer of the cold gas. While its most abundant isotope ^{12}CO is a roughly constant 10^{-4} times less abundant (in number) than H_2 (Frerking et al. 1982; Lacy et al. 1994; Terzieva & Herbst 1998), it is a stable molecule once formed, easy to excite, and possesses the greatest number of strong rotational lines in the millimeter regime, making it one of the most accessible molecules to observations. However, in stark contrast to the dust, molecular line emission is restricted to discrete emission frequencies, and it can only be produced when the local (H_2) density is larger than the critical value for a particular transition. The required density is determined by the collisional pumping needed to offset the spontaneous radiative decay process. This means that molecular transitions with a high critical density can only produce significant emission in high density regions. These excitation properties, which make for fainter lines and more challenging observations, also provide a clever way to trace different density regions within the disk by using a variety of molecular species and rotational transitions. The ^{12}CO molecule is itself characterized by relatively low critical values, meaning that it is capable of tracing most disk conditions, from densities of about 10^{12} molecules per cm^{-3} in the disk midplane to 10^{3} molecules per cm^{-3} at the disk surface. The unfortunate trade-off is that the brightest ^{12}CO lines, with the largest column densities, are then more likely to be optically thick, and so effectively we only probe the upper disk layers (Dutrey et al. 1996, 2003). In addition, processes including freeze-out onto grains can remove CO from the gas-phase in cold and dense regions, depleting its column density in the midplane. When possible, ^{13}CO or C^{18}O are often used in combination, as optically thinner tracers that are expected to probe the entire disk (van Zadelhoff et al. 2001).

Additional bright molecular lines that we will probe in our research include HCO^{+}, HCN, and CN. These molecules have H_2 abundance ratios of 10^{-8}–10^{-9} in molecular clouds (see Terzieva & Herbst 1998), but their ratios are expected to increase in the presence of a strong ionizing X-ray source, like near a magnetically active young star (Lepp & Dalgarno 1996; Aikawa & Herbst 2001; Glassgold et al. 2004). T Tauri stars also possess relatively intense UV radiation, which efficiently photodissociates HCN into its components H and CN (Lepp & Dalgarno 1996; Aikawa et al. 2002; van Zadelhoff et al. 2003). X-ray ionization and UV photodissociation are two of the main drivers of the gas chemistry and gas dispersal in disks. Now by choosing comparable transitions (in terms of excitation energy) from different molecules,

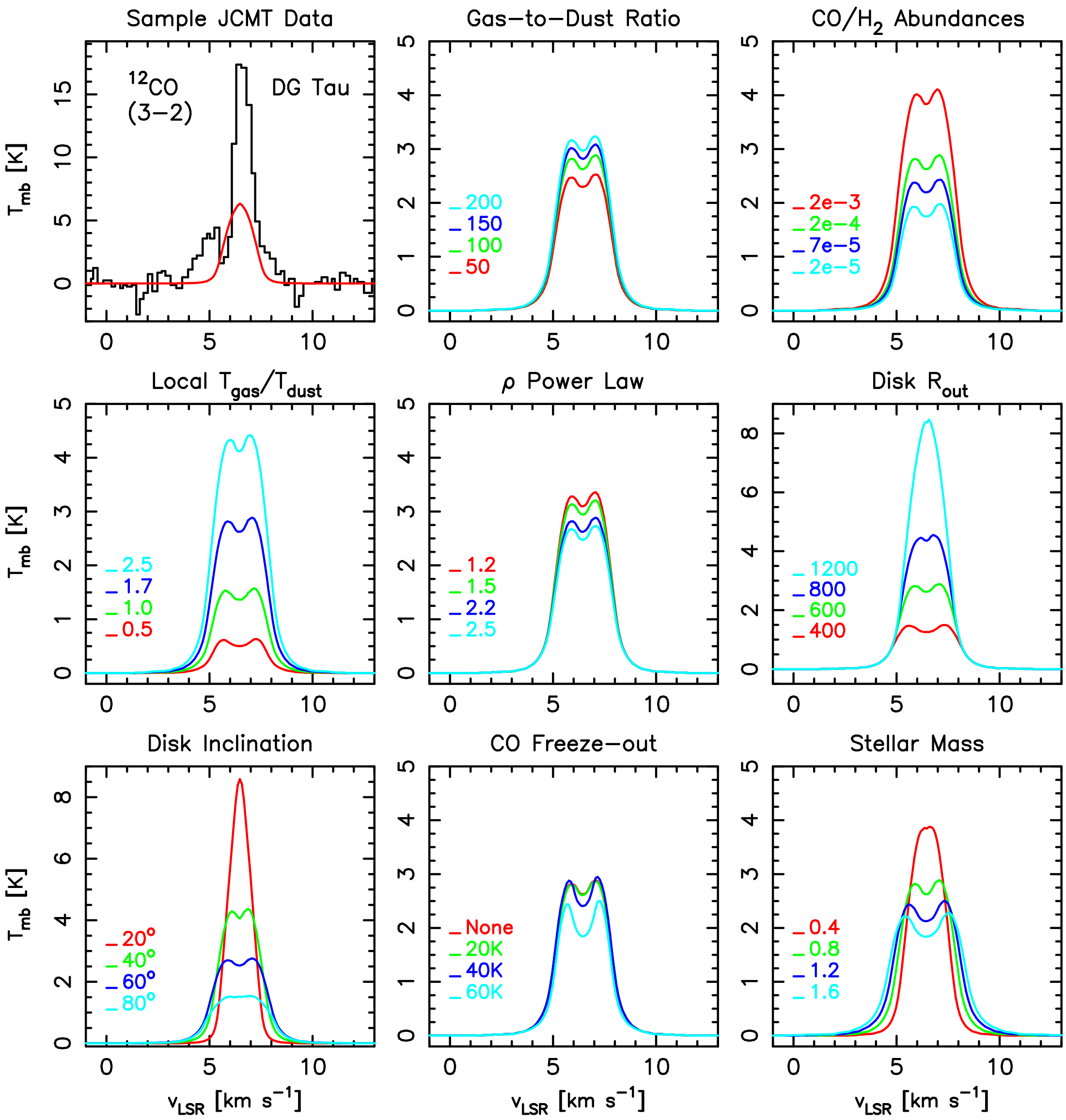

Figure 1.6 — Line models show how altering one parameter changes the predicted ^{12}CO (3–2) line profile for an unresolved disk. Shown from left to right, top to bottom (with default values in parentheses) are: the sample JCMT data and best fit for DG Tau showing contamination from bright cloud emission near $v_{\rm LSR} = 6.1\,{\rm km\,s^{-1}}$ and broad outflow wings (refer to Chapter 2), varying the dust-to-gas ratio (100), varying the CO/H$_2$ abundance ratio (2×10^{-4}), adjusting the gas kinetic temperature with respect to the local dust temperature (1.0), modifying the density power law (1.5), extending the disk to a different outer radii (600 AU), varying the disk inclination (60°), including CO freeze-out below different temperatures (no freeze-out), and altering the kinematical velocity profile by changing the central stellar mass ($0.8\,M_\odot$).

we can probe the same (or similar) disk region and look for variable molecular compositions that trace the level of X-ray ionization and UV photodissociation processing occurring in a uniform sample of disks (see Chapter 2). It is not our intent here to study the large chemical networks in disks, but rather, to apply those results to characterize the relative gas-phase content and chemical evolutionary state in similar disks.

Since several physical parameters of the gas disk may differ from the dust-defined disk structure, we show in Figure 1.6 how changing one parameter at a time alters the predicted line profile for an unresolved disk. By far, the largest effects on the line intensity are the disk inclination and the outer gas radius, which is consistent with the fact that we detect larger gas disks in face-on orientations more often (Chapter 2). We can also see how, for example, the disk inclination and the central stellar mass are degenerate parameters, since both line profiles become stronger and narrower when these parameters are decreased. Similarly, we can increase the line intensity without affecting the line width by either increasing the gas-to-dust ratio or decreasing the density power law in the outer disk. These degenerative effects illustrate why it is challenging in single-dish data to derive the disk gas structure from the gas-line information alone. Resolved observations, on the other hand, allow us to extract the kinematics of the disk ($M_\star \sin i$), the outer radius ($R_{\rm gas}$), and the radial variation in the surface density; which also happen to be disk properties that are not accessible via dust observations. Unfortunately, modern interferometers can only resolve about 3–5 pixel elements across the face of most disks and only with very long-duration observations. This is where ALMA will have a dramatic impact on protoplanetary disk studies.

In the meantime, when we cannot directly compare the (radial and vertical) distribution of the gas and dust reservoirs, our strategy is to populate the solution for the dust structure with the canonical gas abundances, and then compare the resulting line predictions to the real data. A match suggests that the dust and gas structures are well coupled; a mismatch may indicate otherwise.

1.2.4 Relativistic Electrons

The study of synchrotron emission, or the signature radiation emitted by relativistic electrons spiraling along a magnetic field line, is usually restricted to the radio regime when studying PMS stars. There the electron energies involved are consistent with the surface magnetic field strengths typical of T Tauri stars (1–6 kG, or about 1000 times stronger than the Sun's field) (Basri et al. 1992; Johns-Krull et al. 1999). Thus, the discovery of transient high-energy non-thermal emission at millimeter wavelengths is of great interest, especially considering the presumed quiescent nature of the millimeter emission from disks. In this section, we review the role and impact of magnetic fields in T Tauri systems, and then shift our focus to magnetic interactions between stars in close-separation, high-eccentricity binary systems.

In a single CTTS scenario, the central source truncates the inner circumstellar disk in two ways. First, the stellar radiation field photoevaporates dust grains within a region where dust temperatures are ≥ 1500 K, creating a sharp inner dust edge. The second mechanism involves the radius at which material free-falls onto the star, and accretes. This is usually defined by the boundary where the magnetic field pressure is equivalent to the rotation pressure of the disk (governed by the gas kinematics). Within this corotation radius (at about 5 AU), the stellar magnetic field lines channel material onto the star; and beyond this boundary, the field lines become frozen to the Keplerian disk movements and act to slow the stellar rotation (Ghosh & Lamb 1978; Shu et al. 1994). These processes are the foundation of the magnetospheric accretion model, and in Figure 1.7 we illustrate the large-scale topological structure of the stellar magnetic field lines. As long as there is disk material at the co-rotation radius, the CTTS is expected to accrete at the observed rates of about 10^{-7}–$10^{-10}\,M_\odot$ per year (Hartigan et al. 1995; Gullbring et al. 1998). As the inner disk edge migrates outward over time, however, accretion may be halted. This occurs when the disk is photoevaporated from the inside-out or when material in the region is swept up into a protoplanet. At which point, the disk disperses rather rapidly, and the star begins to spin up (Bouvier et al. 1993, 1997). In this scenario, a rotationally generated stellar magnetic dynamo easily explains why a faster-spinning WTTS is even more magnetically active than a disk-bearing CTTS, as determined from X-ray surveys that credit the magnetic activity primarily to coronal reconnection events, or stellar flares (Stassun et al. 2006; Güdel & Nazé 2009).

Stellar flares, like solar flares, release magnetic energy when oppositely-directed field lines in the corona are forced together and re-connect to establish a more stable field configuration (Haisch et al. 1991, for a review). Reconnection is often associated with strong radio, optical, UV, and X-ray out-

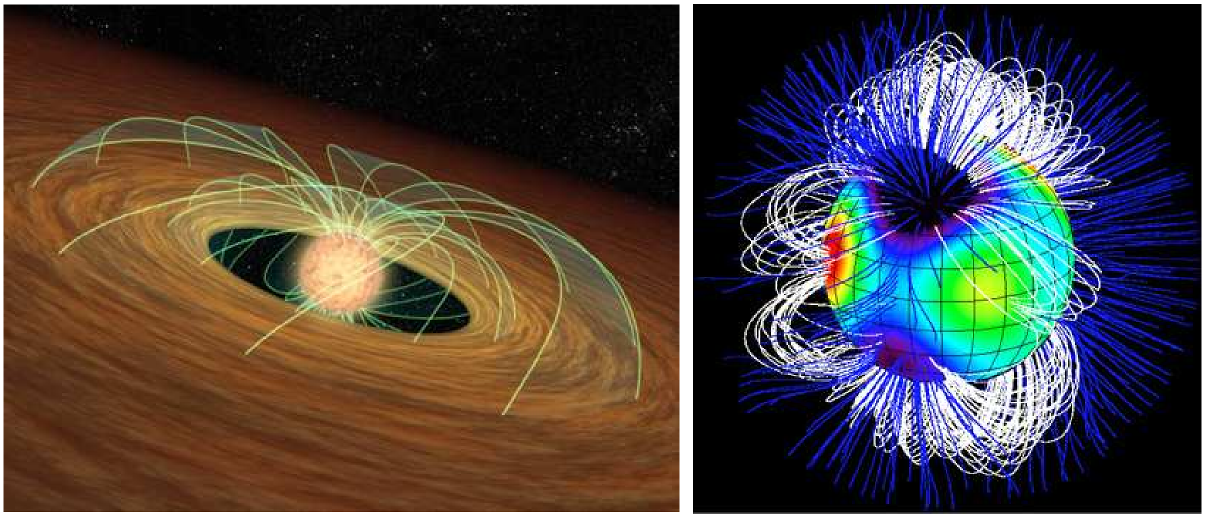

Figure 1.7 — At left, an artist's impression of the stellar magnetic field lines interacting with the circumstellar disk. Near the inner disk edge, material accretes onto the central star via the field lines. At larger radii, the field lines are tied to the disk motions, effectively slowing the stellar rotation. (*Credits: NASA / JPL-Caltech / R. Hurt of SSC*); At right, a topographical view of the magnetic field lines around the star τ Scorpii. Open field lines allow charged particles (and angular momentum) to be ejected from the system with the help of stellar winds. Closed loops indicate where charged particles can become trapped close to the star. (*Credits: ESPaDOnS / CFHT*)

bursts. The released magnetic energy is first converted to kinetic energy when charged particles in the region are accelerated, sometimes to relativistic speeds, and spiral down along the field lines emitting synchrotron radiation at radio frequencies. Then, when the charged particles collide with the stellar atmosphere at one of the two magnetic footprints, the particles heat and ionize the chromospheric plasma, resulting in optical, UV, and X-ray emission. In addition to these single-star magnetic events, other scenarios for reconnection include magnetic interactions between a star and its accretion disk, a star and a planet forming within its circumstellar disk, or a star and a stellar companion (Phillips et al. 1991). An interesting development from recent long-duration X-ray surveys is the once-a-week statistical occurrence of giant X-ray flares, which are consistent with T Tauri surface field strengths and coronal loop structures stretching to many stellar radii (Favata et al. 2005; Getman et al. 2008a,b). This presents an interesting scenario for close-separation binaries that can incur star-star magnetic field interactions (Massi et al. 2002, 2006, 2008; Salter et al. 2008, 2010, Chapters 4 and 5).

Since most stars form in multiple-star systems, there is an established need to study planet formation in these systems as well (Leinert et al. 1993; Simon & Prato 1995). Traditionally, the stellar dynamics were believed to effectively disrupt the disk and prevent stable planetary orbits. On the contrary, observational evidence for exoplanets have been found in a variety systems, including binary and triple systems (Raghavan et al. 2006), around primary host stars with both short- and long-period stellar companions (Chauvin et al. 2006; Eggenberger et al. 2007), and in circumbinary disks around close-separation (≤ 50 AU) binaries (Patience et al. 2002). However, tight binaries like the ones we study in this thesis, present additional challenges to planet formation. Theoretical models derive shorter disk lifetimes, primarily due to tidal truncation of the inner disks (Duchêne 2010), and observational studies show significantly reduced millimeter excess and accretion rates (Beckwith et al. 1990; Jensen et al. 1994). However, one open question in binary star research today concerns how some binaries can continue to accrete across large inner gaps when others cease. Some models are able to show how the dynamical motions in a high-eccentricity system can periodically perturb the outer circumbinary disk, causing material to flow in pulses towards the inner rim, overcoming the tidal barrier and accreting across the gap (Artymowicz & Lubow 1996). We now recall how close binaries, or binaries with small periastron approaches, can experience star-star magnetic interactions. Thus, given the star-disk connection via the magnetospheric accretion model, we must question how a significant re-organization of the stellar magnetosphere might affect material in the disk where the open stellar field lines end. In other words, is it possible that reconnection events can assist, hinder, or explain pulsed accretion processes in these systems?

As it turns out, we can also study high-energy processes in the millimeter spectrum toward PMS stars. Relativistic electrons accelerated by powerful star-star reconnection events can allow us to sample T Tauri magnetic field strengths, sizes, and regeneration timescales. The potential impact for the circumbinary disk lifetime might include assisting or hindering accretion across gaps, extending viscous timescales, or removing more gas from the system through elevated levels of associated X-ray and UV activity. With regards to standard SED modeling of (unresolved) dust continuum fluxes, it should be cautioned that non-thermal contributions will adversely affect the best-fitting solution.

1.2.5 In the Laboratory

One additional way to study planet formation processes is in the laboratory. This requires re-creating the circumstellar disk conditions of a high vacuum ($\ll 10^{-2}$ mbar), cold temperatures (10–300 K), and a reduced-gravity ($\sim 0g$) environment. One additional caveat is that the physical process to be studied must be smaller than one's laboratory. In Chapter 7, this concerned a cylindrical vacuum chamber 110 mm high and 180 mm in diameter (Salter et al. 2009). The subject of the experiment is the collisional grain growth mechanism that currently forms the basis of the core accretion model for planet formation. In Section 1.1.2, we discussed the theoretical challenges to grain growth beyond centimeter sizes (e.g. Dominik & Tielens 1997; Paszun & Dominik 2009). In Chapter 7 we present the construction and early results of an experiment performed during a parabolic flight campaign organized by the European Space Agency (ESA). The flight maneuver simulates weightlessness for a period of 22 seconds (see Figure 1.8), thus achieving the longest duration reduced-gravity experience without going into space. Within this period,

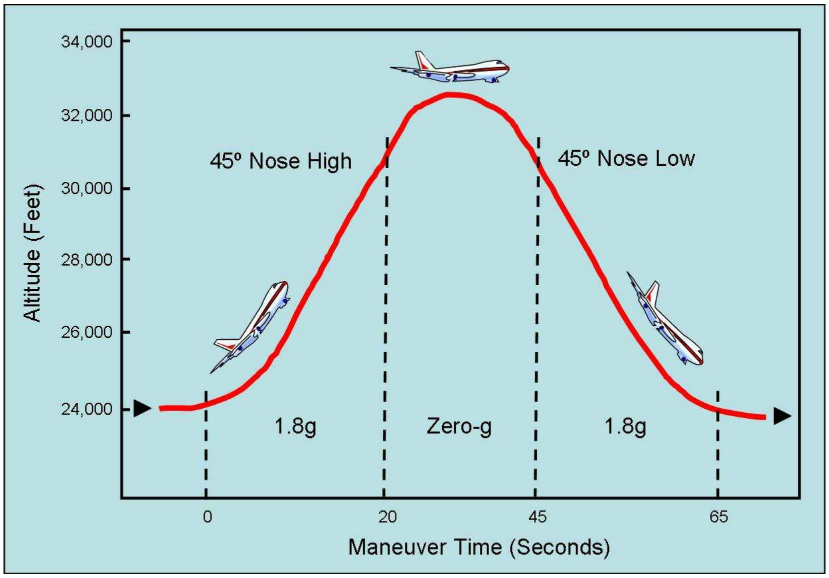

Figure 1.8 — A schematic of the flight profile during a parabolic flight campaign organized by the European Space Agency. A parabolic flight maneuver is just one way to approximate the zero-gravity conditions in a protoplanetary disk when performing experiments to test small-scale processes in disks in 22-second segments.

our goal was to execute several collisions of millimeter-sized protoplanetary dust analogs, and record with unobstructed views the outcome of each collision. This was best accomplished with single collision events, with the turnover time between events determined by the time needed to slowly accelerate each dust analog to the collisional velocity regime being investigated while preserving their porous structure. With the experiment setup defined in the last chapter, a broad range of particle sizes (from millimeter to centimeter), compositions (dust, ice, and dust-ice analogs), temperatures (80–300 K), and velocities (from 1.0–0.1 $\mathrm{m\,s^{-1}}$) are capable of being studied. In this way, we can test in our own laboratories the small-scale planet formation processes occurring in disks many hundreds of parsecs away, and the same processes thought to be responsible for the formation of our own Solar System.

1.3 This Thesis

This thesis is split into three parts. In **Part I** of the thesis, we pursue observational clues from thermal emission processes to address what happens to the gas content in disks as the dust evolves. For example, in **Chapter 2** we examine specifically the effects that grain growth and dust settling have on the photoprocessing of the molecular gas (HCO^+, HCN, and CN) content. In **Chapter 3** we investigate the observational relationship between the CO gas-line measurements and the dust diagnostics. The studies in Part I are helping to identify the most (or least) influential processes driving the disk evolution, and to determine which of our current observational diagnostics are the most robust. **Part II** of the thesis emerged in the midst of observations for Part I, and it cautions against the long-standing notion that the millimeter flux observed toward young PMS stars is always dominated by the quiescent thermal emission from passively heated dust located in a circumstellar disk. In **Chapter 4** we report the serendipitous discovery of a transient millimeter flare toward the young spectroscopic binary DQ Tau; the first millimeter outburst to be documented toward a CTTS. In **Chapter 5** we confirm the recurring nature of the DQ Tau phenomenon. Then, in **Chapter 6**, we consider the proliferation of millimeter flares in a broader sample of young binaries targeted because their orbital parameters were similar to DQ Tau, and thus, presumably susceptible to the same phenomenon. As it turns out in Part II of this thesis, the monitoring of young pre-main-sequence binaries at millimeter wavelengths provides an interesting window into star-star magnetospheric interactions in binary systems. Finally, given the observational challenges present in the first two parts of the thesis, **Part III** documents a laboratory approach to investigate directly the coagulation theory of grain growth in protoplanetary disks. Described in **Chapter 7** are the technical details and initial scientific results of a parabolic flight experiment to study the low-velocity collisional properties of millimeter-sized dust particles. What follows now is a detailed overview of each chapter, concluding with the main results that can be drawn from each study.

1.3.1 Outline of Chapters

In **Chapter 2** we use HCO^+, HCN, and CN gas-line observations and modeling to search for increased photoprocessing effects when the small-grain population in the upper disk layers has been reduced via grain growth and dust settling. This study represents one of the few observational analyses of rarer molecular species toward a large, uniform sample of disks. Using the JCMT, combined with the line data already in the literature, we found no significant trends between the observed gas-line diagnostics (i.e. line strengths, ratios, and integrated fluxes) and either the dust diagnostics (i.e. silicate emission features, mid-infrared slopes, or 1.3 mm fluxes) or several stellar properties (i.e. $M_\star$, L_bol, L_X, or Hα EW). In other words, the expected molecular enhancements do not seem to correlate with the total dust mass or the presence of small grains in the inner and upper disk layers based on the observed line emission, which is most sensitive to the bulk of molecular gas in the outer disk (Figures 2.5–2.7). To derive the underlying (disk-averaged) molecular abundances, we used two different dust model prescriptions from the literature to approximate the temperature and density structure of the gaseous component. The models struggle to reproduce the gas lines, mostly due to system parameters that are not well constrained by the SED (i.e. $M_\star$, i, $R_{\rm gas}$, and $T_{\rm kin}$) and instead represent just one combination of many suitable fits to the profile (Figures 2.8–2.9). We proceeded to model the source DG Tau in greater detail, discovering a reasonable fit to the gas-line data when $M_\star$, i, $R_{\rm gas}$, and $T_{\rm kin}$ were modified (Figures 2.10–2.11). The modeling of DG Tau illustrates the potential discrepancies between the line ratios as abundance tracers and the true underlying abundances, with the measured CN/HCN line ratio (> 12) a factor 13 less than the fitted underlying abundance ratio (> 160). Instead, resolved observations of both the dust and gas alike are necessary in order to contrast their evolution more completely.

We present, in **Chapter 3**, interferometric observations of ^{12}CO ($J = 1$–0) toward five bright CTTSs in Taurus that are presumed gas-rich (from their dust continuum emission); as well as supplementary ^{12}CO ($J = 2$–1) observations toward one of these sources. These observations complete the interferometric sampling of a CO rotational line toward Taurus disks with a 1.3 mm flux ≥ 75 mJy. We report CO emission from three sources, where all integrated spectra are characterized by narrow emission peaks with multiple components spread over a wide velocity range ($< 12\,\mathrm{km\,s^{-1}}$). We find no significant trends in the CO line intensity or detection statistics with any of the current diagnostics for the dust evolutionary state; both in our subsample and in the current literature. We conclude for four of the sources that the CO line profile is obscured by large amounts of optically thick CO along the line-of-sight, which appears as a common trend in most spatially resolved CO analyses. As a result, we caution that observations of the lowest rotational lines of CO are an incomplete tracer of the total gas content, and therefore not a good probe of the gas evolution. We recommend that future observations focus on higher rotational transitions of CO, particularly with ALMA when improved sensitivity capabilities will allow for the detection of these higher frequency transitions.

In **Chapter 4** we report the discovery of a millimeter flare toward the spectroscopic binary DQ Tau in the Taurus star-forming region. The 2008 April 19 detection is the *first* millimeter outburst to be observed toward a classical T Tauri star. The activity was recorded during a 5-day survey of the quiescent thermal emission toward several protoplanetary disks in Taurus using the CARMA array (see Chapter 3). While the other four sources maintained a quiescent flux throughout the survey, DQ Tau brightened on the third night to reach a maximum detected flux of 468 mJy, almost 27 times its quiescent value, within a 2-hour period (Figure 4.1). We attributed the emission to synchrotron radiation. The two stars have a minimum separation of 8 $R_\star$ at their closest approach, whereby their magnetospheres (of theoretical size 5 $R_\star$) are predicted to overlap (Mathieu et al. 1997; Basri et al. 1997). Since the peak of our observed flare occurred just 7.6 hours before periastron, we make a case for colliding magnetospheres and predict that the flare mechanism is linked to the binary orbit and therefore likely to repeat. We also remark that the millimeter activity of DQ Tau could be linked (strictly in timing or via magnetospheric accretion theory) to the variable accretion bursts that explain the source's optical variability. In a broader context, these findings present a significant cautionary tale for millimeter flux points in the SEDs used for disk modeling that could include non-thermal emission contributions if measured only once.

Chapter 5 is a natural follow-up to the initial DQ Tau flare analysis and its implications for millimeter-wave studies of protoplanetary disks. There we present light curves covering a period of 8–16 hours near three additional periastron encounters where we again detected excess flux at 3 mm (Figure 5.1). An analysis of the similar exponential decay profiles allows us to estimate an average flare duration of 30 hours (Figure 5.3). The consistent timing of the flares within a 22-hour window near periastron, corresponding to stellar separations of 8–13 $R_\star$, supports the periodic nature expected from a scenario for colliding magnetospheres (Figure 5.4). We are also able to constrain the main synchrotron emission region to a stellar height of 3.7–6.8 $R_\star$, or about half the stellar separation distance at the time of an event. Assuming a well-ordered dipole topology for each magnetosphere beyond a radius of 3.7 $R_\star$, we determine that the magnetospheres must be misaligned at a significant angle in order for the observed reconnection events to occur (Figure 5.8). We also speculate on an interesting scenario for on-and-off periods of flaring if the magnetic axis of one of the stars was to flip, as occurs in the Sun every 11 years. Otherwise, assuming one 30-hour flare per orbit, DQ Tau could spend as much as 8% of its 15.8-day orbital period in an elevated flux state. In combination with these millimeter observations, we coordinated simulataneous optical (as well as X-ray, see Getman et al. 2010, submitted) monitoring of DQ Tau, which shows that accretion activity can occur coincident in both time and duration with the synchrotron fallout of a magnetic reconnection event (Figure 5.7). Whether a causal or co-dependent relationship between the reconnection and accretion processes is in effect remains undetermined. The potential for bi-weekly flares, on the other hand, exposes the disk to highly elevated levels of X-rays (perhaps up to 100 times brighter in peak luminosity Getman et al. 2008a) and UV radiation; levels that are more likely to destroy HCO^+ and CN rather than enhance their fractional abundances (Lepp & Dalgarno 1996). This probably contributes to the non-detection of both molecules in the JCMT spectra toward DQ Tau (Chapter 2). In this way, we highlight the unknown effects of the stellar magnetospheric activity on disk lifetimes and the destruction processes affecting the gas reservoir.

Chapter 6 considers the proliferation of millimeter flares toward young stars. Stars possess stronger magnetic fields and exhibit their highest levels of magnetic activity during the PMS stage, as documented by recent X-ray surveys (e.g Güdel et al. 2007; Getman et al. 2008a,b). Given the current evidence for colliding magnetospheres in the DQ Tau PMS binary system, as well as the favorable statistics for close-separation binaries, we conducted a targeted monitoring program of the millimeter emission toward a sample of young spectroscopic binaries using the IRAM 30-meter telescope; the first dedicated survey to search for millimeter variability toward PMS stars. The sample includes six binaries of high orbital eccentricity ($e \geq 0.1$) and six binaries with roughly circular orbits ($e \approx 0$). The second group serves as a control sample, since the magnetospheres are not expected to periodically re-organize if the separation distance between the stars is constant throughout the orbit. On the other hand, a statistically significant occurrence of flares in these systems, would suggest an alternative flare mechanism is responsible, or more prevalent. Over five consecutive nights, during which each of the six high-eccentricity binaries completed periastron, only one source displayed millimeter variability. The source, UZ Tau E, is the one that most resembles DQ Tau in terms of orbital parameters and optical accretion activity. We observed a flux range for the combined hierachical quadruple system UZ Tau of 107–199 mJy (see Figure 6.1). The sparsely-sampled light curve, which does not resolve the E and W components of this hierarchichal quadruple system but does cover a broad period around periastron, exhibits behaviors that were predicted in Chapter 5, such as a double brightening and a faster flux decay time at larger stellar separations. The component UZ Tau E appears to be highly variable based on many previous millimeter interferometric observations at different wavelengths, perhaps statistically indicative of activity at many different orbital phases. Therefore, we are unable to confirm definitively that the multiple brightenings observed in this system near one periastron are uniquely explained by colliding magnetospheres. Still, UZ Tau E does present a strong case for multi-wavelength follow-up observations similar to those of DQ Tau. It also suggests that millimeter activity may be more common among PMS stars.

In the final chapter, **Chapter 7**, we use a laboratory experiment to probe grain growth processes in disks. We specifically test the core accretion model for planet formation by colliding protoplanetary dust analogs together in a simulated disk environment. The experiment consisted of two scenarios. In the first, we began by firing individual aggregates at a large target of similar, but denser, dust structure to represent a collision with a larger particle. We then followed with collisions between similarly-sized aggregates. We recorded over 100 separate impacts at 107 frames per second during 33 minutes of combined weightlessness. The results of this warm dust experiment probing collisions of particles measuring 0.2–6 mm across and traveling at speeds of 16–18 $\mathrm{cm\,s^{-1}}$ in ambient temperatures (300 K), showed that the majority of collisions (roughly 80–90%) resulted in semi-elastic re-bounding events. On average, only 15% of the translational energy is conserved during most events, probably due to aggregate compaction. Sticking was observed in only 10% of the particle-target collisions, and fragmentation occurred in roughly 10% of the aggregate-aggregate collisions. These results seem to indicate a critical transition regime for the collision velocities of dust aggregates when interactions start to become more destructive than constructive. Follow-up experiments with icy particles, expected to possess stronger molecular bonds, indicate similar "transition-zone" results (see Heißelmann et al. 2010). Our laboratory results confirm the predicted challenges for the core accretion model when it comes to collisonal growth beyond millimeter-sized aggregates.

1.3.2 Main Results

This thesis covers three major topics in the field of protoplanetary research: 1. The evolution of the dust and gas content with respect to one another, as deduced from observational studies of thermal emission diagnostics; 2. The nature and proliferation of transient non-thermal millimeter flares; and 3. The collisional grain growth processes in protoplanetary disks. The main results of these studies can be summarized in the following bullet points:

- Observations of 21 disks in Taurus show no correlations between their HCO$^+$, HCN, and CN line fluxes or ratios (which trace ionization and photodissociation processes) and their mid-infrared slopes or 10μm silicate emission features (which trace successful grain growth and dust settling). Therefore, the properties and evolution of the regions that dominate the gas-line emission ($R \gtrsim 100$ AU) appear unrelated to the ($R \lesssim 30$–100 AU) regions probed by common tracers of the dust properties and evolution. (Chapter 2)

- Modeling of unresolved gas-line observations is unable to break the degeneracies in the dust model fits. We show for the gas-rich disk around DG Tau how two very different disk temperature and density profiles can produce very similar lines for the same fractional abundances. However, this does not, in turn, necessitate that the abundance estimate is robust. Therefore, gas-line measurements and resolved observations of the dust and gas alike are needed to arrive at the full picture. (Chapter 2)

- Observations of low-J rotational lines of CO toward the brightest ($F_{1.3\mathrm{mm}} \geq 75$ mJy) objects in Taurus reveal very different CO line intensities for dust disks with similar mass, grain growth, and dust settling properties. In addition, two sources that are equally bright in one CO transition line do not necessarily possess similar brightnesses in another transition. Almost all sources exhibit at least some level of obscuration from optically thick CO along the line-of-sight, accounting for some of these observational differences. We caution that low-J transition lines of the main CO isotopologue are often an incomplete tracer of the total gas content and disk dynamics, and therefore not a robust probe of the gas evolution. (Chapter 3)

- Millimeter flares in the DQ Tau PMS binary system ($d_{\mathrm{min}} = 8.1\,R_\star$, $e = 0.56$, and $P = 15.8$ days) are recurring and can be explained by synchrotron emission initiated by a magnetic reconnection event when the two stellar magnetospheres collide during periastron passage. The derived coronal loop sizes of $\sim$3–5 $R_\star$ and surface field strengths of $\sim$3 kG are consistent with T Tauri magnetospheric values and a reconnection site located halfway between the two stars. Consistent activity during 4 separate periastron encounters indicates that the DQ Tau magnetospheres are capable of regenerating their fields on a bi-weekly basis. (Chapters 4 and 5)

- We report that another PMS binary, UZ Tau E, shares similar orbital properties ($d_{\mathrm{min}} = 11.6\,R_\star$, $e = 0.33$, and $P = 19.1$ days) and tentatively exhibits comparable activity (brightens by a factor 2 on two separate occassions). Short-period, close-separation, and high-eccentricity binaries are most likely to experience the same phenomenon, properties that characterize a large number of young stellar systems. (Chapter 6)

- Our flare statistics caution against the long-held notion of a purely quiescent millimeter spectrum and emphasize the need for better characterization of the millimeter variability towards young stars, particularly when relying on one-time millimeter flux measurements to derive the dust (spectral slope) properties and the underlying disk structure. While peak values like those seen toward DQ Tau ($\sim$0.5 Jy) are rarer—but more easily recognized—smaller increases of a factor 2–3 like those observed toward UZ Tau E may remain unnoticed and be more common. (Chapers 5 and 6)

- The collisional growth mechanism for dust (and ice) particles in disks becomes less effective as particles approach centimeter-sizes and 1 $\mathrm{m\,s^{-1}}$ velocities with $\sim$90% of our dusty aggregate collisions resulting in re-bounding events during our initial microgravity experiment. Our laboratory results, together with recent follow-up experiments and complementary theoretical models, suggest that an alternative growth mechanism must be invoked at the intermediate growth stages in order to achieve meter-sized boulders and runaway growth via self-gravity. (Chapter 7)

1.3.3 Outlook

One of the most exciting developments soon to hit the field of protoplanetary disks research at millimeter wavelengths is the newest revolution in astronomical instrumentation, and one of the most ambitious astronomy projects ever undertaken, and that is ALMA. The interferometric telescope will consist of no fewer than 66 individual antennas, defining 2016 separate baselines ranging 15–16,000 meters in length. The antenna receivers will operate at wavelengths of 0.3–9.6 mm, corresponding to 10 frequency bands spanning the 31–950 GHz range. ALMA is currently being constructed at the Chajnantor plateau in the Atacama desert in Chile, one of the driest regions on Earth at an altitude of 5000 m, which puts it above 50% of the Earth's atmosphere, drastically reducing the sky background noise levels. Early science is slated for late 2011 when the first 16 antennas are in place. The array, when complete, will possess an unprecendented combination of sensitivity, angular resolution, spectral resolution, and imaging fidelity (Kurz & Shaver 1999).

In the future, it is our goal to compare the radial gas variations and chemical abundances, which will help us derive better, more complete disk models; and extend our work in Chapters 2–3 (Part I). ALMA will help by drastically reducing the time required for large, multi-epoch surveys, and subsequently allowing us to better characterize any time-dependent millimeter variability toward young stars, as we have initiated in Chapters 4–6 (Part II) of this thesis. As far as identifying the first stages of planet formation, many simulations to date predict that ALMA has the potential to detect the tidal effects of embedded protoplanets in disks using continuum studies (Wolf & D'Angelo 2005), or use high-lying molecular transitions of $\mathrm{HCO^+}$ (or any other dense tracer) to detect disk instabilities or clumpiness (Narayanan et al. 2006). Whereas we show in Chapter 7 (Part III) how the collisional growth mechanism for planet formation faces challenges in both theory *and* experiment, ALMA may provide more definitive, observational evidence to test the current planet formation theories. These are just a few highlights of the possibilities with ALMA, as related to the subjects presented in this thesis.

Bibliography

Aikawa, Y. & Herbst, E. 2001, A&A, 371, 1107
Aikawa, Y., van Zadelhoff, G. J., van Dishoeck, E. F., & Herbst, E. 2002, A&A, 386, 622
Alexander, R. 2008, New A Rev., 52, 60
Alexander, R. D. & Armitage, P. J. 2007, MNRAS, 375, 500

André, P., Ward-Thompson, D., & Barsony, M. 1993, ApJ, 406, 122
Andrews, S. M. & Williams, J. P. 2005, ApJ, 631, 1134
Andrews, S. M. & Williams, J. P. 2007, ApJ, 659, 705
Andrews, S. M., Wilner, D. J., Hughes, A. M., Qi, C., & Dullemond, C. P. 2009, ApJ, 700, 1502
Artymowicz, P. & Lubow, S. H. 1996, ApJ, 467, L77+
Aumann, H. H., Beichman, C. A., Gillett, F. C., et al. 1984, ApJ, 278, L23
Banzatti, A., Testi, L., Isella, A., et al. 2010, ArXiv e-prints
Baranne, A., Queloz, D., Mayor, M., et al. 1996, A&AS, 119, 373
Barge, P., Baglin, A., Auvergne, M., et al. 2008, A&A, 482, L17
Basri, G., Johns-Krull, C. M., & Mathieu, R. D. 1997, AJ, 114, 781
Basri, G., Marcy, G. W., & Valenti, J. A. 1992, ApJ, 390, 622
Basu, S. 1998, ApJ, 509, 229
Beckwith, S. V. W., Henning, T., & Nakagawa, Y. 2000, Protostars and Planets IV, 533
Beckwith, S. V. W., Sargent, A. I., Chini, R. S., & Guesten, R. 1990, AJ, 99, 924
Bergin, E. A. 2009, ArXiv e-prints
Bergin, E. A. & Tafalla, M. 2007, ARA&A, 45, 339
Bitner, M. A., Richter, M. J., Lacy, J. H., et al. 2008, ApJ, 688, 1326
Bizzarro, M., Baker, J. A., Haack, H., & Lundgaard, K. L. 2005, ApJ, 632, L41
Blum, J. 2010, ArXiv e-prints
Blum, J. & Wurm, G. 2008, ARA&A, 46, 21
Blum, J., Wurm, G., Poppe, T., Kempf, S., & Kozasa, T. 2002, Advances in Space Research, 29, 497
Boden, A. F., Akeson, R. L., Sargent, A. I., et al. 2009, ApJ, 696, L111
Bok, B. J. 1948, Harvard Observatory Monographs, 7, 53
Borucki, W. J., Koch, D. G., Lissauer, J., et al. 2007, in Astronomical Society of the Pacific Conference Series, Vol. 366, Transiting Extrapolar Planets Workshop, ed. C. Afonso, D. Weldrake, & T. Henning, 309–+
Bouchy, F., Pont, F., Santos, N. C., et al. 2004, A&A, 421, L13
Bouvier, J., Cabrit, S., Fernandez, M., Martin, E. L., & Matthews, J. M. 1993, A&A, 272, 176
Bouvier, J., Forestini, M., & Allain, S. 1997, A&A, 326, 1023
Brinch, C., Hogerheijde, M. R., & Richling, S. 2008, A&A, 489, 607
Brinch, C., Jørgensen, J. K., & Hogerheijde, M. R. 2009, A&A, 502, 199
Brown, J. M., Blake, G. A., Qi, C., Dullemond, C. P., & Wilner, D. J. 2008, ApJ, 675, L109
Butler, R. P. & Marcy, G. W. 1996, ApJ, 464, L153+
Carpenter, J. M., Mamajek, E. E., Hillenbrand, L. A., & Meyer, M. R. 2006, ApJ, 651, L49
Cassen, P. & Moosman, A. 1981, Icarus, 48, 353
Chandler, C. J., Carlstrom, J. E., & Terebey, S. 1994, in Astronomical Society of the Pacific Conference Series, Vol. 65, Clouds, Cores, and Low Mass Stars, ed. D. P. Clemens & R. Barvainis, 241–+
Charbonneau, D., Brown, T. M., Latham, D. W., & Mayor, M. 2000, ApJ, 529, L45
Chauvin, G., Lagrange, A., Udry, S., et al. 2006, A&A, 456, 1165
Cieza, L., Padgett, D. L., Stapelfeldt, K. R., et al. 2007, ApJ, 667, 308
Colwell, J. & Taylor, M. 1999, Icarus, 138, 241
Colwell, J. E. 2003, Icarus, 164, 188
Colwell, J. E., Sture, S., Cintala, M., et al. 2008, Icarus, 195, 908
Currie, T. & Kenyon, S. J. 2009, AJ, 138, 703
Dobbs, C. L., Bonnell, I. A., & Clark, P. C. 2005, MNRAS, 360, 2
Dominik, C. & Tielens, A. G. G. M. 1997, ApJ, 480, 647
Duchêne, G. 2010, ApJ, 709, L114
Dullemond, C. P. 2002, A&A, 395, 853

Dullemond, C. P. & Dominik, C. 2004a, A&A, 421, 1075

Dullemond, C. P. & Dominik, C. 2004b, in Astronomical Society of the Pacific Conference Series, Vol. 321, Extrasolar Planets: Today and Tomorrow, ed. J. Beaulieu, A. Lecavelier Des Etangs, & C. Terquem, 361–+

Dullemond, C. P., Hollenbach, D., Kamp, I., & D'Alessio, P. 2007, Protostars and Planets V, 555

Dullemond, C. P. & Turolla, R. 2000, A&A, 360, 1187

Duquennoy, A. & Mayor, M. 1991, A&A, 248, 485

Dutrey, A., Guilloteau, S., Duvert, G., et al. 1996, A&A, 309, 493

Dutrey, A., Guilloteau, S., & Guelin, M. 1997, A&A, 317, L55

Dutrey, A., Guilloteau, S., & Simon, M. 1993, Journal des Astronomes Francais, 45, 8

Dutrey, A., Guilloteau, S., & Simon, M. 2003, A&A, 402, 1003

Dutrey, A., Henning, T., Guilloteau, S., et al. 2007, A&A, 464, 615

Eggenberger, A., Udry, S., Chauvin, G., et al. 2007, A&A, 474, 273

Ercolano, B. & Clarke, C. J. 2010, MNRAS, 402, 2735

Ercolano, B., Clarke, C. J., & Hall, A. C. 2010, ArXiv e-prints

Fang, M., van Boekel, R., Wang, W., et al. 2009, A&A, 504, 461

Favata, F., Flaccomio, E., Reale, F., et al. 2005, ApJS, 160, 469

Favata, F., Micela, G., Sciortino, S., & D'Antona, F. 1998, A&A, 335, 218

Fedele, D., van den Ancker, M. E., Acke, B., et al. 2008, A&A, 491, 809

Frerking, M. A., Langer, W. D., & Wilson, R. W. 1982, ApJ, 262, 590

Furlan, E., Hartmann, L., Calvet, N., et al. 2006, ApJS, 165, 568

Getman, K., Broos, P. S., Salter, D. M., Garmire, G. P., & Hogerheijde, M. R. 2010, submitted, ApJ

Getman, K. V., Feigelson, E. D., Broos, P. S., Micela, G., & Garmire, G. P. 2008a, ApJ, 688, 418

Getman, K. V., Feigelson, E. D., Micela, G., et al. 2008b, ApJ, 688, 437

Ghez, A. M., McCarthy, D. W., Patience, J. L., & Beck, T. L. 1997, ApJ, 481, 378

Ghosh, P. & Lamb, F. K. 1978, ApJ, 223, L83

Glassgold, A. E., Najita, J., & Igea, J. 2004, ApJ, 615, 972

Goodman, A. A., Benson, P. J., Fuller, G. A., & Myers, P. C. 1993, ApJ, 406, 528

Greaves, J. S. & Rice, W. K. M. 2010, MNRAS, 1110

Güdel, M., Briggs, K. R., Arzner, K., et al. 2007, A&A, 468, 353

Güdel, M. & Nazé, Y. 2009, A&A Rev., 17, 309

Gullbring, E., Hartmann, L., Briceno, C., & Calvet, N. 1998, ApJ, 492, 323

Haisch, B., Strong, K. T., & Rodono, M. 1991, ARA&A, 29, 275

Haisch, Jr., K. E., Lada, E. A., & Lada, C. J. 2001, ApJ, 553, L153

Hartigan, P., Edwards, S., & Ghandour, L. 1995, ApJ, 452, 736

Hayashi, C. 1961, PASJ, 13, 450

Hayashi, C., Hōshi, R., & Sugimoto, D. 1962, Progress of Theoretical Physics Supplement, 22, 1

Heißelmann, D., Blum, J., Fraser, H. J., & Wolling, K. 2010, Icarus, 206, 424

Henry, G. W., Marcy, G. W., Butler, R. P., & Vogt, S. S. 2000, ApJ, 529, L41

Herschel, W. 1785, Royal Society of London Philosophical Transactions Series I, 75, 213

Hillenbrand, L. A. 2005, ArXiv Astrophysics e-prints

Hirota, T., Bushimata, T., Choi, Y. K., et al. 2007, PASJ, 59, 897

Hogerheijde, M. R. 2001, ApJ, 553, 618

Hollenbach, D. J., Yorke, H. W., & Johnstone, D. 2000, Protostars and Planets IV, 401

Hughes, A. M., Wilner, D. J., Qi, C., & Hogerheijde, M. R. 2008, ApJ, 678, 1119

Ida, S. & Lin, D. N. C. 2004, ApJ, 616, 567

Isella, A., Carpenter, J. M., & Sargent, A. I. 2009, ApJ, 701, 260

Isella, A., Carpenter, J. M., & Sargent, A. I. 2010, ApJ, 714, 1746

Isella, A., Testi, L., Natta, A., et al. 2007, A&A, 469, 213
Jensen, E. L. N., Mathieu, R. D., & Fuller, G. A. 1994, ApJ, 429, L29
Johansen, A. & Lacerda, P. 2010, MNRAS, 404, 475
Johansen, A., Youdin, A., & Mac Low, M. 2009, ApJ, 704, L75
Johns-Krull, C. M., Valenti, J. A., & Koresko, C. 1999, ApJ, 516, 900
Jørgensen, J. K., van Dishoeck, E. F., Visser, R., et al. 2009, A&A, 507, 861
Kalas, P., Graham, J. R., Chiang, E., et al. 2008, Science, 322, 1345
Kant, I. 1755, Allgemeine Naturgeschichte und Theorie des Himmels, ed. Kant, I.
Kawabe, R., Ishiguro, M., Omodaka, T., Kitamura, Y., & Miyama, S. M. 1993, ApJ, 404, L63
Keene, J. & Masson, C. R. 1990, ApJ, 355, 635
Kenyon, S. J., Dobrzycka, D., & Hartmann, L. 1994, AJ, 108, 1872
Kessler-Silacci, J., Augereau, J., Dullemond, C. P., et al. 2006, ApJ, 639, 275
Koerner, D. W., Sargent, A. I., & Beckwith, S. V. W. 1993, Icarus, 106, 2
Krumholz, M. R., Cunningham, A. J., Klein, R. I., & McKee, C. F. 2010, ApJ, 713, 1120
Krumholz, M. R., McKee, C. F., & Klein, R. I. 2005, Nature, 438, 332
Kurz, R. & Shaver, P. 1999, The Messenger, 96, 7
Lacy, J. H., Knacke, R., Geballe, T. R., & Tokunaga, A. T. 1994, ApJ, 428, L69
Lada, C. J., Muench, A. A., Luhman, K. L., et al. 2006, AJ, 131, 1574
Lada, C. J. & Wilking, B. A. 1984, ApJ, 287, 610
Lagrange, A., Bonnefoy, M., Chauvin, G., et al. 2010, Science, 329, 57
Lahuis, F., van Dishoeck, E. F., Blake, G. A., et al. 2007, ApJ, 665, 492
Langkowski, D., Teiser, J., & Blum, J. 2008, ApJ, 675, 764
Laplace, P. S. 1796, Le Systeme du Monde, Vol. II, ed. Laplace, P. S.
Larson, R. B. 1969, MNRAS, 145, 271
Larson, R. B. 2003, Reports on Progress in Physics, 66, 1651
Léger, A., Rouan, D., Schneider, J., et al. 2009, A&A, 506, 287
Leinert, C., Zinnecker, H., Weitzel, N., et al. 1993, A&A, 278, 129
Lepp, S. & Dalgarno, A. 1996, A&A, 306, L21
Lommen, D., Jørgensen, J. K., van Dishoeck, E. F., & Crapsi, A. 2008, A&A, 481, 141
Lommen, D., Maddison, S. T., Wright, C. M., et al. 2009, A&A, 495, 869
Lommen, D. J. P., van Dishoeck, E. F., Wright, C. M., et al. 2010, A&A, 515, A77+
Love, S. G. & Pettit, D. R. 2004, in Lunar and Planetary Institute Conference Abstracts, Vol. 35, Lunar and Planetary Institute Conference Abstracts, ed. S. Mackwell & E. Stansbery, 1119
Luhman, K. L., Allen, P. R., Espaillat, C., Hartmann, L., & Calvet, N. 2010, ApJS, 186, 111
Mamajek, E. E. 2008, Astronomische Nachrichten, 329, 10
Marcy, G. W. & Butler, R. P. 1996, ApJ, 464, L147+
Marois, C., Macintosh, B., Barman, T., et al. 2008, Science, 322, 1348
Massi, M., Forbrich, J., Menten, K. M., et al. 2006, A&A, 453, 959
Massi, M., Menten, K., & Neidhöfer, J. 2002, A&A, 382, 152
Massi, M., Ros, E., Menten, K. M., et al. 2008, A&A, 480, 489
Mathieu, R. D., Stassun, K., Basri, G., et al. 1997, AJ, 113, 1841
Mayor, M. & Queloz, D. 1995, Nature, 378, 355
Merín, B., Brown, J. M., Oliveira, I., et al. 2010, ApJ, 718, 1200
Muzerolle, J., Calvet, N., Briceño, C., Hartmann, L., & Hillenbrand, L. 2000, ApJ, 535, L47
Narayanan, D., Kulesa, C. A., Boss, A., & Walker, C. K. 2006, ApJ, 647, 1426
Natta, A. 2008, Physica Scripta Volume T, 130, 014014
Natta, A., Testi, L., Calvet, N., et al. 2007, Protostars and Planets V, 767
Öberg, K. I., Qi, C., Fogel, J. K. J., et al. 2010, ArXiv e-prints

O’dell, C. R., Wen, Z., & Hu, X. 1993, ApJ, 410, 696
Panić, O. & Hogerheijde, M. R. 2009, A&A, 508, 707
Panić, O., Hogerheijde, M. R., Wilner, D., & Qi, C. 2008, A&A, 491, 219
Panić, O., Hogerheijde, M. R., Wilner, D., & Qi, C. 2009, A&A, 501, 269
Pascucci, I. & Tachibana, S. 2010, The Clearing of Protoplanetary Disks and of the Protosolar Nebula, ed. Apai, D. A. & Lauretta, D. S., 263–298
Paszun, D. & Dominik, C. 2009, A&A, 507, 1023
Patience, J., White, R. J., Ghez, A. M., et al. 2002, ApJ, 581, 654
Phillips, R. B., Lonsdale, C. J., & Feigelson, E. D. 1991, ApJ, 382, 261
Pollack, J. B., Hubickyj, O., Bodenheimer, P., et al. 1996, Icarus, 124, 62
Poppe, T., Blum, J., & Henning, T. 2000, ApJ, 533, 454
Qi, C. 2001, PhD thesis, CALIFORNIA INSTITUTE OF TECHNOLOGY
Queloz, D., Mayor, M., Weber, L., et al. 2000, A&A, 354, 99
Raghavan, D., Henry, T. J., Mason, B. D., et al. 2006, ApJ, 646, 523
Ricci, L., Testi, L., Natta, A., & Brooks, K. J. 2010a, ArXiv e-prints
Ricci, L., Testi, L., Natta, A., et al. 2010b, A&A, 512, A15+
Robitaille, T. P., Whitney, B. A., Indebetouw, R., Wood, K., & Denzmore, P. 2006, ApJS, 167, 256
Rodmann, J., Henning, T., Chandler, C. J., Mundy, L. G., & Wilner, D. J. 2006, A&A, 446, 211
Safronov, V. S. & Zvjagina, E. V. 1969, Icarus, 10, 109
Salter, D. M., Heißelmann, D., Chaparro, G., et al. 2009, Review of Scientific Instruments, 80, 074501
Salter, D. M., Hogerheijde, M. R., & Blake, G. A. 2008, A&A, 492, L21
Salter, D. M., Kóspál, Á., Getman, K. V., et al. 2010, ArXiv e-prints
Santos, N. C., Israelian, G., & Mayor, M. 2001, A&A, 373, 1019
Santos, N. C., Israelian, G., Mayor, M., Rebolo, R., & Udry, S. 2003, A&A, 398, 363
Sargent, A. I. & Beckwith, S. 1987, ApJ, 323, 294
Sargent, A. I. & Beckwith, S. V. W. 1991, ApJ, 382, L31
Schäfer, C., Speith, R., & Kley, W. 2007, A&A, 470, 733
Shu, F., Najita, J., Ostriker, E., et al. 1994, ApJ, 429, 781
Shu, F. H. 1977, ApJ, 214, 488
Sicilia-Aguilar, A., Hartmann, L., Calvet, N., et al. 2006, ApJ, 638, 897
Simon, M. & Guilloteau, S. 1992, ApJ, 397, L47
Simon, M. & Prato, L. 1995, ApJ, 450, 824
Skrutskie, M. F., Dutkevitch, D., Strom, S. E., et al. 1990, AJ, 99, 1187
Smith, B. A. & Terrile, R. J. 1984, Science, 226, 1421
Stahler, S. W. 1983, ApJ, 274, 822
Stassun, K. G., van den Berg, M., Feigelson, E., & Flaccomio, E. 2006, ApJ, 649, 914
Sterzik, M. F., Pascucci, I., Apai, D., van der Bliek, N., & Dullemond, C. P. 2004, A&A, 427, 245
Strom, K. M., Strom, S. E., Edwards, S., Cabrit, S., & Skrutskie, M. F. 1989, AJ, 97, 1451
Swedenborg, E. 1734, Opera Philosophica et Mineralia, ed. Swedenborg, E.
Tanaka, H., Himeno, Y., & Ida, S. 2005, ApJ, 625, 414
Taylor, G. B., Carilli, C. L., & Perley, R. A., eds. 1999, Astronomical Society of the Pacific Conference Series, Vol. 180, Synthesis Imaging in Radio Astronomy II
Terebey, S., Shu, F. H., & Cassen, P. 1984, ApJ, 286, 529
Terzieva, R. & Herbst, E. 1998, ApJ, 501, 207
Testi, L., Natta, A., Shepherd, D. S., & Wilner, D. J. 2001, ApJ, 554, 1087
Testi, L., Natta, A., Shepherd, D. S., & Wilner, D. J. 2003, A&A, 403, 323
Thi, W., Mathews, G., Ménard, F., et al. 2010, A&A, 518, L125+
Thi, W. F., van Dishoeck, E. F., Blake, G. A., et al. 2001, ApJ, 561, 1074

Udalski, A., Paczynski, B., Zebrun, K., et al. 2002, Acta Astron., 52, 1

Udalski, A., Szymanski, M., Kaluzny, J., Kubiak, M., & Mateo, M. 1992, Acta Astron., 42, 253

Udry, S. & Santos, N. C. 2007, ARA&A, 45, 397

van Kempen, T. A., van Dishoeck, E. F., Brinch, C., & Hogerheijde, M. R. 2007, A&A, 461, 983

van Zadelhoff, G., Aikawa, Y., Hogerheijde, M. R., & van Dishoeck, E. F. 2003, A&A, 397, 789

van Zadelhoff, G., van Dishoeck, E. F., Thi, W., & Blake, G. A. 2001, A&A, 377, 566

Visser, R. & Dullemond, C. P. 2010, ArXiv e-prints

Visser, R., van Dishoeck, E. F., Doty, S. D., & Dullemond, C. P. 2009, A&A, 495, 881

Walter, F. M. 1987, PASP, 99, 31

Weidenschilling, S. J. & Cuzzi, J. N. 1993, in Protostars and Planets III, ed. E. H. Levy & J. I. Lunine, 1031–1060

Weintraub, D. A., Zuckerman, B., & Masson, C. R. 1989, ApJ, 344, 915

Wilner, D. J., D'Alessio, P., Calvet, N., Claussen, M. J., & Hartmann, L. 2005, ApJ, 626, L109

Wilner, D. J., Ho, P. T. P., Kastner, J. H., & Rodríguez, L. F. 2000, ApJ, 534, L101

Wolf, S. & D'Angelo, G. 2005, ApJ, 619, 1114

Wolk, S. J. & Walter, F. M. 1996, AJ, 111, 2066

Yasui, C., Kobayashi, N., Tokunaga, A. T., Saito, M., & Tokoku, C. 2009, ApJ, 705, 54

Yorke, H. W., Bodenheimer, P., & Laughlin, G. 1993, ApJ, 411, 274

Part I

The Dust and Gas Content Revealed with Millimeter Telescopes

Chapter 2

A Single-dish Survey of the HCO^+, HCN, and CN Emission Toward the T Tauri Disk Population in Taurus

The gas and dust content of protoplanetary disks evolves over the course of a few Myr. As the stellar X-ray and UV light penetration of the disk depends sensitively on the dust properties, trace molecular species like HCO^+, HCN, and CN are expected to show marked differences from photo-processing effects as the dust content in the disk evolves. We investigate specifically the evolution of the UV irradiation of the molecular gas in protoplanetary disks around a sample of classical T Tauri stars in Taurus that exhibit a wide range in grain growth and dust settling properties. We obtained HCO^+ ($J=3$–2), HCN ($J=3$–2), and CN ($J=2$–1) observations of 13 sources with the James Clerk Maxwell Telescope. Our sample has 1.3 mm fluxes in excess of 75 mJy, indicating the presence of significant dust reservoirs; a range of dust settling as traced through their spectral slopes between 6, 13, and 25 μm; varying degrees of grain growth as extrapolated from the strength of their 10-μm silicate emission feature; and complements data from the literature, essentially completing the molecular line coverage for the 21 brightest millimeter targets in the Taurus star-forming region. We compare the emission line strengths with the sources' continuum flux and infrared features, and use detailed modeling based on two different model prescriptions to compare typical disk abundances for HCO^+, HCN, and CN with the gas-line observations for our sample. We detected HCO^+ (3–2) from 6 disks, HCN (3–2) from 0 disks, and CN (2–1) from 4 disks, with typical 3σ upper limits of 150–300 mK ($T_{\rm mb}$) in 0.2 km s^{-1} channels. For the complete sample, there is no correlation between the gas-line strengths or their ratios and either the sources' dust continuum flux or infrared slope. Modeling shows that fractional abundances of 10^{-9}–10^{-11} can explain the line intensities observed, although significant modeling uncertainties remain. For DG Tau, which we model in great detail, we find that two very different temperature and density disk structures produce very similar lines for the same underlying abundances. Whereas, it is the gas properties and kinematics (determined by $M_\star$, i, $T_{\rm kin}$, and $R_{\rm gas}$) that have the largest impact on line appearance; and these system parameters are not well-constrained by current dust models, but will be probed directly with ALMA. Unresolved observations of the dust continuum provide neither a unique nor a complete picture of protoplanetary disks. Instead, gas-line measurements and resolved observations of dust and gas alike are needed to arrive at a full picture.

D. M. Salter, M. R. Hogerheijde, R. F. J. van der Burg, L. E. Kristensen, and C. Brinch
Astronomy & Astrophysics, submitted (2010)

2.1 Introduction

Many young pre-main-sequence (PMS) stars of a few solar masses or less (T Tauri stars) are surrounded by disks of gas and dust in the midst of forming planetary systems (Beckwith 1996; Dutrey et al. 2007). Observations with new instruments in the sub-millimeter and infrared wavelength regimes have provided a wealth of information about the dust content in these disks. Physical models are now fitted successfully to the observed spectral energy distributions (SEDs), revealing details on their large-scale radial and vertical structure (e.g. Calvet et al. 2002). Meanwhile, the millimeter spectral slope and the silicate emission features at 10 and 20 μm indicate the amount of small-scale dust processing, including grain growth (e.g. Natta et al. 2007, and references therein). These dust properties determine the overall opacity of the disk. A broad range in properties, in turn, implies different self-shielding abilities from the strong X-ray and ultra-violet (UV) radiation fields emitted by the central star. As this high-energy radiation penetrates the disk more or less efficiently, possibly irradiating deeper disk layers or a greater proportion of the available gas reservoir, then any molecular gas content that is left unprotected by the dust is subject to increased photoionization and photodissociation processes.

One key development in the evolution of disks is the growth of dust particles from sub-micron sizes first to larger sizes, and ultimately planets. The SEDs of many disks exhibit clear evidence of this growth to micron and even centimeter sizes (e.g. Beckwith & Sargent 1991; Testi et al. 2003). This process inherently depletes the small-grain population, which is the dominant source of UV opacity in the disk. In addition, as the dust particles grow, they are expected to decouple from the gas and settle to the disk midplane (Weidenschilling 1997; Dullemond & Dominik 2004), once again leaving the gas more exposed to both X-ray and UV irradiation in the upper disk layers. In a recent analysis of Spitzer IRS data for a large sample of T Tauri stars, Furlan et al. (2006) find evidence of this sedimentation of dust particles to the midplane. They conclude from the infrared spectra that the small dust content has already decreased by 2–3 orders of magnitude in the surface layers of many disks in the Taurus star-forming region. Since the processes of grain growth and dust removal (via settling) both correspond to a lower disk opacity, we can now test the link between the dust properties and the photoprocessing effects on the molecular gas composition.

Observations of molecular lines are required to probe the chemical content and evolution of the molecular gas. To date, only about three dozen disks have been detected successfully in rotational lines of CO (Koerner & Sargent 1995; Mannings & Sargent 1997, 2000; Dutrey et al. 1997; Guilloteau et al. 1999; Simon et al. 2000; Thi et al. 2001; van Kempen et al. 2007; Piétu et al. 2007; Chapillon et al. 2008; Schreyer et al. 2008; Schaefer et al. 2009), and only a handful of disks have been searched for rarer species like HCO$^+$, HCN, and CN (e.g Dutrey et al. 1997; Kessler-Silacci 2004; Thi et al. 2004; Kastner et al. 1997, 2008a,b). The latter three molecules are indicative of the rates at which X-ray ionization and UV photodissociation is occurring in the intermediate layers of the disk.

In many observational studies, HCO$^+$ and CN represent two of the strongest emission lines detected towards disks around PMS stars. Models predict that the abundances of HCO$^+$, HCN, and CN should increase similarly as the X-ray ionization rate is increased (Lepp & Dalgarno 1996; Glassgold et al. 2004). However, the UV field then further enhances CN, a photodissociation product, at the expense of HCN, its predecessor (Lepp & Dalgarno 1996; Aikawa et al. 2002). In this way, we can use measurements of HCO$^+$ as a normalization factor for the total ionization (or overall irradiation) effect on the disk, while the ratio of CN to HCN probes the UV photodissociation process, which is most sensitive to grain growth and dust settling.

Young forming stars are the main contributors to the UV interstellar radiation field (Herbig & Goodrich 1986). In star-forming regions permeated by moderate UV radiation fields from newly forming stars, the ratio of CN to HCN is observed to be very strongly enhanced with respect to typical molecular cloud values (Fuente et al. 1993; Hogerheijde et al. 1995; Greaves & Church 1996; Terzieva & Herbst 1998).

The same shift is predicted by chemical disk models where the ratio of CN over HCN changes radically in favor of CN as the stellar UV flux increases (van Zadelhoff et al. 2003). Young stars also possess strong X-ray activity levels (Güdel 2008). Therefore, the brightest HCO^+ lines and largest CN to HCN ratios are expected from luminous sources and optically thin disks.

Previously, Kastner et al. (2008b) summarized the HCO^+, HCN, and CN line observations available in the literature for disks around PMS stars, showing how the chemical impact of the X-ray and UV fields is significant in the general disk population and that the line ratios do exhibit tentative trends that correlate with the expected photoprocessing effects. However, also evident is the small number of *widely-differing* systems that have been studied in any detail at all. This makes it difficult to distinguish evolutionary differences from source-to-source variations in mass, luminosity, environment, and orientation. Naturally, larger homogeneous surveys are neccessary to identify gas-rich disks and to provide observational tests of the processes driving their physical and chemical evolution.

Here we present a study of HCO^+, HCN, and CN line emission toward *all* the classical T Tauri stars in Taurus with a compact 1.3 mm continuum flux ≥ 75 mJy, or equivalently a disk mass $\gtrsim 0.014\,M_\odot$, using the standard flux relation and adopting the same mean disk parameters as Dutrey et al. (1996). These parameters include a disk temperature of 15 K, a dust absorption coefficient $K_{1.3\,\mathrm{mm}}$ of 0.02 $\mathrm{cm}^2\,\mathrm{g}^{-1}$, and a distance to Taurus of 140 pc. Consequently, our selection criterion favors warmer and more massive disks in the star-forming region.

The line data were obtained from new single-dish observations, as well as taken from the literature, where available. In Section 2.2 we describe the details of the observations and in Section 2.3 we report the line intensities and detection limits obtained from our measurements and from the literature. Section 2.4 investigates observational trends between the dust emission properties of the disk sample, such as millimeter flux and infrared slope, and the gas-line strengths or upper limits. Because none of these tracers spatially resolve the disks, and because line strengths depend both on the total amount of molecules and on the excitation conditions, Section 2.5 employs a modeling approach to constrain the HCO^+, HCN, and CN abundances. This is done using two generic models (Section 2.5.2) and, for one source, DG Tau, in particular, a more detailed approach was taken (Section 2.5.3). Section 2.6 discusses our results and the limitations of our methods and Section 2.7 summarizes the main findings.

2.2 Observations

2.2.1 The Taurus Disk Sample

The sample consists of the classical T Tauri stars in the Taurus star-forming region that were included in the Spitzer IRS classification work by Furlan et al. (2006) and possess a 1.3 mm continuum flux larger than 75 mJy (Beckwith et al. 1990). The sources cover a broad range in spectral indices between 6, 13, and 25 μm, and the shape and strength of their 10-μm silicate emission features. The difference in the mid-infrared spectral indices (defined as $\Delta n = n_{13-25} - n_{6-13}$) serves as an indicator of dust settling in the inner disk ($\leq$1 AU, with smaller Δn suggesting more settling) and the strength of the 10μm silicate feature decreases with a depleting population of small grains. This characterization of the current dust properties in the upper surface layers of the disk allows us to explicitly contrast the presence of small grains—the main source of UV opacity—with the line strengths and ratios of the molecular species that trace UV photodissociation.

For better odds of a high signal-to-noise gas-line detection, we imposed the 75 mJy continuum flux minimum cutoff. This criterion results from the millimeter flux being related to the dust mass, and the idea that a larger dust mass is indicative of a potentially large gas reservoir. Our source list includes some of the brightest young stellar objects (YSOs) in Taurus at millimeter wavelengths, many of which already possess HCO^+, HCN, and CN rotational line detections. Consequently, the cutoff value was chosen to

Table 2.1 — Taurus Disk Sample.

(1) Source Name	(2) RA (J2000)	(3) DEC (J2000)	(4) $F_{1.3\,\mathrm{mm}}$ [mJy]	(5) Δn	(6) 10μm Strength	(7) $M_\star$ [$M_\odot$]	(8) Spectral Type	(9) Hα EW [Å]	(10) L_{bol} [$L_\odot$]	(11) L_{X} [10^{30} erg s^{-1}]
Our subsample with new molecular line observations presented here										
CW Tau	04:14:17.00	+28:10:57.8	96 ± 8	0.96	0.16	1.06	K3	135	1.35	2.844
CY Tau	04:17:33.72	+28:20:46.8	133 ± 11	0.50	0.12	0.55	M1.5	70	0.47	0.163
FT Tau	04:23:39.18	+24:56:14.3	130 ± 14	0.31	0.43	-	M3	-	>0.38	0.799
DG Tau	04:27:04.70	+26:06:16.2	443 ± 20	0.44	0.00	0.67	K6	113	0.90	<0.766
IQ Tau	04:29:51.56	+26:06:44.8	87 ± 11	0.40	0.35	0.68	M0.5	8	0.65	0.416
V806 Tau	04:32:15.41	+24:28:60.0	124 ± 13	1.46	0.35	-	M0	88	1.30	-
UZ Tau	04:32:42.96	+25:52.31.1	172 ± 15	0.58	0.45	0.18	M1-2	82	1.06	0.890
CI Tau	04:33:52.01	+22:50:30.1	190 ± 17	0.93	0.54	0.77	K7	102	0.87	0.195
DN Tau	04:35:27.37	+24:14:59.6	84 ± 13	0.33	0.22	0.70	M0	12	0.91	1.155
DO Tau	04:38:28.58	+26:10:49.9	136 ± 11	0.64	0.18	0.70	M0	100	1.20	<0.270
GO Tau	04:43:03.08	+25:20:18.6	83 ± 12	0.97	0.40	0.71	M0	81	0.27	0.249
DQ Tau	04:46:53.06	+17:00:00.2	91 ± 9	0.19	0.14	0.43	M0	113	0.91	-
DR Tau	04:47:06.22	+16:58:42.9	159 ± 11	0.61	0.27	0.38	K5	87	3.00	-
Sources with molecular line data already in the literature (see Table 2.4)										
V892 Tau	04:18:40.62	+28:19:15.5	289 ± 13	-1.22	0.65	-	B9	13	20.90	8.576
RY Tau	04:21:57.41	+28:26:35.6	229 ± 17	0.46	1.36	1.63	K0	20	7.60	5.520
T Tau	04:21:59.43	+19:32:06.4	280 ± 9	1.19	-0.10	-	K7	60	15.50	8.048
GG Tau	04:32:30.41	+17:31:40.2	593 ± 53	0.74	0.64	1.55	K7	54	1.55	0.160
DL Tau	04:33:39.06	+25:20:38.2	230 ± 14	0.24	0.09	0.70	K7	105	0.70	<1.000
DM Tau	04:33:48.73	+18:10:10.0	109 ± 13	1.93	0.96	0.25	M1.5	139	0.25	<0.457
AA Tau	04:34:55.42	+24:28:53.2	88 ± 9	0.50	0.35	0.78	K7	37	0.74	0.690
GM Aur	04:38:21.34	+26:09:13.7	253 ± 12	3.19	1.19	1.00	K7	96	1.00	1.241

Notes. (Columns 1–3) Source name and 2MASS coordinates; (Column 4) 1.3 mm continuum fluxes from Beckwith (1996); (Columns 5–6) Dust settling parameters Δn and the 10μm silicate strength from Furlan et al. (2006); (Column 7) Stellar masses from White & Ghez (2001) or Hartigan et al. (1995); (Column 8) Spectral types from Luhman et al. (2010) or Rebull et al. (2010); (Column 9) Hα equivalent widths (EW) from Herbig & Bell (1988); (Column 10) Bolometric luminosities from Palla & Stahler (2002), except for DQ Tau and DR Tau, which come from Kenyon & Hartmann (1995); (Column 11) X-ray luminosities from Güdel et al. (2007) or Damiani et al. (1995).

be representative of the lowest circumstellar dust mass found in the literature for a disk that had been detected in at least one of the three molecules. Therefore, our study is not necessarily probing a lower dust-mass regime, but rather contributes to completing the sample of sources down to this flux cutoff, and expanding the subgroup of disks with similar dust masses that can be compared.

We restricted the sample to one star-forming region, so that our results are relatively insensitive to the initial cloud conditions. In addition, due to their shared environment, we can assume that the local interstellar radiation field is similar for all disks, and more importantly, that it plays a less significant role in irradiating the disk in the UV regime. It is generally assumed that the external contribution to UV photodissociation of the upper and outer disk layers is roughly 3–4 magnitudes lower in intensity than the stellar excess UV spectrum for T Tauri stars, based on observations of five protostars by Herbig & Goodrich (1986), whereby four were located in Taurus.

The full sample consists of 21 protoplanetary disks, including 13 that had not been observed previously in any of our molecular tracers. Complementery molecular line observations for those 13 sources are presented here. Table 2.1 lists their 2MASS source coordinates (used for our JCMT observations), 1.3 mm continuum fluxes (Beckwith et al. 1990), mid-infrared dust settling parameters (Furlan et al. 2006), as well as several stellar properties that are closely tied to the radiation field.

2.2.2 JCMT Single-dish Millimeter Observations

Using the RxA receiver and the ACSIS backend on the James Clerk Maxwell Telescope (JCMT) on Mauna Kea, we observed the HCO^+ ($J = 3$–2) at 267.558 GHz, HCN ($J = 3$–2) at 265.886 GHz, and CN ($J = 2$–1) hyperfine line centered at 226.800 GHz emission toward the subsample of 13 sources. The observations were made between September 2007 and December 2009. The HCO^+ observations were carried out in position-switched mode with a reference position at a 900″ offset. Although with a 900″ position switch the reference position is unlikely to be off the Taurus molecular clouds, the observed lines trace relatively dense gas and little emission is expected away from the source. For the less abundant HCN and CN species, we used the more time-efficient beam-switching mode with a reference position at a throw of 180″.

All observations had a bandwidth of 250 MHz, giving a channel resolution of 30.5 kHz (or ∼0.034 $\mathrm{km\,s^{-1}}$ for HCO^+ and HCN, and ∼0.040 $\mathrm{km\,s^{-1}}$ for CN), and oversampling the instrumental resolution by a factor 6. The atmospheric opacity was between 0.05 and 0.12 during the observations, with typical on-source integration times of 20 minutes (aside from one extra-deep 60-min observation of HCN toward the brightest source, DG Tau, to establish a deeper upper limit for the subsample).

The JCMT beam is 19″ at 265 GHz and 22″ at 226 GHz, much larger than any protoplanetary disk at the distance of 140 pc to the Taurus star-forming region (Kenyon et al. 1994). Since many young stars are still situated near their parental cloud, any line detection needs to be checked for possible contamination from the extended cloud. Following the strategy of Thi et al. (2001) and van Kempen et al. (2007), every strong detection of HCO^+ was followed up with observations 30″ east and 30″ north of the object.

2.2.3 Data Reduction

The data were calibrated by the RxA pipeline and reduced with the Starlink KAPPA software. The edges of each spectrum were removed and a low-order ($p = 2$) polynomial baseline was subtracted. Multiple integrations on individual lines were averaged at this stage. The resulting spectrum was smoothed using a moving square ‘averaging’ box of width 3 channels. We then binned the smoothed data by 5 channels. The final data resolution is 152.5 kHz (or 0.17 $\mathrm{km\,s^{-1}}$ for HCO^+ and HCN, and 0.20 $\mathrm{km\,s^{-1}}$ for CN). Finally, the reduced spectra were converted from T_A^* to main beam temperatures $T_{\rm mb}$ using a

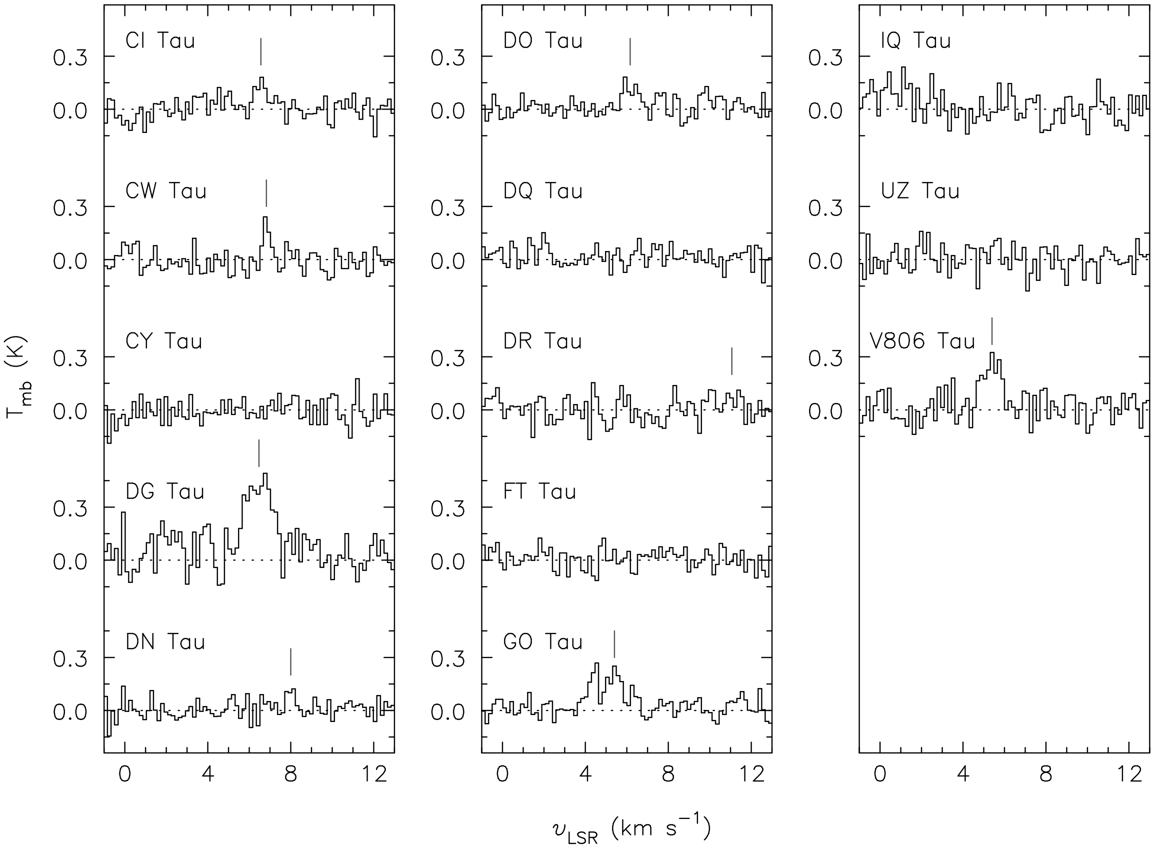

Figure 2.1 — HCO$^+$ ($J = 3$–2) observations of our 13-disk subsample in Taurus. A vertical line above the spectrum indicates the central radial velocity υ_{LSR}, as determined from a Gaussian fit to the emission line. In the case of DR Tau, we indicate υ_{LSR} from a fit to its CN emission (see Figure 2.3).

beam efficiency factor of $\eta = 0.65$.[1] The final spectra are shown in Figures 2.1–2.3, and the resulting rms noise levels are reported in Tables 2.2 and 2.3. The analysis of the reduced data was performed using the GILDAS CLASS software to take advantage of the available hyperfine line-fitting algorithms for blended lines. Results of the Gaussian fits to the data, including the peak temperature (T_{mb}), line widths (FWHM), and the integrated line intensities ($\int T_{mb}\, \delta v$), are also reported for HCO$^+$ and HCN in Table 2.2 and for the CN hyperfine lines in Table 2.3.

2.3 Results

In Figure 2.1 we see that only 7 of our 13 sources show detected emission lines of HCO$^+$ ($J = 3$–2): CI Tau, CW Tau, DG Tau, DN Tau, DO Tau, GO Tau, and V806 Tau. The detected lines have intensities of $T_{mb} = 122$–491 mK and are well fit by single Gaussian profiles with widths of $\sim$1 km s^{-1} FWHM. Remarkably, no double-peaked line profiles characteristic of inclined disks are found. Only DG Tau and GO Tau show wider lines of 1.44 and 1.93 km s^{-1}, respectively. These sources also represent two of the strongest lines, with respective peaks T_{mb} of 491 and 251 mK. GO Tau is the only source for which the line profile is not well described by a single Gaussian. Instead, it consists of a superposition of three, narrow ($\sim$0.5 km s^{-1}) components. Greaves (2004) and Thi et al. (2004) also comment on the complex

---

[1] http://docs.jach.hawaii.edu/JCMT/HET/GUIDE/het_guide/

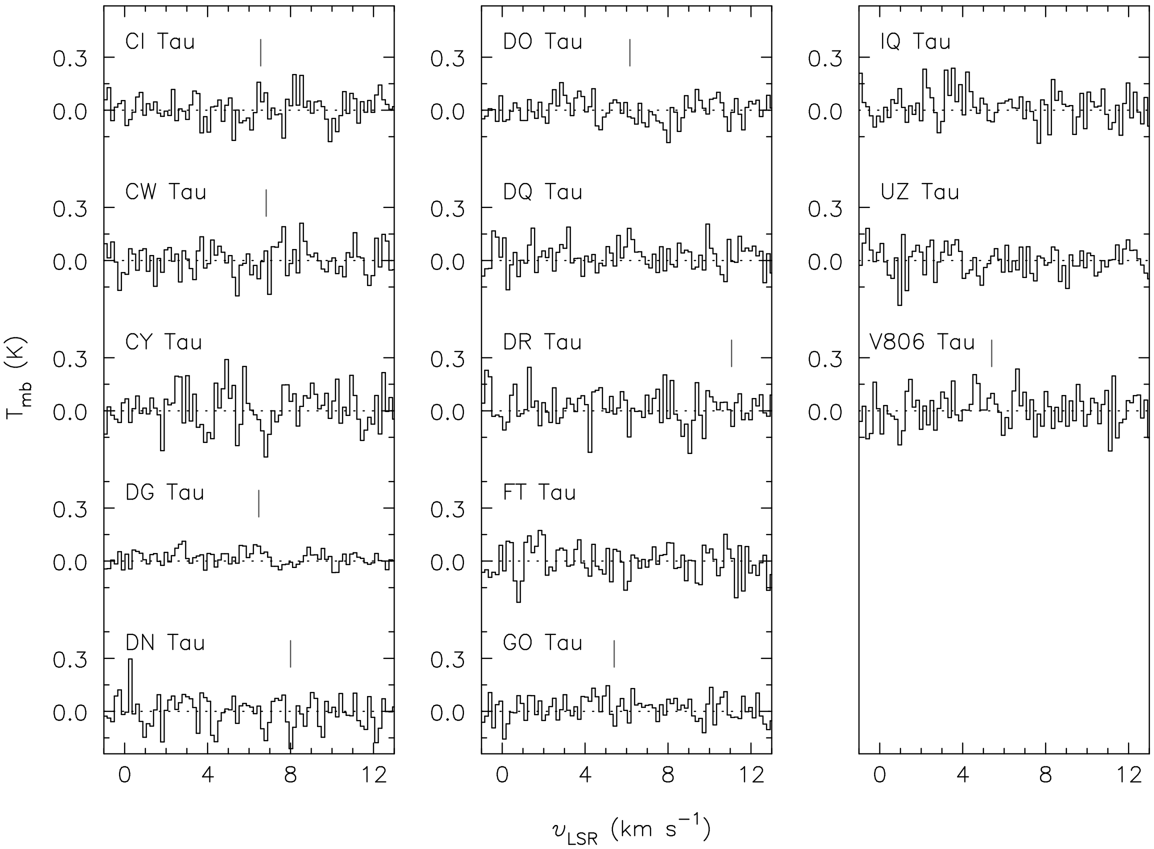

Figure 2.2 — HCN ($J = 3$–2) observations of our subsample in Taurus. A vertical line above the spectrum indicates the central velocity found from the HCO$^+$ emission (see Figure 2.1). We note that HCN emission is not detected toward any of the sources, including the most massive disk DG Tau.

line profiles of GO Tau, attributing some to surrounding cloud material. Section 2.5.4 further discusses these sources further.

Figure 2.4 shows the HCO$^+$ spectra at 30″ east and 30″ north of the four sources with the brightest detected HCO$^+$ lines: CW Tau, DG Tau, GO Tau, and V806 Tau. In all four cases, hints of extended cloud emission are seen. However, only toward CW Tau are they of comparable strength as the on-source emission, and we no longer consider this a detection of emission from the disk. This brings our total *disk* detections in HCO$^+$ down to 6. For the other sources, the off-source emission is $< 30\%$ of the on-source line strength, which we determine is sufficiently small to be inconsequential to our trends analysis (Section 2.4); while our more detailed modeling of DG Tau considers the contributions that remnant envelopes and other circumstellar material can have to the line emission (Section 2.5).

No HCN (3–2) emission was detected toward any of our targets, down to 3σ upper limits of 41–110 mK in 0.17 km s^{-1} bins (see Table 2.2). Following the recipe of Jørgensen et al. (2004), this corresponds to upper limits on the integrated intensities ranging from 61 to 163 mK km s^{-1}. Clearly, toward the sources in our Taurus subsample, the HCN lines are at least a factor of 3 weaker than the HCO$^+$ lines (and a factor of 12 weaker toward DG Tau where a much deeper integration resulted in a lower noise level).

Two sources, DG Tau and GO Tau, show clear detections of the CN (2–1) triplet at frequencies of

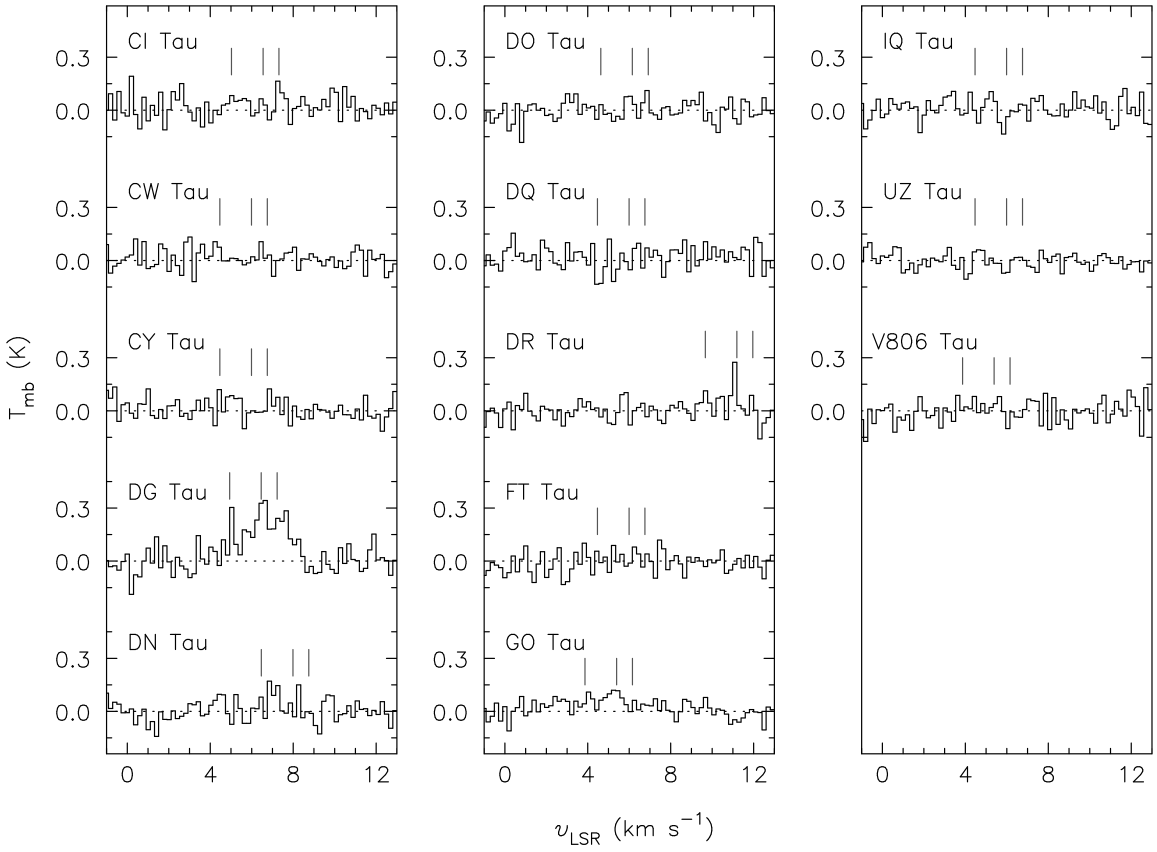

Figure 2.3 — CN ($J = 2$–1) hyperfine line observations of each of our 13 disks in Taurus. The three vertical lines above the spectrum indicate the expected positions of the three strongest hyperfine lines, located at 226874.1660, 226874.7450, and 226875.8970 GHz. The spectra have their velocity axis defined such that the strongest hyperfine component, at 226.8747450 GHz, should appear at the source velocity (υ_{LSR}). In cases where the source velocity is unknown, the Taurus cloud velocity of 6.0 km s^{-1} is indicated instead, as a reference.

226.8741660, 226.8747450, and 226.8758970 GHz.[2] Two additional sources, CI Tau and DR Tau, show tentative detections. No emission was detected from the other targets where the typical rms noise level was 57 mK in 0.20 km s^{-1} bins. Two suggestive peaks in the DO Tau spectrum at the correct position for the CN hyperfine components are likely noise.

2.4 Trends

The previous section shows 6 detections of HCO$^+$ emission, no detections of HCN emission, and 4 detections of CN emission from our subsample of 13 observed sources. Looking at the complete sample of 21 sources yields the following statistics for detections of HCO$^+$ (14/21), HCN (5/21), and CN (8/21) toward the T Tauri disk population thus far in Taurus. Half of the reported detections are taken from the literature (listed here in Table 2.4) and these often include rotational transitions other than the ones observed by us. However, in the present section we focus on general trends in the detected emission strengths, and we assume that the different transitions correspond to line strength differences of no more than a factor of ∼2.

---

[2] The JPL Molecular Spectroscopy Catalog http://spec.jpl.nasa.gov

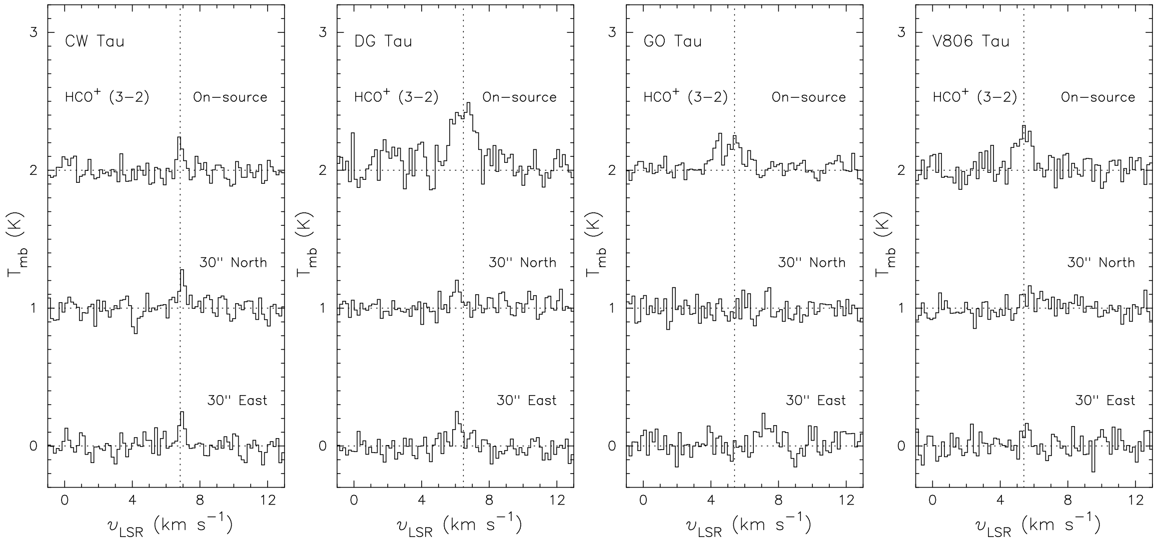

Figure 2.4 — From left to right, the HCO$^+$ ($J = 3$–2) on-source and 30$''$ offset observations for CW Tau, DG Tau, GO Tau, and V806 Tau. These 4 sources show the strongest HCO$^+$ emission profiles in our subsample. A dotted line marks the central radial velocity $\upsilon_{\rm LSR}$ in km s^{-1} for a Gaussian fit to the HCO$^+$ on-source emission. In all cases, HCO$^+$ emission is detected at the off positions. However, with the exception of CW Tau, it is always at a separate velocity or a weaker intensity, which is why we attribute the emission toward CW Tau to the surrounding cloud and *not* the disk.

Our goal is to investigate whether the line strengths (and the upper limits) from the Taurus sample show any correlation with disk or stellar properties. For this purpose, we convert the line strengths to integrated line fluxes (in Jy km s^{-1}) in order to remove the dependences on beam size. The assembled line fluxes for the entire sample are provided in Table 2.4. To trace the disk properties we use the millimeter continuum flux $F_{1.3\rm mm}$, the difference in the mid-infrared slope Δn as defined by Furlan et al. (2006), and the 10-μm silicate feature strength, also from Furlan et al. (2006). Respectively, these trace the disk (dust) mass, dust settling, and small-dust content. Stellar properties are probed by stellar mass $M_\star$, Hα equivalent width, bolometric luminosity $L_{\rm bol}$, and X-ray luminosity $L_{\rm X}$. We stress that all quantities are *observed* quantities, and that a relation (or lack thereof) between the HCO$^+$ line strength and the 1.3 mm continuum flux, for example, does not immediately imply a connection (or lack thereof) between HCO$^+$ abundance and disk (dust) mass. To draw the latter conclusion, detailed modeling of the emission mechanisms is required, which is the topic of Section 2.5.

One of the guiding questions in our research was, whether disks with a lower dust content or with more dust settling have larger gas volumes subject to UV irradiation, and therefore show comparatively stronger lines of HCO$^+$ (more ionization) and CN (more photodissociation). In the following figures, we will explicitely investigate these relations. Figure 2.5 plots the observed HCO$^+$, HCN, CN, and ^{13}CO line fluxes against $F_{1.3\rm mm}$, Δn, 10μm silicate feature strength, and ^{13}CO line flux. The latter quantity serves as a tracer of the total molecular gas content. We choose to plot the logarithm of these quantities because we are primarily interested in large-scale trends and because we want to suppress differences of a factor of $\sim$2 due to variations in source distance, inclination, luminosity, and plotted line transitions. No immediate trends are present in the panels of Figure 2.5. Instead, we find that: (1) the millimeter continuum flux alone is not a clear predictor of line strength since both lower- and higher-mass disks exhibit detections and non-detections alike in all species; (2) disks with and without significant dust settling exhibit equally strong line strengths all around; and (3) a larger ^{13}CO reservoir is not necessarily accompanied with stronger HCO$^+$, HCN, and CN lines. These results hold for a ^{13}CO line flux spanning

Table 2.2 — HCO$^+$ and HCN Line Measurements.

Source	HCO$^+$ (3–2)								HCN (3–2)	
	υ_{LSR} [km s^{-1}]	σ_{rms} [mK]	max T_{mb} [mK]^a	S/N	peak T_{mb} [mK]^b	FWHM [km s^{-1}]	$\Sigma\, T_{\mathrm{mb}}\, \Delta\nu$ [mK km s^{-1}]^c	$\int T_{\mathrm{mb}}\, \delta\nu$ [mK km s^{-1}]^d	σ_{rms} [mK]	$\int T_{\mathrm{mb}}\, \delta\nu$ [mK km s^{-1}]^e
CI Tau	6.56	57	181	3.2	161	0.68	105	117 ± 32	76	< 112
CW Tau	6.83^f	55	241	4.4	259	0.39	92	108 ± 22	76	< 112
off 30″ N	6.95	61	279	4.5	270	0.38	95	109 ± 27	...	...
off 30″ E	6.93	61	248	4.1	251	0.38	88	101 ± 24	...	...
CY Tau	-	62	-	-	-	1.00	-	< 92	110	< 163
DG Tau	6.47	100	491	4.9	424	1.44	695	652 ± 72	41	< 61
off 30″ N	6.07	58	203	3.5	174	0.43	89	79 ± 23	...	...
off 30″ E	6.13	65	251	3.9	247	0.47	107	124 ± 29	...	...
DN Tau	8.00	48	122	2.6	128	0.44	56	60 ± 18	85	< 126
DO Tau	6.16	48	182	3.8	127	0.86	115	116 ± 26	67	< 99
DQ Tau	-	59	-	-	-	1.00	-	< 88	81	< 120
DR Tau	-	65	-	-	-	1.00	-	< 97	93	< 138
FT Tau	-	54	-	-	-	1.00	-	< 80	87	< 129
GO Tau	5.05	47	251	5.3	186^g	1.93	327	383 ± 39	71	< 105
off 30″ N	7.37	68	148	2.2	279	0.17	46	51 ± 19	...	...
off 30″ E	7.30	71	126	1.8	155	1.03	172	170 ± 44	...	...
IQ Tau	-	80	-	-	-	1.00	-	< 119	91	< 135
UZ Tau	-	66	-	-	-	1.00	-	< 98	80	< 119
V806 Tau	5.40	77	345	4.2	271	0.97	297	279 ± 45	100	< 148
off 30″ N	5.80	61	162	2.6	201	0.25	82	52 ± 20	...	...
off 30″ E	5.59	68	164	2.4	149	0.39	76	62 ± 28	...	...
GO Tau 1^h	4.40	47	268	5.7	237	0.54	100	136 ± 28	...	...
GO Tau 2	5.40	47	251	5.3	232	0.75	179	185 ± 28	...	...
GO Tau 3	6.34	47	143	3.0	125	0.35	50	46 ± 19	...	...

Footnotes. (a) The maximum temperature value in the binned data; (b) The maximum determined by a Gaussian fit to the line using the CLASS Gauss fitting routine; (c) A sum of the individual channels from the binned data to be compared to the integrated fit; (d) For non-detections we report a 3σ upper limit where $\sigma = 1.2\, \sigma_{\mathrm{rms}} \sqrt{\Delta V\, \delta\nu}$ and we assume a line width ΔV of 1.0 km s^{-1}; (e) Upper limits are reported in the same way as for HCO$^+$; (f) We have determined that the emission detected here is not associated with the circumstellar disk; (g) Statistics are reported for a single Gaussian fit, which may not be realistic for this source; (h) Statistics for the individual peaks toward GO Tau, measured as they appear from left to right.

Table 2.3 — CN Line Measurements.

Source	CN $(2_{3/2,3/2}\text{–}1_{5/2,5/2})$			CN $(2_{3/2,5/2}\text{–}1_{5/2,7/2})$			CN $(2_{3/2,1/2}\text{–}1_{5/2,3/2})$			Average Stats	
	$\upsilon_{\rm LSR}$ [km s^{-1}]	Peak [mK]	$\int T_{\rm mb}\,\delta v$ [mK km s^{-1}]	$\upsilon_{\rm LSR}$ [km s^{-1}]	Peak [mK]	$\int T_{\rm mb}\,\delta v$ [mK km s^{-1}]	$\upsilon_{\rm LSR}$ [km s^{-1}]	Peak [mK]	$\int T_{\rm mb}\,\delta v$ [mK km s^{-1}]	FWHM [km s^{-1}]	$\sigma_{\rm rms}$ [mK]
CI Tau	7.33	230	52 ± 19	6.51	76	16 ± 19	5.28	65	58 ± 35	0.42	63
CW Tau	-	-	< 94	-	-	< 94	-	-	< 94	1.00	58
CY Tau	-	-	< 97	-	-	< 97	-	-	< 97	1.00	60
DG Tau	7.63	198	171 ± 94	6.45	279	414 ± 124	5.03	294	76 ± 30	0.82	63
DN Tau	-	-	< 104	-	-	< 104	-	-	< 104	1.00	64
DO Tau	-	-	< 90	-	-	< 90	-	-	< 90	1.00	56
DQ Tau	-	-	< 98	-	-	< 98	-	-	< 98	1.00	61
DR Tau	9.65	119	56 ± 26	11.06	297	87 ± 20	11.93	110	24 ± 16	0.31	55
FT Tau	-	-	< 88	-	-	< 88	-	-	< 88	1.00	55
GO Tau	2.56	55	101 ± 41	4.07	103	37 ± 19	5.24	116	129 ± 32	1.03	42
IQ Tau	-	-	< 91	-	-	< 91	-	-	< 91	1.00	57
UZ Tau	-	-	< 79	-	-	< 79	-	-	< 79	1.00	49
V806 Tau	-	-	< 102	-	-	< 102	-	-	< 102	1.00	63

Notes. The velocities reported here are for a $\upsilon_{\rm LSR} = 0$ centered at the theoretical frequency for the strongest hyperfine component, at 226.8747450 GHz. All reported peaks were determined from a Gaussian fit. All upper limits are given by $3 \times 1.2\,\sigma_{\rm rms}\,\sqrt{\Delta V\,\delta v}$ following Jørgensen et al. (2004) where ΔV is set to 1.0 km s^{-1}.

Table 2.4 — Molecular line fluxes used to make the plots in Section 2.4 of this work.

(1) Source Name	(2) $F_{^{13}\mathrm{CO}}$ [Jy km s^{-1}]	(3) ^{13}CO Trans.	(4) Ref.	(5) F_{HCO^+} [Jy km s^{-1}]	(6) HCO$^+$ Trans.	(7) Ref.	(8) F_{HCN} [Jy km s^{-1}]	(9) HCN Trans.	(10) Ref.	(11) F_{CN} [Jy km s^{-1}]	(12) CN Trans.	(13) Ref.
AA Tau	12.4	2–1	2	1.9	1–0	8	1.8	1–0	8	3.8	1–0	8
CI Tau	-	-	-	2.4 ± 0.7	3–2	1	< 1.6	3–2	1	2.6 ± 1.5	2–1	1
CW Tau	8.3	2–1	2	< 1.8	3–2	1	< 1.6	3–2	1	< 1.9	2–1	1
CY Tau	-	-	-	< 1.9	3–2	1	< 2.3	3–2	1	< 2.0	2–1	1
DG Tau	40.0	1–0	3	13.5 ± 1.5	3–2	1	< 0.8	3–2	1	13.7 ± 5.1	2–1	1
DL Tau	< 2.1	3–2	2	-	-	-	-	-	-	-	-	-
DM Tau	6.5	2–1	4	4.1 ± 0.5	3–2	5	2.0 ± 0.3	1–0	6	8.7 ± 0.4	2–1	6
DN Tau	14.5	2–1	2	1.2 ± 0.4	3–2	1	< 1.8	3–2	1	< 2.2	2–1	1
DO Tau	31.0	2–1	2	2.4 ± 0.5	3–2	1	< 1.4	3–2	1	< 1.9	2–1	1
DQ Tau	-	-	-	< 1.8	3–2	1	< 1.7	3–2	1	< 2.0	2–1	1
DR Tau	4.3 ± 1.2	3–2	5	3.7 ± 0.4	4–3	9	< 1.9	3–2	1	3.5 ± 1.3	2–1	1
FT Tau	-	-	-	< 1.7	3–2	1	< 1.8	3–2	1	< 1.8	2–1	1
GG Tau	5.8 ± 0.2	2–1	6	6.7 ± 0.9	3–2	6	2.8 ± 0.7	3–2	6	8.4 ± 0.4	2–1	6
GM Aur	9.3 ± 2.7	3–2	5	9.9 ± 1.2	4–3	9	-	-	-	-	-	-
GO Tau	4.1 ± 1.2	3–2	5	7.9 ± 0.8	3–2	1	< 1.5	3–2	1	5.5 ± 1.9	2–1	1
IQ Tau	-	-	-	< 2.5	3–2	1	< 1.9	3–2	1	< 1.9	2–1	1
RY Tau	4.3 ± 1.2	3–2	5	1.7 ± 0.7	4–3	9	1.6	1–0	8	0.8	1–0	8
T Tau	3.0 ± 0.2	2–1	7	3.1 ± 0.1	1–0	7	1.9 ± 0.8	2–1	10	-	-	-
UZ Tau	-	-	-	< 2.0	3–2	1	< 1.7	3–2	1	< 1.6	2–1	1
V806 Tau	-	-	-	5.8 ± 0.9	3–2	1	< 2.1	3–2	1	< 2.1	2–1	1
V892 Tau	-	-	-	-	-	-	-	-	-	-	-	-

References. 1. This work; 2. Greaves (2005); 3. Kitamura et al. (1996b); 4. Panić et al. (2008); 5. Thi et al. (2001); 6. Dutrey et al. (1997); 7. Hogerheijde et al. (1998); 8. Kessler-Silacci (2004); 9. Greaves (2004); and 10. Yun et al. (1999).

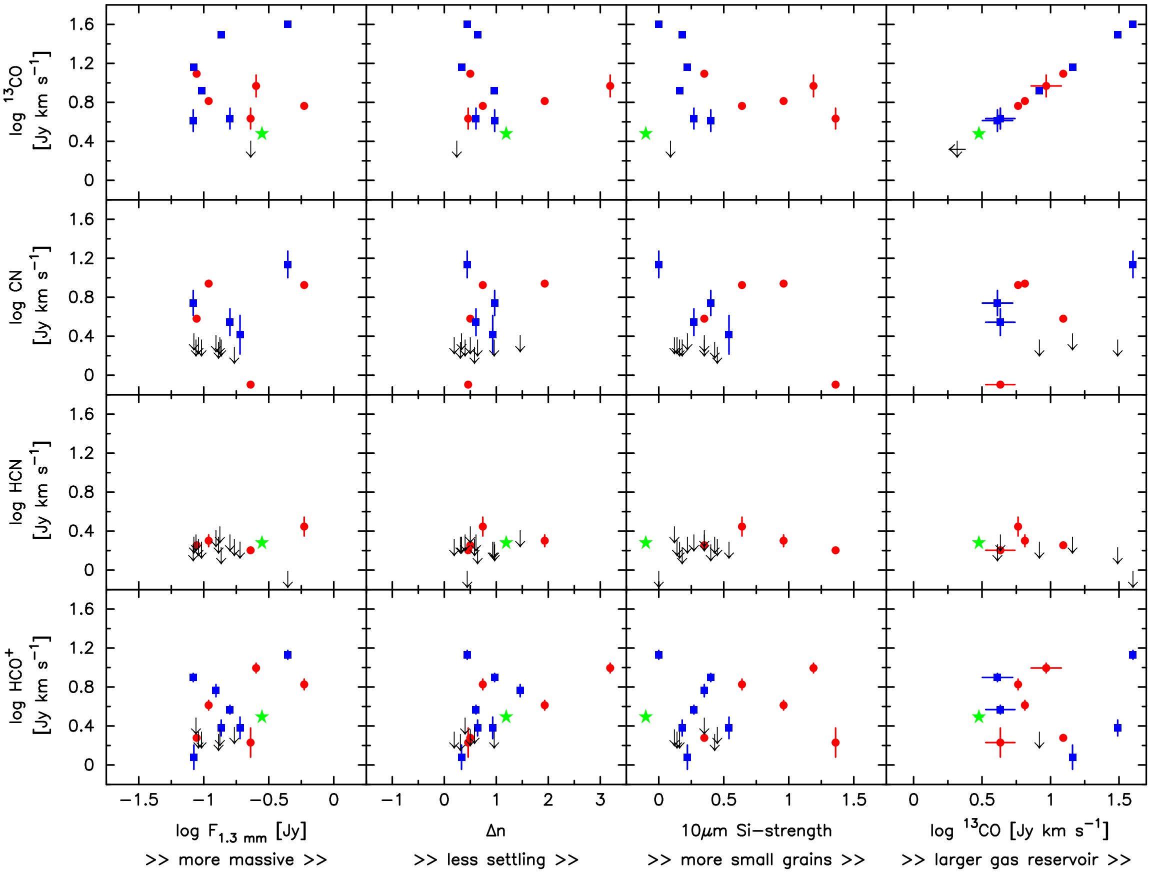

Figure 2.5 — A log plot of the integrated line intensities in Jy km s^{-1} versus several disk parameters that probe the total dust mass ($F_{1.3\text{mm}}$), the mid-infrared spectral slope (Δn), the 10μm silicate emission feature strength (Si-strength), and the total gas mass (inferred from the ^{13}CO line flux). Blue squares represent our JCMT observations, red circles represent data from the literature, and black arrows are used to indicate all upper limits. A green star symbol represents T Tau, whose line emission is contaminated by a large remnant envelope in the single-dish data plotted. The upper-right panel illustrates the dynamic range of the available gas reservoirs.

a factor $\geq$10 in dynamic range.

We then considered the same HCO$^+$, HCN, and CN line strengths versus $F_{1.3\text{mm}}$, Δn, 10μm silicate feature strength, and ^{13}CO line flux, but this time only after normalizing the line fluxes to the ^{13}CO line flux (not shown). This relation represents the line flux per unit gas mass, if we assume that the ^{13}CO line fluxes are reliable tracers of the total amount of molecular gas in each disk. No obvious trends were visible there either. Finally, we explored the equivalent plots of line flux, but then normalizing to $F_{1.3\text{mm}}$, or the line flux per unit dust emission. Again, no trends emerged. Together, the results show that there is no clear correlation between the observed line fluxes of HCO$^+$, HCN, or CN, and the disk dust mass, the degree of settling, the amount of small particles in the disk, or the disk gas mass. Echoing our earlier remarks, we emphasize that only detailed modeling of the emission lines can prove the presence or absence of such a correlation; but judging from the figures that plot general trends only, no strong correlation is expected from this sample.

If the molecular line flux does not depend strongly on the properties of the disk, perhaps it depends on the properties of the star. In Figure 2.6 we plot the line fluxes and upper limits against stellar mass, Hα equivalent width, bolometric luminosity, and X-ray luminosity. Similarly, we also explored the results of normalizing the line fluxes with respect to the ^{13}CO line flux and $F_{1.3\text{mm}}$. While the UV flux could be

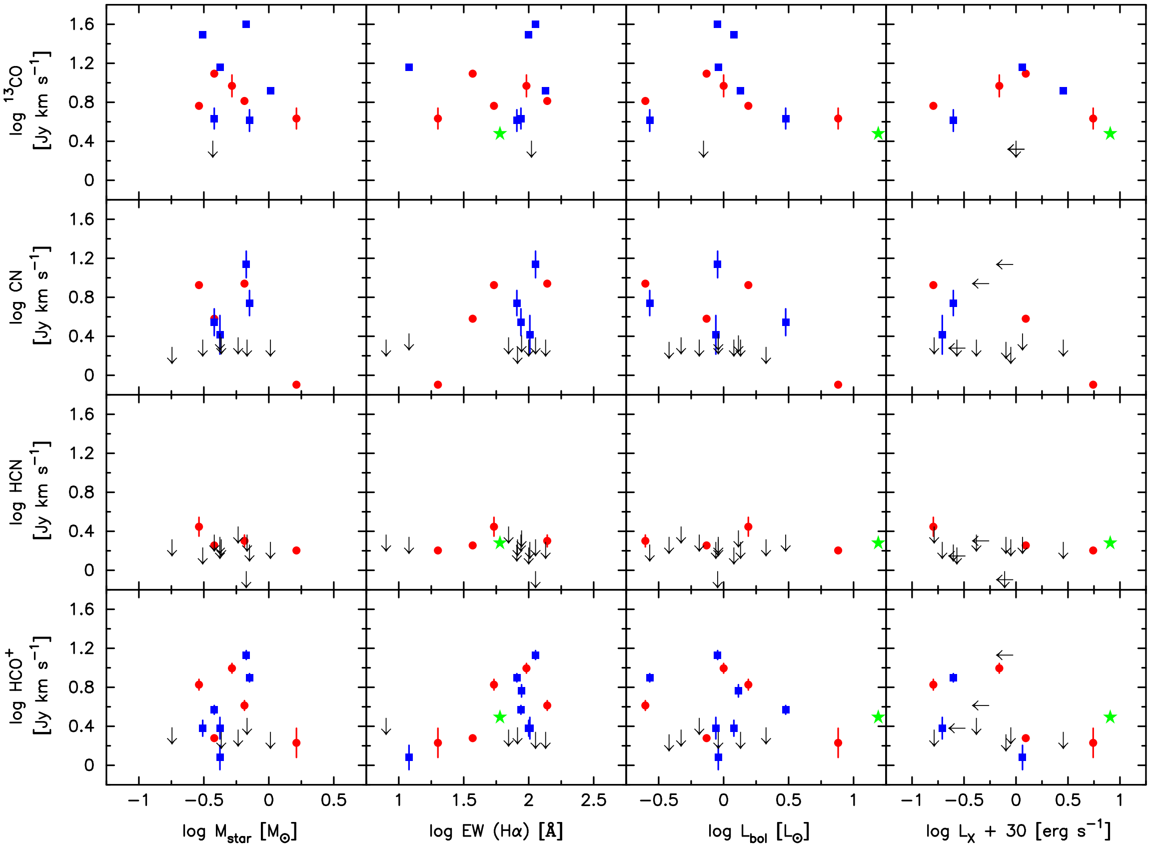

Figure 2.6 — A plot of the integrated line intensities in Jy km s^{-1} versus several stellar parameters from the literature, including: the stellar mass ($M_\star$), the Hα equivalent width (an accretion tracer), the bolometric luminosity ($L_{\rm bol}$), and the X-ray luminosity ($L_{\rm X}$). See Figure 2.5 for an explanation of the symbols.

expected to depend strongly on the mass accretion rate, no homogeneous set of mass accretion rates is available in the literature for this sample, and these can be expected to be variable as well. Instead, we use the Hα equivalent width as a tracer and find no correlation. Indeed, no trends are apparent in any of the plots, suggesting that also such a simple connection between the stellar radiation and the emergent HCO$^+$, HCN, or CN line flux is absent.

In Figure 2.7 we plot the specific relations that served as the primary motivation for this study: the ratio of CN over HCN line fluxes and the HCO$^+$/^{13}CO flux, respectively tracing the degree of photodissociation and the degree of ionization, versus the gas-to-dust ratio (represented by ^{13}CO/$F_{1.3\,\rm mm}$) and the changing mid-infrared slope Δn, representing dust settling. As was the case for our other plots, no significant correlations are apparent. We note that the decreasing line strength with a larger gas-to-dust ratio in the upper-left panel of Figure 2.7, is the likely effect of the incorporation of the ^{13}CO factor into each ratio.

In summary, we find *no* correlation between the HCO$^+$, HCN, and CN line fluxes (or their ratios) and any tracer of the disk properties or those of the stellar radiation field. The line flux does not seem to be affected by any of the investigated parameters. We conclude that *the details of the input radiation field*, such as UV and Lyα strengths (Bergin et al. 2003), may be the deciding factor in the resulting line fluxes. Other contributing factors include the inner versus outer disk contributions and the temperature and density structure in the line-emitting region, both of which are discussed in Section 2.5.

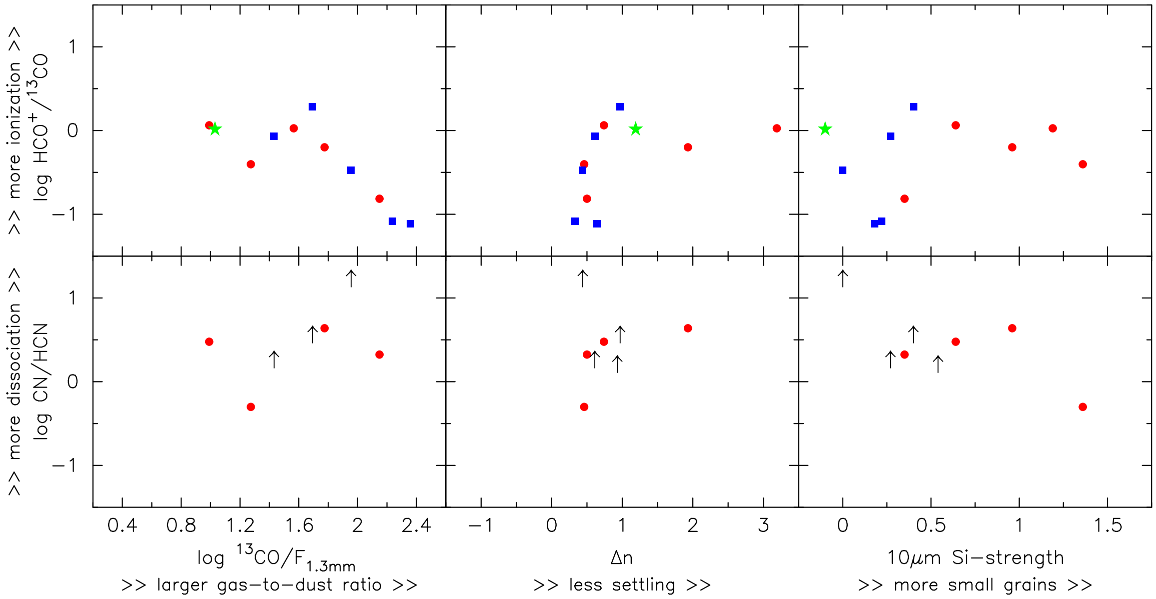

Figure 2.7 — Upper panels: The degree of ionization (traced by $HCO^+/^{13}CO$) versus the gas-to-dust ratio ($^{13}CO/F_{1.3\,mm}$), the difference in the mid-infrared spectral slope between 6, 10, and 25μm (Δn), and the strength of the 10μm silicate emission feature. Lower panels: Similar plots for the photodissociation effect (traced by CN/HCN). See Figure 2.5 for an explanation of the symbols.

2.5 Modeling the Molecular Emission

2.5.1 Disk Models

The previous section investigates the observational correlation between the measured HCO^+, HCN, and CN line intensities and upper limits, and the disk dust observables, such as millimeter continuum flux and infrared slope. While the emergent line intensity depends on the underlying molecular abundance, other factors including the disk density and temperature structure affect the emerging lines through molecular excitation and line radiative transfer. This section addresses how the modeled abundances of HCO^+, HCN, and CN (that can explain the observed emission) are related to the disk dust properties. Rather than developing an *ab initio* description of the disk structure and associated molecular chemistry, this section employs two independent models obtained from the literature (Robitaille et al. 2006; Isella et al. 2009) as starting points, and calculates the molecular abundances (assumed constant throughout the disk except in regions of freeze-out) that are consistent with our line observations.

In the first modeling approach, we make use of the online SED fitting tool[3] of Robitaille et al. (2006), the best-fit parameters of Robitaille et al. (2007), and the visual extinction values from White & Ghez (2001).[4] The continuum radiative transfer code of Whitney et al. (2003) produced the two-dimensional density and temperature structure for the best-fitting model for each source. In some cases (i.e. CI Tau, DO Tau, DR Tau, and FT Tau), the Robitaille models include remnant envelopes; these are not plotted in the figures but are included in the line calculations. However, since their H_2 number densities are $< 10^5$ cm^{-3}, the envelopes are not expected to contribute significantly to the HCO^+, HCN, or CN line emission (e.g. Hogerheijde & Sandell 2000). This first method relies entirely on spatially *unresolved* continuum data, keeping all other stellar and disk parameters free, even in cases where these properties

---

[3] Online SED fitting tool, http://caravan.astro.wisc.edu/protostars

[4] No visual extinction was included in Robitaille et al. (2007) and therefore our best-fit model may differ slightly from the one listed there.

Table 2.5 — Summary of the stellar and disk properties for the best-fitting dust models for our 13 disks.

Source	Robitaille Model						Isella Model				
	A_v [mag]	$M_\star$ [$M_\odot$]	M_d [$10^{-2}\,M_\odot$]	$\mathrm{R_d}$ [AU]	i [°]	$F_{1.3\,\mathrm{mm}}$ [mJy]	$M_\star$ [$M_\odot$]	M_d [$10^{-2}\,M_\odot$]	$\mathrm{R_d}$ [AU]	i [°]	$F_{1.3\,\mathrm{mm}}$ [mJy]
CI Tau	1.80 (1.80)	0.4	1.9	91	57	105	-	-	-	-	-
CW Tau	-	-	-	-	-	-	-	-	-	-	-
CY Tau	0.05 (0.03)	0.9	1.4	97	32	23	0.4	6.92	197	51	117 ± 20
DG Tau	1.60 (1.41)	1.5	3.9	158	50	254	0.3	41.7	89	18	317 ± 28
DN Tau	0.49 (0.49)	0.6	1.0	92	32	39	0.4	1.86	125	30	93 ± 8
DO Tau	4.88 (2.23)	0.8	3.2	104	57	103	-	-	-	-	-
DQ Tau	-	-	-	-	-	-	-	-	-	-	-
DR Tau	0.51 (0.51)	0.8	3.2	104	18	103	0.4	6.31	86	37	109 ± 11
FT Tau	0.00 (-)	0.2	0.8	62	50	36	-	-	-	-	-
GO Tau	-	-	-	-	-	-	0.6	7.10	670	25	57 ± 8
IQ Tau	1.44 (1.44)	1.0	3.0	101	63	74	-	-	-	-	-
UZ Tau	-	-	-	-	-	-	0.3	4.79	260	43	126 ± 12
V806 Tau	-	-	-	-	-	-	-	-	-	-	

Notes. For the Robitaille models, the visual interstellar extinction A_v magnitudes are for the best model fit, only using the measured values from White & Ghez (2001) as an input parameter to the SED fitting tool (in parenthesis). The $M_\star$ values listed for both models are the derived values for each method. For the Isella models, the outer dust radius R_d is from Table 5 in Isella et al. (2009), defined as where the disk becomes optically thin to the stellar radiation. For UZ Tau, the Isella model in fact concerns only the spectroscopic binary component UZ Tau E. The 1.3 mm continuum fluxes ($F_{1.3\,\mathrm{mm}}$) listed for our best-fitting Robitaille model are the SED values of the fit; and for the Isella models we list the resolved (interferometric) dust continuum measurement.

may be well known.

Our second approach uses a model by Isella et al. (2009), which explicitely takes into account the spatial distribution of the millimeter continuum emission observed with the CARMA interferometer. These authors approximate the vertical temperature structure of the disk with the two-layer description by Chiang & Goldreich (1997), and fit the grain size and opacity to resolved 1.3 mm data. In our adaptation of their models, we omit the hot surface layer because it contains insignificant amounts of molecular gas, and we extract the disk's interior temperature from Figure 7 of Isella et al. (2009). The surface density is obtained from their Equation 9 and Table 5. We then calculate the local hydrodynamic equilibrium scale height following Equations 3 and 4 from Hughes et al. (2008). We truncate the models at the transition radius, defined by Isella et al. (2009) as the location where the disk becomes optically thin to the stellar radiation (Section 2.5.3 discusses the effect of extending the disk further).

Figures 2.8 and 2.9 show the resulting temperature and density structures for our sources. For some sources, only one type of model is shown because of the availability of models in Robitaille et al. (2007) and Isella et al. (2009). Table 2.5 summarizes the parameter fits for both models. As can be immediately seen for the four sources for which both a Robitaille and an Isella model are available (i.e. CY Tau, DG Tau, DN Tau, and DR Tau), widely different disk descriptions apparently provide equally good fits to the continuum data.

The vertical height of the Robitaille models is often 4–6 times *smaller* than the Isella models. The radial extents of the disks are comparable for both approaches to within a factor of <2. The resulting masses differ by factors of 2–10, with the Isella models always producing more massive disks. The temperature profiles of the Robtaille models are more detailed (by definition) while the Isella models at large radii are close to isothermal. In general, the temperature between the two models differs by a factor of 3–5 in the midplane. In addition to these parameters, other factors that will affect the emergent lines are the disk inclinations and stellar masses, both of which influence the widths of the lines.

To calculate the resulting molecular line emission, we populate each model disk with gas using the standard 100:1 gas-to-dust ratio, a mean molecular weight of 4.008×10^{-24} g, and constant H_2 relative abundances of 1×10^{-9} for HCO^+, 2×10^{-11} for HCN, and 1×10^{-9} for CN, based on the fractional values in the warm molecular layer for the theoretical models of Aikawa et al. (2002) and van Zadelhoff et al. (2003). In regions where the dust temperature (assumed equal to the gas temperature) drops below the CO ice evaporation temperature of 20 K, these abundances are reduced by a factor 10^3 to account for CO freeze-out. When the H_2 number density drops below $10^{-3}\,\mathrm{cm}^{-3}$, the molecular abundances are set to zero, effectively defining the disk edge.

The gas kinematics follow a cylindrical Keplerian velocity field with stellar masses corresponding to each model fit, as indicated in Table 2.5. A Doppler broadening factor of $0.15\,\mathrm{km\,s^{-1}}$ is also factored into the line calculations. The statistical equilibrium molecular excitation and line radiative transfer was solved using the RATRAN code (Hogerheijde & van der Tak 2000), and the emerging line emission was convolved with the appropriate Gaussian beams. The resulting line profiles are plotted alongside the disk models in Figures 2.8 and 2.9.

2.5.2 Comparison of Fixed-abundance Models

As is immediately obvious from Figures 2.8 and 2.9, the models have difficulty reproducing the detected emission lines. In four cases (CI Tau, DG Tau, DN Tau, and DO Tau) the models predict lines that are weaker than observed; in two cases (GO Tau and UZ Tau), the models predict lines that are stronger than the detected line (for GO Tau) or the obtained upper limits (for UZ Tau). In the remaining four cases (CY Tau, DR Tau, FT Tau, and IQ Tau), the predicted lines are consistent with the achieved upper limits, although for CY Tau the Isella model produces an HCO^+ line that violates the upper limit.

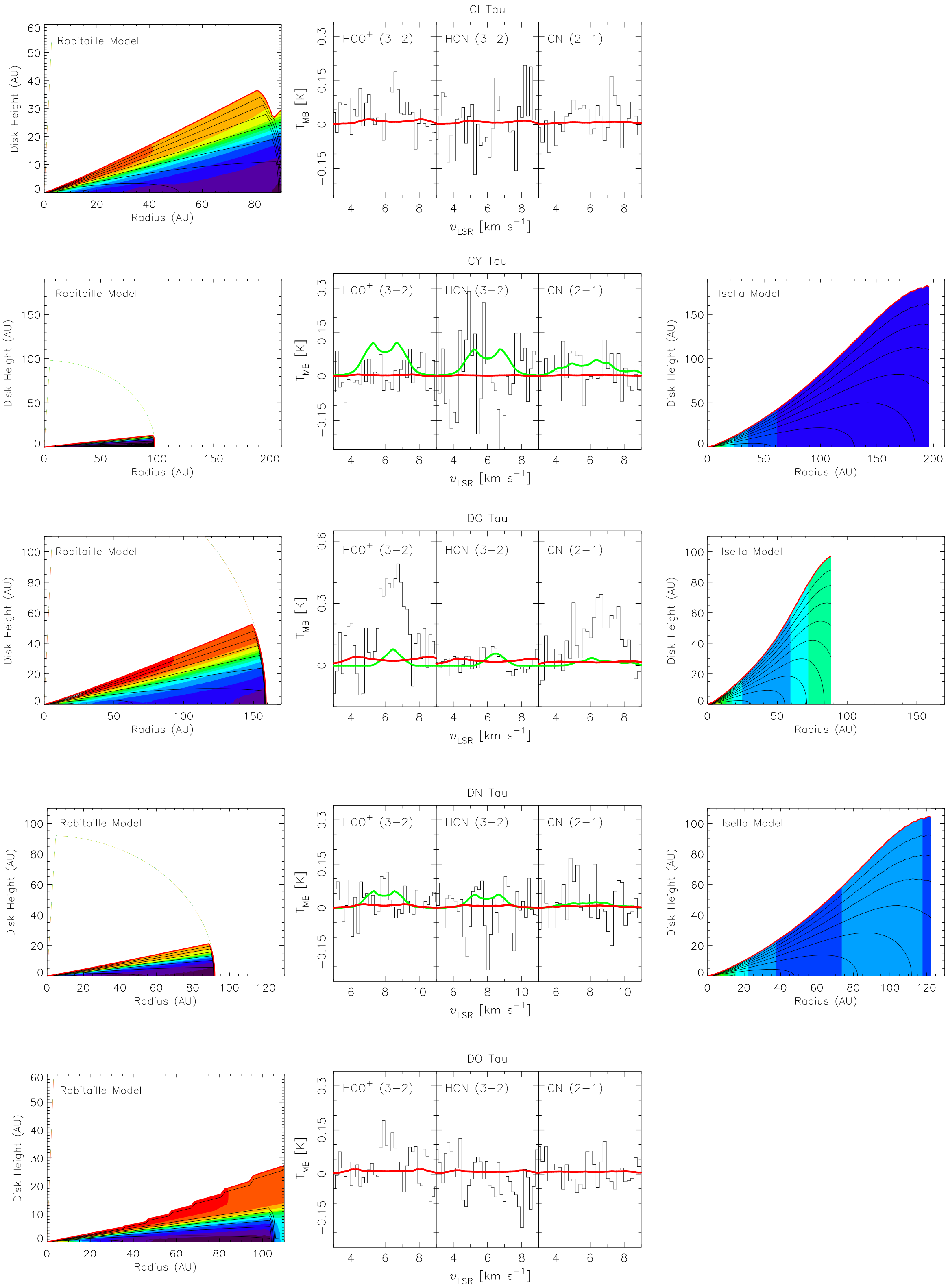

Figure 2.8 — *See caption at the top of page 50.*

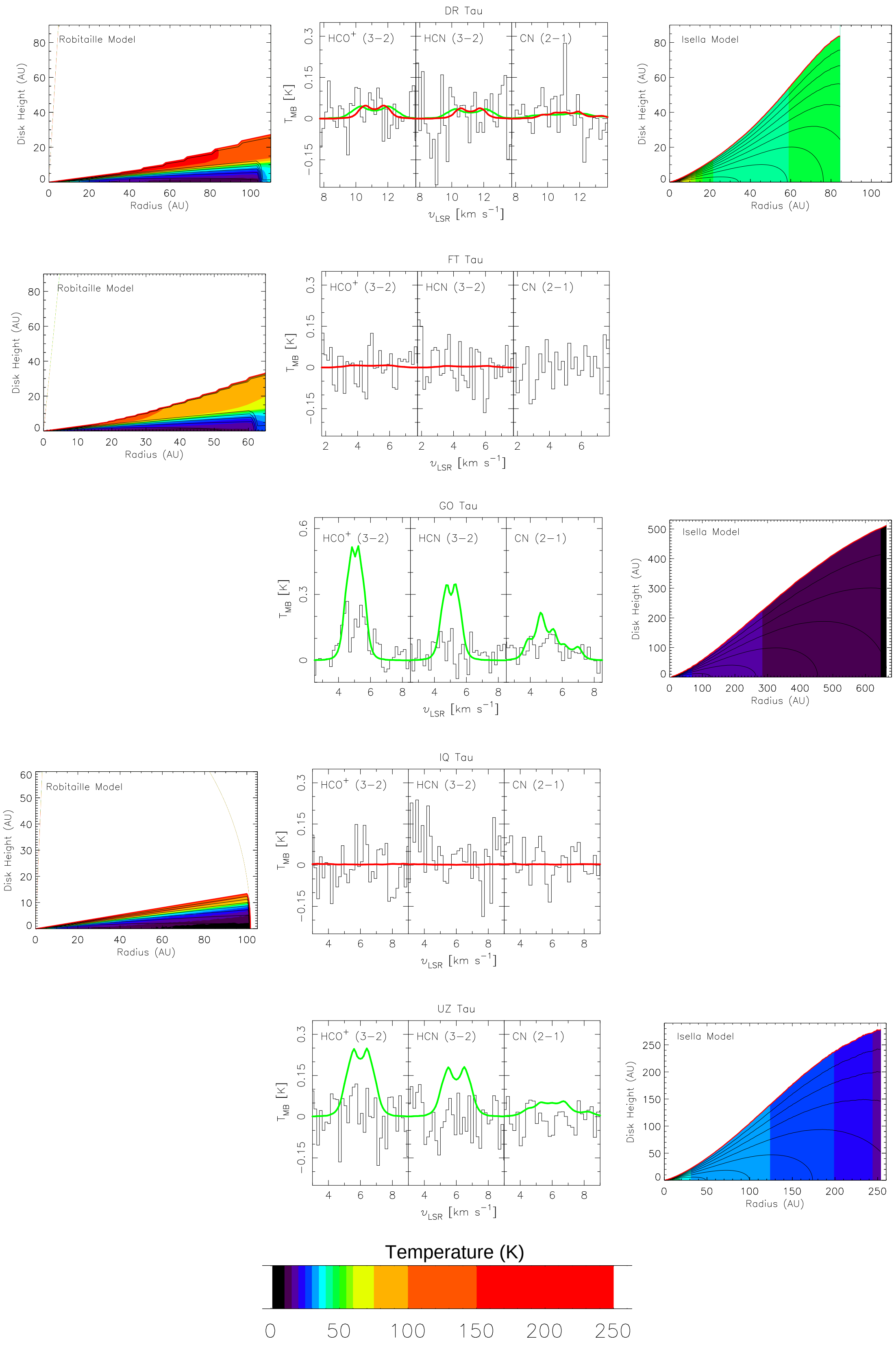

Figure 2.9 — *See caption at the top of page 50.*

Figure 2.8 Caption. Results of the general analysis. From left to right: the Robitaille disk structure; the line predictions for HCO$^+$, HCN, and CN (in red for the Robitaille model, green for the Isella model); and the Isella disk structure. The sources shown from top to bottom are: CI Tau, CY Tau, DG Tau, DN Tau, and DO Tau. For the disk structures, filled contours correspond to the temperature (in K) profile. The temperature levels are identical for all disks, designated at: 10, 15, 20, 25, 30, 35, 40, 45, 50, 55, 60, 75, 100, 150, and 250 K. A color bar is provided in Figure 2.9. The contour lines indicate the log H_2 number density (in cm^{-3}), indicated at whole number integrals from 3 (disk surface/edge) to 12 (typical midplane density).

Figure 2.9 Caption. Continued from Figure 2.8. The sources shown (top to bottom) are: DR Tau, GO Tau, FT Tau, GO Tau, and IQ Tau. A color bar is provided here for the filled temperature contours and applies to all disks.

Where both a Robitaille model and an Isella model are available, the Isella model always produces lines that are stronger and narrower than those of the Robitaille models. The larger stellar masses, by factors 2–5, of the latter, and the larger disk masses of the former, by factors 2–10, contribute to this difference. Inclination also plays a significant role, with more face-on orientations leading to stronger lines (cf. DO Tau and DR Tau, which are fit with the same Robitaille disk structure, but have respective inclinations of $i = 57^\circ$ and $i = 18^\circ$; DR Tau has predicted lines stronger by a factor of $\sim$3). Interestingly, of the six sources from our sample modeled by Isella et al. (2009), the three with *detected* line emission have $i \leq 30^\circ$ (DG Tau, DN Tau, and GO Tau), while the sources with $i > 30^\circ$ (CY Tau, DR Tau, and UZ Tau) are undetected (all have similar $M_\star$). Perhaps the narrower line profiles have helped to make these sources detectable.

Given the general mismatch between the predicted line intensities and widths, and the observations, it is not possible to draw conclusions about the HCO$^+$, HCN, or CN abundances this way. Simply scaling up or down the abundance will not result in a match (to the line shape); only for GO Tau do the abundances appear to lie within a factor of a few above the true values. Furthermore, as illustrated by the case of DR Tau, two *different* disk models (but with more comparable M_d, R_d, and $F_{1.3\,\mathrm{mm}}$ values) produce very similar lines. These degeneracies make it difficult to derive reliable conclusions about the HCO$^+$, HCN, and CN abundances. Instead, more detailed modeling of individual sources may be required.

2.5.3 The Specific Case of DG Tau

Of all the sources in our sample, DG Tau offers the best case to obtain a detailed model. Its 1.3 mm continuum is brighter by a factor ≥ 2.5 than any of the other sources and it emits the strongest HCO$^+$ and CN lines. An extensive literature also exists on DG Tau describing sub-millimeter single-dish (Schuster et al. 1993; Mitchell et al. 1994) and interferometer data (Kitamura et al. 1996a,b; Dutrey et al. 1996; Testi et al. 2002; Isella et al. 2009). Its millimeter continuum emission is compact with $\sim$80% originating from within 95 AU (Isella et al. 2009). The best-fit Robitaille model obtained in the previous section (see Table 2.5, model number 3017659) matches other literature estimates of the DG Tau disk parameters (Table 2.6). Only the disk mass ($M_\mathrm{d} = 0.042\,M_\odot$) is significantly larger than the literature values (0.015–0.025 $M_\odot$); aside from the 10× greater Isella value of 0.4 $M_\odot$. The Isella model, on the other hand, overestimates the stellar mass ($M_\star = 1.5\,M_\odot$), while literature values for $M_\star$ range from 0.3 to 0.8 $M_\odot$ and the Robitaille model yields 0.3 $M_\odot$. To model DG Tau we settle on a central stellar mass of 0.8 $M_\odot$, which is on the high end of the literature values for this object but provides the best fit to the line profiles, as discussed below.

Figure 2.10 reproduces the ^{12}CO (6–5), ^{13}CO (1–0), and C^{18}O (2–1) line observations of Schuster et al. (1993) and Kitamura et al. (1996a). The bright CO isotopologues suggest a significant gas reservoir. Interferometric imaging of the ^{13}CO (1–0) and (2–1) lines in the literature reveal a gaseous disk structure of 600 AU in extent (Kitamura et al. 1996a,b; Testi et al. 2002), about 4–6 times the size inferred from dust emission. Accordingly, we adopt 600 AU for the outer radius of the gas disk, extrapolating the initial Robitaille model outwards. In addition, the ^{13}CO (2–1) emission observed by Testi et al. (2002) is

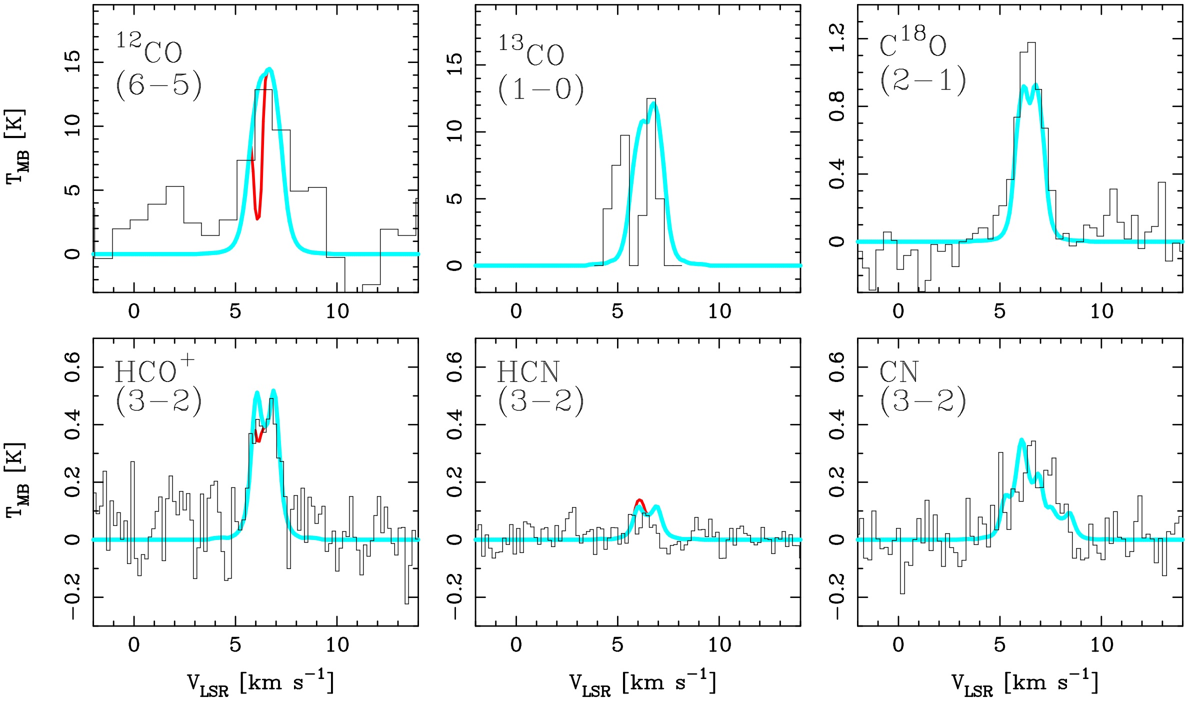

Figure 2.10 — Line predictions for our best-fitting model of DG Tau. The ^{12}CO (6–5) and C^{18}O (2–1) data are taken from Schuster et al. (1993) where their T_R^* scale is equivalent to our $T_{\rm mb}$ scale. The ^{13}CO (1–0) is from Kitamura et al. (1996a), and since we were unable to establish a conversion from Jy to K, we compare the *line shape* only. We have indicated with a thick blue line our fits for a 600 AU disk at an inclination of 25°. Indicated in red is how the (^{12}CO, HCO$^+$, and HCN) line profiles are affected by the absorption or excess emission from a cold, foreground cloud at a radial velocity of 6.1 km s^{-1}. No differences are visible for the ^{13}CO or C^{18}O lines. The effect of the foreground cloud on the CN line is not available; but the expected hyperfine line-splitting is calculated.

consistent with Keplerian rotation around a star of $0.67 \pm 0.25\,M_\odot$, oriented perpendicular (within ±15°) to the highly collimated jet system, which is inclined 38° with respect to the line of sight (Eislöffel & Mundt 1998). Therefore, we adopt an inclination of 25°, which also gives the best fit to the C^{18}O (2–1) line profile. We already show in Figure 2.10—and we will discuss later in this section—the minimal effect from intervening cloud or remnant envelope material in this line.

With the stellar mass ($M_\star = 0.8\,M_\odot$), inclination ($i = 25°$), and outer gas radius ($R_{\rm d} = 600$ AU) now fixed, we use a constant fractional CO abundance of 2×10^{-4} and C^{18}O abundance of 4×10^{-7} (except when $T < 20$ K, where an abundance 10^3 times lower is used) to calculate the simulated line profiles with RATRAN using the extended and modified Robitaille model. To fit the lines, particularly C^{18}O, we find that we need to increase the gas temperature by a factor 1.7; suggesting that the line emission originates in layers where $T_{\rm gas} > T_{\rm dust}$. We adopt this same scaling for the gas temperature for all species, but neglect its effect on the scale height.

For these model parameters, the HCO$^+$ line can be very well reproduced for a disk-averaged abundance of 2×10^{-11} with respect to H_2. This is lower than theoretical predictions for the warm emission layer in many T Tauri disks (Aikawa et al. 2002; van Zadelhoff et al. 2003), but not unlike the beam-averaged fractional abundances ($\sim 10^{-11}$–10^{-12}) inferred from observations of disks around several high-mass (Herbig Ae/Be) stars (see Thi et al. 2004). A low mean abundance is also especially surprising given DG Tau's powerful jets emit significant X-ray radiation (Güdel et al. 2008). Apparently, the disk is sufficiently shielded to retain a low ionization degree. An upper limit for the HCN abundance of 5×10^{-12} is found, while a value of 8×10^{-10} is obtained for CN. This high CN/HCN ratio of >160 suggests efficient HCN dissociation in the bulk of the disk, which is more consistent with its mid-infrared characterization indicating fewer small grains and some dust settling. Here we note the importance of using *abundance* ratios rather than line *intensity* ratios (which contain opacity and excitation effects): the ratio of integrated intensities of CN/HCN used in Section 2.3 is >12, a factor of 13 smaller than the underlying abundance ratio found here.

The disk abundances above have been derived using the density and temperature structure of the best-fitting Robitaille model, with noted modifications. The results are summarized in Table 2.7. Substituting the description of Isella instead, but applying the same values for $M_\star$ and i, and the emergent line intensities are lower by up to a factor of ~16 for HCO$^+$ for the same abundances, and by smaller factors of ~5 and ~10 for HCN and CN, respectively. The large line intensity differences result also from the differences in $R_{\rm gas}$ for each model. Whereas the Robitaille power-law model for the temperature and density description (and sharp outer dust edge) leads easily to extrapolation to larger radii, the Isella model, with its exponentially tapered density structure, does not. Thus, to compare the two disk structures in a uniform way, we plot the temperature and density profiles for each model for the *inner* 160 AU *only* in Figure 2.11. Then, in Figure 2.12 we plot the predicted lines. Unlike Figures 2.8 and 2.9, we now assume identical gas kinematic properties ($M_\star$, i, and $R_{\rm gas}$). The predicted lines for each model in Figure 2.12 are now strikingly similar. The differences in the two emerging line intensities are lower by up to a factor of 2 for HCO$^+$ and much closer for HCN and CN. This suggests that the large CN/HCN ratio of >160 found for the underlying abundances is independent of the temperature and density details of the adopted model (for the inner 160 AU); and leaves only the missing details of the input radiation field uninvestigated.

Table 2.6 — DG Tau star and disk properties from the literature to compare with the two disk models.

Property	Isella Model	Robitaille Model	Literature Range	References
Spectral Type	M0	-	K1–K7	2, 10, 12, 23
$M_\star$ [$M_\odot$]	0.3	1.48	0.3–0.8	4, 5, 17, 20
Age [Myr]	0.1	1.89	0.3–2.0	5, 11, 13
$T_{\rm eff}$ [K]	3890	4560	3890–4395	5, 7, 11, 17
$L_\star$ [$L_\odot$]	1.70	-	1.07–3.62	1, 4, 5, 18
$R_\star$ [$R_\odot$]	2.87	2.427	2.13–2.8	3, 11, 17
$\dot{M}$ [$M_\odot$ yr^{-1}]	4.1e^{-7}	4.5e^{-7}	1.2–20e^{-7}	11, 17, 18
$M_{\rm d}$ [10^{-2} $M_\odot$]	41.7	3.9	1.5–2.51	2, 6, 9, 13
$R_{\rm dust}$ [AU]	89	158	80–300	9, 16, 19
$R_{\rm gas}$ [AU]	160	600	600	16, 24
i [°]	18	25	18-90	3, 9, 14, 16
$A_{\rm v}$ [mag]	-	1.6	1.41–1.6	10, 22
Dist. [pc]	140	140	128–156	10, 21

References. (1) Akeson et al. (2005); (2) Andrews & Williams (2005); (3) Appenzeller et al. (2005); (4) Basri et al. (1991); (5) Beckwith et al. (1990); (6) Beckwith & Sargent (1991); (7) Bouvier et al. (1995); (8) Cieza et al. (2005); (9) Dutrey et al. (1996); (10) Furlan et al. (2006); (11) Hartigan et al. (1995); (12) Hessman & Guenther (1997); (13) Honda et al. (2006); (14) Isella et al. (2009); (15) Kenyon & Hartmann (1995); (16) Kitamura et al. (1996b); (17) Mohanty et al. (2005); (18) Muzerolle et al. (2003); (19) Rodmann et al. (2006); (20) Tamura et al. (1999); (21) Vinković & Jurkić (2007); (22) White & Ghez (2001); (23) White & Hillenbrand (2004); and (24) Testi et al. (2003).

Table 2.7 — Determined abundances for our best-fit DG Tau model.

Molecule	DG Tau	Theoretical
Disk Fractional Abundances (w.r.t. H_2) [a]		
^{12}CO	2.0×10^{-4}	1.0×10^{-4}
^{13}CO	3.3×10^{-6}	1.7×10^{-6}
$C^{18}O$	4.0×10^{-7}	2.0×10^{-7}
HCO^+	2.0×10^{-11}	$1–100 \times 10^{-11}$
HCN	5.0×10^{-12}	$1–100 \times 10^{-11}$
CN	8.0×10^{-10}	$1–100 \times 10^{-11}$
Cloud Fractional Abundances (w.r.t. H_2) [b]		
^{12}CO	2.0×10^{-4}	8.0×10^{-5}
^{13}CO	3.3×10^{-6}	-
$C^{18}O$	4.0×10^{-7}	-
HCO^+	8.0×10^{-9}	8.0×10^{-9}
HCN	8.0×10^{-9}	$4–20 \times 10^{-9}$
CN [c]	-	$3–30 \times 10^{-9}$
Cloud Column Densities (cm^{-2})		
^{12}CO	6.0×10^{16}	…
^{13}CO	1.0×10^{15}	…
$C^{18}O$	1.2×10^{14}	…
HCO^+	2.4×10^{12}	…
HCN	2.4×10^{12}	…
CN	-	…

Notes. (a) The DG Tau abundances are constant throughout the disk (or disk-averaged), whereas the theoretical disk abundances from Aikawa et al. (2002) and van Zadelhoff et al. (2003) represent the ranges expected in the warm molecular layers only; (b) The theoretical cloud values are from Terzieva & Herbst (1998); (c) The online RADEX program does not yet include CN (to calculate the cloud contributions).

Finally, DG Tau is not an isolated source. The environment around the star is dominated by an optical jet (Eislöffel & Mundt 1998), a strong molecular outflow (Mitchell et al. 1994), an expanding circumstellar envelope (Kitamura et al. 1996b), and intervening cloud material (this work). The result of this confused environment is most clearly evident when comparing the ^{12}CO (3–2) line observations presented in Schuster et al. (1993) and Mitchell et al. (1994), which exhibit equally bright line intensities and significant wings at the on-source position and three separate offset positions. We chose to omit the ^{12}CO observations from the fits in Figure 2.10, since they distract from the disk emission. However, we do determine that the ^{12}CO lines are about 3× stronger than predicted for our disk model, suggesting contributions from a surrounding cloud with a CO column density of $N_{CO} \approx 6 \times 10^{16}$ cm^{-2} and line width of 0.3 km s^{-1} for an adopted cloud temperature of 25 K and H_2 number density of 10^4 cm^{-3} (or $N_{CO} \approx 1 \times 10^{16}$ cm^{-2} for an H_2 number density of 10^5 cm^{-3}). For these typical cloud densities, we do not expect significant HCO^+ (3–2), HCN (3–2), or CN (2–1) emission (or absorption); and both Figures 2.4 and 2.10 confirm this.

To determine those line contributions from the cloud, plotted in Figure 2.10, as well as the cloud fractional abundances and column densities listed in Table 2.7, we used the RADEX[5] online calculator. We

---

[5] RADEX is an online, one-dimensional, non-LTE radiative transfer code developed by (van der Tak et al. 2007) to calculate the molecular line intensity, opacity, and excitation temperature. For more information, see http://www.sron.rug.nl/∼vdtak/radex/radex.php

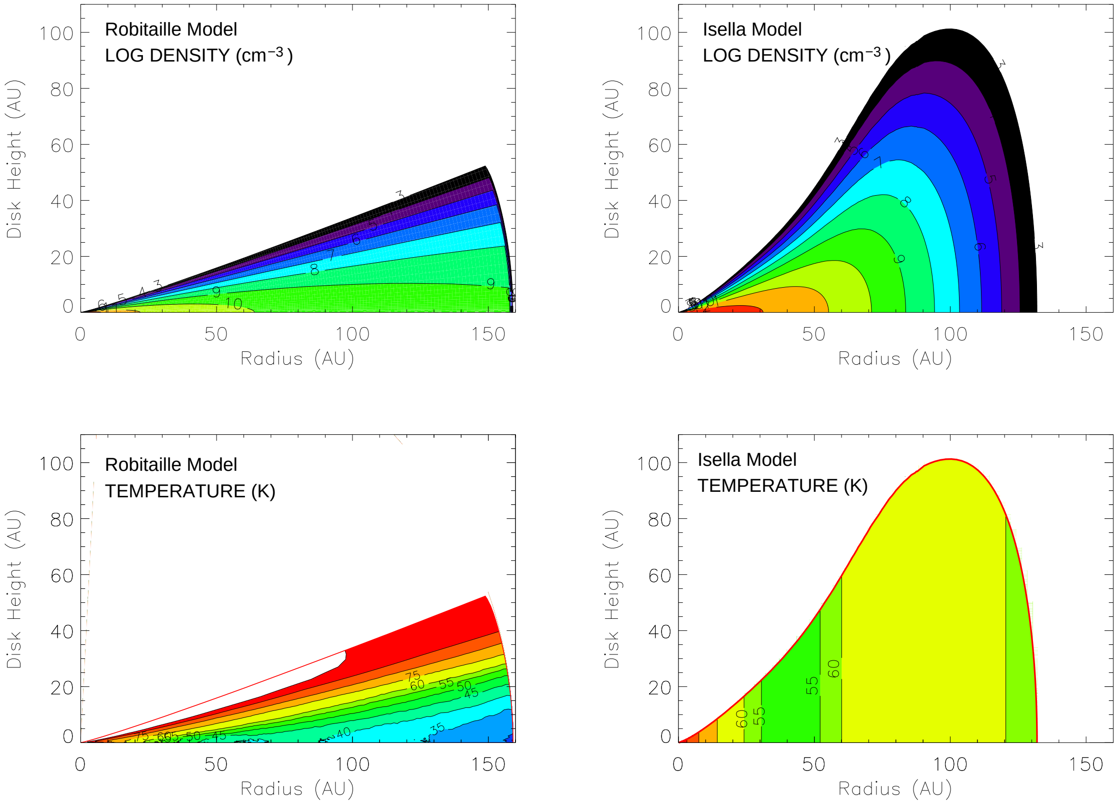

Figure 2.11 — The radial and vertical structures for the *inner* 160 AU of each disk model, for direct comparison. The panels at left show the Robitaille model (without the extended gas reservoir), and the panels at right show the full Isella model (with exponential taper). The upper panels indicate the temperature structures, and the lower panels compare the density structures for each model.

modeled the cloud as a cold intervening layer moving with a radial velocity of 6.1 km s^{-1}. We note that in many of the literature observations, strong absorption is seen near a velocity of 5.8–6.2 km s^{-1}, with several studies reporting these values as the source velocity. We emphasize here that our observations of HCO^{+}, with a critical density 3 orders of magnitudes larger than the CO observations in the literature, are a much better tracer of the disk content, establishing the source radial velocity at 6.47 km s^{-1}. In addition, we confirm that the emerging HCO^{+} line predicted for our intervening cloud fits the detections observed at both DG Tau offset positions (~0.25 K peak centered at 6.1 km s^{-1}, see Figure 2.4). The effect of the intervening material on the observed ^{12}CO, HCO^{+}, and HCN lines is shown in Figure 2.10, while ^{13}CO and C^{18}O exhibit no differences, and the CN cloud predictions are not yet available in the RADEX program.

2.5.4 Notes on Individual Sources

V806 Tau, also called Haro 6–13, has the second strongest HCO^{+} line after DG Tau, but is undetected in HCN and CN. It is a single M0 star. With an $A_{\rm v} = 11.2$, its optical extinction is much larger than our other sources, which might help explain its unique silicate emission feature and positive spectral slope. Furlan et al. (2006) comment that the silicate features are reminsicent of transitional disks, although it also possesses a high mass accretion rate (White & Hillenbrand 2004). Some extended HCO^{+} emission is apparent in Figure 2.4. However, our single-dish radial velocity of 5.40 km s^{-1} is consistent with the

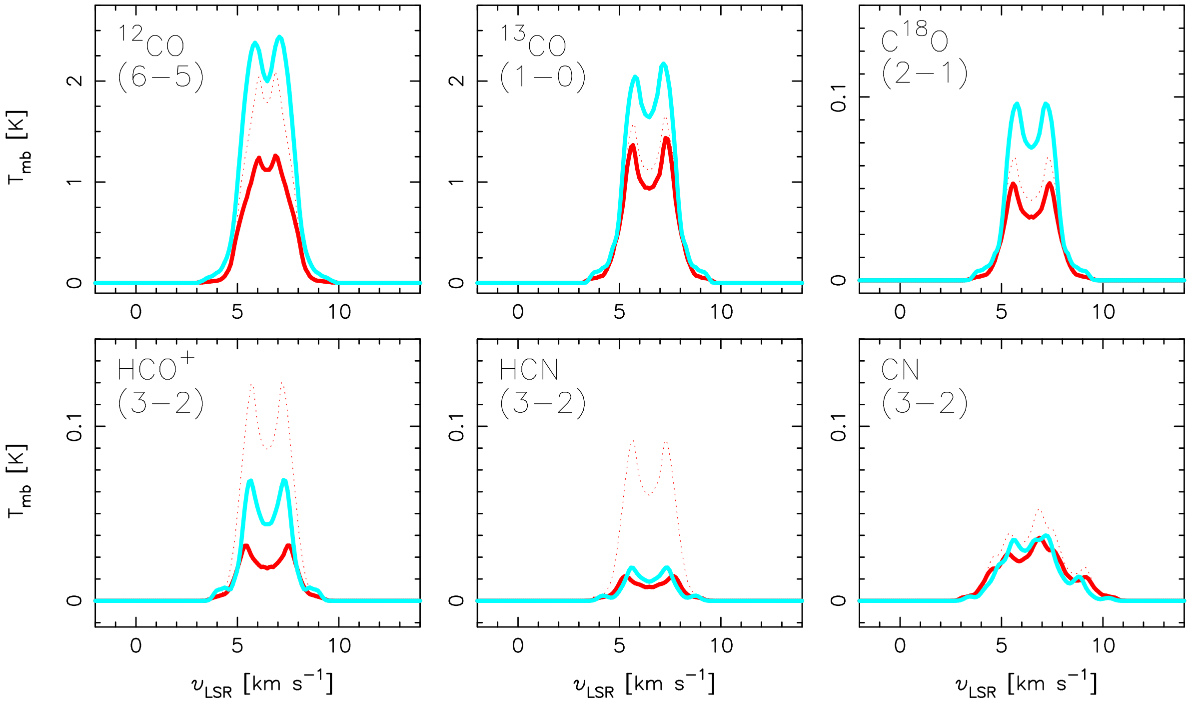

Figure 2.12 — Similar to Figures 2.8 and 2.9, the line predictions for the two models for the *inner* 160 AU, assuming identical abundances, $T_{\rm kin}$, $M_\star$, and i, in order to uniformly compare the predicted emission. A solid blue line represents the Robitaille solution, whilst a red line is the Isella prediction. The corresponding temperature and density structures are given in Figure 2.11. In addition, as a dashed red line, we plot the most extreme solution to the Isella model, based on the provided error bars and the largest possible fractional abundances predicted for disks. For both models, the inner 160 AU structure emits only a small fraction of the total emission necessary to recreate the observed lines, but the two predictions are very similar.

value of 5.10 km s^{-1} from CO interferometric observations (Schaefer et al. 2009). V806 Tau's low disk mass of 0.01 $M_\odot$ (Andrews & Williams 2005; Honda et al. 2006) and large 400 AU radius (Robitaille et al. 2006) suggest that much of the disk of V806 Tau should be UV illuminated, in contrast to our observed upper limit for CN.

GO Tau shows complex line profiles, with peaks at a $\upsilon_{\rm LSR}$ of 4.4, 5.1, 5.5, and 6.3 km s^{-1}. Thi et al. (2001) report ^{12}CO emission peaks at 5.2, 5.5, 6.2, and 7.1 km s^{-1}, and ^{13}CO emission at 4.3 and 7.0 km s^{-1}. They attribute the 5.5 and 6.2 km s^{-1} components to surrounding cloud emission. However, we assign the emission between 4–6 km s^{-1} to the disk of GO Tau, as suggested by the interferometric observations of Schaefer et al. (2009) and Andrews (2007). For GO Tau, the accretion rate is very low (Hartmann et al. 1998), and the amount of dust settling is small if we draw on its mid-infrared spectral slope, suggesting lower rates of UV photodissociation and ionization should be occurring. However, it exhibits one of the brightest HCO^{+} lines, in stark contrast to the rest of the sample since its fainter 1.3 mm continuum flux just straddles our cutoff and yet the source also appears to be associated with a large, and dense, gas reservoir.

DR Tau also has a complicated circumstellar environment, with ^{12}CO emission lines at 6.8, 9.1, 10.0, and 10.3 km s^{-1} and ^{13}CO emission at 6.9 km s^{-1} and near 11 km s^{-1} (Thi et al. 2001). SMA interferometric observations by Andrews (2007) also show strong emission centered on 10.5 km s^{-1}, suggesting that this is the correct source velocity. Our CN spectrum shows a triple-peaked 5.4σ feature centered at 11.2 km s^{-1} (Figure 2.3). Our model results suggest that 'standard' HCO^{+} and HCN abundances are consistent with the non-detections of the lines. The CN detection in the absence of the other lines, on the other hand, indicates a significant CN enhancement.

CW Tau is clearly surrounded by dense cloud material, as witnessed by the eqally strong HCO^+ emission on- and off-source. Our HCO^+ observations (see Figure 2.4) illustrate how, in a crowded star-forming region, measurements at offset positions can be both relevant and useful even for molecular species that preferentially trace much denser material.

CY Tau, DQ Tau, IQ Tau, and **UZ Tau** do not show gas emission lines in our data. Interestingly, they span the full dust classification and morphological sequence of Furlan et al. (2006) with CY Tau and DQ Tau showing rather flat, decreasing mid-infrared SEDs, and IQ Tau and UZ Tau showing evidence for a small grain population. The mass accretion rates – which contribute to the stellar UV excess – range from very low ($10^{-9}\,M_\odot\,\mathrm{yr}^{-1}$) for CY Tau to average ($10^{-7}\,M_\odot\,\mathrm{yr}^{-1}$) for DQ Tau and UZ Tau (Güdel et al. 2007). However, both DQ Tau and UZ Tau E are spectroscopic binaries that exhibit pulsed accretion events on periods of weeks (Basri et al. 1997), and their higher reported accretion rates may overestimate the average, quiescent values.

2.6 Discussion

To return to previous work, Kastner et al. (2008b) showed plots of HCO^+, HCN, and CN line ratios for several PMS stars, showing a tentative correlation between the HCO^+, HCN, CN, and ^{13}CO line ratios. In Figure 2.13 we reproduce their plots and their data points (without error bars), and add our own line ratios. Overall, we find that the trends persist: CN is typically stronger than HCN, CN is also stronger than HCO^+, and the photodissociation rate (as probed by CN/HCN) is roughly constant regardless of the HCN relative line strength. Our contributed line ratios consist largely of upper and lower limits and therefore do not specifically challenge or confirm the trends by probing different regions in the plots. While this complete PMS sample in Figure 2.13 includes sources covering a range in age, mass, and radiation field, the line strengths of HCO^+, HCN, and CN relative to one another do reveal the importance of the ongoing UV photodissociation and X-ray ionization processes in these disks. The results, however, are still limited by small numbers statistics, numerous upper limits, and different rotational transitions (that may trace different regions of the disk).

The motivation of this study was to determine whether disks with a higher degree of dust settling, or with a decreased dust content, have higher abundances of CN and HCO^+ reflecting larger degrees of photodissociation and photoionization. Our data are inconclusive. In Section 2.4 we found that the HCO^+, HCN, and CN line fluxes (or their ratios) do not depend on any other disk or stellar parameter such as millimeter flux, infrared slope, silicate feature strength, stellar spectral type, etc. Section 2.5 shows that detailed SED-based models have intrinsic degeneracies that preclude straight-forward modeling. And even a detailed model, tailored to the case of DG Tau, does not provide unambiguous estimates of the HCO^+, HCN, and CN abundances.

This suggests two possible ways forward. In the first, spatially resolved observations of both the dust continuum and the line emission can be used to obtain *in situ* measurements of the molecular abundances. ALMA will be a powerful instrument for an analysis like this. By addressing localized disk regions, rather than the emission integrated over the entire face of the disk, more simplified modeling approaches can be used (not unlike what is presently state-of-the-art analyses for photon dominated regions, PDRs). In addition, spatially resolved observations provide many more constraints on the underlying disk structure, such as the extent and surface density. This approach addresses the question of how molecular line emission and underlying disk structure are interrelated.

The second approach does not focus on the details of the underlying disk structure, but rather the details of the star's radiation field, which irradiates the disk. Accurate determination of the spectral type and luminosity, the UV and X-ray emission characteristics, and their time dependences should lead to a better

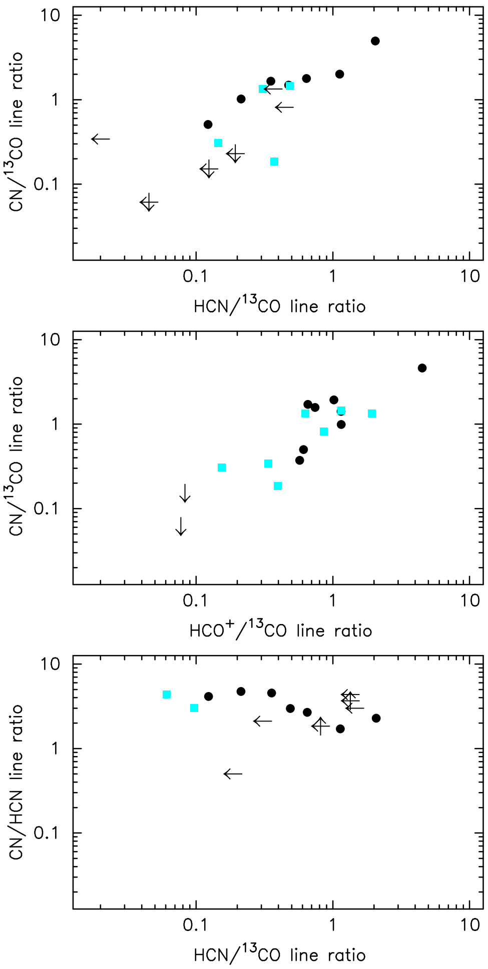

Figure 2.13 — Integrated intensity line ratios for HCO^{+}, HCN, CN, and ^{13}CO plotted alongside other disk systems around PMS stars in the literature. Circles represent data points extracted from Figure 3 of (Kastner et al. 2008b), squares represent data points from our complete Taurus sample, and black arrows represent upper/lower limits.

understanding of the *response* of the molecular gas reservoir to the incident radiation. High-resolution, high signal-to-noise observations are time-consuming but necessary for better stellar characterization of PMS stars, while veiling and other circumstellar environmental effects provide challenges that have been overcome (Merín et al. 2004; Herczeg & Hillenbrand 2008). Recent studies have even argued that the continuum UV spectrum for T Tauri stars must be much weaker, due to the total fraction of the stellar FUV flux that is emitted in the Lyα line alone. Since this fraction can range from 30% up to 85% (for TW Hya), Lyα provides an additional source of photodissociating power that varies from source-to-source and is extremely difficult to measure (Bergin et al. 2003). Which of these two approaches is most fruitful will, of course, depend on which factor dominates the molecular line emission: the underlying disk structure or the stellar irradiation. Since these may be interrelated, both approaches may prove necessary.

2.7 Summary

We surveyed 13 classical T Tauri stars in low-J transitions of HCO^{+}, HCN, and CN to compare the gas structure and chemical abundances within planet-forming disks that possess similar dust masses. We found, conversely, a wide variety of molecular gas properties. For this sample in the Taurus star-forming region, we report 6 new disk detections of HCO$^+$ (3–2), 0 new detections of HCN (3–2), and 4 new detections of CN ($J = 2$–1). These data double the pool of previously known detections, bringing the total detection statistics for the 21 brightest (at 1.3 mm) disks in Taurus to: 14 for HCO$^+$, 5 for HCN, and 8 for CN.

Overall the HCO$^+$, HCN, and CN line ratios for our Taurus disk sample are consistent with the trends identified toward other disks around PMS stars found in the literature, as initially plotted by Kastner et al. (2008a,b). In general, CN is more prevalent than HCN, which suggests that the bulk of the detected emission originates in a UV photodissociating region. Additionally, the fractional molecular ionization ratio, as traced in only slightly denser regions by the HCO$^+$ line, is also enhanced. Both trends agree with the narrow emission lines observed in our sample, which trace the outermost regions where the disk is optically thin to *both* the stellar and interstellar radiation fields.

Despite this disk-to-disk agreement in the line ratios toward the general population of unresolved disks, the gas-line properties reveal *no* observed chemical photoprocessing effects due to the dust properties or several stellar parameters, which was the main motivation for this research. We do not see CN and HCO$^+$ enhancements (via brighter lines) in sources whose mid-infrared spectral slope and silicate emission features indicate more grain growth and dust settling (leading to a lack of UV shielding). In addition, stellar parameters like X-ray luminosity do not seem to influence the observed line intensities of ionization tracers such as HCO$^+$.

The next step was to derive the underlying molecular abundances using two dust models in the literature that are then populated with theoretical values for the fractional molecular abundances. Models for the sample as a whole illustrate the importance of the $M_\star \sin i$ and $R_{\rm gas}$ factors in gas-line abundance studies; parameters that are poorly constrained by the dust properties, but critical to proper line fits. Along these lines, we found during detailed modeling of the source DG Tau that the underlying abundances were less dependent of the temperature and density details in the adopted dust models. We conclude that better characterization of the stellar parameters ($M_\star$), the radiation field itself (UV and Lyα), and spatially-resolved line observations ($R_{\rm gas}$ and i) are necessary to constrain the molecular gas content and evolution.

Large sample statistics are still a challenge. It remains a future task for ALMA, with its the resolution and sensitivity advancements, to resolve these disks (including inner and outer disk differences), their gaseous surface density profiles, and the chemical signatures of changes in the inner dust structure. Only then will we be able to examine how photodissociation, ionization, and freeze-out processes affect the surface density of the gas by comparison to resolved dust observations.

Acknowledgements

We would like to thank Remo Tilanus and Tim van Kempen for help with the data collection and reduction. This research is supported through a VIDI grant from the Netherlands Organization for Scientific Research (NWO).

Bibliography

Aikawa, Y., van Zadelhoff, G. J., van Dishoeck, E. F., & Herbst, E. 2002, A&A, 386, 622
Akeson, R. L., Boden, A. F., Monnier, J. D., et al. 2005, ApJ, 635, 1173
Andrews, S. M. 2007, PhD thesis, University of Hawai'i at Manoa
Andrews, S. M. & Williams, J. P. 2005, ApJ, 631, 1134
Appenzeller, I., Bertout, C., & Stahl, O. 2005, A&A, 434, 1005
Basri, G., Johns-Krull, C. M., & Mathieu, R. D. 1997, AJ, 114, 781

Basri, G., Martin, E. L., & Bertout, C. 1991, A&A, 252, 625

Beckwith, S. V. W. 1996, Nature, 383, 139

Beckwith, S. V. W. & Sargent, A. I. 1991, ApJ, 381, 250

Beckwith, S. V. W., Sargent, A. I., Chini, R. S., & Guesten, R. 1990, AJ, 99, 924

Bergin, E., Calvet, N., D'Alessio, P., & Herczeg, G. J. 2003, ApJ, 591, L159

Bouvier, J., Covino, E., Kovo, O., et al. 1995, A&A, 299, 89

Calvet, N., D'Alessio, P., Hartmann, L., et al. 2002, ApJ, 568, 1008

Chapillon, E., Guilloteau, S., Dutrey, A., & Piétu, V. 2008, A&A, 488, 565

Chiang, E. I. & Goldreich, P. 1997, ApJ, 490, 368

Cieza, L. A., Kessler-Silacci, J. E., Jaffe, D. T., Harvey, P. M., & Evans, II, N. J. 2005, ApJ, 635, 422

Damiani, F., Micela, G., Sciortino, S., & Harnden, Jr., F. R. 1995, ApJ, 446, 331

Dullemond, C. P. & Dominik, C. 2004, A&A, 421, 1075

Dutrey, A., Guilloteau, S., Duvert, G., et al. 1996, A&A, 309, 493

Dutrey, A., Guilloteau, S., & Guelin, M. 1997, A&A, 317, L55

Dutrey, A., Guilloteau, S., & Ho, P. 2007, in Protostars and Planets V, ed. B. Reipurth, D. Jewitt, & K. Keil, 495–506

Eislöffel, J. & Mundt, R. 1998, AJ, 115, 1554

Fuente, A., Martin-Pintado, J., Cernicharo, J., & Bachiller, R. 1993, A&A, 276, 473

Furlan, E., Hartmann, L., Calvet, N., et al. 2006, ApJS, 165, 568

Glassgold, A. E., Najita, J., & Igea, J. 2004, ApJ, 615, 972

Greaves, J. S. 2004, MNRAS, 351, L99

Greaves, J. S. 2005, MNRAS, 364, L47

Greaves, J. S. & Church, S. E. 1996, MNRAS, 283, 1179

Güdel, M. 2008, Astronomische Nachrichten, 329, 218

Güdel, M., Briggs, K. R., Arzner, K., et al. 2007, A&A, 468, 353

Güdel, M., Skinner, S. L., Audard, M., Briggs, K. R., & Cabrit, S. 2008, A&A, 478, 797

Guilloteau, S., Dutrey, A., & Simon, M. 1999, A&A, 348, 570

Hartigan, P., Edwards, S., & Ghandour, L. 1995, ApJ, 452, 736

Hartmann, L., Calvet, N., Gullbring, E., & D'Alessio, P. 1998, ApJ, 495, 385

Herbig, G. H. & Bell, K. R. 1988, Third Catalog of Emission-Line Stars of the Orion Population : 3 : 1988, ed. Herbig, G. H. & Bell, K. R.

Herbig, G. H. & Goodrich, R. W. 1986, ApJ, 309, 294

Herczeg, G. J. & Hillenbrand, L. A. 2008, ApJ, 681, 594

Hessman, F. V. & Guenther, E. W. 1997, A&A, 321, 497

Hogerheijde, M. R., Jansen, D. J., & van Dishoeck, E. F. 1995, A&A, 294, 792

Hogerheijde, M. R. & Sandell, G. 2000, ApJ, 534, 880

Hogerheijde, M. R. & van der Tak, F. F. S. 2000, A&A, 362, 697

Hogerheijde, M. R., van Dishoeck, E. F., Blake, G. A., & van Langevelde, H. J. 1998, ApJ, 502, 315

Honda, M., Kataza, H., Okamoto, Y. K., et al. 2006, ApJ, 646, 1024

Hughes, A. M., Wilner, D. J., Qi, C., & Hogerheijde, M. R. 2008, ApJ, 678, 1119

Isella, A., Carpenter, J. M., & Sargent, A. I. 2009, ApJ, 701, 260

Jørgensen, J. K., Schöier, F. L., & van Dishoeck, E. F. 2004, A&A, 416, 603

Kastner, J. H., Zuckerman, B., & Forveille, T. 2008a, A&A, 486, 239

Kastner, J. H., Zuckerman, B., Hily-Blant, P., & Forveille, T. 2008b, A&A, 492, 469

Kastner, J. H., Zuckerman, B., Weintraub, D. A., & Forveille, T. 1997, Science, 277, 67

Kenyon, S. J., Dobrzycka, D., & Hartmann, L. 1994, AJ, 108, 1872

Kenyon, S. J. & Hartmann, L. 1995, ApJS, 101, 117

Kessler-Silacci, J. 2004, PhD thesis, AA(CALIFORNIA INSTITUTE OF TECHNOLOGY)

Kitamura, Y., Kawabe, R., & Saito, M. 1996a, ApJ, 457, 277
Kitamura, Y., Kawabe, R., & Saito, M. 1996b, ApJ, 465, L137+
Koerner, D. W. & Sargent, A. I. 1995, AJ, 109, 2138
Lepp, S. & Dalgarno, A. 1996, A&A, 306, L21
Luhman, K. L., Allen, P. R., Espaillat, C., Hartmann, L., & Calvet, N. 2010, ApJS, 186, 111
Mannings, V. & Sargent, A. I. 1997, ApJ, 490, 792
Mannings, V. & Sargent, A. I. 2000, ApJ, 529, 391
Merín, B., Montesinos, B., Eiroa, C., et al. 2004, A&A, 419, 301
Mitchell, G. F., Hasegawa, T. I., Dent, W. R. F., & Matthews, H. E. 1994, ApJ, 436, L177
Mohanty, S., Jayawardhana, R., & Basri, G. 2005, ApJ, 626, 498
Muzerolle, J., Calvet, N., Hartmann, L., & D'Alessio, P. 2003, ApJ, 597, L149
Natta, A., Testi, L., Calvet, N., et al. 2007, Protostars and Planets V, 767
Palla, F. & Stahler, S. W. 2002, ApJ, 581, 1194
Panić, O., Hogerheijde, M. R., Wilner, D., & Qi, C. 2008, A&A, 491, 219
Piétu, V., Dutrey, A., & Guilloteau, S. 2007, A&A, 467, 163
Rebull, L. M., Padgett, D. L., McCabe, C., et al. 2010, ApJS, 186, 259
Robitaille, T. P., Whitney, B. A., Indebetouw, R., & Wood, K. 2007, ApJS, 169, 328
Robitaille, T. P., Whitney, B. A., Indebetouw, R., Wood, K., & Denzmore, P. 2006, ApJS, 167, 256
Rodmann, J., Henning, T., Chandler, C. J., Mundy, L. G., & Wilner, D. J. 2006, A&A, 446, 211
Schaefer, G. H., Dutrey, A., Guilloteau, S., Simon, M., & White, R. J. 2009, ApJ, 701, 698
Schreyer, K., Guilloteau, S., Semenov, D., et al. 2008, A&A, 491, 821
Schuster, K. F., Harris, A. I., Anderson, N., & Russell, A. P. G. 1993, ApJ, 412, L67
Simon, M., Dutrey, A., & Guilloteau, S. 2000, ApJ, 545, 1034
Tamura, M., Hough, J. H., Greaves, J. S., et al. 1999, ApJ, 525, 832
Terzieva, R. & Herbst, E. 1998, ApJ, 501, 207
Testi, L., Bacciotti, F., Sargent, A. I., Ray, T. P., & Eislöffel, J. 2002, A&A, 394, L31
Testi, L., Natta, A., Shepherd, D. S., & Wilner, D. J. 2003, A&A, 403, 323
Thi, W., van Zadelhoff, G., & van Dishoeck, E. F. 2004, A&A, 425, 955
Thi, W. F., van Dishoeck, E. F., Blake, G. A., et al. 2001, ApJ, 561, 1074
van der Tak, F. F. S., Black, J. H., Schöier, F. L., Jansen, D. J., & van Dishoeck, E. F. 2007, A&A, 468, 627
van Kempen, T. A., van Dishoeck, E. F., Brinch, C., & Hogerheijde, M. R. 2007, A&A, 461, 983
van Zadelhoff, G.-J., Aikawa, Y., Hogerheijde, M. R., & van Dishoeck, E. F. 2003, A&A, 397, 789
Vinković, D. & Jurkić, T. 2007, ApJ, 658, 462
Weidenschilling, S. J. 1997, Icarus, 127, 290
White, R. J. & Ghez, A. M. 2001, ApJ, 556, 265
White, R. J. & Hillenbrand, L. A. 2004, ApJ, 616, 998
Whitney, B. A., Wood, K., Bjorkman, J. E., & Wolff, M. J. 2003, ApJ, 591, 1049
Yun, J. L., Moreira, M. C., Afonso, J. M., & Clemens, D. P. 1999, AJ, 118, 990

Chapter 3

Observing Low-J ^{12}CO Transitions in Protoplanetary Disks with Varied Dust Properties

Observations of the dust content in protoplanetary disks show a significant spread in the dust properties of disks with similar mass or age. These changes describe an evolution of the dust that occurs on relatively short timescales and concerns just 1% of the total disk mass. If the molecular gas component representing the other 99% of the mass evolves on similar timescales, then we expect a comparable evolutionary picture to emerge from the gas-line observations. We investigate the observational relationship between the dust evolutionary state and the ^{12}CO emission line properties, and we consider the robustness of ^{12}CO as a tracer of the gas reservoir. The dust picture and relevant diagnostics have been determined in the literature from mid-infrared Spitzer IRS observations. Here we present ^{12}CO ($J = 1$–0) interferometry observations toward 5 classical T Tauri stars in Taurus (CW Tau, DQ Tau, IQ Tau, V806 Tau, and V892 Tau), completing the interferometric sampling of a CO rotational line toward Taurus disks with a known 1.3 mm flux ≥ 75 mJy. We also present resolved ^{12}CO ($J = 2$–1) supplementary observations acquired independently toward DQ Tau only. We detect 2/5 sources (V806 Tau and V892 Tau) in the 1–0 transition with CARMA. DQ Tau, which is undetected in 1–0, is very strongly detected ($> 10\sigma$) in 2–1 by the SMA. All three detections are characterized by narrow emission peaks (FWHM $\leq 1.5\,\mathrm{km\,s^{-1}}$), and the 1–0 detections consist of multiple peaks covering a wide velocity range ($< 12\,\mathrm{km\,s^{-1}}$). We report no significant trends in the CO line intensity with any of the current diagnostics for the dust evolutionary state, including the total dust mass, grain growth, or dust settling properties. We conclude for 4/5 sources that the CO line profile is affected by large amounts of optically thick CO in the circumstellar environment and along the line-of-sight that obscures the disk emission unevenly across the full breadth of the line. We caution that interferometric observations of low-J transition lines of CO are an incomplete tracer of the total gas content and disk dynamics, and therefore not a good probe of the gas evolution.

D. M. Salter, M. R. Hogerheijde, G. A. Blake, and T. A. van Kempen
Manuscript in preparation

3.1 Introduction

Modern studies of protoplanetary disks, the birth sites of planetary systems, are largely dominated by millimeter continuum observations of thermal (dust) emission combined with radiative transfer modeling to reproduce source spectral energy distributions (SEDs). These analyses provide a wealth of information on the radial and vertical structure of the disk, including temperature and density profiles (e.g. Calvet et al. 2002; Dullemond et al. 2002). However, the models are derived solely from—and are therefore limited to describing—our knowledge of the dust content in these disks. Meanwhile, fewer studies have targeted the molecular gas, which is a vital ingredient in the formation of gas giant planets and a key probe of the kinematical, chemical, and physical processes affecting the disk evolution.

Now recent molecular line studies are revealing disks with markedly different gas and dust structures (e.g. van Kempen et al. 2007; Fedele et al. 2008). For some of these studies, the fitted mass ratio of dust to gas can be considerably different from the 1:100 value typical of the interstellar medium (e.g. Panić et al. 2009). It remains unclear whether this altered ratio is more representative of the initial star-forming conditions, an evolutionary progression, or an observational effect. The potential implications could affect the outcome for planets since theoretical simulations indicate that the first steps of planet formation in disks occur more quickly above a threshold for the fraction of dust to gas (Ida & Lin 2004; Johansen et al. 2009). Therefore, characterizing the gas content in disks (also relative to the dust content) is a crucial step toward understanding the conditions that affect both disk evolution and planet formation scenarios.

Mid-infrared dust diagnostics already define a progression in the Taurus-Auriga disk population that places each source into an evolutionary context based on its dust mass, degree of grain growth, amount of dust settling, and the concentration of small dust grains present in the warm surface layers of the disk (Kessler-Silacci et al. 2006; Furlan et al. 2006). These differences in the dust properties will affect the disk opacity, the scaleheight, and the irradiation of the molecular gas component. Consequently, we might expect a related evolutionary picture to emerge from the gas-line observations. Therefore, it is important to contrast this dust progression with trends in the molecular gas content, which is significantly more difficult to probe. Only then can we isolate the principle processes driving the disk evolution, as well as explain the large variation seen in the dust properties (as intrinsic or evolved perhaps) amongst a relatively uniform disk sample in terms of mass, age, and environment.

Molecular line studies with *interferometers* are a time-consuming process limited by current instrument sensitivities, such that only a few dozen disks around low-mass pre-main-sequence stars (or T Tauri stars) have been detected successfully in rotational lines of CO. In one of the first large interferometric gas-line surveys of ^{13}CO (1–0) toward 33 T Tauri stars in Taurus-Auriga, Dutrey et al. (1996) reported only 3 detections, defining a 9% success rate for a 3σ detection limit corresponding to a minimum gas mass $\gtrsim 2 \times 10^{-4}\,M_\odot$. In the 10 years since then, a handful of bright low- and intermediate-mass stars in Taurus-Auriga have been studied individually (and in greater detail) with interferometers using several different molecular species (e.g. Koerner et al. 1993a,b; Koerner & Sargent 1995; Dutrey et al. 1998; Guilloteau & Dutrey 1998; Simon et al. 2000; Schreyer et al. 2008; Öberg et al. 2010). More recently, Schaefer et al. (2009) probed a (different) large sample of 23 disks around T Tauri stars in Taurus-Auriga in the ^{12}CO (1–0) and (2–1) transitions. They report only 4 sources (17%) detected, with all 4 being detected in both lines. Andrews (2007) report more success when probing transitions of mostly ^{12}CO (3–2), detecting 8/10 sources (or 80%) in their Taurus sample.

We continue the search for ^{12}CO ($J = 1$–0) line emission at 115 GHz toward 5 additional T Tauri disks in Taurus that are presumed to be gas-rich (from their dust continuum emission). These disks span a range in dust properties, which can reveal clues as to why some disks are detected while others are not. We also present supplementary observations of one source in the ^{12}CO ($J = 2$–1) line near 238 GHz. Because CO is the second most abundant molecule in disks, and it is the most accessible molecule at millimeter wavelengths, it is a logical choice for tracing the gas content (and its evolution) in the brightest disks. Here we contribute 3 additional line detections to the literature statistics, contrast the current CO statistics with the known dust properties for all detected disks, and discuss the challenges of using low-J rotational lines of CO to probe the gas content in protoplanetary disks around the T Tauri population in Taurus.

3.2 Observations

3.2.1 The Disk Sample

We identified 5 bright classical T Tauri stars (CTTSs) in Taurus (CW Tau, DQ Tau, IQ Tau, V806 Tau, and V892 Tau) that each possess a significant dust disk, as determined from their 1.3 mm continuum fluxes, and for which interferometric CO observations were not already available in the literature. These sources were selected from the list of CTTSs in the Taurus star-forming region that had been included in either the Spitzer IRS c2d Legacy survey or as part of the disks GTO program (Kessler-Silacci et al. 2006; Furlan et al. 2006). As a result, all of the disks have been well characterized in terms of their dust content, based on analyses of their mid-infrared spectral slopes and their 10μm and 20μm silicate emission features.

Since Taurus is the nearest low-mass star-forming region at a distance of 140 pc (Kenyon et al. 1994), many of its brightest members have already been probed in rotational transitions of CO with interferometers that preferentially detect compact structure like circumstellar disks. The faintest of these literature sources (at the start of our study) exhibited a continuum flux of ≈ 75 mJy at 1.3 mm. Using the standard mass-flux relation from Beckwith et al. (1990), and adopting the same mean disk parameters as in Dutrey et al. (1996), namely $T_{\rm dust} = 15$ K and $\kappa_{1.3\rm mm} = 0.02$ cm^{-2} g^{-1}, this corresponds to a disk mass of $\sim$0.014 $M_\odot$. Above this flux threshold, delineating the most massive and most promising gas-rich candidate sources, only the 5 sources listed in Table 3.1 had not yet been targeted. Therefore, our observations complete the interferometric sampling of at least one CO rotational line transition toward the brightest 1.3 mm sources in Taurus.

The five targets span a large range in the dust properties probed by the Spitzer IRS surveys (Table 3.1). Some sources exhibit more dust settling than others, as inferred from a shallower mid-infrared spectral slope (defined as $\Delta n = n_{13-25} - n_{6-13}$). A few show evidence for grain growth, or at least a depleting population of small grains, as represented by a weaker 10μm silicate emission feature ($S_{10\mu\rm m}$). Finally, our most massive disk is three times our least massive (since $F_{1.3\rm mm} \propto M_{\rm dust}$). In terms of their disk mass, our 3 least massive sources are expected to be more representative of the broader disk population than the brightest outliers already available in the literature.

Table 3.1 — Taurus disk sample.

Source	RA (J2000)	DEC (J2000)	$F_{1.3\rm mm}$ [mJy]	Δn	$S_{10\mu\rm m}$
CW Tau	4:14:17.00	+28:10:57.8	96±8	0.96	0.16
DQ Tau	4:46:53.06	+17:00:00.2	91±9	0.19	0.14
IQ Tau	4:29:51.56	+26:06:44.8	87±11	0.40	0.35
V806 Tau	4:32:15.41	+24:28:60.0	124±13	1.46	0.35
V892 Tau	4:18:40.61	+28:19:15.5	289±13	−1.22	0.65

Notes. The 2MASS infrared source coordinates used for pointing, the 1.3 mm continuum fluxes from Beckwith et al. (1990), and the infrared dust evolution parameters Δn and $S_{10\mu\rm m}$ from Furlan et al. (2006)

3.2.2 CARMA ^{12}CO ($J = 1$–0) Observations

We observed the ^{12}CO (J=1–0) line emission at 115.271 GHz ($\approx$ 2.7 mm) toward our sample using the Combined Array for Research in Millimeter-wave Astronomy (CARMA) in both its B and C configurations. Located in eastern California (USA), CARMA is a heterogeneous interferometer consisting (at the time of our 2007/2008 observations) of six 10.4-m telescopes from the California Institute of Technology/Owens Valley Radio Observatory (OVRO) and nine 6.1-m telescopes from the Berkeley-Illinois-Maryland Association (BIMA). These 15 antennas provide 150 baselines of 100–1000 m in B array and 30–350 m in C array. All of the receivers currently measure one linear polarization. For all observations, we positioned one correlator band to record the Doppler-tracked line emission in the upper sideband with a bandwidth of 8 MHz, and assigned a second band to a 2 MHz bandwidth. Dual sideband (500 MHz each) continuum data were also collected simultaneously, covering the frequency ranges 110.71–111.18 GHz and 115.04–115.51 GHz.

Each source was observed for one full 8-hour track in B array in the period from 2007 December 24 to 2008 January 03. In C array, we integrated on each source for a total of 3–4 hours, but distributed the sampling over multiple observations between 2008 April 13 and 2008 April 26 to take advantage of track-sharing, which would achieve more efficient u,v-coverage per source. During each C track, our observing script cycled through all 5 sources, scanning each target for 12 minutes at a time, and obtaining 1–6 scans per source depending on the track length, which ranged from 2–8 hours. In comparison, the on-source scans for the B array observations were 24 minutes in length. Multiple observing scripts for the C array tracks allowed for varied rotation of the source order to guarantee a different u,v-sampling for each observation. A 5-minute scan of the gain calibrator 3C 111 or 0530+135 was included every 12–24 minutes for all B and C observations. In addition, we observed the planet Uranus for flux calibration at the start of each track, as well as the radio source 3C 84 or 3C 273 for passband calibration.

All data were processed using the MIRIAD data reduction software program, optimized for CARMA. We calibrated each track separately before combining the source data from all B and C tracks into one calibrated data cube. For the continuum images, which are a composite of the two 500-MHz sidebands, the u,v data were first averaged across all channels, then a natural weighting was used in the inversion step, and finally, cleaning was performed down to a cutoff of 2σ using the *mossdi2* package where σ is defined as the theoretical noise value. The image cell size for all maps is $0.1''$. For the 8 MHz and 2 MHz data, the calibrated data cube was not averaged, so that we preserved the full spectral resolution (63 channels, each of width $\sim$0.13 MHz or 0.32 km s^{-1} for the 8 MHz band and $\sim$0.03 MHz or 0.08 km s^{-1} for the 2 MHz band). As an additional step, we removed the continuum contribution by subtracting a polynomial fit of order 0 (a constant) directly from the u,v amplitudes. Then, the calibrated u,v spectral data were immediately inverted and each channel was cleaned in the same manner as the continuum data. We do note that no passband calibration was performed for the 8 MHz and 2 MHz data after the rms of the data was determined to be greater than the signal variation.

3.2.3 SMA ^{12}CO ($J = 2$–1) Observations

On 2010 January 12, we obtained ^{12}CO ($J = 2$–1) observations at 238.5 GHz ($\approx$ 1.3 mm) of DQ Tau using the Submillimeter Array (SMA), an 8-element array located on the summit of Mauna Kea in Hawaii.[1] The 2–1 data were obtained as a bonus during a follow-up program to investigate the nature of the 27-fold continuum flux increase exhibited by DQ Tau on 2008 April 19 during our third CARMA C track (see Chapter 4, Salter et al. 2008). As a result, a time series analysis of the continuum band data from this SMA track is presented in Chapter 5 (Salter et al. 2010b), where we analyze the recurring nature of

---

[1] The Submillimeter Array is a joint project between the Smithsonian Astrophysical Observatory and the Academia Sinica Institute of Astronomy and Astrophysics and is funded by the Smithsonian Institution and the Academia Sinica.

this flare phenomenon.

The 8-hour track was carried out in the 'Extended' configuration, providing 27 baselines spanning 34–225 m. The 4 GHz bandwidth was uniformly sampled with 128 channels per chunk and a total of 48 chunks. The Doppler-tracked 2–1 line was centered in the S13 chunk of the upper sideband. At the beginning of the track, the opacity was measured independently and the precipitable water vapor (PWV) was estimated to be around 1 mm, rising to 1.3 mm by the close of the track. Scans were shortened to 15 seconds to minimize temporal decorrelation effects on the longest baselines. The source was observed for 7.5-minute integration loops, while the gain calibrators 0423$-$018, 0530$+$135, and 0510$+$180 were observed for 3 minutes each following every on-source loop. The flux scale was checked every 3 hours with an observation of Uranus or Mars, and the source 3C 273 was used to correct for the passband. The data were reduced using the MIR package for IDL, provided by the Smithsonian Astrophysical Observatory. The continuum data were reduced in the same manner as for the CARMA data, but substituting the Clark CLEAN algorithm and using a larger image cell size of $0.2''$. Reduction of the spectral data preserved the resolution specified in our observing scripts, namely 0.8 MHz (or 1.06 km s^{-1}).

3.3 Results

3.3.1 CARMA 2.7 mm Continuum Data

All 5 sources are strongly detected with a peak integrated intensity $\geq 10\sigma$. The Fourier-transformed continuum images are provided in the first column of Figure 3.1, and the corresponding image statistics are reported in Table 3.2. Integrated flux values range from 12.5 mJy (DQ Tau) to 61.1 mJy (V892 Tau) at 2.7 mm when we fit a Gaussian model to the visibility data. We also list in Table 3.2 the fluxes for a Gaussian fit to the image for comparison. For the most part, the numbers are in good agreement; only CW Tau exhibits a difference larger than 15%.

In the reconstructed images, each source appears to be well isolated. Beam sizes are $\sim 1.0'' \times \sim 0.8''$ and 1σ sensitivity limits range 0.9–1.2 mJy bm^{-1}. Alongside each continuum map in Figure 3.1, we plot the average flux measurement as a function of the projected baseline length, where larger baselines probe smaller, more compact structure. These u,v-amplitude plots show how CW Tau, DQ Tau, and IQ Tau are all *un*resolved objects based on their fairly level amplitude profiles. The two brightest sources, V806 Tau and V892 Tau, on the other hand, are clearly resolved. The smoothly decaying brightness profile of V806 Tau is indicative of a single extended structure, perhaps a large disk or a remnant envelope. The profile for V892 Tau, however, exhibits evidence for both a compact component, like a disk, as well as extended structure, such as an envelope.

3.3.2 CARMA ^{12}CO (1–0) Line Data

For the 8 MHz band data, we plot in the first column of Figure 3.2 the CO (1–0) spectra for a $5'' \times 5''$ box (or $3'' \times 3''$ in the case of V892 Tau) centered at the coordinates of the continuum peak emission, which can be referenced in Table 3.1. We note that we do not report further on the 2 MHz band data, since the noise levels were prohibitive to an analysis. In the 8 MHz spectra, we measure bright CO line emission toward V806 Tau at the expected source velocity, and we report a tentative detection toward V892 Tau. Both lines are narrow, spanning just 3–4 channels (or 1.0–1.5 km s^{-1}). No CO emission stands out above the noise levels for CW Tau, DQ Tau, or IQ Tau ($\lesssim$ 20–30 mJy bm$^{-1}\cdot$ km s^{-1}). The CO statistics for all spectra are provided in Table 3.3.

For the CO detections toward V806 Tau and V892 Tau, we provide in the center column of Figure 3.2 an integrated intensity (moment 0) map comprised only of the peak emission channels, which are shaded in the provided spectra. The CO maps indicate 3–4σ peaks at the source position where σ is the

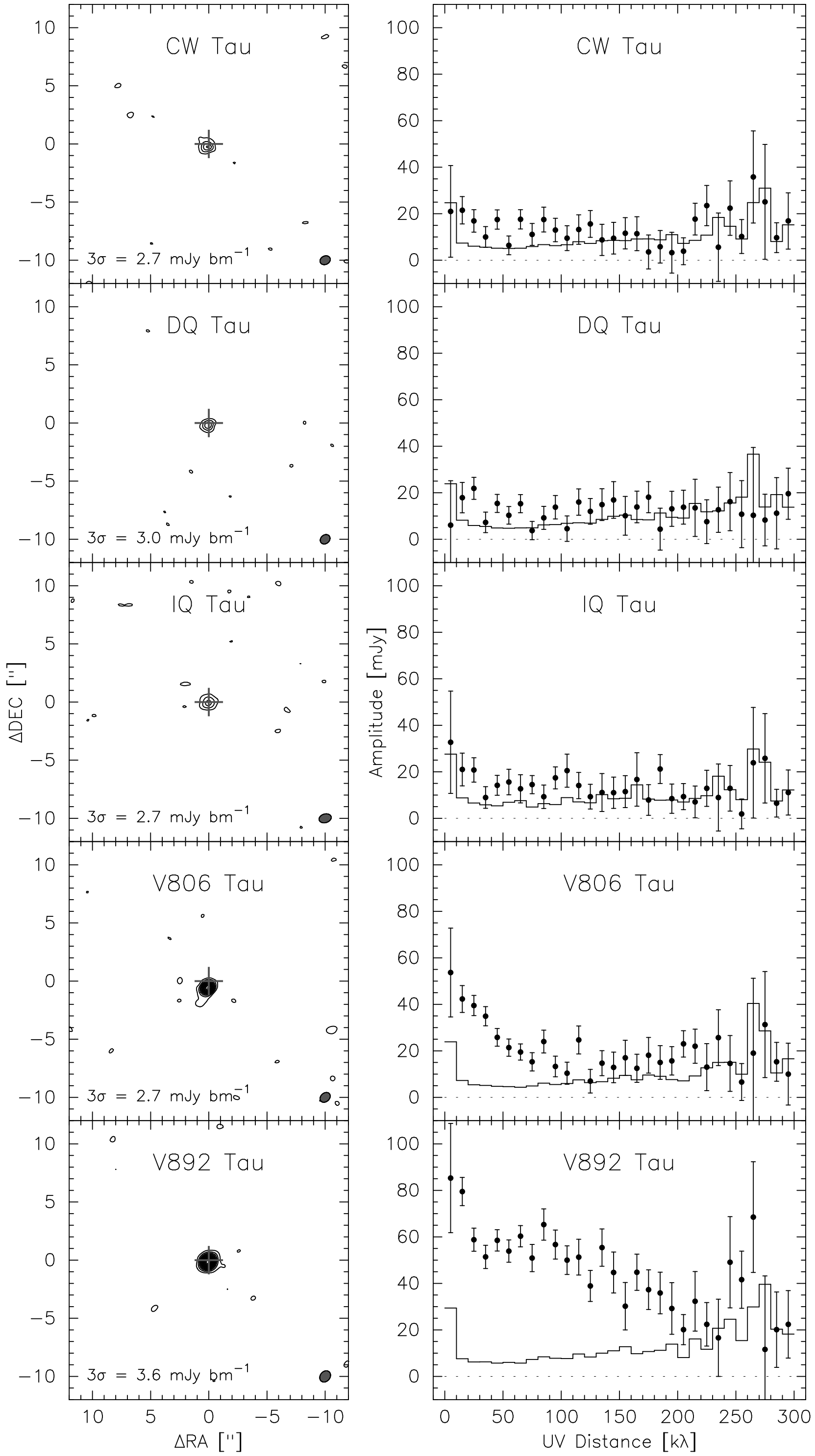

Figure 3.1 — The 2.7 mm dust continuum emission. At left, the combined B+C continuum images for our 5 targets (top to bottom): CW Tau, DQ Tau, IQ Tau, V806 Tau, and V892 Tau. Images are 24″ × 24″ and contours are drawn at multiples of 3σ where σ is the sky rms level, indicated in each image and in Table 3.2. Crosses indicate the 2MASS infrared source position, and the beams (∼1.0″ × ∼0.8″) are shown in the lower right-hand corner. On the right, we plot how the vector-averaged visibility amplitudes vary with the projected baseline length. Error bars are the standard deviation of the mean amplitude, and a solid line indicates the expected amplitude for zero signal.

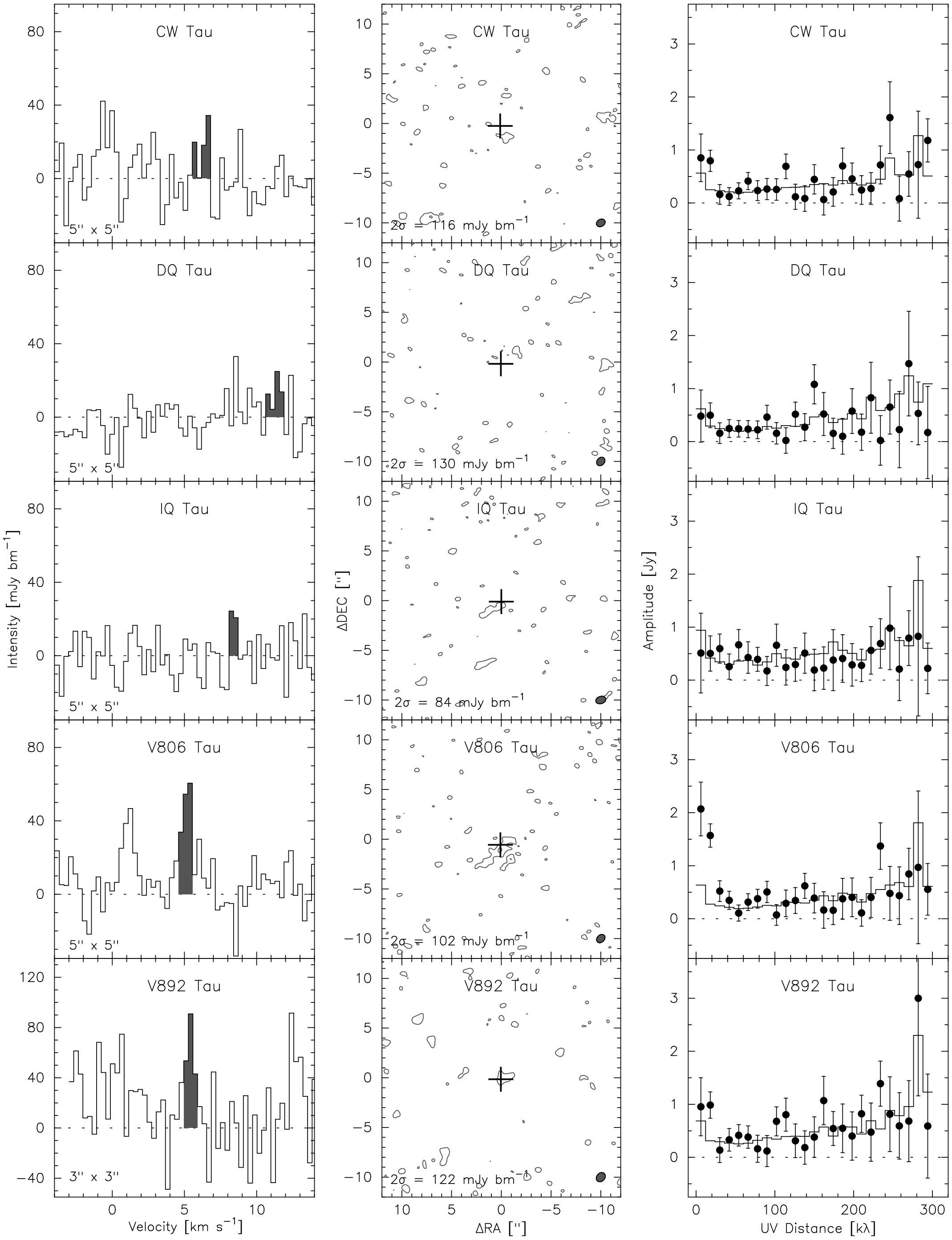

Figure 3.2 — The CO (1–0) line emission. At left, the combined B+C line spectra for our 5 targets (top to bottom): CW Tau, DQ Tau, IQ Tau, V806 Tau, and V892 Tau. The integrated intensity is determined from a $5'' \times 5''$ box (or $3'' \times 3''$ for V892 Tau) centered at the continuum peak emission coordinates. The shaded velocity bins for V806 Tau and V892 Tau represent detections at the source radial velocity. For CW Tau, DQ Tau, and IQ Tau we analyze tentative peaks ($\leq 2\sigma$) and confirm that these are likely noise peaks and therefore *not* real features. At center, the combined CO emission maps for the highlighted velocity bins in the spectra. Images are $24'' \times 24''$ and contours are drawn at multiples of 2σ where σ is the sky rms level indicated at the bottom-left of each map and in Table 3.3. Crosses indicate the 2.7 mm continuum peak emission position, sometimes offset from the 2MASS position, and the beams are shown in the lower right-hand corner. On the right, we show how the source intensity varies with the projected baseline length for the same velocity bins.

sky rms level. For the sources with no clear detections (CW Tau, DQ Tau, and IQ Tau), we analyzed the individual channel maps to identify any emission originating from the source position. In Figure 3.2, we provide similar integrated intensity maps for the most promising features in each spectra, only to confirm that the sources are undetected, and that any coincidently located emission is likely noise.

The u,v amplitudes for the CO emission in the relevant spectral channels (third column in Figure 3.2) support the absence of compact structure toward the undetected sources. V892 Tau presents an unclear case and requires further analysis (see Section 3.4.4), and the emission toward V806 Tau is clearly extended (Section 3.4.4). In both the V806 Tau and V892 Tau systems, the imaged gas in the peak emission channels appears roughly similar in radial extent as the observed dust extent (down to the respective 2σ sensitivity levels). However, fits to the visibility data in the source analysis sections will help us to better constrain the true underlying size scales.

3.3.3 SMA 1.3 mm Continuum and ^{12}CO (2–1) Line Data

We also present results from our supplementary SMA data toward DQ Tau. The source is detected very strongly in both the 1.3 mm continuum ($\sim 100\sigma$) and in the CO (2–1) transition ($\sim 6\sigma$), which are presented together in Figure 3.3. From the time-series analysis of the continuum flux presented in Chapter 5 (Salter et al. 2010b), DQ Tau appears to be quiescent at 1.3 mm for the duration of this observation, even though elevated (non-thermal) flux levels were detected simultaneously at 2.7 mm. This recurring activity, which appears isolated to wavelengths longward of 1.3 mm on this date, is not expected to affect our analysis of the thermal (gas and dust) disk emission. In fact, we suspect that the thermal contribution at 1.3 mm (for which we measure 100.7 mJy versus 12.5 mJy at 2.7 mm) will be much larger than any transient non-thermal emission in this system with a flat spectral curve, thus decreasing the relative impact of any (unknown) superimposed flare emission. For the two millimeter

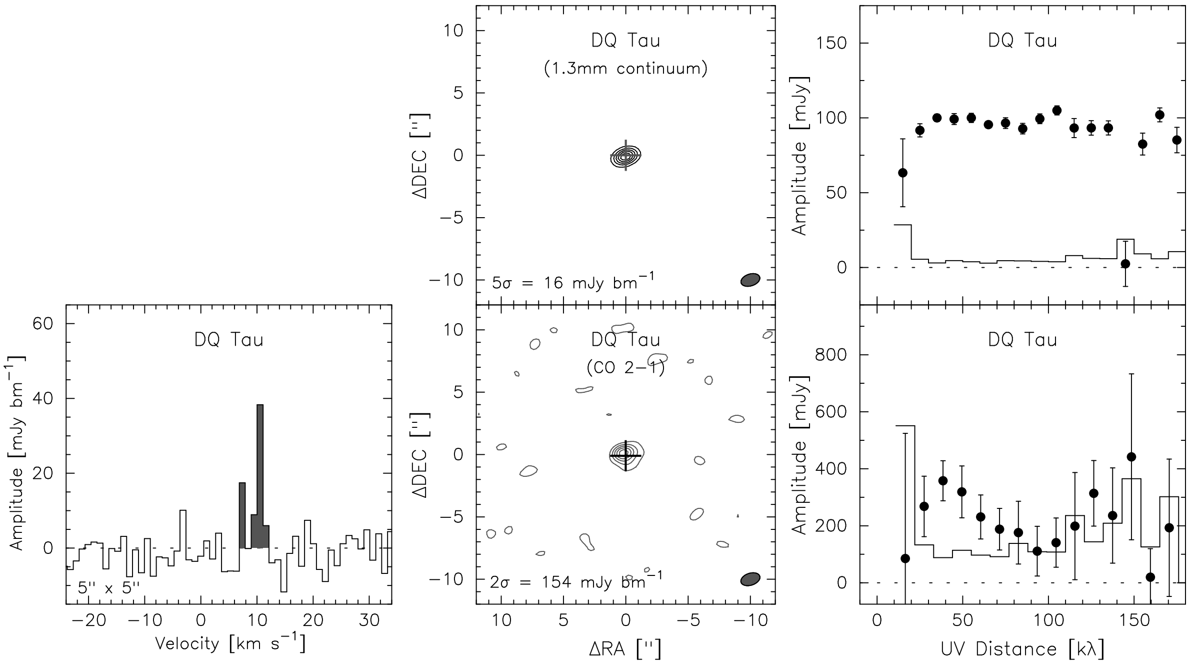

Figure 3.3 — DQ Tau at 1.3 mm (238.5 GHz). *Top row*: The dust continuum image at center and the u,v amplitudes plotted versus the projected baseline length at right; similar to Figure 3.1. The source is detected at 100σ and remains unresolved. *Bottom row*: The CO (2–1) line data with the spectra, integrated intensity map, and visibility amplitudes shown from left to right; similar to Figure 3.2. The CO is detected at 10σ and appears resolved.

flux measurements that we report here, however, we determine a millimeter spectral slope of 2.8, which is within the expected range for thermal emission from a dusty disk.

In the continuum image the source is well isolated and, from the u, v-amplitude plot, unresolved in a beam of size $1.56'' \times 0.95''$. We report a 1.3 mm continuum flux of 100.7 mJy for the combined and averaged visibility data from the entire track. In the line data, the CO (2–1) observations reveal a strong emission line near 10 km s^{-1} that is about 2 km s^{-1} wide. The CO integrated intensity map in Figure 3.3 shows a strong, isolated detection (in comparison to the noisier 1–0 map), and the u, v amplitudes exhibit signs of resolved structure, which we will discuss further in Section 3.4.2. The statistics for the SMA data are reported together with the CARMA data in Tables 3.2 and 3.3.

3.4 Analysis

3.4.1 CW Tau and IQ Tau

As two of the faintest sources, CW Tau and IQ Tau are both unresolved in the continuum and undetected in CO (1–0). Therefore, we only report upper limits for the CO line intensity in Table 3.3. Both sources have similar dust properties, with IQ Tau exhibiting slightly more small-grain depletion and dust settling, properties consistent with a more evolved dust state. Fits to the visibility data for both sources suggest very small dust disks (≤ 85 AU). Our results are consistent (within typical flux calibration errors) with a recent study by Schaefer et al. (2009) where IQ Tau is imaged in the 1–0 and 2–1 transitions of CO with the IRAM PdBI, although they derive a more compact (< 25 AU) disk. There the source is not detected in the 1–0 or the 2–1 line.

In previous single-dish surveys, both sources remain undetected in several other molecular gas tracers, including HCO^+ (3–2), which preferentially traces denser material (Chapter 2, Salter et al. 2010a). However, given the recently derived disk radii, the beam-filling factor for that study would have been $< 0.1\%$. These HCO^+ observations do reveal bright (and dense) cloud emission along the line-of-sight toward CW Tau at a radial velocity of 6.8 km s^{-1}. Clumpy, extended cloud material might explain any excess CO emission in the field of CW Tau, as inferred from the larger visibility amplitudes on the shortest (0–20 kλ) baselines. If CW Tau *is* located in the same velocity bin as the dense cloud material probed by the HCO^+ observations, then little emission ($\leq$32.1 mJy $\text{bm}^{-1} \cdot \text{km s}^{-1}$) appears to be transmitted through the cloud. An alternative possibility is that CW Tau (and IQ Tau) are extremely gas-poor disks.

3.4.2 DQ Tau

DQ Tau is a spectroscopic binary with a circumbinary disk and a cleared out inner dust region (Mathieu et al. 1997; Basri et al. 1997), but warm gas has been detected close to the stars (Boden et al. 2009). The detection of cold CO (2–1) emission toward DQ Tau, however, is interesting and puzzling. The clear detection (10σ at our central map pixel) contrasts the *non*detection of IQ Tau in the 2–1 line (see Schaefer et al. 2009), even though the disks have very similar 1.3 mm fluxes. In fact, DQ Tau is comparable to CW Tau and IQ Tau in most dust diagnostics, except that DQ Tau exhibits the largest amount of dust settling in our sample. In addition, this is the first rotational line transition to be detected toward DQ Tau, which has been probed previously in single-dish observations of HCO^+ (3–2), HCN (3–2), and CN (2–1) as well (Chapter 2, Salter et al. 2010a).

We determine that the CO (2–1) emission is resolved. We perform a Gaussian fit to the visibility data for baselines of length ≤ 80 kλ (where the signal-to-noise is reliable) and retrieve a disk of size 260×122 AU (listed in Table 3.4). This solution extends five times beyond the inferred dust size (56×52 AU), which is never resolved in the continuum. We do, however, derive an inclination of 22° from the aspect ratio of the inferred dust disk size, which is consistent with optical and near-infrared

Table 3.2 — Dust continuum map statistics.

Source	UT Date	Array	On-source [hours]	Beam [″]	$\sigma_{\rm rms}$ ^{a} [mJy bm^{-1}]	Peak Pixel ^{b} [mJy bm^{-1}]	S/N	$F_{\rm imfit}$ ^{c} [mJy]	Peak Offset ^{d} [″]	$F_{\rm uvfit}$ ^{e} [mJy]
				CARMA Observations at 2.7 mm						
CW Tau	24Dec07	B	5.83	0.47×0.34	1.3	9.6	7.4	19.4	0.09, −0.26	13.5
″	13...26Apr08 ^{f}	C	3.40	1.91×1.10	1.2	12.5	10.4	17.9	0.22, −0.18	17.3
″	*(combined)*	B+C	9.23	0.92×0.73	0.9	11.0	12.2	18.3	0.12, −0.25	14.2
DQ Tau	26Dec07	B	5.00	0.43×0.40	1.3	9.9	7.6	17.3	0.04, −0.18	11.1
″	13...26Apr08 ^{g}	C	3.00	1.97×1.10	1.6	13.3	8.3	15.7	0.04, −0.16	14.8
″	*(combined)*	B+C	8.00	0.91×0.74	1.0	11.9	11.9	14.5	0.05, −0.18	12.5
IQ Tau	27,28Dec07	B	8.67	0.84×0.54	1.1	8.4	7.6	15.1	−0.02, −0.13	17.7
″	18...26Apr08	C	3.60	2.21×1.09	1.4	10.6	7.6	22.3	0.10, 0.31	18.9
″	*(combined)*	B+C	7.93	1.07×0.75	0.9	9.2	10.2	15.7	0.00, −0.10	15.9
V806 Tau	30Dec07,03Jan08	B	4.67	0.48×0.41	1.3	30.5	23.5	48.2	0.09, −0.56	42.2
″	13...26Apr07	C	3.40	1.94×1.11	1.5	30.0	20.0	44.4	0.15, −0.66	40.7
″	*(combined)*	B+C	8.07	0.97×0.74	0.9	32.5	36.1	37.5	0.09, −0.57	35.7
V892 Tau	29Dec07	B	6.00	0.61×0.43	1.6	41.7	26.1	73.7	0.05, −0.16	69.4
″	13...26Apr07	C	3.80	1.92×1.09	2.0	49.5	24.8	66.9	0.00, −0.13	62.0
″	*(combined)*	B+C	9.80	1.05×0.84	1.2	49.7	41.4	66.9	0.05, −0.15	61.1
				SMA Observations at 1.3 mm						
DQ Tau	12Jan10	Ext.	8.00	1.56×0.95	1.0	98.1	98.1	100.4	0.01,−0.10	100.7

Notes. [a] The median value for five sky rms measurements. [b] Image cells are 0.1″ × 0.1″ for the CARMA data and 0.2″ × 0.2″ for the SMA data. [c] Determined by a Gaussian fit to the image using the *imfit* routine in Miriad. [d] The offset in arcseconds for the fitted continuum peak using the task *uvfit* in Miriad. [e] The flux value using *uvfit* for a Gaussian fit to the u, v data. [f] In C array, all of the sources were observed in series on 2008 April 13, 18, 19, 21, and 26. [g] Data for DQ Tau taken on 2008 April 19 exhibited unusual activity, which we report separately in Chapter 4 (Salter et al. 2008) it is therefore not included in the final combined image presented here, which only contains thermal emission.

Table 3.3 — CO spectra statistics.

Source	CO Trans.	$v_{\rm LSR}$ [km s^{-1}]	$\sigma_{\rm rms}$ [mJy bm^{-1}]	$I_{\rm max}$ [mJy bm^{-1}]	S/N	$I_{\rm peak}$ [mJy bm^{-1}]	FWHM [km s^{-1}]	$\int I\,dv$ [mJy bm$^{-1}\cdot$ km s^{-1}]
CW Tau	1–0	-	16.0	-	-	-	1.0	$\leq$31.5
DQ Tau	1–0	-	11.4	-	-	-	1.0	$\leq$22.5
	2–1	10.5	6.6	38.3	5.8	38.6	0.5	48.3
IQ Tau	1–0	-	12.1	-	-	-	1.0	$\leq$20.9
V806 Tau	1–0	5.2	11.0	60.5	5.5	53.9	1.2	67.6
	1–0	1.1	11.0	46.7	4.2	45.6	1.0	57.2
	1–0	12.2	11.0	23.4	2.1	35.4	0.4	44.4
V892 Tau	1–0	5.4	26.6	88.2	3.3	82.2	0.9	90.9
	1–0	0.5	26.6	89.3	3.4	98.8	0.5	68.2
	1–0	12.7	26.6	90.7	3.4	76.6	0.9	91.5

Notes. For each source, we give the central radio velocity $v_{\rm LSR}$ for each emission line detected, the noise level $\sigma_{\rm rms}$ for the spectrum, the maximum intensity $I_{\rm max}$ value in the binned data set, the signal-to-noise ratio, the peak intensity $I_{\rm peak}$ from a Gaussian fit to the line, the FWHM of each line, and the integrated line intensity. For non-detections, we report only a 3σ upper limit where $\sigma = 1.2\sigma_{\rm rms}\sqrt{\Delta V\,\delta v}$ following Jørgensen et al. (2004).

Table 3.4 — Disk parameters.

	DUST					*GAS*					
Source	u,v Range [kλ]	Size [$''$]	Size [AU]	i [°]	PA [°]	Line	u,v Range [kλ]	Size [$''$]	Size [AU]	i [°]	PA [°]
CW Tau	(0,200)	0.57 × 0.32	80 × 45	56	42.4	(1–0)	···	···	···	···	···
DQ Tau	(0,200)	0.40 × 0.37	56 × 52	22	42.4	(2–1)	(0,80)	1.86 × 0.87	260 × 122	62	27.8
IQ Tau	(0,200)	0.56 × 0.55	78 × 77	11	80.0	(1–0)	···	···	···	···	···
V806 Tau	(0,70)	1.22 × 0.81	171 × 113	48	-75.2	(1–0)	(0,70)	3.68 × 2.37	515 × 332	50	-77.2
V892 Tau	(0,40)	2.30 × 1.22	322 × 171	58	-62.9	(1–0)	(0,40)	4.90 × 0.56	686 × 78	83	28.7
$''$	(40,200)	0.4 × 0.3	56 × 36	49	48.7	(1–0)	(40,200)	0.25 × 0.21	35 × 29	33	-84.9

Notes. Results of a Gaussian fit to each visibility data set, using the Miriad *uvfit* routine. In the leftmost columns, the derived values are for the continuum (dust) data, and on the right the results are for the spectral line (CO) data. We also indicate the u,v range used where the signal-to-noise was reliable for a good fit.

studies of the system that find a value of 157° (Boden et al. 2009). The projection of the gas disk on the sky appears flatter, suggesting a larger inclination value of 62°. The CO flux returned by the fit is 0.4 Jy.

We also determine that a similarly bright line at the 1–0 frequency may not have been detected in our CARMA observations, peaking instead at about 1.6σ, which is not unlike the noise peak seen in the DQ Tau spectrum at the source radial velocity, determined to be $10.6\,\mathrm{km\,s^{-1}}$ from the 2–1 data (Table 3.3). However, as we determined in Section 3.3.2, the noise peak in the 1–0 data does not originate from the source position. Finally, as a sanity check due to the unusual flare activity observed in the 3 mm continuum band toward DQ Tau on 2008 April 19, we can confirm that the CO (1–0) line remained undetected on the flare date as on the quiescent dates. Therefore, no unexpected behavior is likely (or has been observed) to affect the CO (2–1) detection despite it being observed during a subsequent brightening (as seen at longer wavelengths).

3.4.3 V806 Tau

V806 Tau (also known as Haro 6-13) is the second brightest source in our sample at 2.7 mm, and it is one of only two sources to be resolved in the continuum. Our visibility data seems best approximated by a single structure. We extrapolate from the visibility amplitudes that the source becomes resolved near $100\,\mathrm{k}\lambda$, which corresponds to an angular size of $2.5''$ on the sky. At the distance to Taurus, we estimate that the emission originates in a dust disk of radius 175 AU. This is consistent with the fit found by the Miriad *uvfit* routine, which we provide in Table 3.4.

In the CO (1–0) spectra toward V806 Tau, two strong peaks are detected at radial velocities of 1.1 and $5.2\,\mathrm{km\,s^{-1}}$ (as listed in Table 3.3). The CO emission contributing to both peaks coincides with the source position, as can be seen in the CO maps in Figure 3.4. There we show the integrated intensity maps for an $\sim 1\,\mathrm{km\,s^{-1}}$ wide velocity bin centered around each of the *three* brightest features in the spectra. The third tentative ($\sim 2.9\sigma$) spectal peak at $12\,\mathrm{km\,s^{-1}}$ is related to emission located away from the source position and is likely noise. In the other two bins, the CO distribution measures just 4σ above the sky levels and appears clumpy. At the source radial velocity, presumed to be the central velocity of the brightest peak ($v = 5.2\,\mathrm{km\,s^{-1}}$), the emission is concentrated at the dust continuum peak. In the blueshifted velocity bin near $1.1\,\mathrm{km\,s^{-1}}$, the emission appears as an arc about one side of the continuum source position. It is therefore interesting to return to the redshifted emission map where the prominent (and extended) noise peak lies opposite the blueshifted emission at roughly an equal radial distance from the location of the continuum peak. The velocities of the two bins are also rather symmetric about the central source velocity ($\Delta v \approx \pm 5.5\,\mathrm{km\,s^{-1}}$), leading us to ask whether the CO emission presents a much broader line profile and only these three peaks sit above the noise levels, since emission at these velocity offsets (Δv) can be attributed to gas at a radial distance of ≤ 29 AU from a $1\,M_{\odot}$ central star.

We recall that V806 Tau is the only source to be resolved in the CO (1–0) emission. The visibility data for the emission at the source velocity, as plotted in column 3 of Figure 3.2, detects structure out to $40\,\mathrm{k}\lambda$. Performing a Gaussian fit to the visibility amplitudes for the central line only ($v = 5.2\,\mathrm{km\,s^{-1}}$), we derive a gas disk of size 515×332 AU. The disk inclination from this fit is identical to the inclination determined from the dust, providing support for a similar (gas and dust) disk structure. The derived gas extent is consistent with the $6''$ angular separation between the redshifted “noise” peak and the blueshifted CO peak, even though these channels were not included in the fit. It is still unclear, however, why the highest shifted velocities would be located at the largest disk radii. One explanation might be that a majority of the CO is obscured by intervening cloud material and the emission at these radial velocities and locations are the least affected.

Recently, Schaefer et al. (2009) also presented 3 mm-band data of V806 Tau using the IRAM PdBI. With a higher spectral resolution and sensitivity, they are able to document significant cloud contamination at the central source velocity, confirming obscuration of the line. In general, the rest of our results

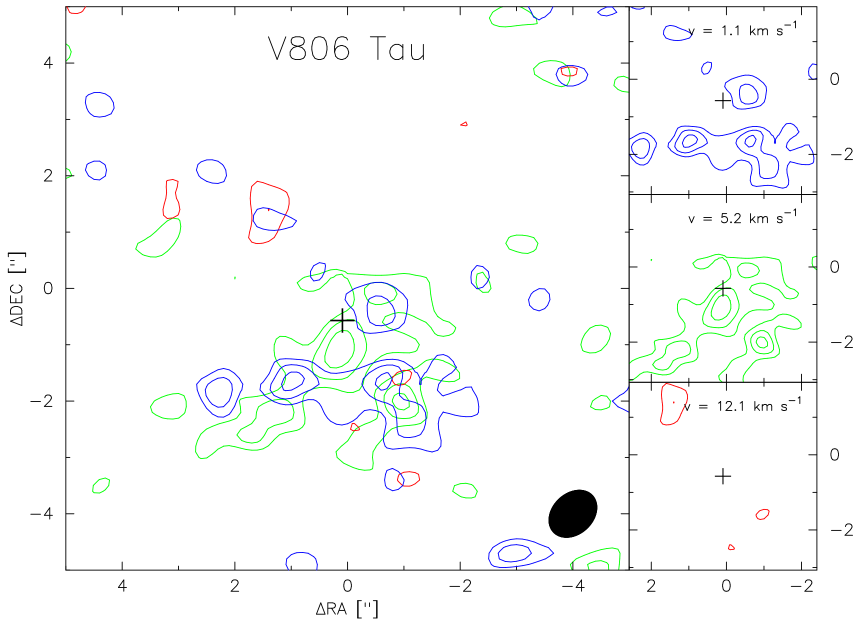

Figure 3.4 — The CO moment 0 maps for V806 Tau. Contours are drawn at 2, 3, and 4σ where σ is 4.7 Jy bm^{-1}· km s^{-1} in all panels. The large panel at left is a 10″ × 10″ composite map overlaying the three velocity ranges corresponding to the brightest peaks in the spectra in Figure 3.2. On the right, the three separate maps are shown in the 5″ × 5″ integration box used to create the spectra. The central velocity for each map is given in the upper right-hand corner and the statistical details are provided in Table 3.3. Crosses indicate the location of the dust continuum peak.

are consistent. They report a continuum flux of 29.5 ± 0.6 mJy at 2.6 mm versus our 35.7 mJy, which is well within typical flux calibration errors. They cover a velocity range of 1.9–8.7 km s^{-1}, and find evidence of extended emission and high-velocity wings, which they attribute instead to a possible outflow. Their maps do not cover the velocity range of our blueshifted peak. However, in CSO single-dish observations of the ^{12}CO (3–2) line towards this source, Moriarty-Schieven et al. (1992) report no evidence for outflows (defined in their sample as wing breadths $\Delta v > 6$ km s^{-1}); but they do find evidence for extended cloud emission in a velocity range of 7–11 km s^{-1}, which may explain the lack of redshifted emission in our own interferometry data. Schaefer et al. (2009) find an inclination of 40° (compared to our 50°) and an outer gas radius > 180 AU (consistent with our projected size of 515 × 332 AU) from a detailed kinematical study of the CO emission that is hindered greatly by obscuration of the line in the outer channel data as well, and indicating that the obscuration is not limited to a small velocity range.

3.4.4 V892 Tau

The V892 Tau (also known as Haro 6-5) spectrum exhibits two emission peaks with a wide velocity separation (at 5.4 and 12.7 km s^{-1}). We also notice that the blueshifted end of the spectrum appears “noisier”. However, an inspection of the inidvidual channel maps suggests that these channels contain low-level (2–3σ) emission originating from near the continuum dust position that may be real. As an example, we include in Figure 3.5 a moment 0 map for the velocity bin at 0.5 km s^{-1} (width ∼1 km s^{-1}) when we analyze the spatial distribution of the spectral line emission peaks.

In the literature, there is evidence for outflows and intervening cloud material along the line-of-sight toward this source. Thi et al. (2001) observed V892 Tau with the JCMT single-dish telescope in the CO (3–2) line and report a broad spectrum (spanning ≈ 6 km s^{-1}) with bright emission, but that emission only possesses radial velocities between our CARMA central (5.4 km s^{-1}) and redshifted (12.7 km s^{-1})

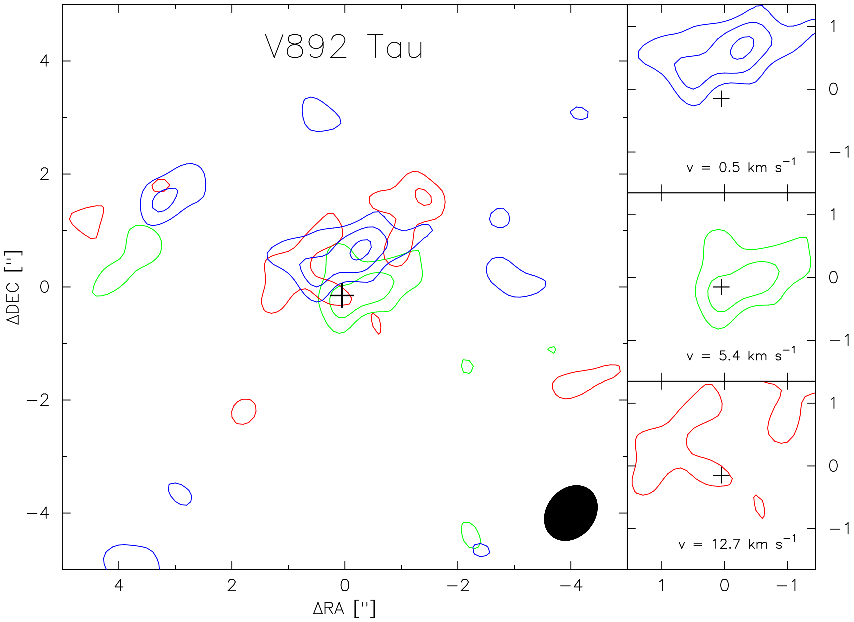

Figure 3.5 — CO moment 0 maps of V892 Tau. Contours are drawn at 2, 3, and 4σ where σ is 5.5 Jy bm^{-1} km s^{-1}. Identical to Figure 3.4, except that the individual maps are shown in a 3″ × 3″ integration box used for the spectra in Figure 3.2.

peaks (see Figure 3.6). In contrast, the complementary (6–5) line observed by Thi et al. (2001) has a strong peak centered at 8.8 km s^{-1} accompanied by a noisy wing extending bluewards until a velocity of about 5.5 km s^{-1}. Given our CARMA (1–0) results, we might also be tempted to identify an isolated redshifted peak near 13 km s^{-1} in the 6–5 data.

A broader line is to be expected from a more massive central star (5.5 $M_\odot$) with a B8 V spectral type (Monnier et al. 2008), especially at a high inclination. However, mapping of a 90″ × 90″ region around V892 Tau with the HARP-B receiver on the JCMT reveals a very similar, broad emission profile at 11 separate off-source positions (see Panić & Hogerheijde 2009). Likewise, we attribute the fact that we do not see bright CO (1–0) emission from such a bright source in the interferometry data to resolved-out, large-scale, optically thick emission over the same velocity range. To better probe the gas content in this disk, it will be necessary to consider optically thinner molecular tracers to better contrast the contribution from the disk versus the surrounding cloud material.

In the continuum, the source is found by dust continuum analyses in the literature to have an inclination of 60° (Hamidouche 2010; Monnier et al. 2008), which is consistent with a double-peaked line as seen clearly in the CO (3–2) and (6–5) data (see Figure 3.6, reproduced from Thi et al. 2001). We report a similar inclination (58°) based on a simple Gaussian fit to our continuum (dust) visibility data and using an analysis of the aspect ratio to derive the source size.

3.5 Discussion

Our gas-line properties (e.g. line intensities and spatial extent) are not always in agreement with predictions made based on the dust properties of each source. For example, our brightest continuum source V892 Tau is only detected weakly in CO (1–0), whereas our second brightest source V806 Tau, at half the flux of V892 Tau, exhibits a strong integrated spectral line and a spatially extended gas reservoir. Along these same lines, DQ Tau and IQ Tau are two equally bright sources in the continuum, both undetected in 1–0, but DQ Tau appears very bright in 2–1 while IQ Tau remains undetected (see Schaefer et al. 2009).

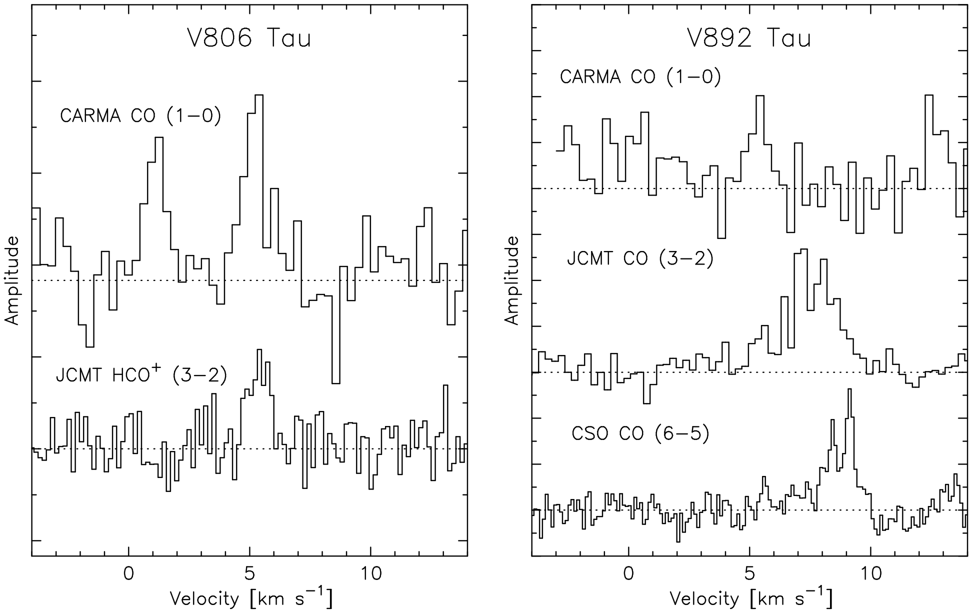

Figure 3.6 — A comparison of our CARMA CO (1–0) data (top spectra in each panel) with other molecular tracers, uncluding a JCMT single-dish HCO$^+$ (3–2) observation of V806 Tau, a JCMT CO (3–2) observation of V892 Tau, and a CSO CO (6–5) observation of V892 Tau (Chapter 2, Salter et al. 2010a; Thi et al. 2001).

Clearly, the 1.3 mm continuum fluxes, which probe the cold dust reservoir at all radii, are a poor predictor of the integrated line strengths in this sample.

The other mid-infrared dust diagnostics (e.g. grain growth and dust settling) also offer few properties aligned with our detection statistics. Both sources with large amounts of dust settling (DQ Tau) and small amounts (V806 Tau) can present similarly bright and resolved CO emission lines ($\sim$40 mJy bm^{-1}); the results are identical for an abundance of small grains (V806 Tau and V892 Tau) versus a more depleted population (DQ Tau) in the disk surface layers. Therefore, the mid-infrared dust properties probing the warm inner regions also appear to be poor indicators of the relative CO line strength in this sample.

We can also compare the dust diagnostics with the gas-line properties for the entire literature for sources in Taurus with $F_{1.3\mathrm{mm}} \geq 75$ mJy, to look for larger observational trends. However, similar examples of contrasting dust and gas observational diagnostics are also present in the larger sample. For example, DN Tau, DM Tau, and GM Aur all exhibit an equally bright 3–2 line, as measured by Andrews (2007), and yet their 1.3 mm continuum fluxes range 84–253 mJy. In addition, DN Tau is not detected in 1–0 or 2–1 (Schaefer et al. 2009), in contrast to the other two sources (Koerner et al. 1993a; Dutrey et al. 1997; Panić et al. 2008; Simon et al. 2000; Kessler-Silacci 2004). CY Tau, DL Tau, and DO Tau are all detected (one faintly, another strongly) in the 2–1 transition (Simon et al. 2000; Koerner & Sargent 1995); and they all possess a depleted small-grain population ($S_{10\mu\mathrm{m}} = 0.09$–$0.18$). In contrast, DM Tau, GM Aur, and RY Tau exhibit more small-grain emission ($S_{10\mu\mathrm{m}} = 0.96$–$1.36$) and are also strongly detected (Koerner et al. 1993a).

In the Dutrey et al. (1996) survey of ^{13}CO, an optically thinner isotope of ^{12}CO, the authors find disk masses predicted from the dust emission were 20–80 times larger than the masses derived from the ^{13}CO of 3 detected sources (DG Tau, Haro 6-5b, and UY Aur), suggesting that the lines toward these sources may not trace the entire gas reservoir. Many explanations can account for this discrepancy, including CO freeze-out onto dust grains in the cold regions of the disk, preferential dispersal of the gas content in disks, or optically thick intervening material. In the case of DG Tau, one of the brightest sources in the continuum in Taurus, several follow-up interferometric studies confirm a highly confused circumstellar environment that significantly obscures the line emission (Kitamura et al. 1996; Testi et al. 2002).

In fact, confusion by foreground material is a common thread in the literature (as well as our own source sample), and particularly apparent in interferometry data where the maximum obscuration of the line typically occurs near the systematic velocity of the cloud (and the star itself). Other confirmed examples of strongly afflicted sources include DL Tau and UZ Tau E (Simon et al. 2000), and V806 Tau and GO Tau (Schaefer et al. 2009). Fewer examples exist of sources that are well isolated, like DM Tau and GM Aur (Dutrey et al. 1998; Simon et al. 2000; Panić et al. 2008). Identifying more *isolated*, gas-rich sources or probing optically thinner molecular species or higher transitions is necessary to achieve a uniform, less contaminated analysis of the observational diagnostics for the gas reservoir.

3.6 Summary

We observed 5 classical T Tauri stars (CW Tau, DQ Tau, IQ Tau, V806 Tau, and V892 Tau) in low-J transitions of ^{12}CO to contrast the observed gas properties in a sample of disks in different dust evolutionary stages. These observations complete the interferometric sampling of at least one CO rotational line toward the brightest 1.3 mm sources ($F_{1.3\mathrm{mm}} \geq 75$ mJy) in the Taurus star-forming region. Here we report 2 new detections of a CO (1–0) line and 1 detection of CO (2–1) to be added to the growing literature of molecular line observations of the protoplanetary disks around T Tauri stars; which are characterized by a low statistical detection rate overall for low-J CO line observations.

Using the CARMA millimeter array, we measured 2.7 mm continuum fluxes for all sources, resolving just the brightest two sources, V806 Tau and V892 Tau. These are also the only two sources to be detected in CO (1–0). The CO emission around V806 Tau is resolved and appears clumpy in nature; V892 Tau is unresolved. In both CO integrated spectra, several peaks are seen spread out over large velocity separations (of full breadth 6–12 km s^{-1}) and still appear to be associated with the source position. Their radial location in the map is consistent with the disk extent and the radial velocity offsets for the peaks are consistent with Keplerian rotational velocities at radii $\lesssim 30$ AU. The surrounding sky regions in the maps of all 5 sources are dotted with 2–3σ emission peaks, suggesting that a lot of CO may be present in the region. This conclusion is supported by the visibility data sets of CW Tau and V892 Tau, in particular, which show that additional CO emission is detected on the shortest baselines only, representing larger-scale structure in the field. When comparing our interferometry data to single-dish observations and other interferometry results in the literature, our CO spectra clearly suffer from obscuration, which is a common trend in studies of the gas structure and kinematics toward sources in crowded, star-forming regions.

In supplementary observations of DQ Tau obtained with the SMA, we report an unresolved 1.3 mm continuum flux measurement and a strong CO (2–1) emission line that *is* resolved. From a Gaussian fit to the visibility data, the gas component extends to a radius three times larger than the dust and has an inclination angle (62°) that differs from the dust disk (62°). It is interesting how DQ Tau, which until now has remained undetected in rotational lines of several molecular tracers, appears as a bright line in this transition. Sensitivity levels may be partly to blame. However, the thin, sharp, double-peak nature of our low spectrally resolved 2–1 line profile is more indicative of absorption effects along the line-of-sight rather than a purely Keplerian disk velocity pattern. Therefore, we suspect that intervening cloud material could likely play a role in the non-detected lines toward this source. This result iterates the unpredictable nature of the observed gas-line intensities, especially if we try to extrapolate directly from the observed dust measurements.

When considering the entire literature sample, we found no significant trends in the CO line intensity or detection statistics with any of the current diagnostics for the dust evolutionary state (e.g. dust mass, grain growth, and dust settling properties). In addition, two sources that are equally bright in one CO transition line do not necessarily possess similar brightnesses in another transition. Almost all sources exhibit some level of obscuration from optically thick CO along the line-of-sight, accounting for some of these observational differences.

Our primary conclusion from this study is that enough CO is confirmed present along the line-of-sight toward 4/5 of our targets (CW Tau, DQ Tau, V806 Tau, and V892 Tau) to be optically-thick in the low-*J* transitions, prohibiting an accurate study of the gas distribution and disk kinematics based on these diagnostics alone, even with interferometers and increased sensitivity observations. We therefore caution that low-*J* CO lines are likely a poor tracer of the total disk gas content and that they may not be accurate predictors of the line strengths of mid-*J* transitions that offer greater contrast with the cloud material. The low-*J* data can only provide constraints, and better characterization of the environment is necessary to determine the robustness of these constraints.

Acknowledgements

Support for CARMA construction was derived from the states of California, Illinois, and Maryland, the Gordon and Betty Moore Foundation, the Kenneth T. and Eileen L. Norris Foundation, the Associates of the California Institute of Technology, and the National Science Foundation. Ongoing CARMA development and operations are supported by the National Science Foundation under a cooperative agreement, and by the CARMA partner universities. The research of DMS and MRH is supported through a VIDI grant from the Netherlands Organization for Scientific Research (NWO).

Bibliography

Andrews, S. M. 2007, PhD thesis, University of Hawai'i at Manoa
Basri, G., Johns-Krull, C. M., & Mathieu, R. D. 1997, AJ, 114, 781
Beckwith, S. V. W., Sargent, A. I., Chini, R. S., & Guesten, R. 1990, AJ, 99, 924
Boden, A. F., Akeson, R. L., Sargent, A. I., et al. 2009, ApJ, 696, L111
Calvet, N., D'Alessio, P., Hartmann, L., et al. 2002, ApJ, 568, 1008
Dullemond, C. P., van Zadelhoff, G. J., & Natta, A. 2002, A&A, 389, 464
Dutrey, A., Guilloteau, S., Duvert, G., et al. 1996, A&A, 309, 493
Dutrey, A., Guilloteau, S., & Guelin, M. 1997, A&A, 317, L55
Dutrey, A., Guilloteau, S., Prato, L., et al. 1998, A&A, 338, L63
Fedele, D., van den Ancker, M. E., Acke, B., et al. 2008, A&A, 491, 809
Furlan, E., Hartmann, L., Calvet, N., et al. 2006, ApJS, 165, 568
Guilloteau, S. & Dutrey, A. 1998, A&A, 339, 467
Hamidouche, M. 2010, ArXiv e-prints
Ida, S. & Lin, D. N. C. 2004, ApJ, 616, 567
Johansen, A., Youdin, A., & Mac Low, M. 2009, ApJ, 704, L75
Jørgensen, J. K., Schöier, F. L., & van Dishoeck, E. F. 2004, A&A, 416, 603
Kenyon, S. J., Dobrzycka, D., & Hartmann, L. 1994, AJ, 108, 1872
Kessler-Silacci, J. 2004, PhD thesis, CALIFORNIA INSTITUTE OF TECHNOLOGY
Kessler-Silacci, J., Augereau, J., Dullemond, C. P., et al. 2006, ApJ, 639, 275
Kitamura, Y., Kawabe, R., & Saito, M. 1996, ApJ, 457, 277
Koerner, D. W. & Sargent, A. I. 1995, AJ, 109, 2138
Koerner, D. W., Sargent, A. I., & Beckwith, S. V. W. 1993a, Icarus, 106, 2
Koerner, D. W., Sargent, A. I., & Beckwith, S. V. W. 1993b, ApJ, 408, L93
Mathieu, R. D., Stassun, K., Basri, G., et al. 1997, AJ, 113, 1841

Monnier, J. D., Tannirkulam, A., Tuthill, P. G., et al. 2008, ApJ, 681, L97
Moriarty-Schieven, G. H., Wannier, P. G., Tamura, M., & Keene, J. 1992, ApJ, 400, 260
Öberg, K. I., Qi, C., Fogel, J. K. J., et al. 2010, ApJ, 720, 480
Panić, O. & Hogerheijde, M. R. 2009, A&A, 508, 707
Panić, O., Hogerheijde, M. R., Wilner, D., & Qi, C. 2008, A&A, 491, 219
Panić, O., Hogerheijde, M. R., Wilner, D., & Qi, C. 2009, A&A, 501, 269
Salter, D. M., Hogerheijde, M. R., & Blake, G. A. 2008, A&A, 492, L21
Salter, D. M., Hogerheijde, M. R., van der Burg, R. F. J., Kristensen, L. E., & Brinch, C. 2010a, A&A submitted
Salter, D. M., Kóspál, Á., Getman, K. V., et al. 2010b, ArXiv e-prints
Schaefer, G. H., Dutrey, A., Guilloteau, S., Simon, M., & White, R. J. 2009, ApJ, 701, 698
Schreyer, K., Guilloteau, S., Semenov, D., et al. 2008, A&A, 491, 821
Simon, M., Dutrey, A., & Guilloteau, S. 2000, ApJ, 545, 1034
Testi, L., Bacciotti, F., Sargent, A. I., Ray, T. P., & Eislöffel, J. 2002, A&A, 394, L31
Thi, W. F., van Dishoeck, E. F., Blake, G. A., et al. 2001, ApJ, 561, 1074
van Kempen, T. A., van Dishoeck, E. F., Brinch, C., & Hogerheijde, M. R. 2007, A&A, 461, 983

Part II

Transient Flares of Non-thermal Millimeter Emission

Chapter 4

Captured at Millimeter Wavelengths: a Flare from the Classical T Tauri Star DQ Tau

For several hours on 2008 April 19, the T Tauri spectroscopic binary DQ Tau was observed to brighten, reaching a maximum detected flux of 468 mJy and likely making it (briefly) the brightest object at 3 mm in the Taurus star-forming region. We present the light curve of a rarely before observed millimeter flare originating in the region around a pre-main-sequence star, and the first from a classical T Tauri star. We discuss the properties and nature of the flaring behavior in the context of pulsed accretion flows (the current picture based largely on studies of this object's optically variable spectrum), as well as magnetospheric reconnection models (a separate theory that predicts millimeter flares for close binaries of high orbital eccentricity). We believe that the flare mechanism is linked to the binary orbit, and therefore periodic. DQ Tau makes a strong case for multi-wavelength follow-up studies, performed in parallel, of future flares to help determine whether magnetospheric and dynamical interactions in a proto-binary system are independent.

D. M. Salter, M. R. Hogerheijde, and G. A. Blake
Astronomy & Astrophysics Letters, **492**, L21–L24 (2008)

4.1 Introduction

Observations of pre-main-sequence (PMS) stars at millimeter wavelengths are used to study thermal emission from gas and dust in their circumstellar disks where planets may be forming. At these wavelengths, the disks are optically thin and the integrated flux is related directly to the total amount of cold, circumstellar material. But on short timescales, we show how the dominating mechanism for millimeter emission can shift to high-energy, short-period processes. We present 3 mm continuum observations of the low-mass, classical T Tauri star (CTTS) DQ Tau, which was observed to brighten for many hours on 2008 April 19, reaching a maximum detected flux of 468 mJy (compared to 17 mJy in the days both before and after the event).

A stellar flare at these typically quiescent wavelengths, like a solar flare in the millimeter, is believed to be the superposition of a gyro-synchrotron spectrum with that from synchrotron emission, the latter peaking in the sub-millimeter to far-infrared (Kaufmann et al. 1986). The first light curve for a strong millimeter flare observed toward a young stellar object (YSO), GMR-A in Orion, was reported by Bower et al. (2003) and attributed to magnetic activity. In protostellar environments, scenarios where magnetic fields can interact, re-connect, and accelerate electrons to high energies are thought to include single-star stellar flares as we see in the Sun, interactions due to changes in the magnetic field lines between a star and its accretion disk, and colliding magnetospheres and coronal flares between components of a multiple-star system.

While longer-term radio variability is well documented in YSOs, and can also be the result of magnetic activity like starspots, few outbursts have been observed (Feigelson & Montmerle 1999). DQ Tau is only the fourth flare detected toward a PMS object, and the first from a CTTS. In addition to GMR-A, our observation follows the re-occurring flares from the weak-line T Tauri star (WTTS) V773 Tau A, studied in depth by Massi et al. (2002, 2006, 2008), and a single 1.3 cm flare from a second YSO in Orion named ORBS by Forbrich et al. (2008).

In Orion, follow-up study of GMR-A confirmed a photospheric origin of gyro-synchrotron emission around a single magnetically-active WTTS (Furuya et al. 2003), whereas observations of the deeply embedded ORBS could only limit the emitting region to a radius ≤ 2 AU (Forbrich et al. 2008). In contrast, the periodic flaring from V773 Tau A is the first extra-solar evidence of interacting coronal flares, attributed in this case to collisions near periastron between extended helmet streamers from the binary components (Massi et al. 2008), a phenomenon closely analogous to the situation for DQ Tau. With a higher orbital eccentricity ($e = 0.556$, versus 0.3 for V773 Tau A), the DQ Tau system geometry predicts an overlap of its two protostellar magnetospheres at each periastron passage without the need for extended structure (Mathieu et al. 1997).

4.2 The DQ Tau System

Mathieu et al. (1997) found DQ Tau ($\alpha_{2000} = 04{:}46{:}53.06$, $\delta_{2000} = +17{:}00{:}00.1$) to be a non-eclipsing, double-lined spectroscopic binary, comprised of two relatively equal-mass stars ($\sim 0.65\,M_{\odot}$) with spectral types in the range of K7 to M1 and a robust orbital period of 15.8043 days. At closest approach, the binary separation is $8\,R_{\star}$ ($= 13\,R_{\odot}$), roughly four times smaller than the $30\,R_{\star}$ ($= 60\,R_{\odot}$) separation for V773 Tau A, and less than twice the expected T Tauri stellar magnetosphere size of $\sim 5\,R_{\star}$ (Shu et al. 1994; Hartmann et al. 1994). As a result of the binary geometry and magnetospheric models, reconnection events have been predicted for this source (Mathieu et al. 1997), but never tested observationally. We provide evidence that this effect is occurring and that it may be repeatable and relevant to many similar T Tauri systems.

The spectral energy distribution (SED) of DQ Tau is fairly typical of a CTTS. It is best fit by Mathieu et al. (1997) using a large circumbinary disk of about $0.002 - 0.02\,M_{\odot}$. They find that an additional

$5 \times 10^{-10}\,M_{\odot}$ of warm ($\sim$1000 K) circumstellar material close to the stars is necessary to explain the near-infrared excess, but not enough to maintain the observed accretion rate of $5 \times 10^{-8}\,M_{\odot}\,\mathrm{yr}^{-1}$ (see Hartigan et al. 1995). DQ Tau must be transporting material into its inner regions. Both a broad bright 10 μm silicate feature (see Furlan et al. 2006), and the absence of strongly blocked forbidden-line transitions in the receding stellar flow, support optically thin material in a region up to 0.4 AU around the binary (Basri et al. 1997; Najita et al. 2003).

At optical wavelengths, the system is known to brighten by 0.5 mag, coinciding with periastron, either shortly before or at closest approach. The mechanism regulating the optical activity is variable, as brightenings have been observed for only 65% of periastron encounters, and in isolated events, multiple brightenings were seen in a single orbit (Mathieu et al. 1997). All brightenings were recorded within an orbital phase window of 0.30 (or 5 days) centered on a phase (Φ) of 0.9, where periastron defines $\Phi = 0.0, 1.0$ (Mathieu et al. 1997). This evidence for accretion presents an additional puzzle, indeed for most binaries, since a large inner gap is expected to be cleared by the resonant and tidal forces generated by stellar movements, thereby quickly isolating a circumbinary disk from one or two circumstellar disks. The small binary separation of DQ Tau, however, reduces the likelihood of stable circumstellar disks. These effects combined should speed up disk dissipation and halt accretion processes. Instead, it is unclear how easily material can cross the predicted gap and why some binaries show inner cleared regions and others, like DQ Tau, do not (Jensen et al. 2007).

In this context, DQ Tau was the first system to be studied in terms of pulsed accretion flows (Mathieu et al. 1997). Extensive observations of the system's optical variability and photospheric line properties show increased veiling effects, spectral bluenings, emergence of outflow signatures in spectral lines, and the double-line structure in Ca II suggesting that bright blue-shifted material is being emitted near the surface of the star during an event (Basri et al. 1997). All these effects at periastron are consistent with pulsed accretion flows based on the theoretical models of Artymowicz & Lubow (1996) that describe how the eccentric binary orbit periodically perturbs the outer disk, causing material to collect at stable points near the inner rim and then to stream across the gap. However, the theory does not require the peak accretion rate to occur near periastron. Instead it has been postulated that the accretion mechanism is further regulated by strongly variable magnetic fields (Mathieu et al. 1997).

4.3 CARMA Observations

We observed DQ Tau at 115 GHz ($\approx$2.7 mm) with the Combined Array for Research in Millimeter-wave Astronomy (CARMA) during 5 tracks in April 2008, totaling 4 hours on-source. The millimeter array, located in eastern California (USA), provides 150 baselines of 30–350 meters in its C configuration and records one linear polarization. Our program cycled through 5 Taurus sources during each track, scanning each object for 12 minutes and obtaining 1–6 scans per source, depending on the track length. A 5-minute scan of the gain calibrator 3C 111 was included every 12–24 minutes. Multiple observing scripts allowed rotation of the source order in each track so that we could achieve more efficient u,v-coverage per source. In addition to the phase calibration using 3C 111, we observed the planet Uranus for flux calibration at the start of each track, as well as the radio source 3C 84 for passband calibration.

All data were processed using the MIRIAD data reduction software program, optimized for CARMA. We calibrated each track separately before combining the data into a final u,v-averaged continuum image. In the inversion step, a natural weighting for the u,v-coverage was applied and cleaning was performed down to a cutoff of 2σ. The continuum maps are a composite of two 500 MHz bands covering the frequency ranges 110.94–111.41 GHz and 114.80–115.27 GHz, corresponding to the lower and upper sidebands, respectively.

4.4 Results and Analysis

In the combined and calibrated DQ Tau image (∼3 hours on-source) we achieved a sky rms noise level of 1.45 mJy bm^{-1} and a beam size of $1.92'' \times 0.99''$ toward the Taurus star-forming region, corresponding to a spatial resolution of ∼140–270 AU at a distance of 140 pc. Since we found that the source was considerably brighter on 19 April than during any other observation date (see Figure 4.1), data for that track were not included in this final continuum image. And thus the quiescent values for the other nights combined then give a peak intensity of 13.3 mJy bm^{-1} and a flux, determined by a Gaussian fit, of 17 mJy.

Review of the unexpected result from 19 April revealed that the brightening was a real effect. Many instrumental and data processing errors could be ruled out because none of the 4 other sources exhibited a similar effect, the brightening persisted throughout 5 source cycles in an 8-hour period, and, the same observing script was used for 3 of the 5 tracks. The location of the peak emission at the time of the flare is consistent with the coordinates of the binary on all nights and therefore no background source is suspected. Finally, while the linear feeds do rotate while tracking the source, we expect a flare mimicked by the presence of strong polarization would not only be present in the nearly identical tracks of the adjacent days, but that the emission profile would be more symmetric about its peak.

To understand the nature of the DQ Tau brightening, we reduced each of the track's five 12-minute source scans separately to produce individual continuum maps. We then plotted the maximum source intensity (Jy bm^{-1} of the peak pixel) as a function of time (Figure 4.1). DQ Tau clearly exhibited a flaring behavior, rising to a maximum brightness in ∼1–2 hours, coinciding with the start of our track, and shortly thereafter, decaying (roughly exponentially) throughout the remainder of the observation, returning to half the observed peak intensity within a 2-hour period.

In Figure 4.1 we show the results of performing the same intensity analysis on the individual scans for three additional sources (our two brightest Taurus sources plus the gain calibrator). These sources appear constant in flux for all observations (distributed over 13 days). The same is not true for DQ Tau, which remains unresolved throughout its brightening event. At peak brightness, its flux during our third scan on 19 April (JD = 2 454 576.4534) was 468 mJy, roughly 27 times the quiescent value (Table 4.1), likely making DQ Tau the brightest object at 3 mm in Taurus at the time of our observation if we consider that the class-defining source T Tau is just 56 ± 10 mJy at 3 mm (Ohashi et al. 1996) and the bright, extended source HL Tau is 100 mJy (Beckwith et al. 1986). Finally, the flare is in stark contrast to (single-dish) measurements of DQ Tau that find 125 mJy at 1 mm and 91 mJy at 1.3 mm (Beckwith & Sargent 1991; Beckwith et al. 1990). Our quiescent value of 17 mJy, on the other hand, is a better fit to the expected millimeter spectral slope.

The true shape of the flare onset and its exact peak are less precise. Larger error bars for this date are a result of significant flagging due to strong de-correlation on longer baselines, particularly during

Table 4.1 — DQ Tau flux and intensity data at 2.7 mm (115 GHz)

JD (2 454 500+) [a]	Intensity (mJy bm^{-1})	Flux (mJy) [b]
76.3330	37.4 ± 15.0 [c]	–
76.3923	345.0 ± 19.8	419
76.4534	355.1 ± 11.4	468
76.5132	216.8 ± 9.2	284
76.5789	150.3 ± 6.1	194
Quiescent	13.3 ± 1.5	17

[a] Indicates the start of the 12-minute scan. [b] Flux determined by a Gaussian fit to the continuum image. [c] Data point suffers from severe de-correlation on longer baselines.

the first half of the track. The gain calibrator, which has an average flux of 3.7 Jy for each track, has a larger standard deviation (σ) for the maximum intensity of each 5-minute calibrator scan on the flare date (0.257 Jy bm^{-1}) than, for example, the longest tracks on 13 April (0.095 Jy bm^{-1}) and 21 April (0.103 Jy bm^{-1}). These effects do not compromise the validity of the flare detection. For comparison, the two brightest Taurus sources observed have a σ of 0.013 Jy bm^{-1} and 0.006 Jy bm^{-1} for their five 12-minute scans during the flare period.

Our flare occurs within the orbital phase window of the known optical brightenings, although it is unknown whether DQ Tau flared simultaneously in the optical. Using a JD$_0$ value of 2 449 582.54 $\pm$ 0.05 and a period of 15.8043 $\pm$ 0.0024 days, as published in Table 2 of Mathieu et al. (1997), we calculate the phase of the flare peak to be 0.98, or $\sim$7.6 hours before closest approach. If we consider the error in the orbital period, propagated over 11 years, the flare in fact could have peaked anywhere between 25.4 hours before periastron ($\Phi = 0.93$) to 11.0 hours after ($\Phi = 0.03$), still well within the window of optical variability. Our other observations began at orbital phases of -0.40, -0.09, 0.11, and 0.42 with respect to the same periastron encounter (corresponding to -6.32, -1.42, 1.74, and 6.64 days to closest approach), but only the track nearest periastron ($\Phi = -0.02$ on 19 April) exhibits a brightening event. Therefore, we strongly suspect that the millimeter flare is connected to the binary motions, as well as to the optical variability, suggesting that this event is likely to be repeatable and even periodic.

4.5 Discussion

Of the three previous examples of flaring activity, DQ Tau draws the strongest parallel to V773 Tau A both in system geometry and flare properties. The similarities include binarity with a fairly equal mass distribution, high orbital eccentricity, and now an observed 3 mm flare that is nearly identical in rise time ($\sim$2 hours), decay time ($\sim$5 hours, if we extrapolate in the case of DQ Tau), peak intensity ($\sim$400 mJy), incidence at periastron, and ratio ($\sim$25) of maximum intensity reached with respect to quiescent levels (see Massi et al. 2006, Figure 2). The most significant difference is the lack of ongoing accretion around V773 Tau A as determined by its Hα equivalent width.

In the other examples, the coronal flare observed toward GMR-A produced millimeter activity for 13 days following its intial outburst. And while it achieved a similar peak flux after distance correction (see Furuya et al. 2003, Figure 2), the outburst activity does not appear to be periodic (like in the case of V773 Tau A) since only a single radio flare was detected in the course of a 7-month monitoring campaign (Felli et al. 1993). As for ORBS, the radio flare shares a similar rise time and remains active several hours later when the track ended (see Forbrich et al. 2008, Figure 1). Unfortunately, little more is known about the deeply embedded YSO or its flare activity. Further comparison between these scenarios and DQ Tau is difficult, given that we are unable to constrain the emission polarization or its extent.

Instead, from the millimeter perspective, the activity occurs within the window when overlapping magnetospheres from the binary components are expected to interact and produce flares like that observed on 19 April. And, in the case of V773 Tau A, similar star-star magnetospheric interactions were responsible for a nearly identical 3 mm flare profile. However, pulsed accretion flows in the DQ Tau system also show a periodicity coinciding with periastron. And while magnetospheric interaction is likely to explain the millimeter flare, the magnetospheres do not possess the energy required to power the optical brightenings with the frequency and duration observed at optical wavelengths (Mathieu et al. 1997).

DQ Tau also possesses an additional component, absent in the V773 Tau A system, which must be considered: a circumbinary disk. Increased accretion at periastron inherently requires inclusion of a star-disk interaction. When stars accrete, material is thought to be swept from the (circumbinary) disk, along the magnetic field lines, and onto the protostars (Shu et al. 1994). These field lines can be stretched or compressed during accretion events, changes that can also produce flares. Furthermore, in accretion

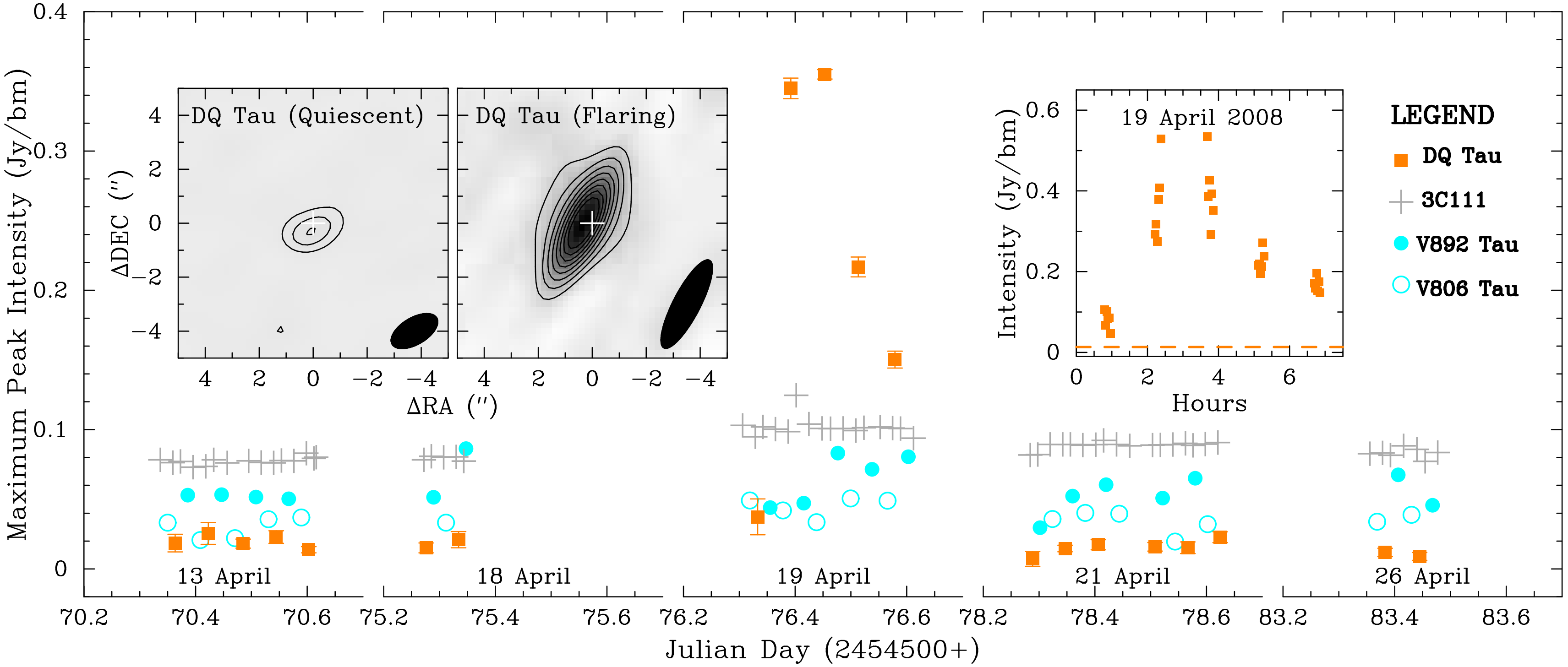

Figure 4.1 — A plot of the maximum intensity of each scan as a function of Julian Day. Filled squares represent DQ Tau, circles the 2 brightest Taurus sources in our tracks, and crosses are the calibrator (divided by a factor 50). Error bars for DQ Tau are the sky rms for each scan. *Upper Left Inset*: Continuum images of DQ Tau at 2.7 mm (115 GHz). White crosses indicate the 2MASS infrared position. Pixels are $0.2'' \times 0.2''$ and the same grayscale is used for both images (ranging -3.14×10^{-2} to 3.55×10^{-1} Jy bm^{-1}). On the left, the combined image from the 4 quiescent tracks. Contours are drawn at 3σ levels where $\sigma = 1.45 \times 10^{-3}$. At right, DQ Tau brightens by a factor of 27 on 2008 April 19 (JD = 2454576.4534), peaking at 355 mJy bm^{-1}. We determine a flux of 468 mJy for this scan. *Upper Right Inset*: The intensity (Jy bm^{-1}) of the peak pixel at the location of DQ Tau throughout the track on 19 April, now sub-divided into 2-minute intervals. The horizontal dashed line indicates the maximum intensity found for the quiescent image. The second and third scans show sharply increasing and decreasing intensity, respectively.

theory, the balance between gas pressure and magnetic pressure often delineates the inner disk boundary. But when a stable accretion disk is disrupted (due to the dynamical motions of a binary) and not available to compress the star-disk field lines, radio flaring may occur more easily, and over larger distances, as the field lines roam more freely (Basri et al. 1997). Increased outflow signatures during optical brightenings are consistent with increased field alignment if magnetic fields drive the outflows, and if pulsed accretion can organize the lines temporarily to power those outflows (Basri et al. 1997).

Because of this, the success with each orbit of a dynamically-driven pulsed accretion mechanism could inhibit the incidence of millimeter activity (through compression of the field lines), resulting in an anti-correlation between optical and millimeter flaring. Alternatively, if the reconnection events provide a necessary pathway for accretion processes, then the haphazard nature of magnetic fields easily could explain the variability in the optical flaring (Mathieu et al. 1997) and the occurrence of millimeter flares and optical brightenings is correlated. Finally, the optical brightenings and the millimeter flares may be independent, only sharing the common periodicity of the binary orbit.

Simultaneous monitoring of this system at both optical and millimeter wavelengths is important for investigating whether magnetospheric and dynamical interactions between the stars around periastron are strongly related. Ultimately, core fragmentation during star formation may favor multiple-star systems like DQ Tau. Binaries comprise 65% or more of the stellar population in the middle of the main-sequence (Duquennoy & Mayor 1991). And because planets have been detected around binaries (Eggenberger et al. 2004), there is an established need to study these systems and the impact of magnetospheric interactions and variable accretion processes on disk evolution.

4.6 Conclusions

The PMS spectroscopic binary, DQ Tau, has a highly eccentric orbit that should allow the stellar magnetospheres of the two components to interact at each periastron passage. We serendipitously observed evidence of this activity in a flare at 3 mm, the first detected around a CTTS. The maximum intensity recorded (355 mJy bm^{-1}) was 27 times the quiescent value (13.3 mJy bm^{-1}). The observed peak occurred roughly 7.6 ($\pm$ 18.2) hours before periastron at $\Phi = 0.98 \pm 0.05$, lasted several hours, and coincided with the average orbital phase ($\Phi = 0.9$) of the well-documented, periodic optical brightenings. Whether a simultaneous optical flare occurred is unknown.

The system's optical brightenings are consistent with the theory for pulsed accretion from the circumbinary disk onto the protostellar surfaces, regulated by the binary orbit, and perhaps assisted by magnetospheric interactions. The role of the magnetospheres during accretion events can now be studied observationally using methods established by Massi et al. (2006, 2008) in the analysis of V773 Tau A, the first example of coronae interactions between protostars where the authors were able to resolve the extent of the emitting region and the emission mechanism using very long baseline interferometry and polarization measurements. A similar observing program aimed at DQ Tau offers a unique opportunity to study star-disk interactions and reconnection events directly, and to test if magnetospheric interactions are necessary to facilitate periodic accretion.

Our findings also offer a small caution for millimeter flux points in SEDs that could contain unrecognized flare contributions if measured only once, with the time-consuming nature of observations at these wavelengths leading to a paucity of follow-up measurements.

Acknowledgements

We would like to thank Jin Koda and Joanna Brown for help with the data collection and reduction. We would also like to thank the referee for many valuable comments that have helped us to improve our manuscript. Support for CARMA construction was derived from the states of California, Illinois, and Maryland, the Gordon and Betty Moore Foundation, the Kenneth T. and Eileen L. Norris Foundation, the Associates of the California Institute of Technology, and the National Science Foundation. Ongoing CARMA development and operations are supported by the National Science Foundation under a cooperative agreement, and by the CARMA partner universities. The research of DMS and MRH is supported through a VIDI grant from the Netherlands Organization for Scientific Research (NWO).

Bibliography

Artymowicz, P. & Lubow, S. H. 1996, ApJ, 467, L77+
Basri, G., Johns-Krull, C. M., & Mathieu, R. D. 1997, AJ, 114, 781
Beckwith, S., Sargent, A. I., Scoville, N. Z., et al. 1986, ApJ, 309, 755
Beckwith, S. V. W. & Sargent, A. I. 1991, ApJ, 381, 250
Beckwith, S. V. W., Sargent, A. I., Chini, R. S., & Guesten, R. 1990, AJ, 99, 924
Bower, G. C., Plambeck, R. L., Bolatto, A., et al. 2003, ApJ, 598, 1140
Duquennoy, A. & Mayor, M. 1991, A&A, 248, 485
Eggenberger, A., Udry, S., & Mayor, M. 2004, A&A, 417, 353
Feigelson, E. D. & Montmerle, T. 1999, ARA&A, 37, 363
Felli, M., Taylor, G. B., Catarzi, M., Churchwell, E., & Kurtz, S. 1993, A&AS, 101, 127
Forbrich, J., Menten, K. M., & Reid, M. J. 2008, A&A, 477, 267
Furlan, E., Hartmann, L., Calvet, N., et al. 2006, ApJS, 165, 568
Furuya, R. S., Shinnaga, H., Nakanishi, K., Momose, M., & Saito, M. 2003, PASJ, 55, L83
Hartigan, P., Edwards, S., & Ghandour, L. 1995, ApJ, 452, 736
Hartmann, L., Hewett, R., & Calvet, N. 1994, ApJ, 426, 669
Jensen, E. L. N., Dhital, S., Stassun, K. G., et al. 2007, AJ, 134, 241
Kaufmann, P., Correia, E., Costa, J. E. R., & Zodi Vaz, A. M. 1986, A&A, 157, 11
Massi, M., Forbrich, J., Menten, K. M., et al. 2006, A&A, 453, 959
Massi, M., Menten, K., & Neidhöfer, J. 2002, A&A, 382, 152
Massi, M., Ros, E., Menten, K. M., et al. 2008, A&A, 480, 489
Mathieu, R. D., Stassun, K., Basri, G., et al. 1997, AJ, 113, 1841
Najita, J., Carr, J. S., & Mathieu, R. D. 2003, ApJ, 589, 931
Ohashi, N., Hayashi, M., Kawabe, R., & Ishiguro, M. 1996, ApJ, 466, 317
Shu, F., Najita, J., Ostriker, E., et al. 1994, ApJ, 429, 781

Chapter 5

Recurring Millimeter Flares as Evidence for Star-Star Magnetic Reconnection Events in the DQ Tau PMS Binary System

Observations of the T Tauri spectroscopic binary DQ Tau in April 2008 captured an unusual flare at 3 mm, which peaked at an observed maximum flux of $\sim$0.5 Jy (about 27 times the quiescent value). Here we present follow-up millimeter observations that demonstrate a periodicity to the phenomenon. While monitoring 3 new periastron encounters, we have detected flares within 17.5 hours (or 4.6%) of the orbital phase of the first reported flare and constrained the main emitting region to a stellar height of 3.7–6.8 $R_\star$. The recorded activity is consistent with the proposed picture for synchrotron emission initiated by a magnetic reconnection event when the two stellar magnetospheres of the highly eccentric ($e = 0.556$) binary are believed to collide near periastron as the stars approach a minimum separation of 8 $R_\star$ ($\sim$13 $R_\odot$). The similar light curve decay profiles allow us to estimate an average flare duration of 30 hours. Assuming one millimeter flare per orbit, DQ Tau could spend approximately 8% of its 15.8-day orbital period in an elevated flux state. These findings continue to serve as a small caution for millimeter flux points in spectral energy distributions that could contain unrecognized flare contributions. Our analysis of the millimeter emission provides an upper limit of 5% on the linear polarization. We discuss the extent to which a severely entangled magnetic field structure and Faraday rotation effects are likely to reduce the observed polarization fraction. We also predict that, for the current picture, the stellar magnetospheres must be misaligned at a significant angle or, alternatively, that the topologies of the outer magnetospheres are poorly described by a well-ordered dipole inside a radius of 7 $R_\star$. Finally, to investigate whether re-organization of the magnetic field during the interaction affects mass accretion, we also present simultaneous optical (VRI) monitoring of the binary, as an established tracer of accretion activity in this system. We find that an accretion event can occur coincident in both time and duration with the synchrotron fallout of a magnetic reconnection event. While the pulsed accretion mechanism has been attributed previously to the dynamical motions of the stars alone, the similarities between the millimeter and optical light curves evoke the possibility of a causal or co-dependent relationship between the magnetospheric and dynamical processes.

D. M. Salter, Á. Kóspál, K. V. Getman, M. R. Hogerheijde, T. A. van Kempen, J. M. Carpenter, G. A. Blake, and D. Wilner

Astronomy & Astrophysics, **521**, 32–49 (2010)

5.1 Introduction

Pre-main-sequence (PMS) stars are characterized by variability in most wavebands. At millimeter wavelengths, however, the dominant emission process is the optically thin, thermal radiation from the dust located in a circumstellar disk. The integrated flux is therefore a measure of the total amount of cold circumstellar material, which evolves on timescales of roughly 10^6 years. Before the discovery of the first strong millimeter flare toward the young stellar object (YSO) GMR-A in Orion (Bower et al. 2003; Furuya et al. 2003), pronounced short-term millimeter variability was undocumented even though radio variability is well known toward YSOs (e.g. Stine et al. 1988; White et al. 1992). The lack of millimeter variability studies in the literature is in large part due to the time-consuming nature of observations at these wavelengths, leading to few follow-up measurements. As a result, DQ Tau is only the fourth YSO to be recognized in outburst at millimeter wavelengths. The initial serendipitous detection occurred during an 8-hour observation on 2008 April 19, when the source brightened at 3 mm (115 GHz) in a matter of hours to reach a maximum detected flux of 468 mJy, in comparison to a quiescent value of 17 mJy in the adjacent days (Salter et al. 2008, Chapter 4). The flare mechanism was attributed to synchrotron emission from a powerful magnetic reconnection event, probably due to the colliding magnetospheres of the binary components near periastron; and similar in nature to the interacting coronae evidenced toward another millimeter-flaring PMS star V773 Tau A (Massi et al. 2002, 2006, 2008).

DQ Tau ($\alpha_{2000} = 04{:}46{:}53.06$, $\delta_{2000} = +17{:}00{:}00.1$) is a double-lined spectroscopic binary that consists of two relatively equal-mass stars ($\sim 0.65\,M_\odot$) of similar spectral type (in the range of K7 to M1); as summarized in Table 5.1. Its highly eccentric ($e = 0.556$) orbit means that the two stars approach to within $8\,R_\star$ ($\sim 13\,R_\odot$) at periastron (Mathieu et al. 1997). This makes the system unique in terms of magnetic reconnection events because the minimal separation of the binary is on the order of the theoretical T Tauri stellar magnetospheric radius of $\sim 5\,R_\star$ (Shu et al. 1994; Hartmann et al. 1994). This radius is generally defined as the range within which the stellar magnetic field lines remain closed, meaning that the field lines both begin and end at the stellar surface. As a result, the geometry of the system alone predicts an overlap of the two magnetospheres at each periastron event; and as the stars approach one another it may become energetically more stable for the fields to briefly merge together. Field lines rooted on one star break and instantly reconnect with the field lines rooted on the companion, releasing magnetic energy into the surrounding region in the process (Vasyliunas 1975; Hesse & Schindler 1988).

Magnetic reconnection events like these are still a poorly understood phenomenon. They occur most notably within the solar corona when oppositely-directed field lines are forced together, typically above magnetically active regions where closed magnetic loops, anchored in sunspots, interact with one another (Haisch et al. 1991). The associated millimeter emission is explained as the superposition of a gyro-synchrotron spectrum with synchrotron emission (Kaufmann et al. 1986), powered by the re-organization of the field lines as they relax into a lower energy state. This solar analogy helps form the basic principles for our stellar scenarios, which can also include magnetic interactions between a star and its accretion disk or a star and a planet forming within its circumstellar disk (Phillips et al. 1991). A consistent flare timing near periastron, however, is a strong indicator that both stellar magnetospheres—as the strongest and most stable magnetic structures in the binary system—are contributors to the transient millimeter activity seen toward DQ Tau.

Here we report on 3 additional flares captured toward this system and discuss what these events mean for the current interpretation of a periodic, star-star magnetic reconnection phenomenon. Our aim is to constrain the nature and regularity of the millimeter emission mechanism by addressing variations in the timing of the flare during the orbit, the duration of the flares, their peak strengths, and the degree of polarization present. For the most recent millimeter flare, X-ray observations were performed in parallel and these will be discussed separately in Getman et al. (2010, submitted). In addition, periastron events in this system are characterized by variable accretion bursts, most likely driven by the dynamical motions

Table 5.1 — DQ Tau Binary System Parameters

System Parameter	Value	Source
Stellar Radius [$R_\odot$]	1.6	1
Stellar Mass [$M_\odot$]	0.65	1
Rotation Period [days]	$\sim$3	2
Orbital Period [days]	15.8043	1
Orbital Eccentricity	0.556	1
Inclination [°]	157	3
Periastron Separation [$R_\odot$]	13	1
Apoastron Separation [$R_\odot$]	56	1

Sources: 1. Mathieu et al. (1997); 2. Basri et al. (1997); 3. Boden et al. (2009).

of the binary components (Artymowicz & Lubow 1996). Therefore, a secondary goal of this work is to explore the relative timing of the two interactions, dynamical and magnetospheric, acknowledging that the two mechanisms may exist independently and only share the common periodicity of the binary orbit. To probe the accretion mechanism we present and analyze simultaneous optical photometry measurements, which have been shown to be excellent tracers of the accretion activity in this system (see Basri et al. 1997; Mathieu et al. 1997).

5.2 Observations and Data Reduction

5.2.1 Millimeter Interferometry

In the follow-up millimeter observations presented here, we chose to observe at slightly lower frequencies in the 3 mm band (90–95 GHz) than those specified during the initial discovery (115 GHz). This strategy takes advantage of greater instrument sensitivities toward lower frequencies and the higher ratio of non-thermal to thermal emission expected toward longer wavelengths. We also supplement the 3 mm band data with a simultaneous observation in the 1 mm band (238 GHz), in order to probe the spectral slope of the transient emission. The technical details for each millimeter data set—all scheduled for observation in the 24-hour period before a periastron event—are summarized in the text below and in Table 5.2. While each millimeter facility may respond differently to a high degree of polarization as its linear feeds rotate while tracking the source, we show in Section 5.4.2 that the polarization fraction is minimal and therefore does not affect the measurements presented here.

IRAM PdBI.[1] Located in the French Alps, the IRAM Plateau de Bure Interferometer (PdBI) is a 6-element millimeter array capable of measuring two linear polarization directions. We observed DQ Tau at 90 GHz ($\approx$ 3.3 mm) on 3 separate UT dates: 2008 December 28–29, 2009 March 17, and 2010 January 11–12. Each observation (or track) was approximately 8 hours in length and, aside from the array configuration on each UT date, the observations had identical receiver setups of 2×1 GHz (V + H dual-polarization) in full-bandwidth mode (4×320 MHz overlapping quarters). The same standard calibration method was applied to all three tracks: we used the radio source 3C 84 for both the passband and flux calibration, and we observed the gain calibrators 0507+179 (a polarized source) and 0446+112 for 2.25 minutes (45 seconds × 3 scans) each between every 22.5-minute (45 seconds × 30 scans) on-source observation. All data sets were processed using the GILDAS CLIC and MAPPING reduction software, developed by the Grenoble Astrophysics Group. To extract the flux density, we assumed a model for a point source and we averaged the weighted visibilities for all baselines in 90-second time steps. The

---

[1] IRAM is supported by INSU/CNRS (France), MPG (Germany) and IGN (Spain).

error bars displayed per flux point represent the 1σ deviation from the average value. Finally, maps for each track were produced using a natural weighting in the inversion step, and Hogbom cleaning was performed down to the rms level of the dirty maps.

CARMA.[2] We observed DQ Tau with the Combined Array for Research in Millimeter-wave Astronomy (CARMA) on UT 2010 January 12 in the 3 mm band. This observation overlapped for 1.5 hours with the end of the third IRAM track, providing continuous coverage on this date for an 18-hour period during a simultaneous *Chandra* X-ray observing campaign (see Getman et al. 2010, submitted). Located in eastern California (USA), CARMA is a heterogeneous interferometer comprised of 23 antennas: six 10.4-meter telescopes from the California Institute of Technology/Owens Valley Radio Observatory (OVRO), nine 6.1-meter telescopes from the Berkeley-Illinois-Maryland Association (BIMA), and eight 3.5-meter telescopes from the University of Chicago's Sunyaev-Zel'dovich Array (SZA). Our program was executed while the antennas were being moved out of the CARMA B configuration, and only 10 of the 6-meter and 10-meter antennas were available to provide baselines between 117 and 946 meters. We used the CARMA Paired Antenna Calibration Systems (C-PACS) to compensate for the rapid phase fluctuations on the long baselines. In the C-PACS observing mode, the CARMA 6-meter and 10-meter antennas observe the phase calibrator and science target as for normal interferometric observations. Simultaneously, the CARMA 3.5-meter antennas observe a bright source at a frequency of 30 GHz to monitor the atmospheric fluctuations. The observed phase fluctuations at 30 GHz were then used to calibrate the observed phases toward DQ Tau, and thereby reduce the flux loss due to atmospheric de-correlation on the longer baselines. A detailed description of C-PACS and the data reduction procedures are presented in Pérez et al. (2010). For our observations, the observing cycle consisted of 3-minute observations of the gain calibrator 0530+135 by both sets of antennas. Then, while the 6-meter and 10-meter antennas observed DQ Tau for 15 minutes, the 3.5-meter antennas observed the calibrator 0440+146. We used 3C 273 for the passband flattening and Uranus for flux calibration. The correlator for the 6-meter and 10-meter antennas was configured with three 500 MHz bands (or 1.5 GHz) per sideband that covered the frequencies 89.2–90.7 GHz in the lower sideband and 94.2–95.7 GHz in the upper sideband. The data were processed using the MIRIAD data reduction software program, optimized for CARMA. In MIRIAD we used *uvfit* for a point source to determine the flux value and error for time intervals of 5 minutes. For mapping we again used a natural weighting for the u,v-coverage in the inversion step and cleaning was performed down to 1.5σ (where σ is the theoretical sensitivity) using the *mossdi2* package.

SMA.[3] The Submillimeter Array (SMA) is an 8-element array located on the summit of Mauna Kea in Hawaii. We observed DQ Tau at the higher frequency of 238.5 GHz (≈ 1.3 mm), also on 2010 January 12, to achieve an 8-hour overlap with the CARMA track. The array was in its 'Extended' configuration, providing 27 baselines spanning 34 to 225 meters. The 4 GHz bandwidth was uniformly sampled with 128 channels per chunk and a total of 48 chunks. At the start of the night, the opacity was measured independently and the precipitable water vapor (PWV) was estimated to be around 1 mm, rising to 1.3 mm at the end of the track. Scans were shortened to 15 seconds while in the extended configuration, and the source was observed for 7.5-minute integration loops. The gain calibrators 0423−018, 0530+135, and 0510+180 were observed for 3 minutes after every on-source loop. The flux scale was checked every 3 hours with an observation of Uranus or Mars, and the calibrator 3C 273 was used to correct for the passband. The data were reduced using the MIR package for IDL, provided by the Smithsonian Astro-

---

[2] Support for CARMA construction was derived from the states of California, Illinois, and Maryland, the James S. McDonnell Foundation, the Gordon and Betty Moore Foundation, the Kenneth T. and Eileen L. Norris Foundation, the University of Chicago, the Associates of the California Institute of Technology, and the National Science Foundation. Ongoing CARMA development and operations are supported by the National Science Foundation under a cooperative agreement, and by the CARMA partner universities.

[3] The Submillimeter Array is a joint project between the Smithsonian Astrophysical Observatory and the Academia Sinica Institute of Astronomy and Astrophysics and is funded by the Smithsonian Institution and the Academia Sinica.

physical Observatory, and subsequently analyzed using the *uvfit* package of the MIRIAD data reduction software program.

5.2.2 Optical Photometry

Optical monitoring of DQ Tau during the first IRAM track on 2008 December 28 was performed simultaneously from the Wellesley College 0.6-meter telescope in Wellesley, MA (USA) and the IAC80 0.8-meter telescope of Teide Observatory, located in the Canary Islands (Spain). Optical coverage in 2 locations allowed us to monitor DQ Tau throughout the 8-hour millimeter track, and for several hours thereafter. We also obtained simultaneous optical (Teide) and millimeter (IRAM) observations for the final follow-up observation on 2010 January 11. To complete the optical characterization of DQ Tau, additional monitoring was carried out from Wellesley and from Teide Observatory in the one-month period from December 2008 to January 2009 (covering the weeks before and after the first millimeter follow-up observation). For part of the observations at Wellesley, DMS was a visiting astronomer, while the observations at Teide Observatory were executed in service mode as part of the IAC80 EXTRA observing program for small projects. A complete listing of the optical measurements is provided in Table A.2.

The detector used during the Teide observations was CAMELOT, a 2048 × 2048 back-illuminated CCD chip with a $0.304''$ pixel scale, corresponding to a $10.4' \times 10.4'$ field of view. The detector on the Wellesley telescope was a 1024 × 1024 CCD chip with a field of view of $15.6' \times 15.6'$ and a pixel scale of $1.829''$ (after binning by 4). We used the standard Johnson V, R, and I filters at both telescopes. All data were reduced using the IRAF data reduction software in the standard way with flats, biases, and for the Wellesley data set, darks. Images with each filter were obtained in blocks of 3 frames. The frames in one block were shifted and co-added. Aperture photometry was performed in IDL using the *cntrd* and *aper* procedures on the co-added images. We used an aperture with an 8-pixel radius for the Wellesley data and a 15-pixel radius for the Teide data.

In order to convert instrumental magnitudes to the standard system, we observed the equatorial standard stars HD 65079 and GD 50 at different airmasses on 2008 December 25 and 28 at Wellesley. Atmospheric extinction coefficients and zero-magnitude offsets were calculated by comparing our instrumental magnitudes above the atmosphere to the standard values in the literature (Menzies et al. 1991; Landolt 1992). These corrections were then applied for six comparison stars in the vicinity of DQ Tau, observed on the same two nights. The comparison stars are identified in a sample optical image in Figure A.1, and their final absolute magnitudes are provided in Table A.1. We estimate a photometric uncertainty of about 0.5 magnitudes. Two of our comparison stars (#4 and #5) were included in the Droege et al. (2007) study, and they have a very low Welch-Stetson variability index, confirming that they are sufficiently constant to be used as comparison stars. The absolute magnitudes that we derived for these two comparison stars agree to within 0.2 magnitudes with the catalog values (Droege et al. 2007). Since all six comparison stars are bluer than DQ Tau, we did not attempt to determine a color term, but simply averaged the differential magnitudes obtained with the six comparison stars. Using this method, we estimate that the precision of the repeatability is 0.05 magnitudes, meaning that we take changes in the light curve larger than the precision value to be real.

5.3 Results and Analysis

5.3.1 Millimeter Flare Properties

For all millimeter tracks, DQ Tau remains unresolved at all times. Given a distance of 140 pc to the Taurus star-forming region (Kenyon et al. 1994), and a maximum instrument resolution of $0.7''$ (Table 5.3), we can already constrain the millimeter emission to a region within 100 AU of the binary. The corresponding

Table 5.2 — Millimeter Observing Log

UT Date [track start]	Observatory	Array Config.	Antennas	Baselines [kλ]	ν_c [GHz]	Bandwidth [GHz]	H.A. Range [hrs]	Optical Coverage	X-ray Coverage
2008 Dec 28	IRAM	B	1, 2, 4, 5, 6	26–136	90.0	1.0	-2.9 to 5.3	Yes	No
2009 Mar 17	IRAM	C	All	7–53	90.0	1.0	-4.1 to 4.1	No	No
2010 Jan 11	IRAM	A	All (Ant. 4 fails at 22:30h)	48–228	90.0	1.0	-2.6 to 5.9	Yes	Yes
2010 Jan 12	CARMA	B	1, 2, 3, 4, 5, 8, 9, 10, 13, 14	36–292	92.5	3.0	-3.2 to 5.2	No	Yes
2010 Jan 12	SMA	Ext.	All	27–179	238.5	4.0	-3.7 to 4.8	No	Yes

Table 5.3 — Millimeter Track and Light Curve Statistics

UT Date	Track ID	Beam Size [$''$]	ν_c [GHz]	F_{start} [mJy]	F_{end} [mJy]	σ_{avg} [mJy]	Linear Polariz.	Orbital Phase Coverage [Φ]	Hours from Periastron (0.0)	$t=0$ [Φ]
2008 Dec 28	Dec08-IRAM	1.34×1.02	90.0	43.0	20.2	1.2	$< 4.65\%$	-0.02 to 0.00	-6.8 to 1.5	-0.056
2009 Mar 17	Mar09-IRAM	3.39×2.79	90.0	12.6	16.9	1.1	$< 8.15\%$	-0.03 to -0.01	-13.7 to -5.3	-0.007
2010 Jan 11	Jan10-IRAM	1.32×0.70	90.0	62.4	29.2	1.1	$< 7.60\%$	-0.04 to -0.02	-14.4 to -6.5	-0.067
2010 Jan 12	Jan10-CARMA	0.87×0.67	92.5	30.3	12.4	3.9	-	-0.02 to 0.00	-7.2 to 1.1	-0.067
2010 Jan 12	Jan10-SMA	1.25×1.00	238.5	95.6	85.2	5.6	-	-0.01 to 0.01	-4.7 to 3.6	-0.067
2008 Apr 19	Apr08-CARMA	3.66×1.00	113.1	468	194	-	-	-0.02 to -0.01	-8.7 to -2.7	-0.020

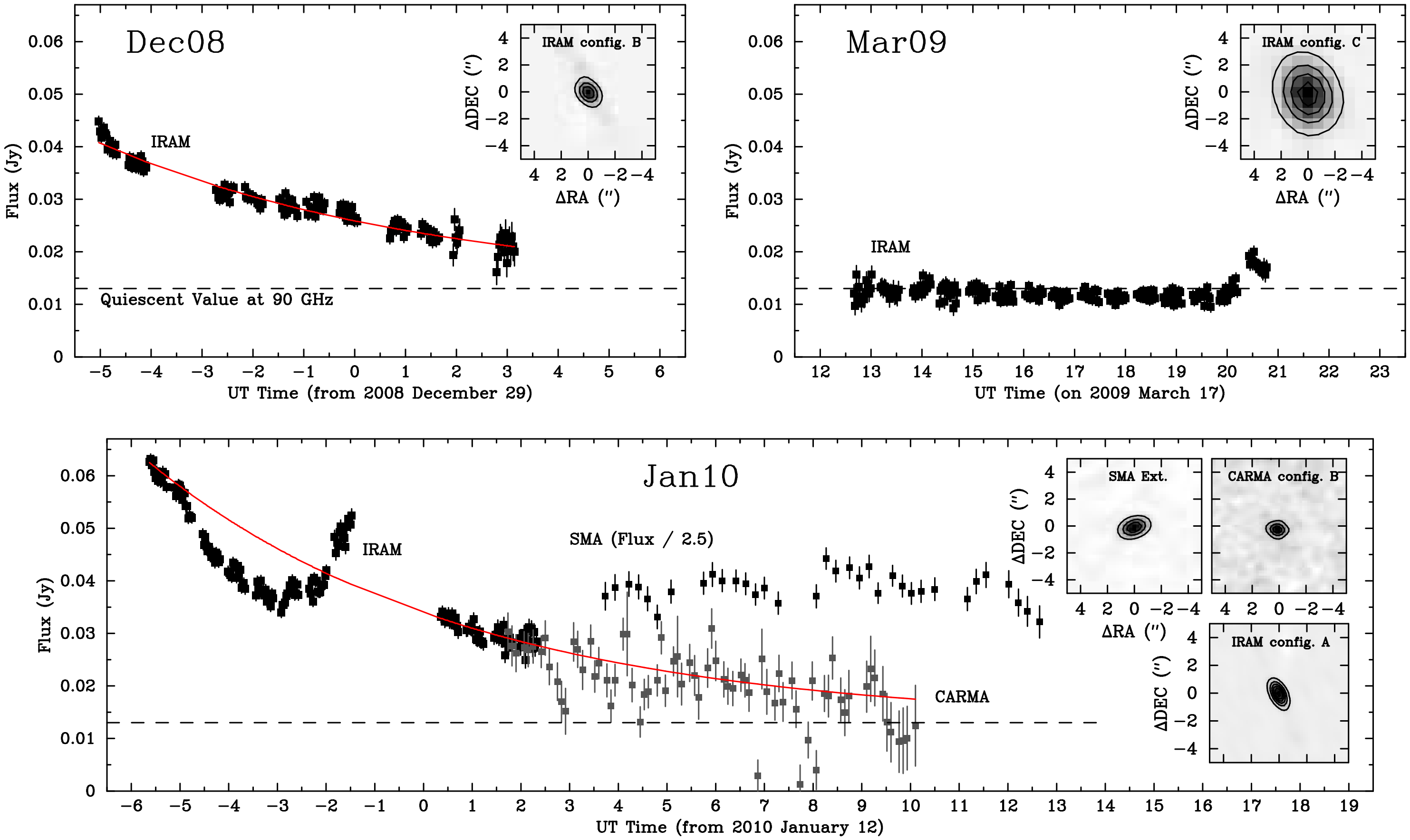

Figure 5.1 — The millimeter fluxes versus time for DQ Tau, as observed with the IRAM PdBI, CARMA, and SMA on 2008 December 28–29 (upper left), 2009 March 17 (upper right), and 2010 January 11–12 (lower panel). All fluxes have been determined from a fit to the visibilities using a point source model. Each IRAM data point represents an on-source time interval of 1.5 minutes. The CARMA and SMA (divided by 2.5) values are for 5-minute intervals. The light curves reveal a (track-averaged) quiescent flux level of 13 mJy at 90 GHz during the March IRAM observation and 97 mJy at 238.5 GHz for the January SMA observation. During the December and January observations, we caught the flare decay phase and fitted an (identical) exponential decay with an e-folding time of 6.55 hours (solid red line) to both light curves. We note that the fit does not apply to the initial decay of the original April 2008 light curve (see Section 5.3.1). The March observation only indicates elevated activity near the end of the track, which we take to be the start of a flare. In the upper right-hand corner of each panel, we give the (unresolved) continuum images for the entire track where the continuum contours are drawn for 3σ levels and each σ is of the order 1 mJy bm^{-1}.

light curves and track statistics retrieved from the data reduction are plotted in Figure 5.1 and summarized in Table 5.3.

In the follow-up observing campaigns, we report confirmed elevated millimeter activity showing a clear decline in brightness with time on 2008 December 28 and 2010 January 11 (hereafter abbreviated as the 'Dec08' and 'Jan10' periastron events). The activity supports a periodic behavior linked to the binary orbit. However, the variable nature of the magnetospheres, and in particular their tendency to fluctuate in size, means that the exact timing of a flare is understandably difficult to predict. On 2009 March 17 (hereafter the 'Mar09' event) the light curve is quiescent until the last hour of the track when it increases in brightness to 1.5 times its quiescent value. At this point the source was nearing an elevation of just 15°, but since the gain calibrator remains at a reliable elevation, we might only expect a *loss* in source flux at such a low elevation. Therefore, we conclude that the brightening is a real effect and very likely the start of a flare, occurring a mere 6 hours later than we had predicted. It is certainly unlikely in a (magnetospheric) collision scenario that a significant flare could have occurred much earlier in the orbit when the stars are at a much greater separation. In this regard, the incompletely-observed onset could raise questions as to whether the millimeter flares share more in common with the optical brightenings, which have been shown to occur for most but not all periastron encounters (Mathieu et al. 1997).

To calculate the timing of each periastron event, we used the orbital parameters determined by Mathieu et al. (1997), specifically $\mathrm{JD}_0 = 2\,449\,582.54 \pm 0.05$ and $P = 15.8043 \pm 0.0024$ days. We note that a revised period has since been published by Huerta et al. (2005), where their more recent data suggests a shortening of P to $15.8016 \pm^{0.002}_{0.006}$. This new period is within the initial error bars of the original, confirming the overall robustness of the orbital period, but the newer value is itself less precise. In Figure 5.2 we illustrate how the assumed period affects the perceived timing of the flares within the orbit. Along one orbital path, we highlight the section that would correspond to our millimeter observations for each proposed period. The original period indicates that our observed events occur as the stars approach one another, whereas the revised period consistently places the observed activity at or after periastron. Due to the irregular nature of the magnetic fields, our data cannot differentiate between the correctness of one

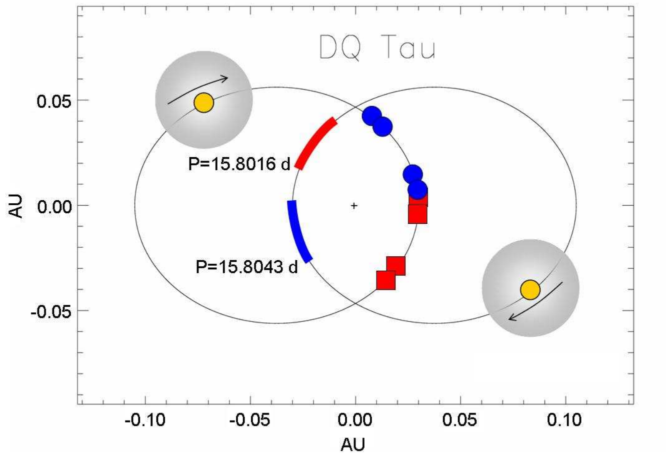

Figure 5.2 — The effect of the assumed orbital period on the estimated timing of the flares. A cross indicates the barycenter of the binary system while ellipses trace out the retrograde motions of the binary components. Along one ellipse, we highlight the orbital segment covered by the observations, as determined for each period. On the other ellipse, we indicate the point in the orbit when the trigger event is presumed to have occurred for each periastron monitored. We use blue circles for the Mathieu et al. (1997) value of 15.8043 days and red squares for the 15.8016-day period from Huerta et al. (2005). Set at a greater distance from periastron, we indicate DQ Tau A and DQ Tau B drawn to scale ($R_\star = 1.6\,R_\odot$) with an accompanying magnetosphere of $R = 5\,R_\star$.

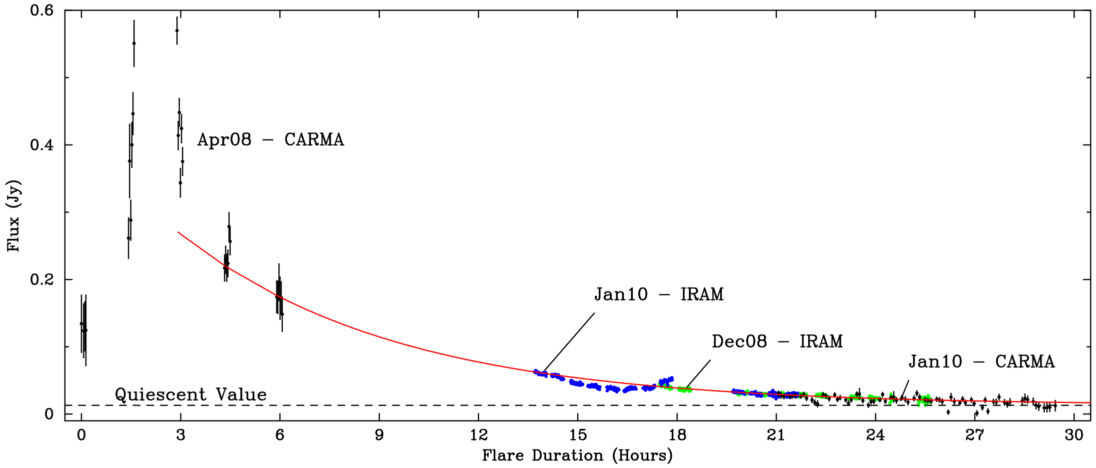

Figure 5.3 — The 3 mm band light curves are shifted along a common exponential decay curve with an e-folding time of 6.55 hours. For a zoomed-in version of how well the model fits the decays from Dec08 and Jan10, please refer back to Figure 5.1. Based on this fit, we loosely establish the upper limit on an average flare duration to be 30 hours.

period over the other. And, in fact, flares both before and after periastron are possible, as we discuss in Section 5.4.3. Instead, we suspect that the most energetic events in this system are more likely to occur during the initial interaction, upon approach. Therefore, the orbital phases reported in Table 5.3—and throughout this paper—are calculated using the original period of $P = 15.8043$ days.

In none of the follow-up observations do we succeed in capturing a single flare in its entirety. The longest continuous coverage is for 18 hours in January 2010 when IRAM, CARMA, and SMA observed DQ Tau in succession. The source remains in an elevated flux state at 90–95 GHz for the duration of this joint observation, but appears quiescent (within the noise levels) at 238 GHz. The Jan10-SMA track-averaged flux at 238 GHz is 97 mJy versus 13 mJy at 90 GHz during the quiescent portion of the Mar09-IRAM track. Together, these flux values define a millimeter spectral index α of $\sim$2, which is consistent with thermal emission from an optically thick disk. During the Jan10 flare, however, the starting flux measurements at SMA (97 mJy) and CARMA (30 mJy) document an α of 1.2, providing strong evidence for the presence of non-thermal emission (see Section 5.4.1).

Since DQ Tau is only above the horizon for 8–10 hours at any given site, each observation date covers an even smaller window of the recurring activity. However, the separate flare events from Dec08 and Jan10 exhibit very similar flux levels and large-scale decay profiles. When we independently fit an exponential curve to the decaying flux intensities from both dates (shown atop the data in Figure 5.1), we found identical e-folding times of 6.55 hours. (We will return to their sub-structure shortly.) If the same e-folding time holds for more (or even all) flares, then each individual observation could loosely correspond to a different portion of the same decay curve. Thus by shifting the separate flare profiles with respect to one another, as is shown in Figure 5.3, we can attempt to re-construct an “average” flare profile. We can even place constraints on the duration of an outburst if we know the peak flux for each flare. With only one peak flux for reference, we extrapolate the exponential fit back through the last flux value from the original Apr08 event. In this way, we estimate a flare duration of approximately 30 hours.

This calculation for the flare duration should be regarded with some caution, and taken as an upper limit only in most cases. First, the initial decay slope following the strongest outburst in Apr08 is much steeper than the long steady decays observed in Dec08 and Jan10. As a result, a disjointed superposition of two decay profiles, rooted in two separate energy dissipating processes, may prove a better model and ultimately shorten the flare length. (In Section 5.4.1 we discuss these loss mechanisms further.) Secondly, the assumption of a similar peak flare intensity from one periastron to the next is one property where we lack sufficient millimeter data. To reinforce this idea, simultaneous X-ray observations during the Jan10 event indicate only a relatively weak X-ray flare; one that is hardly powerful enough to expect a radio counterpart with a peak flux as explosive as the original Apr08 event (Getman et al. 2010, submitted). Finally, it is improbable that the peak fluxes are identical given the complicated nature of the magnetic fields, the dependence on the ionized particle reservoir, the magnetic energy released during an event, as well as the diversity that we can already document in the decay profiles. However, this method provides some necessary constraints to characterize the millimeter activity. In turn, for a 15.8043-day period assuming one 30-hour flare per orbit, we suspect that DQ Tau could spend up to 8% of its time exhibiting excess flux that is unrelated to the thermal continuum emission from its circumbinary disk.

If we take this analysis one step further, we can use the relative offsets from Figure 5.3 (e.g. $\sim$13.5 hours for Jan10 and $\sim$17.5 hours for Dec08) to estimate the orbital phase Φ for the initial outburst event (or $t = 0$). These are the orbital points indicated along the second ellipse in Figure 5.2, and in numerical form in Table 5.3 (Column 10) where $\Phi = 0.0, 1.0$ defines periastron. If we now continue to assume that the Mar09 track signals the start of a large flare, then the Jan10 and Mar09 flares exhibit the largest separation in orbital phase, suggesting an outburst event window of $\sim$22 hours (or $\sim$6% of the orbital phase). Physically, this window encompasses a stellar separation of 8–13 $R_\star$ and is equivalent to roughly one-third the time needed for the stars to swap positions about the system center ($\sim$2.8 days; Basri et al. 1997). In Figure 5.4 we plot the millimeter flux versus the orbital phase for all tracks, to show how the elevated activity shifts back and forth in the orbit, yet consistently occurs in the day before periastron ($-0.06 < \Phi < 0.0$). Together, the estimated flare duration plus the variable orbital timing for the outburst event, define a window of breadth 52 hours (or $\sim$2.2 days) when the millimeter flux may exceed the thermal quiescent value.

While the similarity in the large-scale decay times for both Dec08 and Jan10 is quite striking, the curves show sub-structure that is rather diverse. During the Apr08 and Dec08 events, we captured a smooth exponential decay, exhibiting only very small variations in the measured flux values. The Jan10 light curve, however, features a sharp break in the general decay profile one hour into the observation,

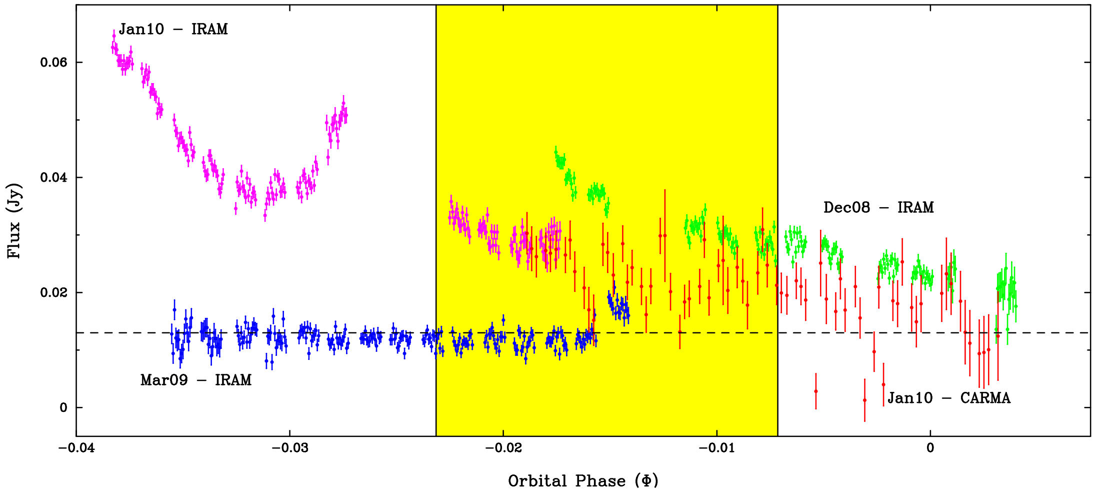

Figure 5.4 — A plot of the 3 mm band fluxes versus orbital phase, illustrating how the activity shifts around slightly in the orbit. An orbital phase Φ of 0 defines periastron. The shaded region indicates the phase coverage for the initial Apr08 flare and is equivalent to 8 hours. During the Dec08 and Jan10 follow-up observations, the flare occurred earlier in the orbit, while the Mar09 follow-up observation may have occurred later, but not earlier (at least not within the previous day).

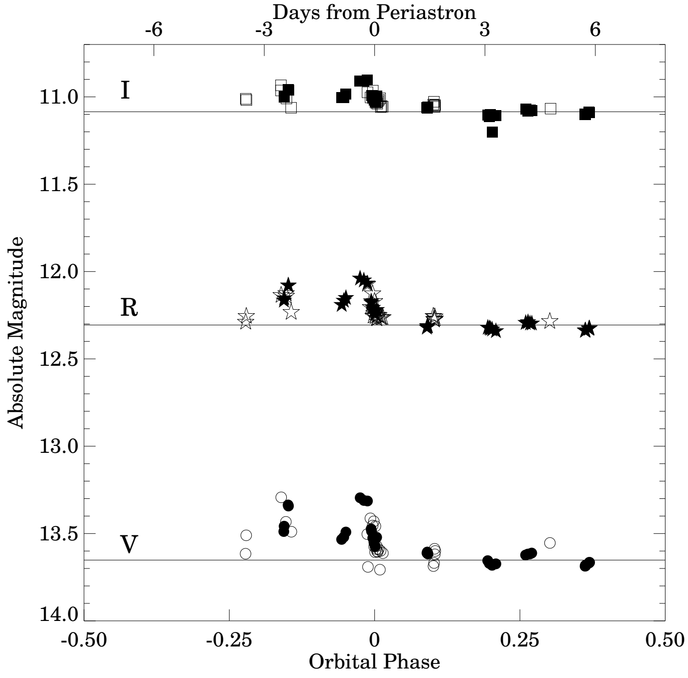

Figure 5.5 — The VRI photometry values wrapped with the 15.8043-day orbital period for DQ Tau, where $\Phi = \pm 0.5$ indicates apoastron and $\Phi = 0$ is periastron. The optical brightenings occur within a 5-day window near periastron, as was first shown by Mathieu et al. (1997). Filled symbols represent data taken with the Teide IAC-80 telescope and unfilled data points are from the Wellesley telescope. Horizontal lines indicate the quiescent absolute magnitude per filter.

initially dropping more rapidly before giving rise to a milder secondary peak, and then finally resuming the original decay profile. (We note that the 2-hour gap in the data during this time was the result of an antenna error, and that the observations quickly resumed without the faulty antenna.) We interpret the sub-structure from Jan10 to be due to a secondary event, occurring about 15 hours after the estimate for the initial outburst, and involving a smaller energy release than the preceding flare. In fact, this occurrence of successive events suggests that a series of (probably less powerful) flares can take place, possibly in lieu of one giant outburst.

Additional small-scale variations in the total flux density are likely due to atmospheric and instrumental effects. Larger systematic changes can help us test for strong linear polarization using the new, dual linear polarization receivers available at IRAM PdBI in combination with Earth rotation polarimetry, as described in Trippe et al. (2010). There the authors show how the difference in flux between the two orthogonal polarization feeds, divided by their sum, changes in a systematic way when a linearly polarized source transits. Unfortunately, this technique and the instrumentation available does not allow us to constrain the presence or amount of circularly polarized light. Using this method in the absence of detecting all 4 Stokes parameters, we determine 3σ upper limits of 4.65% and 7.60% for the linear polarization during the flare decay phases from Dec08 and Jan10, respectively. During the quiescent Mar09 track, our upper limit is 8.15%. In Section 5.4.2, we discuss the implications of the linear polarization fractions for the proposed picture and the emission mechanism.

5.3.2 Coincident Optical Brightenings

DQ Tau is perhaps best known as the first system to be studied in terms of pulsed accretion flows to explain its optical variability near periastron. The binary has therefore been characterized extensively

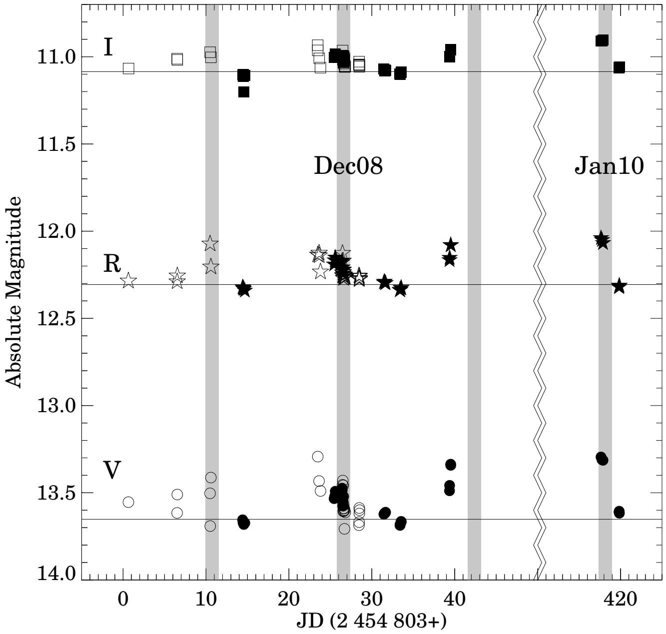

Figure 5.6 — A plot of the VRI photometry values for the Julian dates from December 2008 through January 2009, as well as January 2010. The shaded columns indicate periastron events. The source brightens irregularly prior to all four newly documented periastron encounters.

at optical and near-infrared wavelengths, using both photometric and spectroscopic observations (Herbst et al. 1994; Mathieu et al. 1997; Basri et al. 1997; Huerta et al. 2005; Boden et al. 2009). In Table A.2, we provide the photometry results from our own observing campaigns in December 2008, January 2009, and January 2010. We note here that when we compare the Teide and the Wellesley data obtained on 2008 December 28—the only night for which the two telescope observations overlap in time—we find a slight offset between the magnitudes obtained with the two telescopes, which is within the uncertainties stated in Section 5.2.2. Consistency can be achieved by subtracting 0.08 mag from the Wellesley V magnitudes and 0.05 mag from the Wellesley R and I magnitudes. We emphasize that, while the photometry table does contain the original *un*shifted magnitudes per telescope, we have shifted these data accordingly for all plots displayed here for the purpose of our analysis and the discussion that follows.

In Figure 5.5 we plot our photometry values first as a function of the orbital phase Φ for all three optical filters. In the optical V band, the source is known to brighten by $\approx$0.5 mag within an orbital phase window of breadth 0.30 (or $\sim$5 days), centered on a phase of -0.1 (or about 1.6 days before closest approach). The V filter always shows the greatest amplitude change, but the variations are mirrored in all filters. This “bluening” effect caused by increased veiling is just one of the expected results from the ongoing accretion processes (Basri et al. 1997). We also observe the same 5-day activity window for the optical brightenings, which is a window 2.3 times broader than the millimeter window documented thus far. Our photometry results are indeed consistent with previous studies (see Mathieu et al. 1997, Figure 4). One unique feature in our data, however, is the apparent double-peaked nature of these most recent brightenings, indicating a clustering of events around two phases. We caution against overinterpreting this effect since the data set is sparsely-sampled, covers only 4 periastron encounters, and is heavily dominated by the Dec08 event in particular (see Figure 5.6). Nevertheless, the behavior is intriguing given the emerging picture for star-star reconnection events, and we will return breifly to this result in Section 5.4.4.

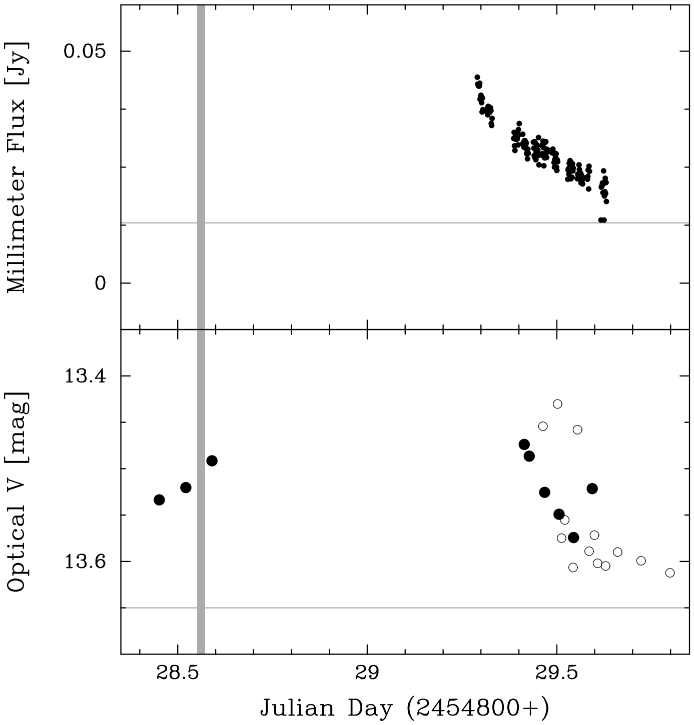

Figure 5.7 — A plot showing the simultaneous millimeter (upper panel) and optical (lower panel) coverage for the Dec08 periastron encounter. A thin gray horizontal line in each panel represents the quiescent value. The optical light curve begins to brighten the night before, returning to quiescence in time with the millimeter decay. We indicate with a thick vertical line $t = 0$ for the estimated time of the trigger event, assuming an average 30-hour flare. In this case, the optical activity appears coincident in both time and duration with the millimeter activity.

In Figure 5.6 we unwrap the optical data and show the results of continuous monitoring from December 2008 to January 2009, as well as several measurements from January 2010. We indicate the absolute magnitude versus Julian Day, where the bi-weekly periastron events are indicated with a shaded column. The source is found to increase in brightness in the days leading up to each of the 4 periastron encounters that we monitored, even though optical brightenings were not seen for all encounters monitored by Mathieu et al. (1997). Of particular interest are the second and fourth shaded columns in Figure 5.6 (at JD = 2 454 829 and 2 455 221, respectively), which represent the dates for the Dec08 and Jan10 observations, confirming coincident optical and millimeter activity on each date. No optical data is available for Mar09 and Apr08, corresponding to a time of year when the source is below the horizon at night.

The Dec08 event offers the most extensive simultaneous optical coverage. In Figure 5.7 we show how the optical and millimeter outbursts are related in time. On the night before the millimeter track, the optical light curve begins to brighten. During the millimeter decay the following night, the optical light curve decreases in step with the millimeter flare. This brightening and subsequent decay shows that the optical activity is not only coincident in time, but also in duration, with the average millimeter profile.

5.4 Discussion

5.4.1 Signatures of Synchrotron Emission

The millimeter emission is almost certainly non-thermal in origin given the sudden flare onset and the fast decay time. In the solar analogy, it is generally accepted that this type of extraneous emission from high-energy electrons is synchrotron in origin, and that emission at shorter millimeter wavelengths results from the most energetic (MeV) electrons (Silva et al. 2007). We eliminate non-relativistic cyclotron radiation as a primary emission process because the magnetic field strength required to produce cyclotron emission ($B = 2\pi m_e/q$) at 90 GHz is 30 kG; increasing to 80 kG at 238 GHz. These values are much larger than the 1–6 kG surface field strengths expected (or measured) for TTSs (Guenther et al. 1999; Johns-Krull 2007). Instead, the electron population probed by our observations must possess mildly to highly relativistic properties, representing gyro-synchrotron and synchrotron radiation mechanisms, respectively.

In this subsection, we follow closely an analysis similar to that presented in Massi et al. (2006) for synchrotron emission from the interacting coronae of V773 Tau A. We model the outer (large-scale) structure of the DQ Tau magnetospheres to be well-ordered dipoles and we take the magnetic axes to be aligned parallel to the rotational axes, assumptions that are consistent with recent 3D extrapolations of the coronal field topology for several young stars (Gregory et al. 2008). We do assume that the rotational axes are both aligned perpendicular to the plane of the system, although we acknowledge that, in rare cases, large misalignments have been documented around a short-period binary (Albrecht et al. 2009). We know that the DQ Tau system is inclined 157° to the line-of-sight (Boden et al. 2009), and we presume that the reconnection events occur in the equatorial region between the two stars. For a synchrotron spectrum, Ginzburg & Syrovatskii (1965) showed that the maximum spectral frequency (in Hz) is proportional to the perpendicular component of the magnetic field $B_\perp$ (in Gauss) and the Lorentz factor γ squared:

$$\nu_{\rm max} = 1.2 \times 10^6 B_\perp \gamma^2 \tag{5.1}$$

Since millimeter brightenings have been consistently observed near 90 GHz, we conservatively assume this value for $\nu_{\rm max}$, meaning that there must be an electron population whose relativistic properties in vacuum satisfy the following relation:

$$B\gamma^2 = 8.1 \times 10^4 \tag{5.2}$$

Using an average surface field strength of 3 kG, we can calculate the Lorentz factor for several relevant distances, including: half the minimum binary separation ($d = 4\,R_\star$, $B = 47$ G, $\gamma = 42$); the minimum binary separation ($d = 8\,R_\star$, $B = 6$ G, $\gamma = 116$); and the distance to the inner rim of the circumbinary disk in the case of a star-disk interaction ($d = 54\,R_\star$, $B = 0.02$ G, $\gamma = 2012$). All scenarios give rise to highly relativistic ($\gamma \gg 1$) particles, and thus synchrotron emission. For gyro-synchrotron ($\gamma \approx 5$) emission only, contributions would be restricted to stellar heights of 0.3–1.5 $R_\star$ and most likely indicate single-star magnetic activity that is independent of the orbital period.

Due to the nature of synchrotron emission and the local magnetized environment, competition between radiation and collisional losses represent the largest impactors on the exponential decays that characterize our millimeter light curves. We start with the following expression for synchrotron radiation losses (in hours) for a well-ordered field (Blumenthal & Gould 1970):

$$\tau_{\rm s} = \frac{1.6 \times 10^5}{B^2 \gamma} \tag{5.3}$$

In combination with Eq. 5.2, we can solve for the two unknowns when we use a synchrotron decay time $\tau_{\rm s}$ equal to the e-folding time of 6.55 hours. We find $B = 19$ G and $\gamma = 65$. For the full range of dipolar field strengths expected for a TTS (1–6 kG), this result localizes the main emitting region to a stellar height of 3.7–6.8 $R_\star$. We note that the values are centered around the theoretical size for a T Tauri magnetosphere. They are also consistent with a site located halfway between the two stars for the separation distances at the times of outburst (∼8–13 $R_\star$ as determined in Section 5.3.1). This range compares well with the coronae loop size infered by Getman et al. (2010, submitted) to explain the X-ray activity, which derives from a related process but a separate electron population. Alternately, if significant emission were to be observed near a $\nu_{\rm max}$ of 238 GHz, then the stellar height range identified would increase (unless a weaker stellar magnetic field or a faster decay time at the higher frequency were to compensate).

Next we constrain the maximum density of the electrons spiraling along the field lines by calculating what the thermal Coloumb collisional losses (in hours) would need to be in order to shorten the observed decay time. We use (Petrosian 1985; Massi et al. 2006):

$$\tau_{\rm c} = 4.16 \times 10^{8} \frac{\gamma}{n_{\rm e}} \tag{5.4}$$

to derive a maximum electron density of $n_{\rm e} \leq 3.7 \times 10^{9}$ cm^{-3}. A final check of the condition (Ginzburg & Syrovatskii 1965):

$$\nu \gg \nu_{\rm c} \simeq 20 \frac{n_{\rm e}}{B_{\perp}} \tag{5.5}$$

confirms that the vacuum approximation used throughout these calculations is valid in the case of the DQ Tau magnetospheres as accelerated electrons spiral down from large stellar heights.

The fact that synchrotron losses explain the light curve profiles well implies that the relativistic electron reservoir is sufficiently confined, or trapped, within the global magnetic structure. One of the key conclusions from the Massi et al. (2006) model for V773 Tau A was that electrons must leak out at magnetic mirror points in order to diffuse the synchrotron emission fast enough to achieve their observed e-folding time of 2.31 hours. While evoking this effect is unnecessary late in our own flare timeline, we note that a much steeper decay is present in the initial hours of the Apr08 flare (refer to Figure 5.3). It is possible that a similar leakage of electrons could also occur in the DQ Tau system shortly after the initial outburst, or perhaps as (accreting) charged particles are initially expelled from the system in a manner similar to a coronal mass ejection in the Sun. Or perhaps a more probable scenario is that the Apr08 decay, like the Jan10 dip, is the result of the Neupert effect and the thick-target mechanism (see Getman et al. 2010, submitted). We do rule out several geometrical effects, including an eclipse due to rotation, because the stellar rotational periods have been determined to be ∼3 days (see Basri et al. 1997), while the maximum deviation from the decay profile lasts at most 5.5 hours. In the end, the geometry-independent, natural synchrotron decay process (vs. particle loss or leakage) as the primary loss mechanism agrees much better with the persistent, large-scale decay profiles observed from one flare to the next.

5.4.2 De-polarization Effects

Synchrotron emission predicts a high fraction of linearly polarized light, up to 70% in a well-ordered magnetic field, although it is rarely observed to be maximally polarized (e.g. Sokoloff et al. 1998; Trippe et al. 2010). Our own observations limit the polarization fraction toward DQ Tau to < 5–8%. The measurements sample both a quiescent state as well as two flare decays, and do not rule out the presence of linear polarization altogether. Instead, we explore de-polarization effects that can reduce the observed polarization fraction.

Polarized light originates in regions where the magnetic field lines are stable, well-ordered, of a single orientation, and of a single magnetic polarity. Since the plane of polarization is perpendicular to the magnetic field, a tangled field unresolved by the telescope beam leads to beam averaging of the different polarization vectors, effectively de-polarizing the light. In Section 5.3.1 our resolution constrained the emission to a region 100 AU from the binary, an area that encompasses the two independent magnetospheres. Within this view, dipolar magnetospheric field lines on one star begin in its northern magnetic hemisphere and end in its southern magnetic hemisphere, effectively doubling back 180° in direction within the telescope beam. In addition, the field polarity of one star may be reversed with respect to the companion's. In fact, we show in Section 5.4.3 how this is probably the case for DQ Tau. Therefore, the geometry of the field lines where the accelerated electrons are trapped has a very important impact on the net polarization observed, and any positive polarization detections may favor emitting regions at larger stellar heights where the magnetic field is simpler and well-ordered, since higher-order field components typically fall off more quickly (Gregory et al. 2008).

Nevertheless, linear polarization has been measured toward V773 Tau A, the only other known PMS binary to exhibit evidence of star-star magnetic interactions. Phillips et al. (1996) detected a significant fractional polarization of 2% at centimeter wavelengths. However, follow-up polarization observations of V773 Tau A during periods of millimeter activity produced only non-detections at both millimeter and centimeter wavelengths (Massi et al. 2008). Generally, polarization is considerably weakened toward the radio end of the spectrum, mainly due to Faraday rotation effects (Ginzburg & Syrovatskii 1965). The effect occurs as linearly polarized light passes through a dense, magnetized medium causing the polarization angle θ to rotate by an angle equal to $RM\,\lambda^2$ where RM is the rotation measure (in rad m^{-2}) defined as:

$$RM = 8.1 \times 10^5 \int n_{\mathrm{e}} B_{||}\, ds \tag{5.6}$$

Here n_{e} is the electron density (in cm^{-3}), B is the longitudinal magnetic field strength (in Gauss), and ds is the line-of-sight path length (in pc) through the magnetized medium. When the rotation measure is larger than $\sim 10^5$ rad m^{-2} at 3.3 mm, Faraday de-polarization is complete in a homogeneous medium. This is equivalent to a rotation angle of 90°, although rotation angles as small as 5–10° (or $RM \approx 10^4$) can also be sufficiently effective, depending on the method detection threshold and the intrinsic polarization fraction.

Faraday rotation can occur in any magnetized region along the line-of-sight, including the interstellar medium and the Earth's ionosphere. However, the synchrotron emission from DQ Tau predicts large electron densities (10^9 cm^{-3}) and strong magnetic fields (3 orders of magnitude greater than the Sun's field), suggesting that the emitting region itself has the potential for the greatest de-polarization effect. To test this possibility, we model electrons trapped in the magnetospheres with a shell of outer radius $5\,R_\star$ and a thickness of $1\,R_\star$. The electron density is set to the maximum determined from synchrotron losses and taken to be constant throughout the shell. The magnetic field strength is modeled as a dipole with a surface field strength of 3 kG. In this scenario, we derive an RM of $\sim 10^9$ rad m^{-2}, which undoubtably results in complete de-polarization of the synchrotron emission.

Conceding that this initial calculation may represent a case of maximized extremes, we can do the same calculation for an electron density of 10^3 cm^{-3} (essentially an upper limit in a molecular cloud of typically 10^3 *molecules* per cm^{-3}), a shell thickness of $0.1\,R_\star$ (equivalently the size of the stellar corona), and a reduced dipole field of surface strength 1 kG. We find an RM value of $\sim 10^2$, which is below the cutoff for complete de-polarization. To recover a factor 100 in the RM, we determine that a minimum density of 10^5–10^6 cm^{-3} is needed to sufficiently de-polarize the millimeter emission. These values are representative of the density in the uppermost layers of the circumbinary disk, and for a source experiencing (simultaneous) accretion, should be easily obtained, at least along the accretion streams. Therefore, we predict that the synchrotron source is sufficiently self de-polarizing to result in the complete absence of linear polarization for most geometries.

5.4.3 Orientation and Topology of the Magnetospheres

A dipole representation of the magnetospheres remains an adequate and consistent model for the analysis, and is the simplest valid structure. When we illustrate the corresponding field lines in Figure 5.8,

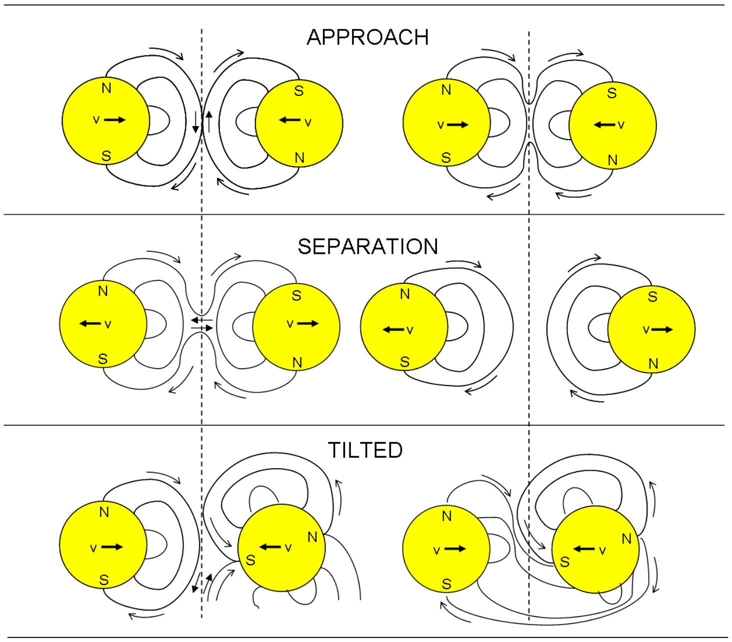

Figure 5.8 — An illustration of the scenarios for reconnection events in the DQ Tau binary system during approach (upper panel) and separation (middle panel). In the lower panel, we show a variation to the upper panel if the magnetic axes are tilted with respect to one another. This misalignment can also occur into or out of the page, causing field lines to cross at intermediate angles that may or may not result in reconnection. Similar variations to the middle panel are also possible.

there are, in fact, two scenarios for the timing of the reconnection events: during both the approach and separation phases. During approach, the field lines are oppositely-directed in the equatorial region and undergo compression as the stars approach periastron and the fields repel one another. At the vertical boundary layer between the two magnetospheres, where their merging plasma flows and induced electrical currents resist one another, reconnection can occur. The two magnetospheres join together via shared field lines that begin on one star and now end on the other. During separation, the global field is split into two closed magnetospheres through stretching, and thus compression of the lines near the orbital plane of the system. Both scenarios release energy into the surrounding region, accelerating charged particles at large stellar heights down along the magnetospheric field lines toward the star, which is when both scenarios produce (gyro-)synchrotron radiation in a relatively indistinguishable manner.

In Figure 5.8, we point out that the magnetic axes are drawn with an inverse alignment. In an aligned system, trying to connect the field lines from the magnetic north of one star to the magnetic south of the other results in crossed lines, which would quickly reconnect, reverting back to two dipole structures. Thus, in this arrangement, the global magnetic topology is strictly maintained. The magnetic density still increases upon approach, building up magnetic energy stores, but the boundary layer between the two magnetospheres is imperceptable to the local plasma and electrical currents. There is far less resistance to the re-arrangement (e.g. compression) of the field lines, as compared to the reverse case, and reconnection is not favored as a result.

Assuming parallel rotational axes perpendicular to the orbital plane, and that magnetic axes tend to be aligned with the rotational axis in many astrophysical bodies (as we justified in Section 5.4.1), the two magnetospheres should be either aligned (0°) or inversely aligned (180°). Undoubtedly, in this bimodal interpretation, the DQ Tau magnetospheres therefore must be inversely aligned to produce the flares observed. This does present an interesting consequence for the millimeter flares if one of the magnetic fields were to flip, as the Sun's field is prone to do once every 11 years; an effect that has been observed toward other PMS stars with short rotation periods (Donati et al. 2008; Fares et al. 2009; Petit et al. 2009). In this case, if the magnetospheres are the principle mechanism for the flaring phenomenon, and if their magnetic axes are indeed more or less aligned, then we could expect on-and-off periods of millimeter activity near periastron.

Finally, there are the oblique cases when the field lines forced together are not similary- or oppositely-directed, but rather cross at an intermediate angle. This can occur if the magnetic axes are tilted with respect to one another. The occurrence of reconnection then depends on the orientation angle, the field strengths, the merging systems of flux, and the resistivity to the topological changes caused by the induced currents. Consequently, one conclusion to make is that the DQ Tau magnetospheres must be misaligned by a significant angle to produce reconnection events and their associated millimeter flares.

Another possibility is that the magnetospheres are poorly modeled by a dipole between 4–7 $R_\star$ (or 6.4–12 $R_\odot$), which is the half-distance separation of the two stars during the observed flares. In the Sun, the dipole component dominates beyond 2.5 $R_\odot$, but in PMS stars the relative strengths of the field components can vary widely (Gregory et al. 2008). For example, toward the TTS V2129 Oph the octopole component was found to dominate out to 6.7 $R_\star$ (Donati et al. 2007), providing ample opportunity in a binary system for opposite-polarity regions to interact and reconnect at large separations. Other deviations include the winding up of the field lines as the stars rotate faster in the equatorial region. This effect is amplified with respect to the Sun given that these stars rotate 10 times faster. However, we expect that the winding effect should act to slow the rotation in an aligned system, and encourage reconnection as usual in an inversely aligned system.

The accretion streams can also produce local changes in the field lines, including compression and ordering of the magnetosphere during episodic events. It is unclear what should be expected from a collision of two streams with equivalent mass accretion rates, but it may mirror the complex and unstable merging of two stellar jets, as modeled by Mundt et al. (2010). There the authors predict that, as the outflows in a binary system combine at large stellar distances, reconnection events should result near the intersection point. Finally, the trigger might simply be a inter-coronal interaction very similar to the Massi et al. (2006, 2008) scenario for V773 Tau A. There the extended magnetic structure was imaged at a stellar height of 48 $R_\odot$. Thus, if similarly extended structure were present on the stars in the DQ Tau system, then flares could result at any time in the orbit. Although currently, all observations outside our defined outburst event window report quiescent fluxes (Chapter 4, Salter et al. 2008; Guilloteau et al., in prep), suggesting that this is not the most robust description for the current observations. Of course, we cannot rule out millimeter contributions from a combination of scenarios.

5.4.4 Optical Emission Mechanisms

The coincident timing and duration of the optical and millimeter brightenings in Figure 5.7 is intriguing, but the physical interpretation remains a challenge. While we have presented evidence that the millimeter emission arises from recurring star-star reconnection events, the origin of the optical emission can be rooted in both dynamical processes (e.g. accretion pulses due to the binary motions) and magnetospheric processes (e.g. reconnection events). In this section, we consider whether both processes are required to explain the optical behavior.

Flare models often include an optical emission component due to the heating and ionization of the chromospheric plasma where the non-thermal electron population spirals down into the stellar atmosphere, typically at a magnetic field footprint (Haisch et al. 1991; Güdel 2002). In this picture, an optical brightening is normally expected to accompany the millimeter activity, just like we currently observe. It is thus tempting to recall the double-peaked nature of the optical brightenings in Figure 5.5, in light of our scenario for interacting magnetospheres, which predicts two reconnection events associated with first the joining and then the separation of the magnetospheres. The data presented in Mathieu et al. (1997) do not preclude optical brightenings clustered around two separate phases, spaced apart in time by roughly 3 days ($\Delta\Phi \approx 0.2$). In addition, Mathieu et al. (1997) also determined that enough magnetic energy is available in the outer magnetospheres to power the average DQ Tau optical brightening, even though the authors questioned whether the field could regenerate itself on a bi-weekly basis. Although our millimeter observations do not cover back-to-back periastron encounters, our consistent flare detection rate suggests that reconnection occurs during most, if not all, orbits. However, it remains unclear whether this result favors a quick and efficient regeneration of the field or an alternative mechanism to drive the optical brightenings.

Instead, other observational results favor optical brightenings linked to independent accretion processes. Mathieu et al. (1997) noted first that the optical brightenings occur quite far from periastron to be the result of reconnection, as well as the spectral bluenings seem to disagree with the optical flat-spectrum (or “white-light") continuum enhancements that more typically accompany flares (e.g. Hudson et al. 1992; Güdel et al. 2004). Likewise, some of the DQ Tau optical brightenings appear to last continuously for up to 4 days (Figure 2 of Mathieu et al. 1997), much longer than an “average" millimeter flare. In Section 5.3.2 we determined that the observed millimeter activity window was 2.3 times smaller than the optical, but we concede that our phase sampling was intentionally restricted to the 24-hour period before periastron, and therefore we lack a detailed overview of the millimeter perspective at larger separations. This fact, combined with the Massi et al. (2008) evidence for interacting coronae at large ($\geq 30\,R_\odot$) stellar separations, suggest that only a prolonged multi-wavelength monitoring program over several cycles, and covering all orbital phases, can best characterize the relationship between the optical and millimeter activity, and the relevant dynamical and magnetospheric contributions.

In summary, it is not straight-forward to assign all of the elevated optical acitivity in this sytem to dynamically induced pulsed accretion events, particularly near periastron. Accretion appears to be ongoing at different levels throughout the orbit (Basri et al. 1997), with features that fit well the models by Artymowicz & Lubow (1996). Reconnection events, on the other hand, have only been documented near periastron thus far, but seem to always accompany an optical event. Thus, in all likelihood, reconnection and accretion processes are both contributing to the elevated optical activity, occurring simultaneously at periastron. To better ascertain the causal or co-dependent nature of the dynamical and magnetospheric processes, it is necessary to separate out the optical effects of each process.

5.5 Conclusions

We confirm periodic, elevated millimeter flux levels toward the DQ Tau PMS binary while monitoring 3 recent periastron encounters. The regularity of the flare timing is consistent with the proposed scenario for colliding magnetospheres within a day of closest approach, although the initiating event appears to vary within a 22-hour window corresponding to a binary separation of 8–13 $R_\star$. The flaring mechanism can be explained by synchrotron emission from highly relativistic electrons accelerated near the reconnection site that begin to spiral down along the magnetospheres toward one or both stars. The main emission region is localized near a stellar height of 3.7–6.8 $R_\star$, about halfway between the two stars at the time of an event. Synchrotron losses easily explain the similar (late-time) decay profiles, indicating both a well-confined electron population and a large stable magnetic structure from one event to the next. We estimate that the flares can last up to 30 hours per event, corresponding to 8% of the orbital period. In addition, multiple millimeter flares during a single periastron event have been observed within approximately 15 hours ($\Delta\Phi \approx 0.04$) of one another, with the secondary event being less powerful. The succession of events may correspond to first the merging and then the separation of the two magnetospheres, or simply to a trade-off between a slow sequential release of stored magnetic energy in lieu of one large outburst. A star-star magnetic reconnection event remains the simplest, most straight-forward interpretation in terms of the timing of the activity, the regularity of the occurrence, the magnetic field strengths implied, and the field sizes.

We measure an upper limit of 5–8% for the fractional linear polarization of the light, but we predict that both beam dilution and Faraday rotation in the DQ Tau system are probably sufficient to result in a net polarization of 0. We determine an upper limit of 3.7×10^9 cm^{-3} for the electron density in the field lines. However, if a non-zero polarization fraction is eventually detected, suggesting that Faraday rotation in particular is ineffective, then the upper limit for the emitting region must be revised to $\leq 10^5$–10^6 cm^{-3}. Otherwise, another hinderence to the detection of polarization is the preferred orientation and topologies for the magnetic axes in order for reconnection to occur: either the dipoles are misaligned at a significant angle or else complex, higher-order magnetic structures are present at large stellar heights. In both cases, and for low-resolution observations specifically, reversed polarity footprints on each stellar surface will affect the measured polarization fraction. All things considered, the upper limit for the polarization in no way contradicts a synchrotron emission process.

The results of the simultaneous millimeter and optical monitoring reveal a particularly striking coincidence between the timing and duration of the multi-wavelength activity, but ultimately unravels little of the relationship between the dynamical and magnetospheric processes. We cannot distinguish between optical brightenings due to accretion events, reconnection processes, or a combination thereof. The current window for elevated millimeter activity is about 2.5 times smaller than the window for the optical brightenings. This preliminary statistic suggests that dynamically-induced accretion can occur independently; while each reconnection event thus far has been accompanied by an optical brightening that may, or may not, be associated with the accretion process only. Perhaps the only true test for the possible dependence of one process on the other, is to study similar binary systems where one effect is absent. We do suspect that this flaring phenomenon may be relevant to many similar T Tauri binary systems of high eccentricity, as we expect to see when new millimeter instrumentation reduces the time required for large, multi-epoch surveys.

Acknowledgements

We would like to thank Vincent Piétu and Jan-Martin Winters at IRAM for their assistance in scheduling and carrying out the observations, as well as Sascha Trippe for help with the PdBI data reduction and analysis. At CARMA we are grateful to Lee Mundy and Nikolaus Volgenau for their assistance in acquiring the data in Director's discretionary time. We would like to thank the observing staff at Teide Observatory for the IAC80 observations, including Álex Oscoz Abad, Cristina Zurita, and Rafael Barrena Delgado. At Wellesley College, we are grateful to Kim McLeod, Wendy Bauer, Steve Slivan and the undergraduate observers Kirsten Levandowski, Kelsey Turbeville, and Kathryn Neugent. Finally, we thank Y. Boehler, A. Dutrey, V. Piétu and S. Guilloteau for communicating data prior to publication. Financial support for travel to Wellesley and IRAM for observational duties was provided by a Leids Sterrekunde Fonds grant. The research of DMS, AK, and MRH is supported through a VIDI grant from the Netherlands Organization for Scientific Research (NWO).

Appendix A

A.1 Optical Data

Table A.1 — Comparison Stars

Number[a]	V [mag]	R [mag]	I [mag]
1	15.79	14.68	13.81
2	14.86	13.95	13.18
3	14.43	13.33	12.27
4	13.72	12.61	11.66
5	11.84	11.05	10.43
6	15.30	14.12	13.19

Notes. [a] The numbers correspond to the labels in Figure A.1.

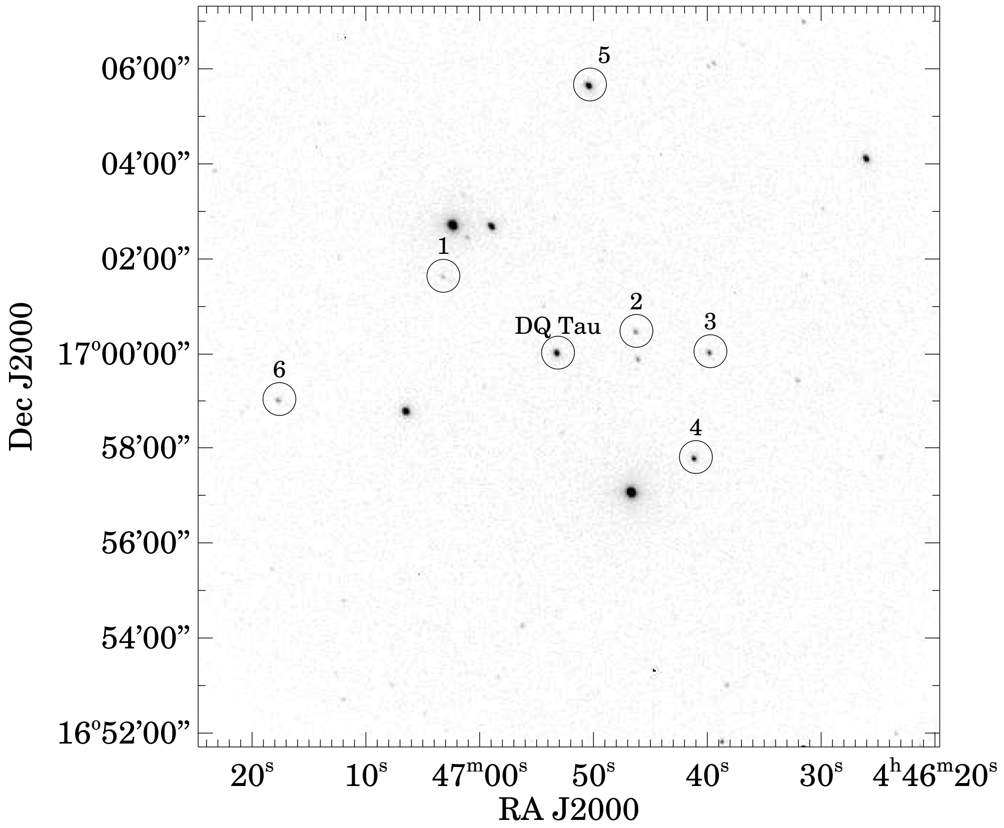

Figure A.1 — The comparison stars used to derive the differential photometry for DQ Tau. The figure shows the complete 15.6′ × 15.6′ field of view for the Wellesley 0.6-meter telescope. This I-band image was obtained on 2008 December 25.

Table A.2 — Optical Observing Log

JD 2 450 000+	Observatory[a]	V [mag]	JD 2 450 000+	Observatory	R [mag]	JD 2 450 000+	Observatory	I [mag]
4803.640	Wellesley	13.64	4803.635	Wellesley	12.34	4803.661	Wellesley	11.12
4809.513	Wellesley	13.70	4809.517	Wellesley	12.34	4809.519	Wellesley	11.07
4809.534	Wellesley	13.59	4809.538	Wellesley	12.31	4809.540	Wellesley	11.07
4813.484	Wellesley	13.59	4813.489	Wellesley	12.13	4813.491	Wellesley	11.03
4813.506	Wellesley	13.77	4813.589	Wellesley	12.26	4813.591	Wellesley	11.06
4813.585	Wellesley	13.49	4817.416	Teide	12.32	4817.418	Teide	11.10
4817.414	Teide	13.66	4817.468	Teide	12.32	4817.469	Teide	11.11
4817.466	Teide	13.67	4817.503	Teide	12.33	4817.504	Teide	11.10
4817.501	Teide	13.67	4817.558	Teide	12.33	4817.560	Teide	11.20
4817.557	Teide	13.68	4817.682	Teide	12.34	4817.683	Teide	11.11
4817.680	Teide	13.67	4826.476	Wellesley	12.19	4826.472	Wellesley	10.99
4826.480	Wellesley	13.37	4826.640	Wellesley	12.18	4826.473	Wellesley	11.02
4826.632	Wellesley	13.51	4826.645	Wellesley	12.19	4826.651	Wellesley	11.06
4826.812	Wellesley	13.57	4826.805	Wellesley	12.29	4826.801	Wellesley	11.12
4828.451	Teide	13.53	4828.454	Teide	12.19	4828.455	Teide	11.00
4828.522	Teide	13.52	4828.523	Teide	12.17	4828.524	Teide	11.00
4828.591	Teide	13.49	4828.592	Teide	12.15	4828.593	Teide	10.98
4829.414	Teide	13.47	4829.415	Teide	12.17	4829.430	Teide	10.99
4829.427	Teide	13.49	4829.429	Teide	12.18	4829.459	Wellesley	11.05
4829.464	Wellesley	13.54	4829.462	Wellesley	12.18	4829.470	Teide	11.01
4829.468	Teide	13.53	4829.469	Teide	12.21	4829.471	Wellesley	11.02
4829.502	Wellesley	13.51	4829.479	Wellesley	12.31	4829.505	Wellesley	11.06
4829.506	Teide	13.55	4829.507	Teide	12.23	4829.508	Teide	11.02
4829.513	Wellesley	13.66	4829.508	Wellesley	12.29	4829.547	Teide	11.03
4829.521	Wellesley	13.64	4829.525	Wellesley	12.23	4829.548	Wellesley	11.06
4829.543	Wellesley	13.69	4829.527	Wellesley	12.28	4829.560	Wellesley	11.09
4829.544	Teide	13.57	4829.546	Wellesley	12.31	4829.591	Wellesley	11.09
4829.555	Wellesley	13.54	4829.546	Teide	12.24	4829.596	Teide	11.00
4829.585	Wellesley	13.67	4829.558	Wellesley	12.29	4829.604	Wellesley	11.08
4829.593	Teide	13.52	4829.589	Wellesley	12.32	4829.613	Wellesley	11.09
4829.599	Wellesley	13.65	4829.595	Teide	12.22	4829.635	Wellesley	11.08
4829.607	Wellesley	13.68	4829.603	Wellesley	12.32	4829.667	Wellesley	11.07
4829.629	Wellesley	13.69	4829.611	Wellesley	12.30	4829.707	Wellesley	11.06
4829.661	Wellesley	13.67	4829.633	Wellesley	12.30	4829.728	Wellesley	11.11
4829.702	Wellesley	13.79	4829.665	Wellesley	12.31	4829.756	Wellesley	11.11
4829.722	Wellesley	13.68	4829.726	Wellesley	12.32	4829.794	Wellesley	11.11
4829.798	Wellesley	13.69	4829.753	Wellesley	12.32	4831.440	Wellesley	11.10
4831.448	Wellesley	13.77	4829.796	Wellesley	12.32	4831.463	Wellesley	11.08
4831.468	Wellesley	13.75	4831.444	Wellesley	12.31	4831.479	Wellesley	11.11
4831.485	Wellesley	13.67	4831.465	Wellesley	12.33	4831.488	Wellesley	11.11
4831.493	Wellesley	13.70	4831.481	Wellesley	12.33	4831.502	Wellesley	11.10
4831.508	Wellesley	13.68	4831.489	Wellesley	12.31	4834.461	Teide	11.07
4834.454	Teide	13.62	4831.504	Wellesley	12.32	4834.536	Teide	11.08
4834.529	Teide	13.62	4834.458	Teide	12.29	4834.603	Teide	11.07
4834.596	Teide	13.67	4834.533	Teide	12.29	4834.661	Teide	11.08
4834.654	Teide	13.61	4834.600	Teide	12.30	4836.390	Teide	11.10
4836.396	Teide	13.69	4834.658	Teide	12.30	4836.398	Teide	11.10
4836.404	Teide	13.68	4836.393	Teide	12.34	4836.407	Teide	11.10
4836.413	Teide	13.69	4836.401	Teide	12.34	4836.519	Teide	11.09
4836.525	Teide	13.67	4836.410	Teide	12.34	4836.528	Teide	11.09
4836.534	Teide	13.66	4836.522	Teide	12.33	4836.536	Teide	11.09
4836.542	Teide	13.67	4836.530	Teide	12.33	4842.375	Teide	11.00
4842.369	Teide	13.49	4836.539	Teide	12.32	4842.387	Teide	11.00
4842.380	Teide	13.46	4842.372	Teide	12.17	4842.517	Teide	10.96
4842.510	Teide	13.34	4842.384	Teide	12.15	4842.527	Teide	10.96
4842.520	Teide	13.34	4842.513	Teide	12.08	5208.351	Teide	10.91
5208.360	Teide	13.30	4842.523	Teide	12.08	5208.474	Teide	10.91
5208.482	Teide	13.31	5208.357	Teide	12.04	5208.592	Teide	10.90
5208.597	Teide	13.31	5208.480	Teide	12.05	5210.532	Teide	11.06
5210.540	Teide	13.61	5208.596	Teide	12.07	5210.542	Teide	11.06
5210.550	Teide	13.61	5210.537	Teide	12.32	5210.553	Teide	11.06
5210.560	Teide	13.62	5210.547	Teide	12.31	5210.563	Teide	11.06
5210.571	Teide	13.62	5210.558	Teide	12.31			
			5210.568	Teide	12.31			

Bibliography

Albrecht, S., Reffert, S., Snellen, I. A. G., & Winn, J. N. 2009, Nature, 461, 373
Artymowicz, P. & Lubow, S. H. 1996, ApJ, 467, L77+
Basri, G., Johns-Krull, C. M., & Mathieu, R. D. 1997, AJ, 114, 781
Blumenthal, G. R. & Gould, R. J. 1970, Reviews of Modern Physics, 42, 237
Boden, A. F., Akeson, R. L., Sargent, A. I., et al. 2009, ApJ, 696, L111
Bower, G. C., Plambeck, R. L., Bolatto, A., et al. 2003, ApJ, 598, 1140
Donati, J., Jardine, M. M., Gregory, S. G., et al. 2007, MNRAS, 380, 1297
Donati, J., Moutou, C., Farès, R., et al. 2008, MNRAS, 385, 1179
Droege, T., F., Richmond, et al. 2007, VizieR Online Data Catalog, 2271, 0
Fares, R., Donati, J., Moutou, C., et al. 2009, MNRAS, 398, 1383
Furuya, R. S., Shinnaga, H., Nakanishi, K., Momose, M., & Saito, M. 2003, PASJ, 55, L83
Getman, K., Broos, P. S., Salter, D. M., Garmire, G. P., & Hogerheijde, M. R. 2010, submitted, ApJ
Ginzburg, V. L. & Syrovatskii, S. I. 1965, ARA&A, 3, 297
Gregory, S. G., Matt, S. P., Donati, J., & Jardine, M. 2008, MNRAS, 389, 1839
Güdel, M. 2002, ARA&A, 40, 217
Güdel, M., Audard, M., Reale, F., Skinner, S. L., & Linsky, J. L. 2004, A&A, 416, 713
Guenther, E. W., Lehmann, H., Emerson, J. P., & Staude, J. 1999, A&A, 341, 768
Haisch, B., Strong, K. T., & Rodono, M. 1991, ARA&A, 29, 275
Hartmann, L., Hewett, R., & Calvet, N. 1994, ApJ, 426, 669
Herbst, W., Herbst, D. K., Grossman, E. J., & Weinstein, D. 1994, AJ, 108, 1906
Hesse, M. & Schindler, K. 1988, J. Geophys. Res., 93, 5559
Hudson, H. S., Acton, L. W., Hirayama, T., & Uchida, Y. 1992, PASJ, 44, L77
Huerta, M., Hartigan, P., & White, R. J. 2005, AJ, 129, 985
Johns-Krull, C. M. 2007, ApJ, 664, 975
Kaufmann, P., Correia, E., Costa, J. E. R., & Zodi Vaz, A. M. 1986, A&A, 157, 11
Kenyon, S. J., Dobrzycka, D., & Hartmann, L. 1994, AJ, 108, 1872
Landolt, A. U. 1992, AJ, 104, 372
Massi, M., Forbrich, J., Menten, K. M., et al. 2006, A&A, 453, 959
Massi, M., Menten, K., & Neidhöfer, J. 2002, A&A, 382, 152
Massi, M., Ros, E., Menten, K. M., et al. 2008, A&A, 480, 489
Mathieu, R. D., Stassun, K., Basri, G., et al. 1997, AJ, 113, 1841
Menzies, J. W., Marang, F., Laing, J. D., Coulson, I. M., & Engelbrecht, C. A. 1991, MNRAS, 248, 642
Mundt, R., Hamilton, C. M., Herbst, W., Johns-Krull, C. M., & Winn, J. N. 2010, ApJ, 708, L5
Pérez, L. M., Lamb, J. W., Woody, D. P., et al. 2010, ArXiv e-prints
Petit, P., Dintrans, B., Morgenthaler, A., et al. 2009, A&A, 508, L9
Petrosian, V. 1985, ApJ, 299, 987
Phillips, R. B., Lonsdale, C. J., & Feigelson, E. D. 1991, ApJ, 382, 261
Phillips, R. B., Lonsdale, C. J., Feigelson, E. D., & Deeney, B. D. 1996, AJ, 111, 918
Salter, D. M., Hogerheijde, M. R., & Blake, G. A. 2008, A&A, 492, L21
Shu, F., Najita, J., Ostriker, E., et al. 1994, ApJ, 429, 781
Silva, A. V. R., Share, G. H., Murphy, R. J., et al. 2007, Sol. Phys., 245, 311
Sokoloff, D. D., Bykov, A. A., Shukurov, A., et al. 1998, MNRAS, 299, 189
Stine, P. C., Feigelson, E. D., Andre, P., & Montmerle, T. 1988, AJ, 96, 1394
Trippe, S., Neri, R., Krips, M., et al. 2010, A&A, 515, A40+
Vasyliunas, V. M. 1975, Reviews of Geophysics and Space Physics, 13, 303
White, S. M., Pallavicini, R., & Kundu, M. R. 1992, A&A, 257, 557

Chapter 6

Hunting for Millimeter Flares from Magnetic Reconnection in Pre-main-sequence Spectroscopic Binaries

Recent observations of the low-mass pre-main-sequence (PMS), eccentric spectroscopic binaries DQ Tau and V773 Tau A reveal that their millimeter spectrum is occasionally dominated by flares from non-thermal emission processes. The transient activity is believed to be synchrotron in nature, resulting from powerful magnetic reconnection events when the separate magnetic structures of the binary components are briefly capable of interacting and forced to reorganize, typically near periastron. We conducted the first systematic study of the millimeter variability toward a sample of 12 PMS spectroscopic binaries with the aim to characterize the proliferation of flares amongst sources likely to experience interbinary reconnection events. The source sample consists entirely of short-period, close-separation binaries that possess either a high orbital eccentricity ($e > 0.1$) or a circular orbit ($e \approx 0$). Using the MAMBO2 array on the IRAM 30m telescope, we carried out continuous monitoring at 1.25 mm (240 GHz) over a 4-night period during which all of the high-eccentricity binaries approached periastron. We also obtained simultaneous optical VRI measurements, since a strong link is often observed between stellar reconnection events (traced via X-rays) and optical brightenings. UZ Tau E is the only source to be detected at millimeter wavelengths, and it exhibited significant variation ($F_{1.25\mathrm{mm}} = 87$–179 mJy); it is also the only source to undergo strong simultaneous optical variability ($\Delta R \approx 0.9$ mag). The binary possesses the largest orbital eccentricity in the current sample, a predicted factor in star-star magnetic interaction events. With orbital parameters and variable accretion activity similar to DQ Tau, the millimeter behavior of UZ Tau E draws many parallels to the DQ Tau model for colliding magnetospheres. However, on the basis of our observations alone, we cannot determine whether the variability is repetitive, or if it is due to variable free-free emission in an ionized wind. UZ Tau E brings the number of known millimeter-varying PMS sources to 3 out of a total of 14 monitored binaries now in the literature. We favor a model whereby repeated magnetospheric interactions near closest approach are responsible for the millimeter-wave variability of UZ Tau E, analogous to the model for DQ Tau. However, given the small number statistics, we cannot exclude powerful interbinary reconnection events as a rare, stochastic phenomenon.

Á. Kóspál, D. M. Salter, M. R. Hogerheijde, A. Moór, and G. A. Blake
Astronomy & Astrophysics, submitted (2010)

6.1 Introduction

Recent observations of young stellar objects (YSOs) are challenging the long-standing notion that the millimeter continuum emission characterizing these objects is always dominated by the quiescent thermal emission from passively-heated circumstellar dust. Powerful, transient millimeter flares attributed to synchrotron continua have now been reported toward two embedded protostars in the Corona Australis cloud (Choi et al. 2009), one protostar in the Orion BN/KL star-forming region (Forbrich et al. 2008), the embedded YSO GMR-A in Orion (Bower et al. 2003; Furuya et al. 2003), the classical T Tauri star (CTTS) DQ Tau in Taurus (Chapters 4 and 5, Salter et al. 2008, 2010), and the weak-line T Tauri star (WTTS) V773 Tau A, also in Taurus (Massi et al. 2002, 2006, 2008).

These millimeter flares are thought to be more powerful examples of the prevalent, lower-energy radio activity observed toward YSOs, and are not unlike flares accurring on the Sun (Stine et al. 1988; White et al. 1992). The emission is attributed to a combination of gyrosynchrotron and synchrotron radiation powered by magnetic reconnection events in the stellar coronae, which occur when oppositely directed magnetic field lines interact (Bastian et al. 1998). The radio flare resulting from this magnetic activity is also expected to be accompanied by an X-ray flare of proportional luminosty according to the Neupert effect (Neupert 1968; Güdel 2002). In this way, large X-ray surveys are contributing to the characterization of the magnetic activity during the T Tauri phase (e.g. Getman et al. 2005; Güdel et al. 2007), which represents the period during the formation and main sequence life of a solar-type star when magnetic activity levels are highest and when reconnection—and not accretion—is believed to be the primary X-ray production mechanism (Preibisch et al. 2005; Stassun et al. 2006, 2007; Forbrich et al. 2007; Feigelson et al. 2007). The X-ray data confirm analogous solar-type coronal activity, but with luminosities 10^3–10^5 times higher (Testa 2010). Uninterrupted, long-duration observing campaigns of star-forming regions also document a once-a-week statistical occurrence of giant X-ray flares, representing the most powerful events and an estimated 1% of all flares (Favata et al. 2005; Getman et al. 2008a,b). If magnetic activity is indeed the trigger, then these X-ray events are most likely to be associated with synchrotron emission processes extending into the millimeter regime.

It is noteworthy that in the two best-studied millimeter flare cases, both DQ Tau and V773 Tau A are close-separation, eccentric, pre-main-sequence (PMS) binaries with similar orbital characteristics. In addition, their flaring was recurring, leading the authors in the latest study to conclude that DQ Tau could display excess millimeter flux as much as 8% of the time, with consistency near periastron. One can thus speculate that in close binaries, in addition to the single-star coronal activity described until now, two additional magnetic activity scenarios might exist. An example of the first is V773 Tau A, where interbinary interactions due to chance alignments of narrow extended coronal features, like helmet streamers, cause the flares. The second binary-specific phenomenon is the current model for DQ Tau where colliding dipolar magnetospheres represent a simple geometric scenario for periodic events, with two primary determining factors: a periastron approach smaller than twice the magnetospheric radius ($R \sim 5\,R_\star$) and a high eccentricity. In this arrangement, the closed stellar magnetospheres must overlap near periastron, but only temporarily.

Again, X-ray studies can provide constraints on the coronal extent of PMS stars, with the result that typical inferred loop lengths are 4–20 $R_\star$ for the most powerful outbursts. This is much larger than any coronal structure observed toward more evolved stars (Favata et al. 2005), and consistent with the T Tauri stage being the most magnetically active phase of star formation. In the case of the WTTS binary system V773 Tau A, two separate coronal structures extending to $\geq 15\,R_\star$ each are necessary to bridge the interbinary gap (Massi et al. 2008). Toward DQ Tau the derived loop lengths from both X-ray and millimeter analyses are $5\,R_\star$ in height (Getman et al. 2010, submitted; Chapter 4, Salter et al. 2010). If the X-ray statistics predict correctly a common once-a-week occurrence with consistently large loop lengths, then more interbinary collisions might be expected in a number of close-separation binaries, in addition to any single-star events that may occur. Binary systems also occur frequently, representing 65% or more of the local field population in the middle of the main-sequence (Duquennoy & Mayor 1991). The fraction increases to up to 75% for the population in the Taurus star-forming region (Leinert et al. 1993; Ghez et al. 1997; Kohler & Leinert 1998; Luhman et al. 2010), suggesting that more systems could start out as binaries. Thus, candidate millimeter-variable systems are worthy of investigation.

To assess the proliferation of significant millimeter variability among PMS binaries, we report here on a targeted millimeter variability survey of 12 PMS spectroscopic binaries that are most likely to experience millimeter flares, based on predictions by the current interbinary magnetic reconnection models, either following the V773 Tau A scenario and exhibiting strong flares at many orbital phases, or exhibiting the DQ Tau phenomena showing flares with more regularity around periastron. Since in both the DQ Tau and UZ Tau E cases, optical brightenings are common near periastron due to periodic accretion events (Jensen et al. 2007), and because the optical light curve of DQ Tau was found to mirror its millimeter flare activity in both time and duration (Chapter 5, Salter et al. 2010), we complemented our millimeter data with simultaneous optical monitoring of our targets.

6.2 Observations

6.2.1 Target Selection

The study of PMS binaries is a relatively young field, due in large part to the difficult and time-consuming nature of spectroscopic observations, while sometimes further impeded by a complicated circumstellar environment. To date, orbital parameters have been published for only a few dozen young spectroscopic binaries. These parameters include the *necessary* selection criteria for the present study: known eccentricity (e), orbital period (P), projected semimajor axis ($a \sin i$), and the epoch of periastron passage. From the available sources in the literature, we selected objects that are observable from the northern hemisphere (located primarily in Taurus and Orion), and that possess an orbital period of less than 50 days. The latter constraint means that the periastron distances for these objects are in the range where magnetospheric or coronal interactions have occurred in similar systems. In addition, shorter periods make it easier to observe large numbers of binaries as they complete periastron passage around the same time.

The resulting list of targets, along with their most important orbital parameters, can be found in Table 6.1. Our sample is comprised of two separate groups. In the first group, we specifically target short-period binaries of high orbital eccentricity ($e > 0.1$) and small periastron separations similar to DQ Tau and V773 Tau A. In this half of the sample, the binary components are suspected to undergo a change in their large-scale magnetospheric topology as the binary separation distance varies greatly and rapidly near periastron. This group is most likely to experience a merging of the two magnetospheres near closest approach with a subsequent detachment at larger separations—much like the current picture for DQ Tau (Chapter 5, Salter et al. 2010). Although we note that none of the targets quite approach the exceptional combination of large eccentricity and close approach as DQ Tau (with its $e = 0.556$ and $d_{\rm min} = 13\,R_\odot$). The second group serves as a “control sample” and includes close-separation binaries with circular orbits ($e \approx 0$). Since the binary separation in these systems remains constant, there is no variable compression or relaxation of the component magnetospheres throughout the orbit, and therefore the global magnetospheric topology is relatively unchanged; reconnection is not expected to occur except sporadically in chance collisions of extended coronal features due to the stars’ close proximity—similar to the current model for V773 Tau A (Massi et al. 2008).

6.2.2 Observations and Data Reduction

Millimeter Observations

We obtained millimeter data with the IRAM 30 m telescope on Pico Veleta (Spain) between 17–21 November 2009. We used the 117-pixel Max-Planck Millimeter Bolometer array (MAMBO2) in the standard ON/OFF mode, using a $35''$ wobbler throw, and making sure that the target fell on the most sensitive pixel (pixel #20) during each on-source exposure. One scan consisted of four (on the first night) or eight (on the remaining three nights) subscans of 60 s exposure time. The MAMBO2 bandpass was centered at $\lambda = 1.25$ mm ($\nu = 240$ GHz). At this wavelength, the half power beamwidth is $11''$ and the pixel spacing is $20''$.

We monitored our targets for four consecutive nights, covering also the periastron events for most of the high-eccentricity binaries. We observed each target 1–3 times per night depending on weather conditions. The atmospheric transmission at 1.25 mm was usually good, with the zenith atmospheric opacity being monitored with sky dips every 1–2 hours. Opacity was consistently found to be between 0.1–0.4, except for a few peaks on the night of November 19/20. Sky noise levels were typically very low, except again for a few hours on the night of November 19/20. Mars and Uranus were used for focusing and gain calibration every 3–4 hours. Pointing was checked every 1–2 hours using Mars, Uranus, or a nearby quasar. Occasionally, high wind velocities during our observing run resulted in a lower pointing

Table 6.1 — Orbital parameters for the binaries.

Name	D [pc]	e	P [days]	$a \sin i$ [AU]	i [°]	$d_{\rm min}$ [$R_\odot$]	Ref.
High-eccentricity binaries							
EK Cep	164	0.109	4.43	0.077	89.3^*	14.7	1,2
UZ Tau E	140	0.33	19.13	0.124	54	22.1	3
RX J0530.7−0434	460	0.32	40.57	0.336	78.5	>49.1	4,5
Parenago 1540	470	0.12	33.73	0.188	···	>35.6	6
Parenago 2494	470	0.257	19.48	0.146	···	>23.3	7
GG Ori	438	0.222	6.63	0.116	89.2^*	19.4	8
Circular binaries							
RX J0350.5−1355	450^{**}	0	9.28	0.115	···	>24.7	4
V826 Tau	150	0	3.89	0.013	13	12.6	9
RX J0529.4+0041	325	0	3.04	0.053	86.5^*	11.5	10
Parenago 1802	420	0.029	4.67	0.050	78.1^*	10.7	11
RX J0541.4−0324	450^{**}	0	4.99	0.074	···	>15.9	4
NGC 2264 Walk 134	913	0	6.35	0.099	<73	>21.3	12,13
Binaries already known to exhibit flares							
DQ Tau	140	0.556	15.80	0.053	23	12.9	14
V773 Tau A	148.4	0.272	51.10	0.35	66.0	60.0	15

Notes. e is eccentricity; P is orbital period; a is semimajor axis; i is inclination; $d_{\rm min}$ is separation during periastron (or a lower limit for systems with an unknown inclination); * indicates eclipsing binaries; ** means the average distance to Orion was used. **References.** (1) Gimenez & Margrave (1985); (2) Torres et al. (2010); (3) Jensen et al. (2007); (4) Covino et al. (2001); (5) Marilli et al. (2007); (6) Marschall & Mathieu (1988); (7) Reipurth et al. (2002); (8) Torres et al. (2000); (9) Reipurth et al. (1990); (10) (Covino et al. 2004); (11) Stassun et al. (2008); (12) Padgett & Stapelfeldt (1994); (13) Baxter et al. (2009); (14) Mathieu et al. (1997); (15) Boden et al. (2007).

precision for some of the scans. As a result, we have determined that the absolute flux calibration for all data points is accurate to within ∼20%.

The data were reduced using the MOPSIC pipeline (developed by R. Zylka), and included steps to remove the atmospheric emission (using the two wobbler offset positions), to correct for extinction due to atmospheric water vapor (using the skydips), to perform gain calibration (using the calibration observations of bright sources with known 1.25 mm flux), and to calculate a noise-weighted average of the subscans. The obtained flux densities usually have a root mean square noise of 2–3 mJy bm^{-1}, and are listed per source in Table A.1.

Optical Observations

Simultaneous optical monitoring of our targets was conducted from two telescopes: the 60/90/180 cm (aperture diameter/primary mirror diameter/focal length) Schmidt telescope of the Konkoly Observatory (Hungary), and the 80 cm (primary mirror diameter) IAC-80 telescope of the Teide Observatory in the Canary Islands (Spain). The Konkoly Schmidt telescope is equipped with a 1536 × 1024 pixel Photometrics AT 200 CCD camera (pixel scale: 1.03″), and a Bessel UBV(RI)$_C$ filter set. The Teide IAC-80 telescope is equipped with a 2048 × 2048 pixel Spectral Instruments E2V 42-40 back-illuminated CCD camera ‘CAMELOT’ (pixel scale: 0.304″), and a Johnson-Bessel UBV(RI)$_J$ filter set. Images with the Schmidt telescope were obtained on 9 nights in the period between 13–26 November 2009, and with the IAC-80 telescope for 3 nights between 18–22 November 2009. With the IAC-80, only R-band images were taken, whereas with the Schmidt, R and I, and additionally for the brighter stars, V, images were also obtained. One of our targets, UZ Tau E, was observed with the IAC-80 telescope using VRI filters also between 25 October and 7 November 2009.

The images were reduced in IDL following the standard processing steps of bias subtraction, dark subtraction (for the Photometrics camera on the Schmidt telescope only) and flat-fielding. On each night, for each target, images were obtained in blocks of 3 or 5 frames per filter. Aperture photometry for the target and other field stars were performed on each image using IDL’s *cntrd* and *aper* procedures. For the Schmidt images, we used a 5-pixel radius aperture, and a sky annulus between 10 and 15 pixels. For the IAC-80 images, the aperture radius was 8 pixels, and the sky annulus was between 30 and 40 pixels. In the case of RX J0529.4+0041, a hierarchical triple system, the spectroscopic binary and the tertiary component were partially resolved, so we increased the Schmidt aperture to 10 pixels and the IAC-80 aperture to 30 pixels, in order to make sure that the aperture included the total flux from all three components. In the case of UZ Tau, a hierarchical quadruple system, we obtained separate photometry for UZ Tau E and UZ Tau W in the following way. The small pixel scale and the good seeing at the IAC-80 telescope made it possible to obtain separate photometry for both the E and the W components, by using an aperture radius of 4 pixels. The results indicated that the W component was constant within 0.02 mag. For the Schmidt images, we used an aperture radius of 10 pixels (encompassing both UZ Tau E and W), and we subtracted the contribution of the W component (calculated as the average magnitude measured on the IAC-80 images).

For the purpose of differential photometry, we selected a comparison star for each of our targets. Our main selection criterium for the comparison stars was constant brightness during our observing period (compared to other stars in the field). The selected comparison stars are listed in Table A.2. We calculated the magnitude difference between our target and the comparison stars for each frame. Then, these differential magnitudes were averaged for each night, while their standard deviation was quadratically added to the formal photometric uncertainty. Due to the different filter sets on the two telescopes, the resulting magnitudes were slightly different, especially in cases where the comparison star was much redder than the target star. In these cases, we shifted the IAC-80 magnitudes by 0.03–0.08 mag so that they overlap with the Schmidt magnitudes obtained on the same nights. The resulting (shifted) values can be found in Table A.3, and the light curves for the R filter are plotted in the top panels of Figure 6.1. The light curves for the other filters look very similar, but often have fewer available data points.

6.3 Results

In Figure 6.1 we show the optical and millimeter light curves for all of our targets, as well as the separation distances between the binary components, as a function of time. The optical light curves indicate that most of our targets showed variability at a certain level throughout our observing campaign. By far the highest amplitude in our sample was displayed by UZ Tau E, (with $\Delta R \approx 0.9$ mag), but NGC 2264 Walk 134 ($\Delta R \approx 0.2$ mag), and GG Ori ($\Delta R \approx 0.3$ mag) also varied significantly. The rest of the sample were either constant (EK Cep, RX J0529+0041), or showed slight variations of <0.1 mag. While UZ Tau E and NGC 2266 Walk 134 show variability on a daily timescale, the light curve for GG Ori exhibits only one dip, corresponding to an eclipse shortly before periastron. The sparsely-sampled optical light curves do not display any obvious periodicities in their own right, even with the broader optical monitoring period of 12-14 days and covering multiple orbital periods for some sources. However, in many cases the shapes and amplitudes may be consistent with rotational modulation of the light curve due to stellar spots (RX J0530.7−0434, Parenago 1540, Parenago 2494, RX J0350.5−1355, V826 Tau, Parenago 1802, and RX J0541.4−0324). Thus, a brightening of an eccentric source during periastron may be a chance coincidence. A more detailed analysis of the optical data on a source-by-source basis is given in Section 6.4.3.

At millimeter wavelengths, only one of our targets, UZ Tau, was detected. The other sources remained undetected with typical 3σ upper limits between 4 and 11 mJy. Apparently, UZ Tau is the only

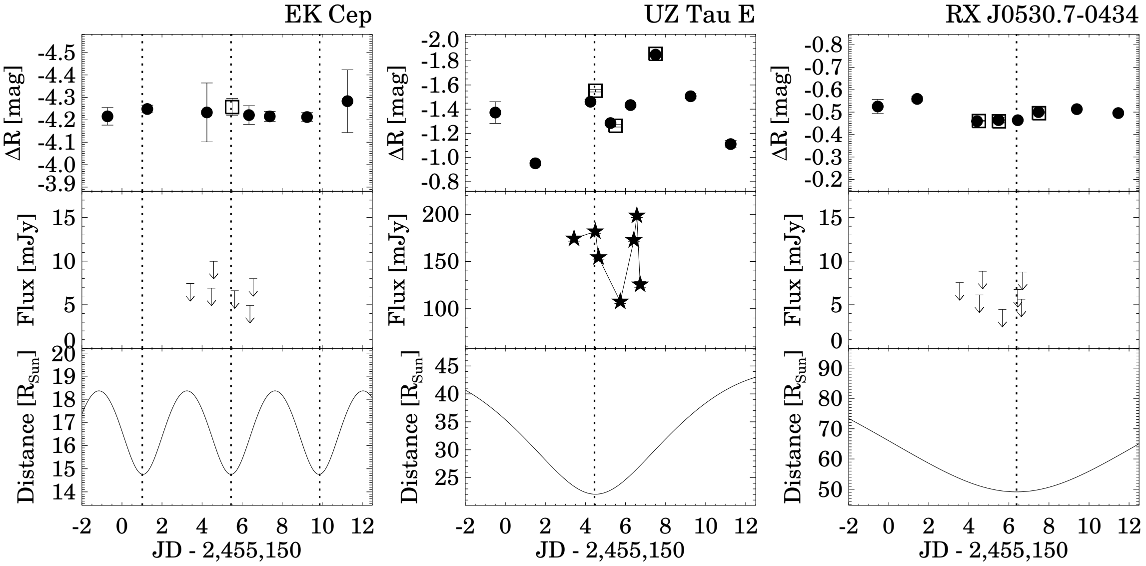

Figure 6.1 — Optical (top) and millimeter (middle) light curves for each of the spectroscopic binaries, as well as separation distances for the binary components as a function of time (bottom). *Filled dots:* R_C-band observations from the Konkoly Schmidt telescope in Hungary; *Open squares:* R_J-band observations from the Teide IAC-80 telescope in Spain; *Filled asterisks:* 1.25 mm observations with the IRAM 30 m telescope in Spain; *Arrows:* 3σ upper limits for the 1.25 mm fluxes. Note that the millimeter fluxes of UZ Tau E contain an ≈20 mJy contribution from UZ Tau W. For the high-eccentricity binaries, a vertical line indicates the time of periastron, while for the circular binaries, thick horizonal lines indicate the length of the orbit.

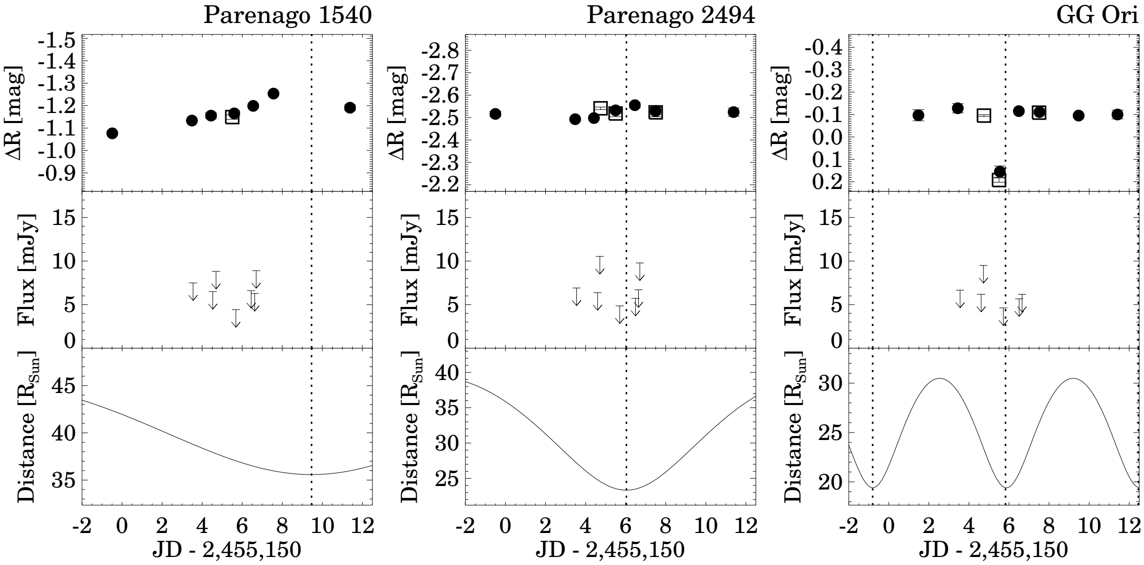

Figure 6.1 — (Continued)

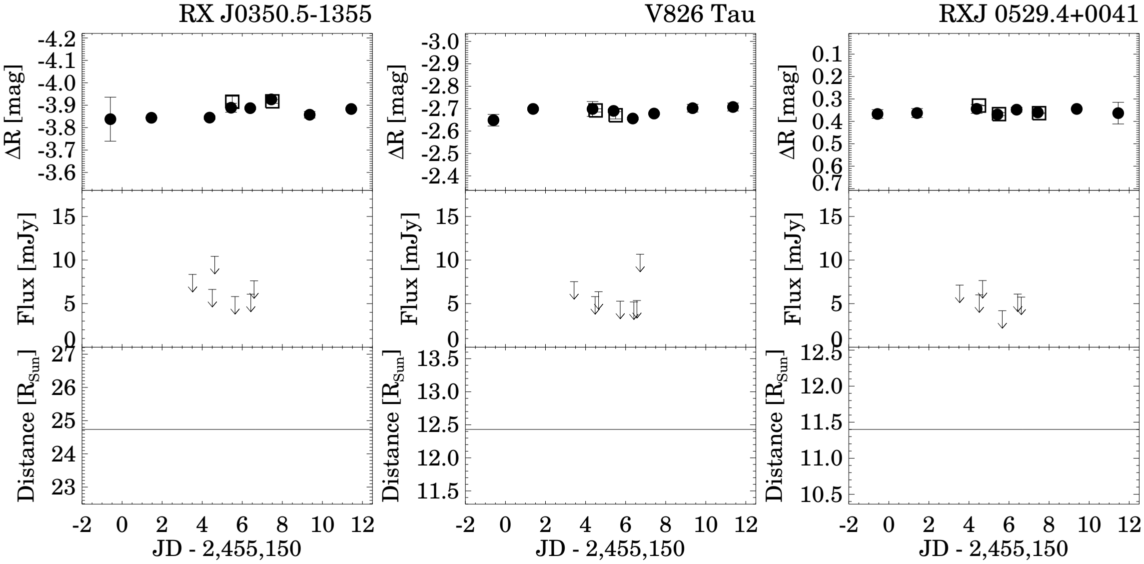

Figure 6.1 — (Continued)

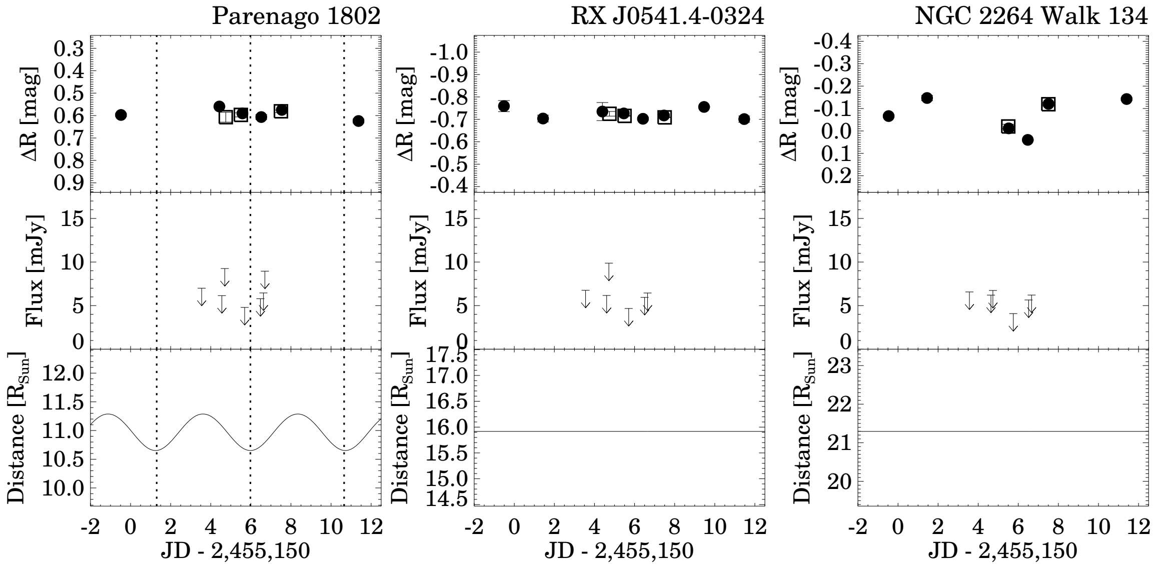

Figure 6.1 — (Continued)

source for which a potentially significant outer circumstellar disk may still be present. The other sources in our sample are more similar to V773 Tau A, with little to no remaining circumstellar material. We derive upper dust mass limits for the small-grain population of $\leq 3.0\times10^{-5}\,M_{\odot}$ ($0.003\,M_{\odot}$ for the total gas plus dust mass) for the sources in Taurus and $\leq 2.5\times10^{-4}\,M_{\odot}$ ($0.025\,M_{\odot}$ for the total gas plus dust mass) for the sources in Orion, on average. To make these dust mass estimates, we used the basic millimeter flux–mass relation of Dutrey et al. (1996) and take $\kappa_{\nu} = 0.02$ g cm^{-2} and $T_{\rm dust} = 45$ K. These upper limits are consistent with the optical–near infrared SEDs for these sources, which are usually fit well by a single-temperature stellar photosphere in the available literature.

The fact that 10 out of 12 of our sources are WTTS is largely a selection effect, due to the orbital parameters being easier to determine when stellar photospheric lines are not obscured by circumstellar material. In reality, the multiplicity ratio for CTTSs and WTTSs in Taurus is essentially identical (Kohler & Leinert 1998). Interestingly, WTTSs tend to dominate the X-ray sky in Taurus (Neuhaeuser et al. 1995; Güdel et al. 2007), suggesting that they are more magnetically active. If WTTSs are also more likely to experience the most powerful magnetic outbursts, our survey failed to detect an example of such an event.

Instead, it is the CTTS UZ Tau that exhibits millimeter variability. We detected UZ Tau at a level of 38–105σ over the course of our monitoring program, with its 1.25 mm flux varying between 107 and 199 mJy in a period of less than 4 days, a clear indication of a significant contribution of non-thermal emission processes. The millimeter light curve in Figure 6.1 shows two peaks: one at around periastron, and another one about two days later, with a deep minimum in-between the two maxima. Since UZ Tau is composed of two binaries, the telescope was always centered on the spectroscopic binary UZ Tau E, but UZ Tau W, at a distance of 3.8″, also had a contribution to the measured flux. As discussed later, we can assume that UZ Tau W is not brighter than UZ Tau E, and that its millimeter flux is constant in time, thus we attribute the observed variability to UZ Tau E. To rule out any instrumental artifacts (due to severe winds during the observing run), we re-checked the pointing, which we found to be good to within 2″ during all seven UZ Tau observations. Therefore, the absolute flux calibration for UZ Tau is precise to within 15%, which is better than the reported value for the entire sample. To produce a factor of 2 *decrease* in the flux—since a mispointing can only reduce the measured flux—the pointing error would have to be 5″, which is clearly not the case. Moreover, the highest fluxes we observed are higher than values reported elsewhere, which cannot be created by mispointing. Thus, we take the flux changes reported here and in Figure 6.1 to be real.

6.4 Discussion

6.4.1 Event Statistics

Our goal was to understand the proliferation of millimeter flare events and variability within the context of a model for colliding magnetospheres, a phenomenon that on the surface appears fairly regular, is well described by a simple geometric model for overlapping fields, and has a relatively clear combination of parameters (e and d_{min}) that are predicted to lead to powerful reconnection events visible at millimeter wavelengths. The idea is that the two stars at apoastron possess strong independent magnetospheres, but near periastron, the fields are more inclined to merge, or at least stretch or compress in the presence of one another, leading to reconnection events. This interaction radius is typically estimated to be $5\,R_{\star}$ based on a dipole magnetic topology and inner disk truncation models. However, in a binary system with a dynamically cleared inner disk and reduced magnetic braking of the stellar rotation from star-disk field lines, the fields may become stronger and extend further outwards. In our subsample of high-eccentricity candidate systems, we observed 1/6 sources to be active in the millimeter; and 0/6 sources for the circular orbits. This brings the number of documented millimeter-variable binaries to 3 (or 21%) of the combined 14-source sample, and includes V773 Tau A, DQ Tau, and now UZ Tau E (see Section 6.4.2).

We begin our analysis with the high-eccentricity sources. To proceed, we must make use of several derived quantities from the DQ Tau study to establish some detection constraints by generalizing all flares due to interbinary, large-scale magnetospheric collision events (Chapter 5, Salter et al. 2010). The borrowed properties include: the flare duration ($\sim$30 hours), peak brightness (100–500 mJy at 3 mm), occurrence ($\sim$2 events per orbital period), and decay time ($\sim$6.5 hours). All of our sources were observed approximately twice per night over a 4-day period, with a maximum average gap in the sampling of 16 hours. For DQ Tau, a typical event is estimated to maintain a flux $>$2 times quiescence for $\sim$75% of a flare (or $\sim$23 hours for the largest outbursts), meaning that our two high-eccentricity sources located in Taurus (140-160 pc away) were reasonably well sampled. However, for the four sources located in Orion (440-470 pc), at a distance 3 times further away where the flux density falls off as D^{-2}, our detection limit is reduced by a factor 9, meaning that a large flare may have only been detectable for about 5-6 hours. In these systems, flares might have been missed by the sparse sampling. This effect might explain the non-detection toward Parenago 2494, which is remarkably similar, in terms of orbital parameters, to UZ Tau E.

For the circular binaries, statistics are more difficult to discern since the phenomenon is based on chance collisions of extended coronal structures. Stars that are more magnetically active are likely, in theory, to exhibit statistically more common events, but this requires a large sample and an uninterrupted, long-duration monitoring program. If, instead, we consider the once-a-week statistical occurrence of giant X-ray outbursts (assuming these are magnetically driven), then having monitored the circular sources for half a week, we might have expected half of (all) the sources to have flared; instead, we detected no flares toward the circular binaries. Again, distance effects and sampling may have affected the five most distant ($>$ 400 pc) sources.

Our study highlights the challenges of establishing a statistically significant sample of well-parameterized spectroscopic binaries and carrying out sufficient monitoring of the sample. In Section 6.4.3, we discuss the systems on a source-by-source basis and we are able to attribute many system and stellar properties to our non-detection statistics, including: the sensitivity of our observations (which is a combination of a flare's flux density, the source distance, and our 3σ detection threshold), binary separation, orbital eccentricity, duration of the flare, spectral peak wavelength of the synchrotron emission, stellar magnetic field strength and activity levels (also a function of spectral type), magnetosphere topology, and flare decay time (a function of field strength and separation distance). These factors may act to reduce our detection statistics, but not the actual rate of occurrence.

In the combined 14-source sample, it is the 3 most extremely eccentric, close-separation binaries that seem to experience very powerful magnetic events. Therefore, while a well-defined subclass of millimeter-flaring binaries may be taking shape, we also cannot exclude the detected flares as a potentially rare phenomenon amongst high eccentricity binaries.

6.4.2 UZ Tau

UZ Tau is a hierarchical quadruple system consisting of two binary systems UZ Tau E and UZ Tau W. The E component is a spectroscopic binary with an orbital period of 19.1 days (Mathieu et al. 1996), and at an angular separation of 3.8$''$ is the W component, which is itself a 0.34$''$ binary (Simon et al. 1995; Prato et al. 2002, and references therein). For the primary component of UZ Tau E, Jensen et al. (2007) give a spectral type of M1 and a photometric radius of 1.9 $R_\odot$. The UZ Tau E system is a CTTS system with ongoing accretion and clear infrared excess, indicating that warm material can be found close to the stars (see e.g. Furlan et al. 2006).

The Millimeter Picture

At millimeter wavelengths, Simon & Guilloteau (1992) observed UZ Tau with the IRAM PdBI in continuum at 2.7 mm and found that the resolved E and W components had equal fluxes of 13±1 mJy. Later, Dutrey et al. (1996) observed the system again with the IRAM PdBI at the same wavelengh, only to report that the E component had a flux of 25.5±1.6 mJy, this time about 3 times brighter than the W component, which measured a more consistent 8±2 mJy. These contrasting observations suggest that the E component is highly variable, whereas W is more or less constant. We note that in both papers, data obtained at different orbital phases of the E component were combined to obtain one single flux value.

In our own survey, the UZ Tau source flux varied between 107 and 199 mJy, over a period of 4 days, and between orbital phases of -0.07 and 0.09. Although the IRAM 30 m telescope was centered on UZ Tau E, we did not completely resolve the system, therefore the W component had some contribution to these values ($\approx$ 70% of its flux may be included in the beam). Thus, we conclude that UZ Tau E varied between approximately 87 and 179 mJy at 1.25 mm. In comparison, previous 1.3 mm resolved fluxes from Jensen et al. (1996) and Isella et al. (2009) are respectively: 137±28 mJy and 126±12 mJy for UZ Tau E, and 32±9 mJy and 30±8 mJy for UZ Tau W. The sum of these are roughly centered between our most extreme values. These 1.3 mm flux values are very similar given the earlier 2.7 mm variability observed and the 13-year gap in time.

If we quickly compare these multi-wavelength fluxes for UZ Tau W, then for an average $F_{1.3\text{mm}} \approx 31$ mJy and $F_{2.7\text{mm}} \approx 10.5$ mJy, we find a millimeter spectral slope of $\alpha \approx 1.5$, which is consistent with an optically thin circumstellar (or circumbinary) disk. Performing a similar analysis on UZ Tau E, with $F_{1.3\text{mm}} \approx 131.5$ mJy and a $F_{2.7\text{mm}} \approx 20$ mJy, we derive an $\alpha \approx 2.6$, which is steeper but not unreasonable. We remark that our minimum $F_{1.25\text{mm}}$ of 107 mJy (or ≈ 87 mJy without the W component) gives an $\alpha \approx 1.9$ that is also consistent with an optically thin disk, as well as the apparent dust evolutionary state of its neighboring W component, which likely formed at the same time and in the same local environment. Of course, due to the different geometry and system parameters, they might have evolved differently. In the end, what is most apparent, is how UZ Tau E seems to be characterized more often than not by excess non-thermal flux. Given the observations to date, our minimum UZ Tau E observation of 87 mJy represents our best measurement for the true quiescent thermal dust emission at 1.25 mm.

The example of UZ Tau E shows that large variations in millimeter brightness do occur, but they may have many explanations. UZ Tau E was perhaps the most promising binary in the initial list because of its many shared traits with fellow spectroscopic binary DQ Tau. This includes of course the highest eccentricity in the sample and a close periastron approach, but also bipolar outflows and episodic accretion bursts from its own circumbinary disk (Basri et al. 1997; Jensen et al. 2007; Hirth et al. 1997). In the following paragraphs, we shall attempt to analyze the UZ Tau E data within the context of the DQ Tau model for colliding magnetospheres to see if this scenario might plausibly explain the active millimeter light curve.

In such a scenario, the apparent double-brightening present in the UZ Tau E millimeter light curve must represent two sequential events occurring two days apart. Salter et al. (2010, Chapter 5) also captured a secondary brightening toward DQ Tau within an estimated 15 hours of the first. In fact, there the authors predict a minimum of two events per periastron encounter in a scenario for colliding magnetospheres, corresponding to first the joining, and then the separation, of the two magnetospheres; a phenomenon that their restricted monitoring window was unable to test fully. In this work, covering a period of 4 days (or an observing window 6 times broader), we find it reasonable that the first break might occur more suddenly and closer to periastron, while the timing of the second event is likely to occur at a much larger separation distance as the magnetospheres slowly stretch and pinch off (see Figure 8 in Chapter 5, Salter et al. 2010). This would then result in an asymmetry of events around periastron. The UZ Tau E data show exactly this, where the first event occurs around the predicted periastron, and the second event seems to peak two days after periastron.

The two brightenings toward UZ Tau E possess similar recorded maximum fluxes, unlike the sequential events captured toward DQ Tau where the secondary is less bright. However, our sparse sampling means that in all likelihood we have missed the true maxima. In the second, third, and fourth data points represent a single, smooth decay, the duration of the first brightening appears comparable to those characteristic of DQ Tau ($\sim$30 hours). The second event is much more abrupt, with the last two data points being separated by only 4 hours, during which the source flux dropped by 73 mJy. The first peak observed toward UZ Tau occurs when the E component stars are separated by $\sim 22\,R_\odot$, and the second peak occurs when they are at a distance of $\sim 27\,R_\odot$. If reconnection occurs halfway between the stars in both cases, equivalent to stellar heights of $5.8\,R_\star$ and $7.1 R_\star$, then the synchrotron decay profiles should possess a factor of 2.5 difference in decay times, with the e-folding time for the first event approximately 4.3 hours and for the second event about 10.6 hours (see the analysis of Massi et al. 2006). The sampling of our data is too coarse to verify this.

The Optical Picture

Jensen et al. (2007) obtained BVRI photometry of UZ Tau E between 2003 and 2006, and claimed that its light curve is periodic on timescales equivalent to the orbital period. They interpreted these results as pulsed accretion from a circumbinary disk, according to the model by Artymowicz & Lubow (1996); an accretion model that, incidentally, was first tested observationally on data from DQ Tau (see Mathieu et al. 1997). In this model, the circumbinary disk is periodically perturbed by the eccentric binary components, causing the disk material to cross the gap between the disk and the stars and fall onto the stellar surfaces. The model predicts a smoothly varying accretion rate which can be more or less strongly peaked at periastron depending on the orbital parameters of the binary, and fits well the light curve presented in Jensen et al. (2007). They note, however, that the significant scatter in the light curves indicate that pulsed accretion does not occur during every binary orbit. Based on arguments concerning the amplitude and timescale of the variability, Jensen et al. (2007) discarded the possibility of rotational modulation due to stellar spots.

Our optical light curves obtained during the time of the millimeter observations indicate two peaks: one at periastron and the other about 3 days later. The peak-to-peak amplitude is 1.19, 0.96, and 0.57 mag

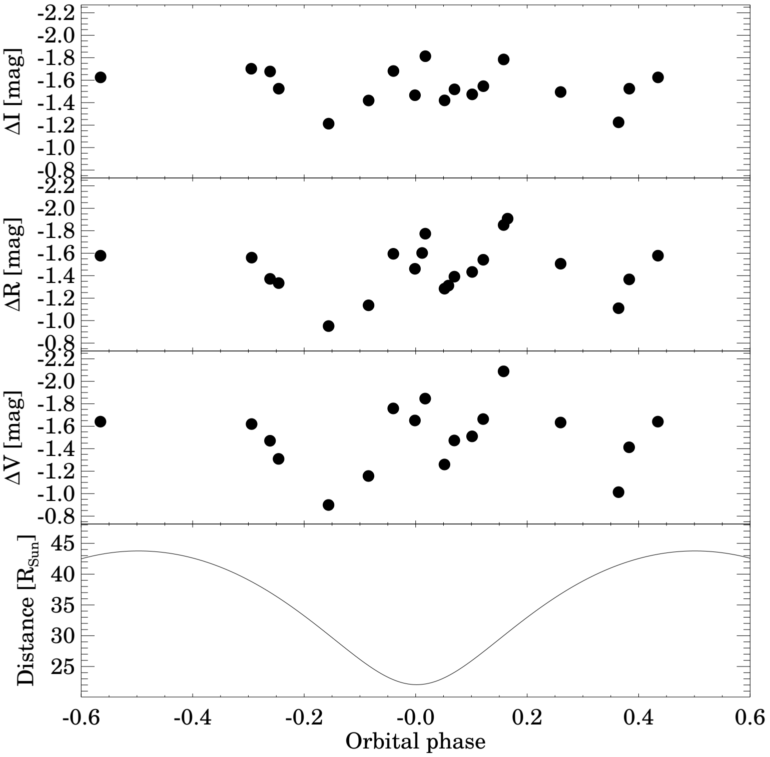

Figure 6.2 — Phase-folded optical light curves of UZ Tau E, and the separation of the binary components. A peak at an orbital phase of 0.00 and another one at 0.15 are clearly visible in the light curves, but the source was not completely quiescent even far from periastron.

in the V-, R-, and I-band, respectively indicating an amplitude decreasing with increasing wavelength. Additional optical observations obtained during the previous periastron show a very similar double-peaked light curve shape, suggesting that—at least for two adjacent periastrons—the optical light curve is periodic. Figure 6.2 shows the light curves folded with the orbital period of 19.131 days, clearly showing the two peaks: one at around 0.00 orbital phase, and another one at around 0.15. Although the light curves are not very well sampled far from periastron, it is evident that the source was not quiescent even when the binary components were far from each other.

Our results indicate that apart from varying accretion rate, a secondary contribution to the brightness changes can also be considered. The similar shape of the millimeter and the optical light curves suggest the possibility that optical flux changes may also be fueled by strong magnetic activity.

6.4.3 Other Sources

In the following paragraphs, we briefly discuss our results for the rest of the binaries within the context of the available literature data and our current analysis of the proliferation of powerful star-star magnetic reconnection events.

EK Cep is an eclipsing binary consisting of an A1.5V primary and a G5Vp secondary, with radii of 1.58 and 1.31 $R_\odot$, respectively (Torres et al. 2010). While the primary is already in the main-sequence phase, the secondary is still a PMS star (Marques et al. 2004). When referencing published photometry and the AKARI/IRC mid-IR all-sky survey (Ishihara et al. 2010), we found no evidence for infrared excess emission that is typically associated with ongoing accretion or warm inner circumstellar dust. Photometric observations by Antonyuk & Rostopchina (2009) indicate that, outside of the eclipse, no trends are noticeable in the light curves, although the scatter of data points does exceed their photometric uncertainty (±0.04 mag). Antonyuk & Rostopchina (2009) detected variable polarization, which they attribute to surface magnetic activity of the secondary component. Our optical photometry shows that EK Cep was constant within our measurement uncertainties (±0.02 mag), and the source was not detected during our millimeter observations. Our millimeter non-detection offers an upper limit of $M_{\rm disk} \leq 0.003\,M_\odot$ for the amount of material in the cold outer disk, if we use the basic flux-mass relation of Dutrey et al. (1996). EK Cep appears to be a fairly quiescent source from optical to millimeter wavelengths, and absent of very powerful star-star magnetic interactions throughout an entire orbital period.

RX J0530.7−0434 is a WTTS binary consisting of two identical, K2-K3 type stars with photometric radii of 3.40 $R_\odot$ (Covino et al. 2001; Marilli et al. 2007). Optical photometry by Covino et al. (2001) revealed photometric variations with a periodicity of 13.5 days (cf. the orbital period of 40.57 days). They interpret these results by supposing that the periodicity of the light curve is the rotation period (which is assumed to be similar for the two binary components), indicating non-synchronous rotation. Marilli et al. (2007) give a V-band amplitude of 0.22 mag and a rotational period of 12.9 days. We found no evidence in the literature for infrared excess to indicate the presence of warm circumstellar material. Our optical light curve shows slight variations with amplitudes of 0.12, 0.10, and 0.08 mag in V-, R-, and I-band, respectively, with the observed peaks approximately 5 days before and 3 days after periastron. The source was not detected during our millimeter observations, giving an upper limit of $M_{\rm disk} \leq 0.024\,M_\odot$ on the disk mass.

Parenago 1540 is a WTTS binary consisting of a K3V primary and a K5V secondary with no evident infrared excess (Marschall & Mathieu 1988). Manset & Bastien (2002) detected photometric variations with a V-band amplitude of < 0.5 mag, as well as periodic variations in the polarization, which they attribute to the orbital motion and the fact that there is still enough dust in the environment of the binary to produce polarization, despite the lack of infrared excess. Favata et al. (2005) reported the detection of an X-ray flare from this source observed during the COUP survey of the Orion Nebula Cluster. Our optical light curve shows a gradual brightening before periastron, and a fading after periastron. The amplitude of the variability is very similar in all bands (0.19 mag in V, 0.18 mag in R, and 0.13 mag in I). The source was not detected during our millimeter observations ($M_{\rm disk} \leq 0.025\,M_\odot$).

Parenago 2494 is a WTTS binary, the primary being an K0IV/V star (Reipurth et al. 2002). (Reipurth et al. 2002) found that the star shows periodic variability in the V-band with an amplitude of 0.10 mag and a period of 5.77 days (cf. the orbital period of 19.48 days). They interpret these variations as the result of large stellar spots on the primary component (which is assumed to dominate the optical light curve). We found no evidence in the literature for infrared excess. Our optical light curves also show variability with amplitudes of 0.12, 0.06, and 0.06 mag in V-, R-, and I-bands, respectively. Our coverage is not enough to do a period analysis, but the shape of the light curves is not inconsistent with a period of about 6 days. The source was not detected during our millimeter observations. Other than the absence of a significant circumstellar dust reservoir ($M_{\rm disk} \leq 0.028\,M_\odot$), Parenago 2494 possesses extremely similar orbital parameters to UZ Tau E. Located at a distance 3 times further away, a similar outburst as the one observed towards UZ Tau E would appear 9 times weaker, and just a few times the noise level.

GG Ori is a PMS eclipsing binary consisting of two nearly identical B9.5-type stars with radii of 1.852 and 1.830 $R_\odot$ (Torres et al. 2000). B- and V-band light curves by Torres et al. (2000) display a scatter that is significantly larger than the photometric errors, thus intrinsic variability of one or both components is suspected. We found no evidence in the literature for infrared excess to indicate warm material close to the stars. Our optical observations show that GG Ori was constant within the measurement uncertainties outside of the primary eclipse recorded on the night of 20/21 November 2009, shortly before periastron. The source was not detected at all during our millimeter observations ($M_{\rm disk} \leq 0.023\,M_\odot$). We do remark how an eclipse that lasts longer than the flare event itself is likely to completely obscure it, assuming the trapped electron population lies within the eclipsing plane. In the case of GG Ori, at a distance 3 times further than our outbursts in Taurus, the detection window is also shortened as it is for Parenago 2494. Moreover, B-type stars are reported to be less magnetically active than later spectral types (their magnetic fields are below a few hundred G, and their X-ray emission is not due to magnetospheric reconnections but shocks in the stellar wind, Damiani et al. 1994; Hubrig et al. 2009).

RX J0350.5−1355 is a WTTS binary consisting of a K0-K1 primary and a K1-K2 secondary (Covino et al. 2001). Covino et al. (2001) and Marilli et al. (2007) found modulations in the optical light curve with a periodicity close to the orbital period. They attribute the 0.2 mag amplitude photometric variability to rotational modulation due to stellar spots, suggesting that the rotational and the orbital period is synchronized. They also note that the spectral lines of the primary indicate faster rotation and strong magnetic activity. We found no evidence in the literature for infrared excess. Our optical observations show variations with amplitudes of 0.08, 0.09, and 0.12 mag in V-, R-, and I-band, respectively. Our coverage is not enough to do a period analysis, but the shape of the light curves are not inconsistent with a period of about 9 days. The source was not detected during our millimeter observations, which cover an entire orbital period ($M_{\rm disk} \leq 0.030\,M_\odot$). If the primary is magnetically active, then the reconnection events may not be powerful enough or frequent enough to be detected in the millimeter.

V826 Tau is a WTTS binary consisting of two very similar K7V-type stars with radii of $1.44\,R_\odot$ (Reipurth et al. 1990). Reipurth et al. (1990) found sinusoidal light variations with an amplitude of 0.06 mag and a period that is slightly smaller than the orbital period. They attribute the variability to rotational modulation due to stellar spots. We found no evidence in the literature for infrared excess; Furlan et al. (2006) classifies it as a Class III (diskless) source. Using XMM-Newton observations, Giardino et al. (2006) detected significant X-ray variability with a factor of 2 amplitude on a five-day timescale, possibly related to coronal magnetic activity. Our light curves show slight variations with amplitudes of 0.05, 0.07, and 0.04 mag in V-, R-, and I-band, respectively. The source was not detected during our millimeter observations ($M_{\rm disk} \leq 0.003\,M_\odot$), which cover 1.5 orbital periods.

RX J0529.4+0041 is a WTTS triple system, consisting of RX J0529.4+0041 A, an eclipsing spectroscopic binary, and RX J0529.4+0041 B, a single star at a projected distance of $1.3''$ (Covino et al. 2004). The eclipsing binary consists of a K1V-type primary and a K7-M0 secondary, with radii of 1.44 and $1.35\,R_\odot$, respectively. Covino et al. (2000) reported B- and V-band brightness variations unrelated to the eclipses, possibly connected to rotational modulation due to stellar spots and other phenomena driven by magnetic activity. Covino et al. (2004) found that the out-of-eclipse JHK light curves of the source can be best fitted if stellar spots are included in their model. Marilli et al. (2007) also observed out-of-eclipse variations with a V-band amplitude of 0.1 mag. Our VRI light curves show that this source was constant within 0.03 mag in all three bands. A possible explanation is that the stars experienced a less active period and had no spots on their surface during our optical observing campaign. We found no evidence in the literature for infrared excess, and the source was undetected during our millimeter observations ($M_{\rm disk} \leq 0.011\,M_\odot$).

Parenago 1802 is a WTTS eclipsing binary consisting of two very similar M2-type stars with radii of 1.82 and 1.69 $R_\odot$ (Stassun et al. 2008). Cargile et al. (2008) observed 0.05 mag peak-to-peak variations in the out-of-eclipse I-band light curve, indicating intrinsic variability. They claim that these variations have both a periodic and a stochastic component, suggesting that spots and chromospheric activity may both be present in the system. Our light curves also show variability with amplitudes 0.06 and 0.05 mag in R- and I-band, respectively. Stassun et al. (2008) found weak evidence for infrared excess at $> 5\mu$m, indicating the presence of a circumbinary disk and/or a faint third component in the system. However, the source was not detected during our millimeter observations ($M_{\rm disk} \leq 0.022\,M_\odot$).

RX J0541.4−0324 is a WTTS binary consisting of a G8 primary and a K3 secondary (Covino et al. 2001), with photometric radii of 2.8 and 1.8 $R_\odot$, respectively. Marilli et al. (2007) observed rotational modulation in the V-band light curve with an amplitude of 0.1 mag and period of 5 days, equal to the orbital pediod, indicating a synchronous rotation. Our VRI light curves show slight variations with an amplitude of 0.06 mag in all three bands, not inconsistent with a 5-day period. We found no evidence in the literature for infrared excess. The source was not detected during our millimeter observations ($M_{\rm disk} \leq 0.024\,M_\odot$).

NGC 2264 Walk 134 is a PMS binary consisting of two similar G-type stars with radii of 3.2 $R_\odot$ (Padgett & Stapelfeldt 1994). Koch et al. (1994) reported V- and R-band variability with an amplitude of 0.35 mag, but found no periodicity in the light curves. They also found that the V brightness of the object is not correlated with the V−R color. Using Chandra observations, Ramírez et al. (2004) found that the source is variable in the X-ray, but found no periodicity in the data, and the variability was not flare-like either. Although its weak emission lines make it a WTTS, it has a near-IR excess that is more typical of CTTS (Padgett & Stapelfeldt 1994). Archival Spitzer IRS spectra also indicates significant infrared excess up to 30μm. Our optical light curves show peak-to-peak variations of 0.22, 0.19, and 0.18 mag in V-, R-, and I-band, respectively. The source appears redder when fainter. This binary was not detected during our millimeter observations ($M_{\rm disk} \leq 0.088\,M_\odot$).

6.5 Summary and Conclusions

Using the IRAM 30m telescope, we have conducted a monitoring program covering 4 consecutive nights to study the millimeter variability toward 12 PMS spectroscopic binaries mostly in the Taurus and Orion star-forming regions. Here we report that one source, the CTTS UZ Tau E, experiences significant millimeter flux variations ($F_{1.25\,\rm mm}$ ranges from 87 to 179 mJy) on daily timescales, a clear indication of non-thermal emission processes near periastron. The rest of the sample, consisting mainly of WTTS up to three times more distant, remain undetected in the continuum for the duration of the campaign, defining upper flux limits of 5–10 mJy at 1.25 mm (240 GHz).

The motivation for our survey follows the recent discoveries of recurring, bright (up to 27 times quiescent values or peaking at about 0.5 Jy) millimeter outbursts toward the T Tauri binaries V773 Tau A (Massi et al. 2008) and DQ Tau (Chapter 5, Salter et al. 2010). Attributed to synchrotron activity from interbinary interactions of large magnetic structures, the phenomenon toward V773 Tau A is described as chance collisions between extended coronal features, whereas it has been proposed that the geometry of the DQ Tau system alone (specifically a large e and small $d_{\rm min}$) results in global interactions between the two closed stellar magnetospheres near periastron (Mathieu et al. 1997; Basri et al. 1997). Therefore, our target list consisted of 6 close-separation binaries with circular orbits ($e \approx 0$) that may experience activity at any time (but apparently did not do so during our observing run), as well as 6 geometrically favorable high-eccentricity systems with activity most likely to occur near periastron (where we detect two possible events toward the source UZ Tau E).

In our sample, no system geometry is quite as extreme as DQ Tau, although our detected source UZ Tau E comes closest. Therefore, a positive detection of (double-peaked) variability near periastron toward UZ Tau E lends strong support to a similar global interbinary interaction; but does not confirm it. Instead, this detection brings our total millimeter-variable source statistics to 3 (i.e. V773 Tau A, DQ Tau, and UZ Tau E) out of 14 observed sources, and means that we may need to consider that millimeter flares are not so uncommon. In addition, as we examine the other systems in much greater detail, it becomes clear why we might not have expected to see, or might have missed, evidence of flares in these systems. The most important factor seems to be the flux-distance inverse relation, which affects our detection limits and sampling coverage. The study itself was also limited by the number of close-separation binaries that have been both identified and well characterized.

UZ Tau E should certainly be considered for follow-up observations to help characterize the light curve profile, also on orbital timescales, and to assess potential contributions from strongly varying free-free emission processes. We must also strongly caution against the reliability of any disk model for UZ Tau E that is based on continuum flux measurements until the true quiescent flux level can be established. In the future, ALMA will allow better monitoring of these systems, leading to a more complete analysis of the proliferation of strong millimeter activity in low-mass PMS binary systems, as well as how much energy can be released during a millimeter outburst and the magnetic field regeneration timescales possible in systems known to experience recurring outbursts.

Acknowledgements

This article publishes observations made with the IAC-80 telescope, operated by the Instituto de Astrofísica de Canarias at the Teide Observatory (Spain), and with the Schmidt telescope at the Piszkéstető Mountain Station of the Konkoly Observatory (Hungary); we are grateful for the granted telescope time. We thank C. Zurita Espinosa for obtaining the IAC-80 data as part of a routine observing program. We are also grateful to B. Ocaña and J. Santiago for their help during the IRAM 30 m observations. The research of ÁK, DMS, and MRH is supported by the Nederlands Organization for Scientific Research (NWO). This work has benefitted from research funding from the European Community’s Seventh Framework Programme.

Appendix A

A.1 Millimeter and Optical Data

Table A.1 — Millimeter photometry

JD−2,450,000	$F_{1.25\,\mathrm{mm}}$ [mJy]	$\sigma_{1.25\,\mathrm{mm}}$ [mJy]
	EK Cep	
5152.91	0.04	2.48
5153.96	-6.31	2.30
5154.08	1.14	3.33
5155.13	-0.85	2.20
5155.89	-0.22	1.64
5156.05	-3.61	2.66
	RX J0350.5−1355	
5153.02	-1.13	2.78
5154.00	0.47	2.21
5154.12	-0.86	3.47
5155.14	-1.21	1.94
5155.93	-1.82	2.03
5156.09	4.86	2.54
	V826 Tau	
5152.93	-1.16	2.51
5153.98	0.46	1.94
5154.15	-2.02	2.12
5155.23	-3.84	1.76
5155.91	1.91	1.73
5156.06	1.20	1.79
5156.22	-2.82	3.56
	UZ Tau	
5152.93	174.3	2.7
5153.99	181.9	2.0
5154.15	154.5	2.0
5155.24	107.4	2.0
5155.91	172.7	1.6
5156.07	198.7	2.0
5156.23	125.5	3.3
	RX J0529.4+0041	
5153.04	-0.66	2.38
5154.02	-2.61	2.00
5154.18	-0.58	2.55
5155.16	-1.00	1.40
5155.93	-2.56	2.03
5156.11	-1.82	1.92
	RX J0530.7−0434	
5153.04	2.74	2.51
5154.02	2.78	2.04

Table A.1 — continued.

JD−2,450,000	$F_{1.25\,\mathrm{mm}}$ [mJy]	$\sigma_{1.25\,\mathrm{mm}}$ [mJy]
5154.19	2.23	2.95
5155.17	0.81	1.49
5155.94	0.79	2.25
5156.12	-2.16	1.88
5156.19	3.67	2.92
	Parenago 1540	
5153.04	-2.35	2.50
5154.03	-0.64	2.17
5154.19	9.87	2.94
5155.18	0.22	1.47
5155.95	1.45	2.20
5156.12	5.12	2.09
5156.20	2.65	2.97
	Parenago 1802	
5153.05	0.07	2.33
5154.05	4.97	2.05
5154.20	4.11	3.08
5155.19	4.58	1.60
5155.98	1.06	1.93
5156.13	10.7	2.2
5156.20	11.1	3.0
	Parenago 2494	
5153.05	3.86	2.30
5154.10	-0.06	2.13
5154.21	2.27	3.51
5155.20	0.71	1.62
5155.99	1.12	1.91
5156.14	1.42	2.23
5156.21	-5.40	3.26
	RX J0541.4−0324	
5153.05	0.14	2.25
5154.11	-1.88	2.06
5154.22	0.84	3.29
5155.21	0.25	1.56
5156.00	1.19	1.98
5156.15	5.00	2.15
	GG Ori	
5153.06	2.11	2.22
5154.11	-2.09	2.06
5154.22	-5.52	3.16
5155.21	-0.81	1.54
5156.00	-3.06	1.89
5156.15	-1.94	2.06
	NGC 2264 Walk 134	
5153.06	-2.41	2.19

Table A.1 — continued.

JD−2,450,000	$F_{1.25\,\mathrm{mm}}$ [mJy]	$\sigma_{1.25\,\mathrm{mm}}$ [mJy]
5154.14	2.51	2.07
5154.23	-1.56	2.25
5155.25	3.18	1.36
5156.02	-0.99	1.88
5156.16	-2.00	2.07

Table A.2 — Comparison stars used in the optical photometry

Target	Comparison
EK Cep	2MASS J21402804+6940328
RX J0350.5−1355	2MASS J03501856−1354489
V826 Tau	2MASS J04320358+1806038
UZ Tau E	2MASS J04323023+2552413
RX J0529.4+0041	2MASS J05291738+0042581
RX J0530.7−0434	2MASS J05303150−0434536
Parenago 1540	2MASS J05343988−0526420
Parenago 1802	2MASS J05351235−0536403
Parenago 2494	2MASS J05370922−0606445
RX J0541.4−0324	2MASS J05412862−0326581
GG Ori	2MASS J05431553−0036546
NGC 2264 Walk 134	2MASS J06405783+0956299

Table A.3 — Optical photometry. The magnitudes are differential magnitudes with respect to the comparison stars in Table A.2. S is for the Konkoly Schmidt Telescope (Hungary) and I is for the Teide IAC-80 telescope (Spain).

JD−2,450,000	ΔV [mag]	ΔR [mag]	ΔI [mag]	Tel.
		EK Cep		
5149.28		−4.22(4)	−3.91(3)	S
5151.27	−4.61(6)	−4.25(2)	−3.89(5)	S
5154.24	−4.56(11)	−4.23(13)	−3.91(13)	S
5155.35	−3.76(5)	−3.44(1)	−3.18(7)	S
5155.41		−4.26(4)		I
5156.34		−4.22(4)	−3.89(2)	S
5157.38	−4.62(6)	−4.22	−3.89(3)	S
5159.24	−4.61(4)	−4.21(2)	−3.90(7)	S
5161.26	−4.61(8)	−4.28	−3.96(5)	S
		RX J0350.5−1355		
5149.42	−3.82(1)	−3.84(10)	−4.03(7)	S
5151.47	−3.75(11)	−3.84(1)	−3.88(28)	S
5154.37	−3.77(5)	−3.84(1)	−3.98(4)	S
5155.44	−3.81(1)	−3.89(2)	−4.00(1)	S
5155.50		−3.92(2)		I
5156.40	−3.80(1)	−3.89(1)	−3.99(2)	S

Table A.3 — continued.

JD−2,450,000	ΔV [mag]	ΔR [mag]	ΔI [mag]	Tel.
5157.45	−3.82(1)	−3.93(1)	−4.01(1)	S
5157.52		−3.92(1)		I
5159.37	−3.80(5)	−3.86(1)	−3.98(3)	S
5161.44	−3.76(6)	−3.88(1)	−3.91(6)	S
V826 Tau				
5149.40	−3.18(6)	−2.65(3)	−2.16(3)	S
5151.38	−3.21(4)	−2.70(1)	−2.15(1)	S
5154.35	−3.24(3)	−2.70(3)	−2.17(3)	S
5154.59		−2.69(1)		I
5155.40	−3.20(1)	−2.69(1)	−2.16(1)	S
5155.50		−2.67(2)		I
5156.36	−3.17(1)	−2.66(1)	−2.14(1)	S
5157.42	−3.20(1)	−2.68(1)	−2.16(1)	S
5159.35	−3.27(4)	−2.70(2)	−2.17(1)	S
5161.36	−3.25(8)	−2.71(2)	−2.16(3)	S
UZ Tau E				
5129.62	−1.57(1)	−1.51(1)	−1.65(1)	I
5130.55	−1.26(1)	−1.28(1)	−1.47(3)	I
5133.63	−1.11(1)	−1.09(1)	−1.37(3)	I
5134.48	−1.71(1)	−1.54(3)	−1.63(1)	I
5135.58	−1.80(1)	−1.72(7)	−1.76(1)	I
5136.58	−1.42(4)	−1.34(2)	−1.47(4)	I
5137.57	−1.61(1)	−1.49(1)	−1.50(3)	I
5142.58	−1.36(1)	−1.32(1)	−1.47(4)	I
5143.57	−1.59(1)	−1.53(1)	−1.57(1)	I
5149.38	−1.47(36)	−1.37(9)	−1.68(2)	S
5151.39	−0.90(5)	−0.95(2)	−1.21(3)	S
5154.36	−1.65(2)	−1.46(2)	−1.47(1)	S
5154.60		−1.55(1)		I
5155.37	−1.26(2)	−1.28(1)	−1.42(1)	S
5155.50		−1.26(1)		I
5156.32	−1.51(1)	−1.43(1)	−1.47(1)	S
5157.40	−2.09(3)	−1.85(1)	−1.78(1)	S
5157.54		−1.86(1)		I
5159.36	−1.63(7)	−1.51(2)	−1.49(1)	S
5161.34	−1.01(7)	−1.11(3)	−1.23(2)	S
UZ Tau W				
5129.62	−1.21(1)	−1.22(1)	−1.60(1)	I
5130.55	−1.17(1)	−1.21(1)	−1.56(1)	I
5133.63	−1.27(1)	−1.27(1)	−1.66(3)	I
5134.48	−1.27(6)	−1.24(2)	−1.59(3)	I
5135.58	−1.25(2)	−1.34(8)	−1.65(2)	I
5136.58	−1.30(5)	−1.32(3)	−1.70(2)	I
5137.57	−1.27(1)	−1.29(1)	−1.62(1)	I
5142.58	−1.19(1)	−1.22(1)	−1.60(3)	I

Table A.3 — continued.

JD−2,450,000	ΔV [mag]	ΔR [mag]	ΔI [mag]	Tel.
5143.57	−1.22(1)	−1.26(1)	−1.59(1)	I
5154.60		−1.16(1)		I
5155.50		−1.25(1)		I
5157.54		−1.17(1)		I
RX J0529.4+0041				
5149.44	0.64(2)	0.37(2)	0.12(2)	S
5151.41	0.65(3)	0.36(2)	0.10(1)	S
5154.38	0.62(2)	0.34(2)	0.09(1)	S
5154.61		0.33(1)		I
5155.42	0.64(1)	0.37(1)	0.10(1)	S
5155.51		0.37(1)		I
5156.38	0.62(1)	0.35(1)	0.09(1)	S
5157.43	0.64(1)	0.36(1)	0.11(1)	S
5157.54		0.36(1)		I
5159.38	0.61(1)	0.34(1)	0.08(1)	S
5161.45	0.63(1)	0.36(5)	0.10(1)	S
RX J0530.7−0434				
5149.45	−1.05(2)	−0.53(3)	0.10(2)	S
5151.42	−1.12(1)	−0.56(1)	0.07(1)	S
5154.41	−1.02(1)	−0.46(1)	0.12(1)	S
5154.62		−0.46(1)		I
5155.48	−1.00(1)	−0.46(1)	0.15(1)	S
5155.51		−0.46(1)		I
5156.44	−1.01(1)	−0.46(1)	0.14(1)	S
5157.48	−1.04(1)	−0.50(1)	0.11(1)	S
5157.54		−0.50(1)		I
5159.39	−1.06(1)	−0.51(1)	0.10(1)	S
5161.46	−1.03(1)	−0.50(1)	0.12(2)	S
Parenago 1540				
5149.51	-0.92(1)	−1.08(1)	−1.19(1)	S
5153.49	-1.04(7)	−1.13(1)		S
5154.44	-1.02(1)	−1.16(1)	−1.26(2)	S
5155.52		−1.15(1)		I
5155.60	-1.02(1)	−1.17(1)	−1.26(3)	S
5156.55	-1.06(1)	−1.20(1)	−1.29(1)	S
5157.56	-1.11(1)	−1.25(1)	−1.32(2)	S
5161.38	-1.08(1)	−1.19(1)	−1.30(5)	S
Parenago 1802				
5149.52		0.60(1)	−0.26(2)	S
5154.43		0.56(1)	−0.30(1)	S
5154.65		0.61(2)		I
5155.52		0.60(1)		I
5155.58		0.59(1)	−0.27(1)	S
5156.52		0.61(1)	−0.26(1)	S
5157.55		0.57(1)	−0.28(1)	S

Table A.3 — continued.

JD−2,450,000	ΔV [mag]	ΔR [mag]	ΔI [mag]	Tel.
5157.55		0.58(1)		I
5161.37		0.62(1)	−0.25(1)	S
		Parenago 2494		
5149.50	−2.78(1)	−2.52(1)	−2.36(1)	S
5153.47	−2.70(2)	−2.49(1)	−2.34(1)	S
5154.42	−2.73(3)	−2.50(1)	−2.35(3)	S
5154.66		−2.54(1)		I
5155.50	−2.78(1)	−2.53(1)	−2.37(1)	S
5155.53		−2.52(1)		I
5156.46	−2.82(1)	−2.56(1)	−2.40(1)	S
5157.50	−2.77(2)	−2.53(2)	−2.39(1)	S
5157.56		−2.52(2)		I
5161.39	−2.79(2)	−2.52(2)	−2.39(4)	S
		RX J0541.4−0324		
5149.49	−0.60(1)	−0.76(2)	−0.90(2)	S
5151.44	−0.55(1)	−0.70(2)	−0.84(1)	S
5154.40	−0.59(1)	−0.73(4)	−0.90(2)	S
5154.67		−0.72(1)		I
5155.46	−0.58(1)	−0.73(1)	−0.88(1)	S
5155.53		−0.72(1)		I
5156.42	−0.54(1)	−0.70(1)	−0.85(1)	S
5157.47	−0.57(1)	−0.72(1)	−0.86(1)	S
5157.56		−0.71(1)		I
5159.47	−0.60(1)	−0.76(1)	−0.88(1)	S
5161.47	−0.55(1)	−0.70(1)	−0.84(1)	S
		GG Ori		
5151.48		−0.10(2)	−0.06(3)	S
5153.44	−0.31(1)	−0.13(2)	−0.05(1)	S
5154.67		−0.10(1)		I
5155.54		0.19(1)		I
5155.54	−0.03(3)	0.15(3)	0.22(2)	S
5156.49	−0.31(1)	−0.12(1)	−0.05(1)	S
5157.52	−0.30(1)	−0.11(1)	−0.05(1)	S
5157.55		−0.11(1)		I
5159.48	−0.29(1)	−0.10(1)	−0.01(1)	S
5161.42	−0.29(2)	−0.10(2)	−0.04(1)	S
		NGC 2264 Walk 134		
5149.53	0.10(1)	−0.07(1)	−0.23(1)	S
5151.45	−0.01(1)	−0.15(1)	−0.31(1)	S
5155.52	0.15(1)	−0.01(1)	−0.19(1)	S
5155.54		−0.02(1)		I
5156.48	0.22(1)	0.04(1)	−0.13(1)	S
5157.51	0.04(1)	−0.12(1)	−0.28(1)	S
5157.51		−0.12(1)		I
5161.40	0.02(1)	−0.14(1)	−0.29(1)	S

Bibliography

Antonyuk, K. A. & Rostopchina, A. N. 2009, Astrophysics, 52, 103
Artymowicz, P. & Lubow, S. H. 1996, ApJ, 467, L77+
Basri, G., Johns-Krull, C. M., & Mathieu, R. D. 1997, AJ, 114, 781
Bastian, T. S., Benz, A. O., & Gary, D. E. 1998, ARA&A, 36, 131
Baxter, E. J., Covey, K. R., Muench, A. A., et al. 2009, AJ, 138, 963
Boden, A. F., Torres, G., Sargent, A. I., et al. 2007, ApJ, 670, 1214
Bower, G. C., Plambeck, R. L., Bolatto, A., et al. 2003, ApJ, 598, 1140
Cargile, P. A., Stassun, K. G., & Mathieu, R. D. 2008, ApJ, 674, 329
Choi, M., Tatematsu, K., Hamaguchi, K., & Lee, J. 2009, ApJ, 690, 1901
Covino, E., Catalano, S., Frasca, A., et al. 2000, A&A, 361, L49
Covino, E., Frasca, A., Alcalá, J. M., Paladino, R., & Sterzik, M. F. 2004, A&A, 427, 637
Covino, E., Melo, C., Alcalá, J. M., et al. 2001, A&A, 375, 130
Damiani, F., Micela, G., Sciortino, S., & Harnden, Jr., F. R. 1994, ApJ, 436, 807
Duquennoy, A. & Mayor, M. 1991, A&A, 248, 485
Dutrey, A., Guilloteau, S., Duvert, G., et al. 1996, A&A, 309, 493
Favata, F., Flaccomio, E., Reale, F., et al. 2005, ApJS, 160, 469
Feigelson, E., Townsley, L., Güdel, M., & Stassun, K. 2007, Protostars and Planets V, 313
Forbrich, J., Menten, K. M., & Reid, M. J. 2008, A&A, 477, 267
Forbrich, J., Preibisch, T., Menten, K. M., et al. 2007, A&A, 464, 1003
Furlan, E., Hartmann, L., Calvet, N., et al. 2006, ApJS, 165, 568
Furuya, R. S., Shinnaga, H., Nakanishi, K., Momose, M., & Saito, M. 2003, PASJ, 55, L83
Getman, K. V., Feigelson, E. D., Broos, P. S., Micela, G., & Garmire, G. P. 2008a, ApJ, 688, 418
Getman, K. V., Feigelson, E. D., Micela, G., et al. 2008b, ApJ, 688, 437
Getman, K. V., Flaccomio, E., Broos, P. S., et al. 2005, ApJS, 160, 319
Ghez, A. M., McCarthy, D. W., Patience, J. L., & Beck, T. L. 1997, ApJ, 481, 378
Giardino, G., Favata, F., Silva, B., et al. 2006, A&A, 453, 241
Gimenez, A. & Margrave, T. E. 1985, AJ, 90, 358
Güdel, M. 2002, ARA&A, 40, 217
Güdel, M., Briggs, K. R., Arzner, K., et al. 2007, A&A, 468, 353
Hirth, G. A., Mundt, R., & Solf, J. 1997, A&AS, 126, 437
Hubrig, S., Stelzer, B., Schöller, M., et al. 2009, A&A, 502, 283
Isella, A., Carpenter, J. M., & Sargent, A. I. 2009, ApJ, 701, 260
Ishihara, D., Onaka, T., Kataza, H., et al. 2010, A&A, 514, A1+
Jensen, E. L. N., Dhital, S., Stassun, K. G., et al. 2007, AJ, 134, 241
Jensen, E. L. N., Koerner, D. W., & Mathieu, R. D. 1996, AJ, 111, 2431
Koch, R. H., Perry, P. M., & Kilambi, G. C. 1994, Information Bulletin on Variable Stars, 4032, 1
Kohler, R. & Leinert, C. 1998, A&A, 331, 977
Leinert, C., Zinnecker, H., Weitzel, N., et al. 1993, A&A, 278, 129
Luhman, K. L., Allen, P. R., Espaillat, C., Hartmann, L., & Calvet, N. 2010, ApJS, 186, 111
Manset, N. & Bastien, P. 2002, AJ, 124, 1089
Marilli, E., Frasca, A., Covino, E., et al. 2007, A&A, 463, 1081
Marques, J. P., Fernandes, J., & Monteiro, M. J. P. F. G. 2004, A&A, 422, 239
Marschall, L. A. & Mathieu, R. D. 1988, AJ, 96, 1956
Massi, M., Forbrich, J., Menten, K. M., et al. 2006, A&A, 453, 959
Massi, M., Menten, K., & Neidhöfer, J. 2002, A&A, 382, 152
Massi, M., Ros, E., Menten, K. M., et al. 2008, A&A, 480, 489

Mathieu, R. D., Martin, E. L., & Magazzu, A. 1996, in Bulletin of the American Astronomical Society, Vol. 28, Bulletin of the American Astronomical Society, 920–+
Mathieu, R. D., Stassun, K., Basri, G., et al. 1997, AJ, 113, 1841
Neuhaeuser, R., Sterzik, M. F., Schmitt, J. H. M. M., Wichmann, R., & Krautter, J. 1995, A&A, 297, 391
Neupert, W. M. 1968, ApJ, 153, L59+
Padgett, D. L. & Stapelfeldt, K. R. 1994, AJ, 107, 720
Prato, L., Simon, M., Mazeh, T., Zucker, S., & McLean, I. S. 2002, ApJ, 579, L99
Preibisch, T., Kim, Y., Favata, F., et al. 2005, ApJS, 160, 401
Ramírez, S. V., Rebull, L., Stauffer, J., et al. 2004, AJ, 127, 2659
Reipurth, B., Lindgren, H., Mayor, M., Mermilliod, J., & Cramer, N. 2002, AJ, 124, 2813
Reipurth, B., Lindgren, H., Nordstrom, B., & Mayor, M. 1990, A&A, 235, 197
Salter, D. M., Hogerheijde, M. R., & Blake, G. A. 2008, A&A, 492, L21
Salter, D. M., Kospal, K., Getman, K. V., Hogerheijde, M. R., & Blake, G. A. 2010, A&A, 123, in press
Simon, M., Ghez, A. M., Leinert, C., et al. 1995, ApJ, 443, 625
Simon, M. & Guilloteau, S. 1992, ApJ, 397, L47
Stassun, K. G., Mathieu, R. D., Cargile, P. A., et al. 2008, Nature, 453, 1079
Stassun, K. G., van den Berg, M., & Feigelson, E. 2007, ApJ, 660, 704
Stassun, K. G., van den Berg, M., Feigelson, E., & Flaccomio, E. 2006, ApJ, 649, 914
Stine, P. C., Feigelson, E. D., Andre, P., & Montmerle, T. 1988, AJ, 96, 1394
Testa, P. 2010, Proceedings of the National Academy of Science, 107, 7158
Torres, G., Andersen, J., & Giménez, A. 2010, A&A Rev., 18, 67
Torres, G., Lacy, C. H. S., Claret, A., & Sabby, J. A. 2000, AJ, 120, 3226
White, S. M., Pallavicini, R., & Kundu, M. R. 1992, A&A, 257, 557

Part III

Protoplanetary Dust Experiments in the Laboratory

Chapter 7

A Zero-Gravity Instrument to Study Low Velocity Collisions of Fragile Particles at Low Temperatures

We discuss the design, operation, and performance of a vacuum setup constructed for use in zero (or reduced) gravity conditions to initiate collisions of fragile millimeter-sized particles at low velocity and temperature. Such particles are typically found in many astronomical settings and in regions of planet formation. The instrument has participated in four parabolic flight campaigns to date, operating for a total of 2.4 hours in reduced gravity conditions and successfully recording over 300 separate collisions of loosely packed dust aggregates and ice samples. The imparted particle velocities achieved range from 0.03–0.28 m s^{-1} and a high-speed, high-resolution camera captures the events at 107 frames per second from two viewing angles separated by either 48.8° or 60.0°. The particles can be stored inside the experiment vacuum chamber at temperatures of 80–300 K for several uninterrupted hours using a built-in thermal accumulation system. The copper structure allows cooling down to cryogenic temperatures before commencement of the experiments. Throughout the parabolic flight campaigns, add-ons and modifications have been made, illustrating the instrument flexibility in the study of small particle collisions.

D. M. Salter, D. Heißelmann, G. Chaparro, G. van der Wolk, P. Reißaus, A. G. Borst, R. W. Dawson,
E. de Kuyper, G. Drinkwater, K. Gebauer, M. Hutcheon, H. Linnartz, F. J. Molster, B. Stoll,
P. C. van der Tuijn, H. J. Fraser, and J. Blum
Review of Scientific Instruments, **80**, 74501–74509 (2009)

7.1 Introduction

The origin of the Solar System and the formation of planets, including the enticing implications for the distribution of life in the universe, are key avenues pursued in modern astronomy by observational astronomers, theoretical physicists, and to a substantially smaller extent, experimentalists. Given the unresolvable scale size at interstellar distances, the embedded environment, and the uncertainty of the dominating physical processes, it is a challenging task to understand planetary origins when applying observation techniques and theoretical modeling alone. Now recent progress in laboratory experiments has yielded insight into particle collisions during the *initial* planet formation stages (e.g. growth to millimeter-sizes), complementing observational and theoretical work while providing a repeatable and consistent recipe to describe individual particle interactions (Blum & Wurm 2008). In this chapter, we present a new laboratory instrument to test the *next* stage of coagulation theory (e.g. growth to centimeter-sizes), which is the leading scenario for planet formation that describes a collisional growth mechanism.

The scientific goals specifically target the properties of fragile, millimeter-sized ice and dust aggregates during collisions. The aggregates are analogous to the prevalent material found in protoplanetary disks around young stars and therefore are believed to be the progenitors for rocky Earth-like planets, as well as the core beginnings of gas giants like Jupiter (Weidenschilling & Cuzzi 1993; Natta et al. 2007). But until now the physical processes governing this crucial *intermediate* stage of collisional growth (from millimeter- to kilometer-sizes) have remained largely uninvestigated. The most challenging aspects to these studies involve re-creating the reduced-gravity environment for the timescales necessary to observe particle growth through collisional sticking mechanisms. In this respect, ground-based drop tower experiments (Blum et al. 2002; Langkowski et al. 2008), parabolic flight maneuvres (Colwell et al. 2008), space shuttle payload missions (Colwell & Taylor 1999; Colwell 2003), and the space-based laboratory on board the International Space Station (ISS) (Love & Pettit 2004) offer unique ways to counter the effects of the Earth's gravitational field by creating a temporary condition of weightlessness.

The indirect detection of more than 300 extra-solar planets suggests that planet formation might well be a commonly occuring process, even a fundamental by-product of star formation. In previous laboratory and micrograplity experiments, the inital growth period for silicate dust particles (up to millimeter-sizes) has already been shown to occur quickly and effectively, due to van der Waals forces, achieving a sticking probability of unity during particle collisions of low relative velocities ($v_\mathrm{c} \leq 1\,\mathrm{m\,s^{-1}}$) that result in larger, fluffy, and porous aggregate structures (Blum & Wurm 2008). Observationally, spectroscopic studies of silicate dust emission features at 10 and 20 μm emanating from a large sample of circumstellar disks around young forming stars that exhibit convincing evidence of the initial grain growth process from small, sub-micron interstellar particles up to aggregates of several microns (Kessler-Silacci et al. 2006; Furlan et al. 2006). In addition, probing these disks at longer, millimeter wavelengths reveals a slower drop-off in emission than expected for some sources, which can be explained by a population of particles that have already grown to millimeter-sizes (Lommen et al. 2007; Natta et al. 2007).

The conclusions of both observation and experiment are consistent with coagulation theory in these earliest stages, but the dominant physical processes begin to change in yet unidentified ways as particles grow larger and begin to settle within the circumstellar disk midplane. We know that once the objects reach kilometer-sizes, they possess sufficient gravitational attraction to capture and retain additional mass, kicking off a gravitationally-dominated period of runaway growth leading to planetary status (Wetherill & Stewart 1989, 1993). But how do millimeter-sized aggregates attain kilometer-sizes, and thereafter runaway growth? What are the dominant processes or conditions that allow, or prevent, particles from growing beyond centimeter sizes for which observational diagnostics are lacking? It is this *intermediate* growth stage that may be the crux to questions regarding the ease, efficiency, and proliferation of planets and planetary systems in the universe. It is also here where our physical interpretation is insufficient, and thus where we shall focus our current experimental efforts and draw comparisons to recent theoretical models.

At the intermediate growth stage, the particle size and the density of particles required to guarantee a chance collision within a 4–10 second drop tower experiment, is prohibitive to a video analysis capable of capturing an unobstructed view. Instead, a more direct design was developed to initiate and observe individual collisions. For this, parabolic flight was selected to preserve the flexibility and diversity of the experiments in 22-second intervals. Parabolic flights take place on board a specially designed Airbus A300 aircraft and are organized regularly by the European Space Agency (ESA) and the German Space Agency (DLR), and they are operated by the French company, Novespace. During each flight campaign, approximately 10–15 experiments are accomodated on 3 separate flights of 30 parabolic trajectories each. Between parabolas, regular ($1g$) horizontal flight is maintained for several minutes to give experimenters working alongside their setups a chance to quickly review the data collected and to make necessary adjustments or corrections to their setup. In total, one flight campaign offers a combined weightless (or microgravity) period of approximately 30 minutes.

To account for the low gas densities of circumstellar disks, our instrument uses laboratory pumps and a vacuum chamber. Previous experimental studies give us an idea of the aggregate structure of the millimeter-sized particles expected in the solar nebula from collisional sticking (Blum 2004; Blum et al. 2006). Observations of young disks tell us about the environment and composition, including the temperature range (30–1500 K) and the presence of ices, respectively. Our design is able to achieve cold temperatures ($\simeq$ 250–300 K) to probe dust interactions, as well as cryogenic temperatures ($\simeq$ 80–250 K) where ices may play an important role in offering additional routes to more efficient sticking processes. In addition, theoretical work reveals the kinematics in the layers of the disk at these temperatures (Weidenschilling & Cuzzi 1993). For the particle sizes that we wish to study, the aggregates are just beginning to de-couple from the pressure-supported gas that has governed their motion up to this point and kept them suspended higher in the disk atmosphere. This growth causes them to sink toward the dense mid-plane of the disk, giving the larger particles a non-zero relative velocity with respect to the other (smaller) particles still coupled to the turbulent gas. This defines the collision velocities expected, on the order of $0.10\,\mathrm{m\,s^{-1}}$, for the planet-forming regions we are studying (Weidenschilling & Cuzzi 1993; Weidenschilling 1997). These velocities do, however, present a great challenge to ground-based studies where the Earth's gravitational field makes relative particle velocities of $\ll 1\,\mathrm{m\,s^{-1}}$ very hard to achieve, and where it may prevent, or favor, sticking processes unrealistically.

In October 2006, we proved our experimental setup during ESA's 45th Parabolic Flight Campaign on the Novespace premises at the Bordeaux-Merignac airport in Bordeaux, France. Additional flight campaigns followed, including the November 2007 (ESA and DLR) campaigns and the April 2008 DLR campaign, all also held in Bordeaux. This paper reports on the instrument design. In Section 7.2 we describe the separate components of the experiment, in Section 7.3 we report on the instrument performance in microgravity, and in Section 7.4 we offer a short summary of some preliminary results for the purpose of illustrating the effectiveness of the instrument with respect to our scientific goals.

7.2 Experiment Design Overview

The science goals driving our experiment design are the collisional properties of fragile, millimeter-sized, protoplanetary dust and ice analogs in young circumstellar disks. To obtain a large statistical sample of this collision behavior in a simulated early protoplanetary disk environment, a particle storage and cooling system built from copper (Section 7.2.1) was developed to fit inside a cylindrical vacuum chamber (of diameter 250 mm and height 290 mm), and to operate over a broad range of cold (250–300 K, for protoplanetary *dust* analogs) and cryogenic temperatures (80–250 K, for protoplanetary *ice*

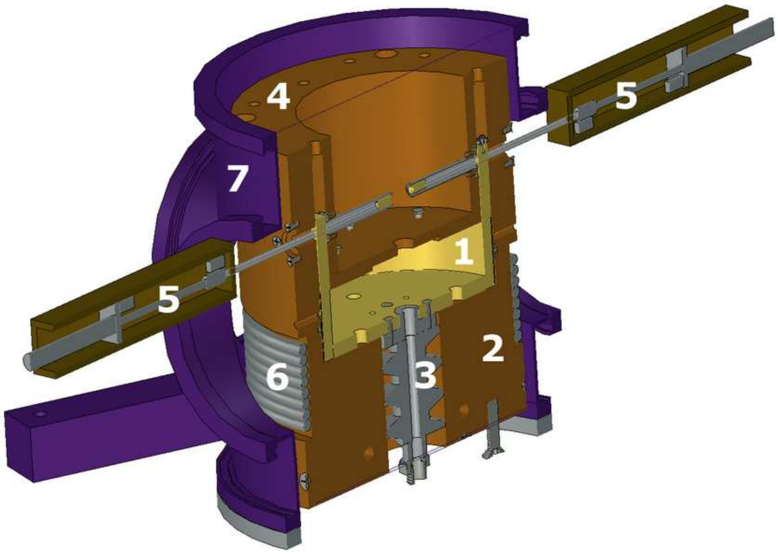

Figure 7.1 — A CAD schematic showing a cut through the center of the experiment chamber. The particle storage device (1) sits on top of the thermal reservoir (2) built of copper. The particle storage unit rises up and down with a cork-screw system (3) to rotate additional particles into the fixed line of fire. A copper shield (4) protects the storage device from thermal irradiation. The two "firing" pistons of the particle acceleration system stretch from opposite sides beginning outside the side flanges and continuing toward the center of the chamber (5). The whole system is chilled through contact with a copper tubing (6) that contains a flow of liquid N_2. The entire instrument is situated within a vacuum chamber (7). Collisions are monitored from above with the image acquisition system via a transparent viewport on the top flange.

analogs). A hydraulically-driven, synchronized particle acceleration system rapidly initiated collisions during the initial flight, but was later replaced by two synchronized electrical DC-motors operating in a master-and-slave configuration (Section 7.2.3). For the purpose of the experiments, the functionality of these setups are identical in every way, differing only in the synchronization design. Both acceleration systems specify the velocity and trajectory of two separate dust or ice analogs approaching from opposite directions so that the projectiles either collide simultaneously with a removable, dual-sided, centrally-located dust/ice target (Section 7.2.4), or with one another within the field of view of a high-speed, high-resolution imaging and data recording system (Section 7.2.5). Finally, the vacuum chamber and the support equipment were fit into two separate aluminum-strut support racks to be placed on board the parabolic flight aircraft, according to safety guidelines. A blueprint of the overall experiment design is shown in Figure 7.1 and the following sections describe the separate components and capabilities in greater detail.

7.2.1 Particle Storage and Cooling

An original design for particle storage was engineered based on the requirements that the setup is capable of operating at low and cryogenic temperatures, possesses fast and controlled collision reloadability, obeys physical size restrictions, has maximum sample capacity, and is in accordance with safety regulations for parabolic flights. The result is a cylindrical storage device, or particle reservoir, built from copper (see Figure 7.2). It has a diameter of 180 mm and stands 110 mm high. In the upper half of the reservoir we drilled 180 identical, cylindrical compartments (each of diameter 8 mm and depth 9 mm) situated at regular intervals (separated by a turn of 12.5°) in a double-helix pattern, such that each hole is aligned exactly opposite a corresponding hole. When fully loaded in this configuration, 90 separate collisions between fragile particles (or 180 collisions of particles and central target) can be performed. During the 2007 and 2008 follow-up flights, an additional storage chamber of the same dimensions was designed to hold 64 compartments of slightly larger volume (for 32 collision pairs). The 64 holes have a diameter of 16 mm with a 24° turning separation. Built this time of aluminum, the new particle storage device can be easily swapped for the original to probe the collision properties of larger particles, up to 15 mm.

On the lower half of the copper reservoir exterior, below the storage compartments, vertical grooves were cut into the copper (see Figure 7.2). This way a small gear (20 mm in diameter and 10 mm high), situated to the side of the storage unit, and possessing the same groove pattern as the storage unit, can be used to turn the selected reservoir unit (automatically or manually) with a hand wheel that passes out of the chamber through the bottom flange. Later, due to difficulties operating the small gear at cryogenic temperatures (80–250 K), the rotation of the sample repository was revised, such that the handwheel now directly couples to the brass-made cork-screw system (see Figure 7.1, label 3) with a double-Cardanic joint to prevent canting. For this reason, a similar groove pattern was no longer necessary on the bottom half of the aluminum version of the storage unit.

Since cryogenic liquids and pressurized vessels are prohibited during flight, it was necessary to devise a thermal accumulation system to achieve, and maintain, cold and cryogenic temperatures for several uninterrupted hours. A copper construction was deemed most suitable based on copper's high heat capacity per unit volume, high thermal conductivity, and ease of manufacturing for adjustments and customization. Thus, the copper *particle* reservoir is situated on top of a 45 kg copper *thermal* reservoir, or copper block (see label 4 in Figure 7.3). The two reservoirs (particle and thermal) fit together via a custom-made, quintuple thread (essentially a large screw of diameter 30 mm and length 70 mm), which is firmly attached to the bottom of the particle reservoir and fits a hollowed out groove in the thermal block. The thread steadies the particle reservoir as it raises out of, or lowers into, the thermal block during rotation (supporting a height change of 5 cm). This vertical movement allows us to increase the storage capacity, by achieving a continuous, winding row of samples that completes two rotations of the

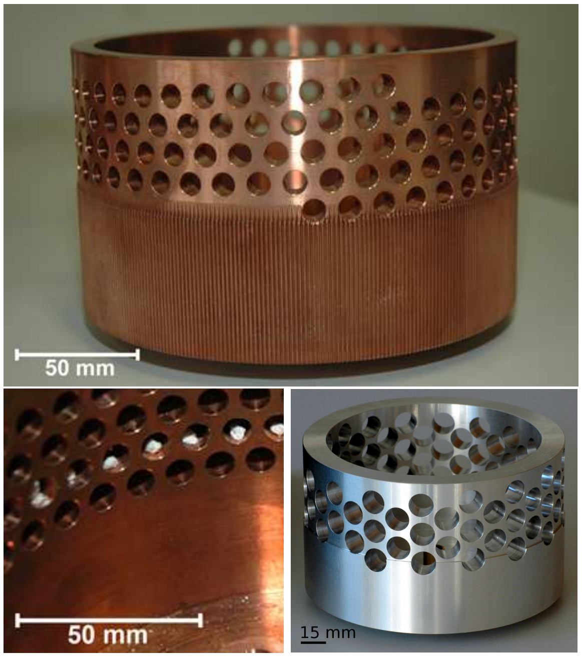

Figure 7.2 — At top, the original copper particle storage device with the storage compartments on the upper half and the vertical grooves to fit a gear on the lower half. Below left, individual compartments in one row are filled with the fragile millimeter-sized dust aggregates described in the text (see Section 7.3). At right, the aluminum version with 64 holes for larger particle collisions. The grooves are no longer necessary with the revised handwheel system (see Section 7.2.1).

reservoir. In this setup, more samples can be loaded in front of the fixed firing system during flight, all the while maintaining thermal contact between the storage device and the thermal reservoir for the duration of the experiment.

Finally, a 10 mm thin, U-shaped copper casing, or cover (label 2 in Figure 7.3), slips over the particle reservoir on top. This cover shields the storage device from external radiative warming effects, and serves to "seal" the fragile samples in their respective compartments, until primed for release. The cover is fixed to the thermal block during flight, locking the (loaded) reservoir inside and fixing the alignment. In combination with the quintuple support thread, the slip cover helps prevent the sample repository from tilting while still leaving enough vertical space within (above and below) so that the reservoir can wind up and down freely. Together the entire copper construction, shown in Figure 7.3, is then placed within the vacuum chamber atop insulation "feet" constructed from Polyetheretherketones (PEEK).

7.2.2 Cryogenic Operation

Once sealed, the vacuum chamber is pumped using the combination of a turbo-molecular pump (TMP) and a membrane pump in series. When a pressure of $< 10^{-2}$ mbar is achieved, cooling of the internal environment can commence without any significant heat transfer due to the residual gas inside the chamber. This prevents the vacuum chamber from accumulating condensation or becoming frosted on the outside. The best vacuum attainable in this setup is 10^{-6} mbar. Liquid N_2 (LN2) enters the chamber through a LN2 feedthrough on the bottom flange. It is connected on the inside to flexible copper tubing that has been molded around the thermal reservoir (label 3 in Figure 7.3). The fluid winds upwards, conductively cooling the copper tubing, the copper block, and finally the particle reservoir and radiation shield. K-type thermocouples monitor the system temperature at up to 8 separate (and distributed) locations during this process. The residual nitrogen gas and liquid that reaches the top of the coiled tube flows back out of the chamber through the second "exit" port. At no point does LN2 flow freely within the chamber itself.

Cryogenic temperatures of $\sim$80 K can be achieved with our setup using approximately 45 liters of LN2, when pumped through the flexible copper tubing for 90 minutes. Once the flow of LN2 is stopped, the system heats up at a rate of approximately $5\,\mathrm{K\,h^{-1}}$ if left unto itself under our best vacuum (see Section 7.3 for data taken during an experiment). After a completed series of experiments, but before the vacuum seal is broken, the entire system can be brought back up to 300 K by a heat rope wound around

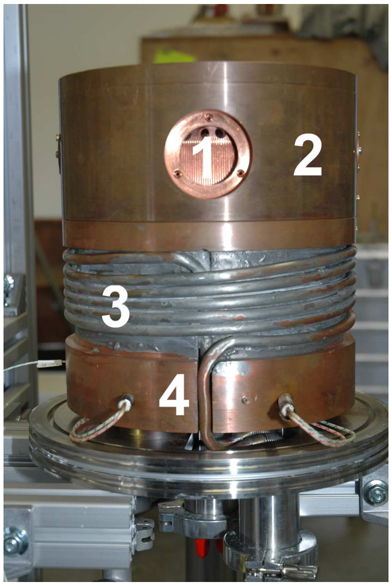

Figure 7.3 — The copper construction affixed atop the bottom flange of the vacuum chamber and isolated from the external environment by insulating "feet" constructed from PEEK. Label 1 shows a glimpse of the reservoir via the entrance portal for the firing system (see Section 7.2.3); label 2 identifies the radiation shield; label 3 indicates the copper tubing for the liquid nitrogen (LN2); and label 4 highlights the thermal block.

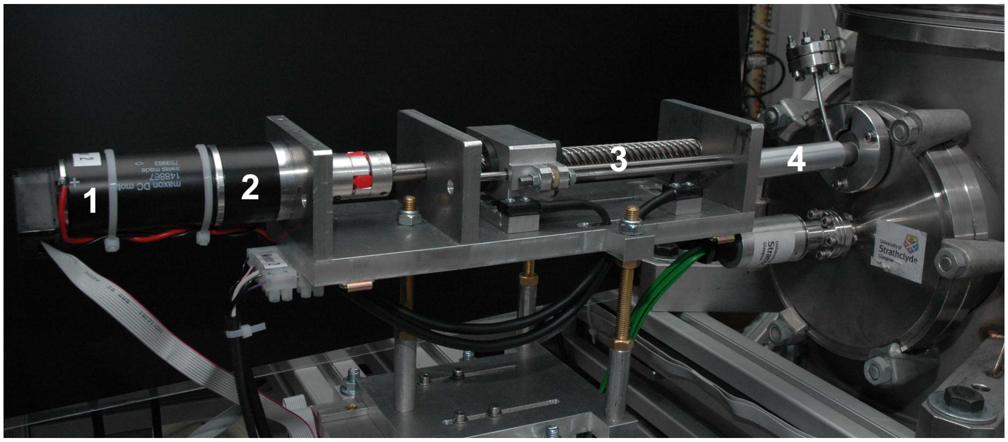

Figure 7.4 — A close-up view of one of the two pistons in the new design. The labels indicate the DC-motor (1), the gear box (2), the stainless steel lead screw (3) with both the front and back switches, and finally, the vacuum feedthrough (4) with a protective cover.

the copper base block, which is triggered via an external electrical control unit. The heat rope, which is 34 m long, has a cross-section of 3 mm and a heat output of 840 Watts.

7.2.3 Particle Acceleration System

To study astrophysically important collisions in this setup, we require: very low impact velocities, constant acceleration with no spiking due to the delicate nature of the aggregates, clean release of the particles, and precise alignment and synchronization of the trajectories to intersect within the camera's field of view. Although our fluffy and porous dust aggregates are capable of sustaining accelerations up to $100\,\mathrm{m\,s^{-2}}$, we limit the maximum acceleration of the particles to $10\,\mathrm{m\,s^{-2}}$ in order to prevent compaction, and thus preserve their astrophysical aggregate design.

In the updated design, a versatile piston driving mechanism was implemented using a master-and-slave DC-motor-system combination to replace a hydraulically-driven setup (Figure 7.4). Two synchronized pistons approach the center of the particle reservoir (and chamber) from fixed positions opposite one another. The piston back-ends extend about 0.5 meters outside the vacuum chamber and each piston rod must pass through two separate vacuum feedthroughs before finally breaching the internal environment. Thus, the additional pass-through introduces an intermediate vacuum environment by applying a chamber extension piece. This design reduces the leak rate associated with the moving parts, as the extensions can also be pumped in parallel, if necessary, although pumping proved nonessential in our construction. Inside the chamber, the stainless-steel piston rods first pass through the outer radiation shield and then through one of the storage compartments, collecting a dust or ice aggregate on each side with each concave-shaped piston head. The pistons accelerate the samples towards the center of the chamber, and one another, guided along two 80 mm long trajectory-confining tubes, before stopping abruptly (for particle detachment in cases of sticking) once the samples have achieved the intended velocity.

7.2.4 Removable Target Holder

To simulate impacts of our millimeter-sized particles against much larger protoplanetary dust aggregates, a removable target holder was crafted from copper to fit within the collision space between the two guiding tubes (see Figure 7.5). The target is 17 mm in diameter and approximately 2 mm deep. The

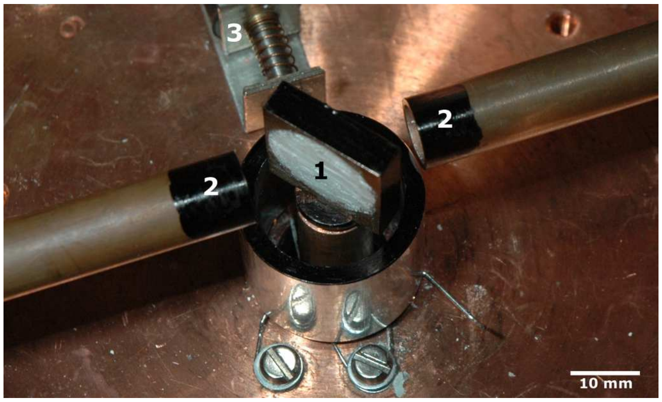

Figure 7.5 — The dust-filled target (1) is the square piece at the center of the collision space. To the left and right are the two guiding tubes (2) within which the dust aggregates are accelerated. Above center, the solenoid release mechanism (3) for the target is visible (see Section 7.2.4).

dual-sided, concave structure allows us to affix loose or compacted dust or ice samples into the mold on each side and attach the samples with vacuum grease. The embedded target sample is representative of a larger, possibly more rigid, compact, and sturdier protoplanetary aggregate or particle. The target holder itself is attached at its base to the particle storage device. This allows it to turn throughout the experiment (synchronized with the particle storage unit) and offers a wide range of impact angles to be studied, from 0° (head-on) to approximately 75° (almost glancing, but before the target is edge-on and begins to block the exits of the guiding tubes). The largest impact angles therefore place additional limitations on the total number of collisions that can be executed when the target is in place. To remove this constraint at any time during the experiment, a solenoid release mechanism allows the target holder to drop out of the way of the collision path during normal ($1g$) horizontal flight. Using a 24V DC signal, a lifting magnet is triggered to pull on a small bolt that releases the two latches that fix the target in place. Once released, and the target has dropped out of the collision space, an additional latch fixes the target in this lowered position until the vacuum chamber can be safely re-opened and the target reset manually. Then, from this point forward, only particle-particle collisions are possible.

7.2.5 Data Acquisition and Imaging

Capturing the collision events is achieved by a high-speed, high-resolution state-of-the-art CMOS camera and a recorder computer system that is capable of writing a sustained maximum data rate of $133\,\mathrm{MB\,s^{-1}}$ directly to the hard disks for an uninterrupted duration of about 33 minutes. The latter feature makes the system indispensable for parabolic flight experiments with only short breaks between the experiments, which do not provide sufficient time for a read-out of imaging systems with internal memories (either camera internal or frame grabber on-board memories).

The camera is operated at 107 frames per second (fps) and features $1280\,(\mathrm{h}) \times 1024\,(\mathrm{v})$ pixels with an 8-bit pixel depth (gray scale), a pixel size of $12\,\mu\mathrm{m} \times 12\,\mu\mathrm{m}$, a fill factor of 40%, and a Base/Full CameraLink® interface. The digital recording system is a high-performance PC system that, in this special configuration, is able to handle and store the generated data streams of the camera. Its most prominent features comprise 2 CPUs with 2.66 GHz each, a PCI-X based frame grabber with 2 GB of internal memory, and 4 SATA-I hard disks totaling 260 GB when bundled as a RAID 0 array.

The camera is mounted on top of the chamber and captures the collisions below through a transparent viewing port. Two synchronized stroboscopic Xenon flash lamps of $1\,\mu$s flash duration are mounted on the top flange and provide for shadow-free illumination of the collision volume. The flash lamps are syn-

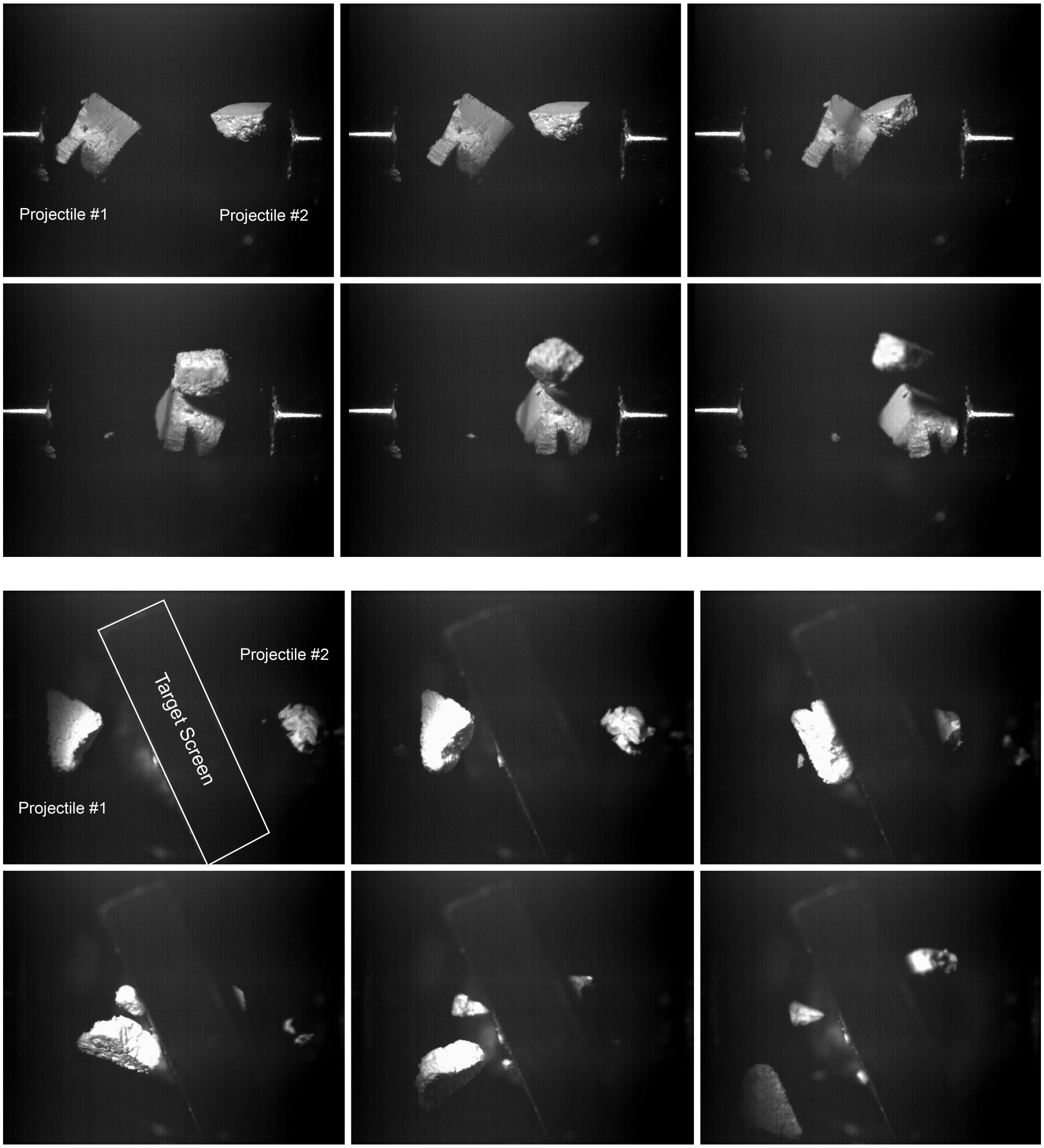

Figure 7.6 — Image sequences recorded during ESA's 45th Parabolic Flight Campaign. The sequence at top are frames showing aggregate-target dust collisions at a particle velocity of $0.2\,\mathrm{m\,s^{-1}}$ and ambient temperature. The time-series on the bottom shows an aggregate-aggregate collision at a relative velocity of $0.4\,\mathrm{m\,s^{-1}}$. All frames measure approximately 24 mm across and capture the end of the guiding tubes, which are more clearly visible in the lower sequence. In both cases, the dust aggregates do not stick, but instead rebound after the collision.

chronized with the camera via a small strobe pulse adaptor box, which reverses and amplifies the control pulses that are generated by the camera towards the illumination source. To retrieve imaging information from multiple viewing angles with only one camera, a 3D optics system was recently introduced, which uses a beam splitter placed above the collision space to capture light from two vantage points separated by either 48.8° or 60.0°. The field of view covers a horizontal grid area of approximately 24 mm × 20 mm at the focal distance. The focal depth limits the (focused) vertical range to 5 mm near the collision plane. This places limitations on ground-based testing of the setup when used for the lowest available velocity settings.

7.3 Performance in Microgravity

The system performance in microgravity proved stable, reliable, and accurate when flown at ambient (300 K) and cryogenic (130–180 K) temperatures in vacuum. Here we will focus our performance analysis entirely on the inaugural flight (October 2006), which was flown at ambient temperatures. Our fragile samples were selected to simulate dust grains in the relatively warm parts (300 K) of the protoplanetary disk. These dust aggregates were assembled from 1.5 μm monodispersed monomer SiO_2 spheres using Random Ballistic Deposition (Blum & Schräpler 2004), measured 0.2–6 mm in diameter, and were 85% porous (Blum et al. 2006) giving an approximate mass range of 0.01–3.0 g. They possessed translational velocities of 0.10–0.28 $m\,s^{-1}$ (the upper range of the available experiment velocities) as they entered the collision space, accelerated by the original hydraulically-driven piston setup. This imparted velocity range tested during the inaugural flight was slightly lower than expected from ground tests, but consistent overall. Synchronization of the particle acceleration system proved flawless and all collisions were easily observed to occur at the center of the collision volume, and within the camera's focal plane.

We began this first experiment with aggregate and target collisions of dust. Once we were satisfied with the resulting number of central target collisions, we dropped the target and proceeded to study dust aggregate-aggregate collisions. Both scenarios in this initial experiment offer important astrophysical insight into grain growth by probing two *collisional* velocity ranges (0.10–0.28 $m\,s^{-1}$ for aggregate-target collisions and 0.20–0.56 $m\,s^{-1}$, or twice the *imparted* velocities, for aggregate-aggregate collisions), as well as the influence of relative sizes (e.g. small projectile against a large target versus similarly-sized colliding aggregates). Examples of the data for both types of collision events are given in recorded image

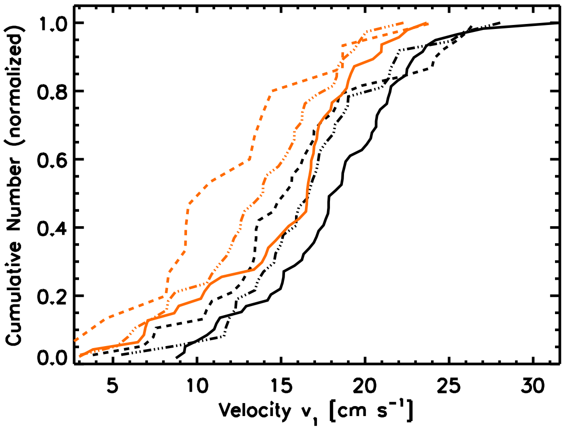

Figure 7.7 — The cumulative number of all particles in the inaugural flight with an exit velocity $\leq v_1$, using the hydraulically-driven piston setup. The solid, dotted, and dashed lines represent 3 velocity settings A, B, and C (intended to serve particles at speeds of 0.17, 0.19, and 0.20 $m\,s^{-1}$). Black and orange lines differentiate between the right and left piston. Each line is normalized by the total number of observed particles per piston at that velocity setting. For the right piston, this is 59, 37, and 38 for setting A, B, and C, respectively. For the left piston, this is 47, 38, and 15 for each velocity setting. The plot illustrates how switching to a lower velocity setting indeed results in lower velocities, and that the left-hand piston consistently delivers particles at a slightly higher speed.

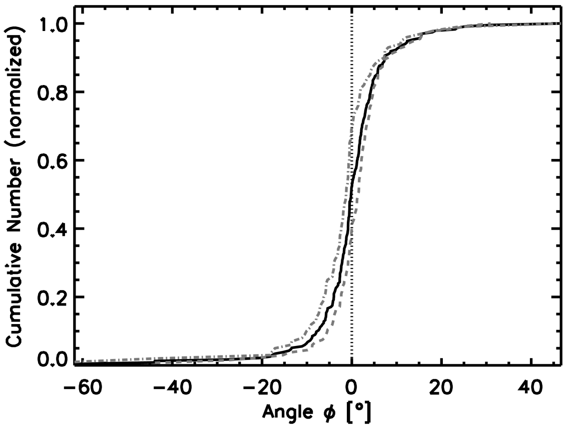

Figure 7.8 — The cumulative number of all projectiles in the inaugural flight delivered within an exit angle $\leq \Phi$. The solid line represents all particles whereas the dashed and dash-dotted curve represent the particles from the left and right piston, respectively. The distribution is very steep, showing that the angular distribution is very narrow.

sequences in Figure 7.6. In addition, the histograms in Figure 7.7 and 7.8 show the distribution of the exit velocities and angles for all particles with this setup, illustrating the accuracy and consistency of particle speeds and trajectories, as designed.

We achieved 3–4 collisions per 22-second microgravity period with manual rotation of the particle reservoir and visual verification of the alignment. This was one collision more per parabola than initially anticipated when designing and testing an automated system for exit velocities of 0.10–0.28 m s^{-1} (e.g. during our first flight in 2006). Of course, for slower exit velocities (0.03–0.15 m s^{-1}) when using larger particles in the aluminum storage unit during the follow-up campaigns, the number of possible collisions per parabola is reduced to 1–2. Ultimately, the manual rotation system proved far more reliable and flexible than the autonomous design. This was largely a result of a hand-operated turning system, which could rotate the coliseum with larger accelerations and abrupt stops during alignment.

Finally, the additional cryogenic functionality, as stated, also allows for the experimentation with interstellar ice analogs, since the abundance of ice in protoplanetary disks is high, as supported by the high abundance of icy bodies in the outer solar system, including the Kuiper-belt objects, icy moons, and comets. In the 2007 and 2008 follow-up flights, we initiated more than 64 additional collisions of (larger) dust aggregates at cold temperatures (250 K) and slower velocities, whereby 26 clean collisions could be analyzed, and the rest were contaminated either by third-party collisions with previously-fired particles remaining in the collision area, or by other complications. Finally, the experiments at cryogenic

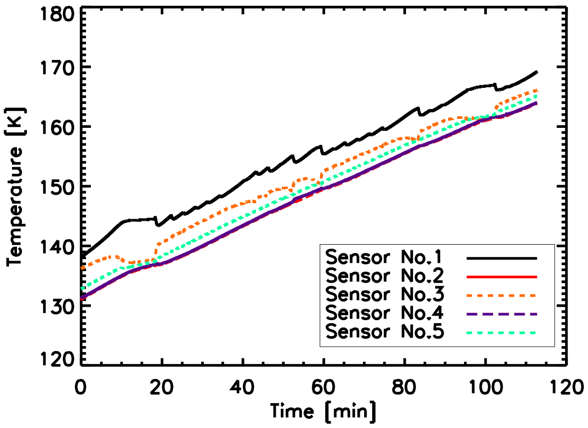

Figure 7.9 — The plot above shows how the temperature evolves during a typical parabolic flight at cryogenic temperatures and low (10^{-2} mbar) vacuum. Small fluctuations (± 4 K) result from different contact between the thermocouple and the instrument during the 0, 1, and 2*g* phases of the flight. Thus thermocouples located on top (#3) or below (#1) the structure will report mirrored fluctuations, while smaller effects are seen for thermocouples attached to the side.

temperatures (130–180 K) produced more than 113 collisions of ice particles to be analyzed.

The temperature gradients during ground-based and in-flight testing measured just a few Kelvin across the entire copper structure, even throughout pre-flight cooling of the experiment from 300 K down to 80 K via the LN2 system described in Section 7.2.2. However, due to the weak pumping capabilities available during flight, the system operated more often under a pressure of 10^{-2} mbar. This translated to a larger warm-up rate during the cold ice experiments, as shown in Figure 7.9 where the warming rate for a two-hour flight was measured to be $\sim$15 K h^{-1}. We note that the change in the initial cooling temperature of 80 K to the 130 K that was measured at the start of the experiment (Figur 7.9), is due to the time between closing of the aircraft doors and the time to reach the approved air space to perform the flight maneuver.

7.4 Conclusions

Our instrument design to probe the collisions of fragile particles at low velocities proved successful in its inaugural run at ambient temperatures (300 K) in vacuum, as well as during the follow-up campaigns at cold (250 K) and cryogenic (130–180 K) temperatures. For the ambient dust experiments in the 2006 campaign, the 6 mm in diameter and 85% porous SiO_2 aggregates possessed translational velocities from 0.10–0.28 m s^{-1}, resulting in particle-particle collisional energies of 1–5 μJ and particle-target collisional energies of 0.5–2.5 μJ. The majority of all collisions (roughly 80–90%) resulted in semi-elastic rebounding events, likely due to aggregate compaction. Fragmentation occurred in about 10% of the aggregate-aggregate collisions, but played a much smaller role during particle-target impact events. And finally, sticking was observed only in 10% of the particle-target collisions. However, the forces responsible remain unclear and warrant additional investigation. Still, the sticking and fragmentation statistics from this inaugural campaign suggest that we are probing a critical transition region for the collision velocities of dust agglomerates. And eventually it is the competition between sticking probability, fragmentation efficiency, mass exchange, and compaction behavior during encounters that helps shape disk lifetimes and the effectiveness of planet formation via grain coagulation. These early results from dust collisions at ambient temperatures exhibit the flexibility and power of this instrument in the study of particle collisions. Planned refinements to the experiments that have not yet been implemented include: icy additives of amorphous (in place of hexagonal) crystallographic structure, and the use of cryogenic temperatures ($<$ 130 K) and high vacuum.

Acknowledgements

We thank J. Barrie (University of Strathclyde), M. Costes (University of Bordeaux I), F. Gai (Novespace), J. Gillan (University of Strathclyde), E. Jelting (Technical University at Braunschweig), L. Juurlink (Leiden University), M. Krause (Technical University at Braunschweig), A. Orr (ESA), C. Sikkens (Nijmegen University), the Department of Molecular and Laser Physics of the Radboud University for their donation of the vacuum chamber, and the members of the ESA Topical Team: PhysicoChemistry of Ices in Space, ESTEC Contract No: 15266/01/NL/JS.

The ICES experiment was co-funded by the German Space Agency (DLR) under grant No. 50 WM 0636, the Scottish Universities Physics Alliance (SUPA) Astrobiology Equipment Fund, University of Strathclyde Research Enhancement Fund, the Netherlands Research School for Astronomy (NOVA), and the Netherlands Institute for Space Research (SRON) under grant No. PB-06/053. The project was generously supported by Air Liquide, KayserThrede GmbH, Pfeiffer Vacuum, and VTS Ltd. DMS and GvdW thank Leids Kerkhoven-Bosscha Fonds (LKBF) for assistance in attending the first parabolic flight campaign with this instrument. We thank the European Space Agency (ESA) and the German Space Agency (DLR) for providing the parabolic flights.

Bibliography

Blum, J. 2004, in Astronomical Society of the Pacific Conference Series, Vol. 309, Astrophysics of Dust, ed. A. N. Witt, G. C. Clayton, & B. T. Draine, 369
Blum, J. & Schräpler, R. 2004, Physical Review Letters, 93
Blum, J., Schräpler, R., Davidsson, B. J. R., & Trigo-Rodríguez, J. M. 2006, ApJ, 652, 1768
Blum, J. & Wurm, G. 2008, ARA&A, 46, 21
Blum, J., Wurm, G., Poppe, T., Kempf, S., & Kozasa, T. 2002, Advances in Space Research, 29, 497
Colwell, J. & Taylor, M. 1999, Icarus, 138, 241
Colwell, J. E. 2003, Icarus, 164, 188
Colwell, J. E., Sture, S., Cintala, M., et al. 2008, Icarus, 195, 908
Furlan, E., Hartmann, L., Calvet, N., et al. 2006, ApJS, 165, 568
Kessler-Silacci, J., Augereau, J.-C., Dullemond, C. P., et al. 2006, ApJ, 639, 275
Langkowski, D., Teiser, J., & Blum, J. 2008, ApJ, 675, 764
Lommen, D., Wright, C. M., Maddison, S. T., et al. 2007, A&A, 462, 211
Love, S. G. & Pettit, D. R. 2004, in Lunar and Planetary Institute Conference Abstracts, Vol. 35, Lunar and Planetary Institute Conference Abstracts, ed. S. Mackwell & E. Stansbery, 1119
Natta, A., Testi, L., Calvet, N., et al. 2007, in Protostars and Planets V, ed. B. Reipurth, D. Jewitt, & K. Keil, 767–781
Weidenschilling, S. J. 1997, Icarus, 127, 290
Weidenschilling, S. J. & Cuzzi, J. N. 1993, in Protostars and Planets III, ed. E. H. Levy & J. I. Lunine, 1031–1060
Wetherill, G. W. & Stewart, G. R. 1989, Icarus, 77, 330
Wetherill, G. W. & Stewart, G. R. 1993, Icarus, 106, 190

Nederlandse Samenvatting

In de 18e eeuw werd duidelijk dat de planeten in ons zonnestelsel allemaal in dezelfde richting rond de zon draaien en in hetzelfde baanvlak. Dit bracht verscheidene Europese filosofen ertoe te opperen dat ons zonnestelsel gevormd moest zijn in een platte, roterende schijf. Meer dan 200 jaar later, en met name in de jaren 60 en 70 van de vorige eeuw, begonnen sterrenkundigen die zich gespecialiseerd hadden in stervormingstheorieën te beseffen dat het overblijvende materiaal van dit proces zich in een schijf rondom de centrale ster moet bevinden, een zogenaamde circumstellaire schijf. In de daarop volgende decennia leidden steeds betere telescopen en instrumenten tot de ontdekking van deze schijven rond jonge, vormende sterren en bleek bovendien dat deze schijven alom vertegenwoordigd zijn. Het doorslaggevende en indrukwekkendste bewijs voor het bestaan van circumstellaire schijven kwam wellicht van de Hubble Ruimte Telescoop, die in 1993 afbeeldingen maakte van een aantal schijven in silhouet (Figuur 1). Deze circumstellaire schijven van gas en stof, met afmetingen vergelijkbaar met ons zonnestelsel, worden proto-planetaire schijven genoemd, omdat ze het materiaal vasthouden waaruit planeten gevormd kunnen worden. Deze ontdekkingen hebben veelbelovende implicaties voor het bestaan van andere planeten en van leven in het heelal.

Vlak nadat zo het veelvuldig voorkomen van proto-planetaire schijven was vastgesteld, volgde in 1995 de eerste indirecte ontdekking van een planeet rond een verre zonachtige ster. In de 15 jaar die daarop volgden zijn meer dan 500 mogelijke planeten gevonden met zowel directe als indirecte methodes. Indirecte ontdekkingen komen het vaakst voor, aangezien de planeten zelf veel te zwak zijn om direct

Figuur 1 — Vier proto-planetaire schijven in de Orion Nevel, hier getoond in silhouet. De grootste schijf heeft een doorsnede van 800 AE, waarbij 1 AE (ongeveer 150 miljoen kilometer) de afstand is van de aarde tot de zon. Deze foto is in 1993 genomen door de Hubble Ruimte Telescoop. (*Credit: C.R. O'Dell of Rice University / NASA*)

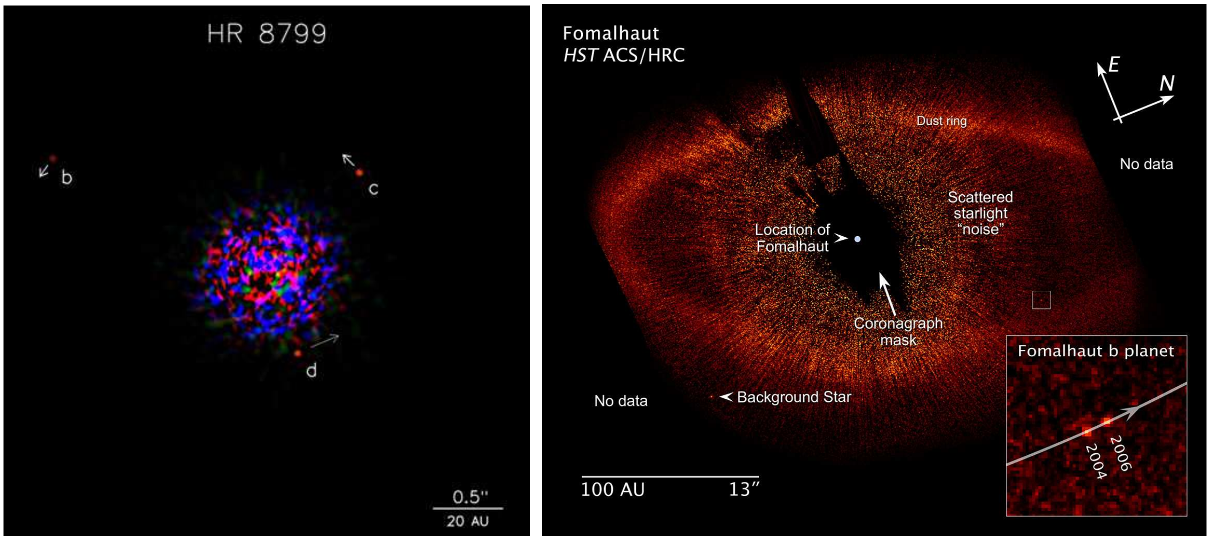

Figuur 2 — De eerste directe afbeeldingen van een exoplaneet. Links: de ster HR 8799 en drie dichtbijstaande mogelijke planeten, aangegeven met b, c en d. (*Credit: Gemini Observatory / NRC / AURA / Marois et al. 2010*). Rechts: opnamen met tussenposen van 2 jaar (2004 en 2006) met de Hubble Ruimte Telescoop van de ster Formalhaut. Hierop is een mogelijke planeet zichtbaar in zijn baan op grote radiële afstand. Deze afbeelding is gemaakt met coronografische technieken, die het licht van de centrale ster afdekken. Dit leidt tot het 'gat' in het midden van de afbeelding, waar de ster zich zou moeten bevinden. (*Credit: NASA / ESA / P. Kalas van de Universiteit van Californië te Berkeley*).

te kunnen worden waargenomen naast hun felschijnende ster. Zulke methodes bestaan bijvoorbeeld uit het ontdekken van een 'wiebelende' ster veroorzaakt door de omlopende planeet, of een periodieke dip in de helderheid van een ster als de planeet in zijn omloopbaan voor de ster langs gaat. De eerste methode vindt vooral zware planeten, vaak met massa's groter dan Jupiter, die erg dicht bij hun ster staan. De tweede methode kan alleen planeten vinden die in onze gezichtslijn de planeet passeren, en die groot genoeg zijn om een groot gedeelte van het sterlicht te blokkeren. Geen van beide methodes is waterdicht en de bevestiging van de mogelijke planeet kan vele jaren (of decennia) in beslag nemen, afhankelijk van de omlooptijd van de planeet en de technieken die gebruikt kunnen worden om de massa en samenstelling van de planeet te bepalen. Directe waarnemingen van een planeet daarentegen vangen licht op van de planeet zelf, en dit werd pas mogelijk in 2008. Figuur 2 laat twee voorbeelden zien van inventieve waarneemtechnieken, waarbij het licht van de ster wordt afgedekt om de lichtzwakke planeet zichtbaar te maken.

De meeste van deze zogenaamde exoplaneten verschillen erg van de planeten in ons eigen zonnestelsel, en zijn zelfs in strijd met de traditionele theorieën over hoe planeten vormen. Veel van de grote vragen binnen de sterrenkunde—en in dit proefschrift—hebben betrekking op het identificeren van de fysische en chemische processen die proto-planetaire schijven omvormen tot de grote variëteit in planetenstelsels die we vandaag om ons heen zien, inclusief de vraag waarom sommige schijven geen enkele planeet lijken te produceren.

1 De vorming van sterren als de zon

Lang werd gedacht dat sterren eeuwig en onveranderlijk aan de hemel staan, maar inmiddels weten we dat ook zij een levenscyclus doorlopen. Ze worden geboren, worden ouder en gaan uiteindelijk dood. Het onderzoek in dit proefschrift richt zich op de processen die vooraf gaan aan de geboorte van een nieuwe ster, die een tijdsbestek van meer dan 10 miljoen jaar in beslag kunnen nemen. Omdat niet alle sterren een zelfde geboorteproces doormaken, specialiseren wij ons hier tot sterren met een massa vergelijkbaar met de zon. Deze lage-massa sterren variëren in massa van 0,5 tot 2,0 keer de massa van de zon $M_\odot$, met $M_\odot = 2 \times 10^{30}$ kg.[1] Als lage-massa sterren nog in vorming zijn, worden deze voorlopers van de zon ook wel T Tauri sterren genoemd.

Voor stervorming is een grote voorraad gas en stof nodig, meer nog dan de massa van de uiteindelijke ster, omdat veel materiaal verloren gaat tijdens het vormingsproces. Gemiddeld bevat de interstellaire ruimte ongeveer 1 deeltje per cm^3, wat de ruimte tussen de sterren tot de dichtst mogelijke benadering van een perfect vacuüm maakt, zelfs al is deze ruimte verre van leeg. Om een klomp gas en stof gravitationeel instabiel te laten worden zodat hij instort is een dichtheid nodig van 10^5 deeltjes per cm^3. Ter vergelijking: de atmosfeer op aarde bevat 10^{19} deeltjes per cm^3. Soms, als een ster aan het eind van zijn leven explodeert in een supernova, kan een nabije gaswolk door de schokgolf van de explosie samengeperst worden, waardoor de dichtheid in het gas toeneemt en de vorming van een nieuwe generatie van sterren kan beginnen.

Er is genoeg materiaal beschikbaar om een enkele ster te vormen, als een bolvormige, gravitationeel gebonden wolk van gas en stof een dichtheid heeft zoals hierboven beschreven en een omvang van ongeveer 2×10^5 Astronomische Eenheden (AE), waarbij 1 AE (ongeveer 150 miljoen km) gelijk is aan de afstand van de aarde tot de zon. Om in te kunnen storten moet het materiaal in de wolk extreem koud zijn, zo'n 10 K ($-263\,^\circ$C), om de inwendige druk door de aanwezige hitte te overkomen. Het instorten zelf begint van binnenuit en materiaal van grotere en grotere straal wordt naar het centrum getrokken. De instortende wolk begint te roteren, en de rotatie neemt toe naar mate de wolk kleiner en compacter wordt. Dit is te vergelijken met een schaatser die tijdens een pirouette haar armen en benen intrekt om sneller rond te kunnen draaien. Deze rotatie heeft twee belangrijke gevolgen, namelijk dat de instortende wolk afplat en dat de individuele gas- en stofdeeltjes in de wolk genoeg rotatie-energie verzamelen om in een baan rond de zich vormende ster te blijven draaien in plaats van erop te vallen. Zo is een proto-planetaire schijf ontstaan als een logisch en natuurlijk gevolg van een stergeboorte.

2 De geboorteplekken van planetaire stelsels

Hoewel proto-planetaire schijven een intrinsiek gevolg zijn van het stervormings proces hoeft dit niet te betekenen dat planeten dat ook zijn. Onder welke omstandigheden planeten vormen, of juist niet, blijft onduidelijk. Uiteindelijk zal dit afhangen van een directe competitie tussen de tijd die de schijf nodig heeft om uit elkaar te vallen (of om al zijn massa kwijt te raken), en de tijd die de planeet nodig heeft om te vormen.

Schijven komen in vele vormen en afmetingen voor, afhankelijk van de verschillende stadia in hun formatiegeschiedenis. Eerst heeft de schijf een afmeting van een paar honderd AE en is zijn massa grofweg gelijk aan 5% van die van de centrale ster. In de loop der tijd wordt de schijf dunner en neemt de totale massa af. Dit zorgt voor een levensspan van een paar miljoen jaar voor de schijf, wat de belangrijkste beperking aan de vorming van een planeet is. Er zijn verschillende mogelijkheden voor een schijf om zijn materiaal te verliezen, maar één ding is duidelijk: de leeftijd van de ster is niet de belangrijkste factor voor de snelheid waarmee de schijf oplost. Stoffige schijven rond koele sterren leven zelfs 2–3 keer langer dan rond hetere sterren, wat betekent dat andere eigenschappen van de centrale ster een belangrijke rol kunnen spelen om de levensloop van de schijf te verlengen. Aan de andere kant lijkt ook de snelheid waarmee planeten vormen te variëren in verschillende schijven. Modellen van planeetvorming en statistieken van exoplaneten suggereren beide dat schijven met een hogere stof/gas ratio sneller planeten vormen, wat zou betekenen dat ook de samenstelling van de schijf grote invloed

---

[1] Om grote getallen uit te drukken gebruiken sterrenkundigen exponenten zoals 10^{30} om aan te geven dat de 10 nog 30 keer met zichzelf vermenigvuldigd moet worden.

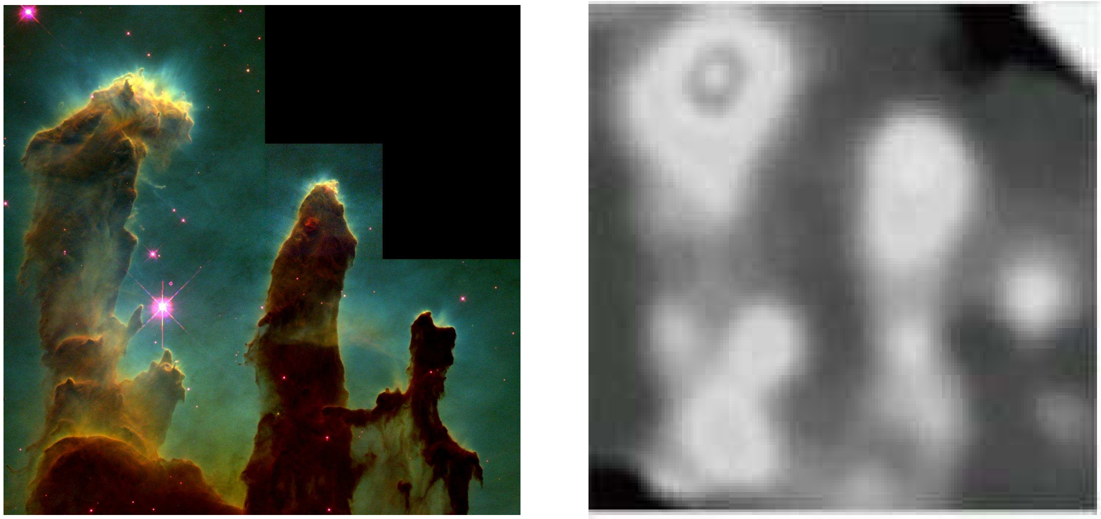

Figuur 3 — De kraamkamers van de sterren. Links: afbeelding van de Adelaarsnevel, getiteld “Zuilen der Schepping”, door de Hubble Ruimte Telescoop in 1995. In de zuilen bevinden zich jonge sterren in wording. (*Credit: NASA / ESA*). Rechts: dezelfde zuilen, maar nu afgebeeld op langere millimeter golflengten (en daardoor met lagere resolutie) door de JCMT schotelantenne op Mauna Kea in Hawaï. (*Credit: Scott et al. 2010*).

heeft op het proces van planeetvorming. Deze twee voorbeelden laten mooi het contrast zien tussen de invloed van de samenstelling van de schijf (omgeving) en de invloed van de evolutie van de ster (ontwikkeling) op de vorming van planeten: hier kunnen we dus spreken van een ‘nature vs nurture’ vraagstuk.

Om onderscheid te kunnen maken tussen deze twee invloeden moeten we begrijpen wat de ratio en de verdeling van het gas en stof in de schijven zijn, en hoe deze misschien zelfs onafhankelijk van elkaar veranderen als functie van tijd. Zo vindt bijvoorbeeld het ontbinden van de schijf plaats van binnen naar buiten, waarbij eerst een gat rond de centrale ster wordt gevormd dat zich naar buiten toe uitbreidt. Zulke gaten in schijven zijn inderdaad waargenomen rond verscheidene jonge sterren als gekeken wordt naar het stof. Dit zou dus kunnen duiden op een grotere invloed van de ster (‘nurture’), maar het kan ook zijn dat we de eerste stappen zien voor de vorming van een planeet, waarbij het stof is opgeveegd door een niet zichtbare proto-planeet. Er is dus geen eenduidig antwoord te geven, zeker niet als we niet weten wat de eigenschappen van de ster zijn die invloed hebben op de schijf, of wat de belangrijkste mechanismen zijn om een schijf uit elkaar te laten vallen, waarbij het stof misschien makkelijker is kwijt te raken dan het gas. Waarnemingen van het gas in proto-planetaire schijven kunnen ons helpen na te gaan welke processen zich afspelen in de schijf zelf, zeker als we deze combineren met waarnemingen van het stof. Daarom is het waarnemen van moleculair gas het belangrijkste doel in twee van de waarneemprojecten die in dit proefschrift beschreven worden. Grote statistische studies naar het stof in proto-planetaire schijven hebben laten zien dat in sommige schijven het stof gelijktijdig verdwijnt. Hier zijn verschillende verklaringen voor, waaronder de beginomstandigheden van de schijf (‘nature’), of andere invloeden van buitenaf die de schijf als geheel beïnvloeden en niet zoals de centrale ster vooral het binnenste gedeelte van de schijf verhitten.

In de meeste gevallen is het waarnemen van stof onze enige mogelijkheid om iets te weten te komen over het vormen van planeten in de schijf. Maar de schijf bestaat typisch slechts voor maar 1% uit stof (koolstof en silicium), terwijl de overige 99% uit koud gas bestaat (vooral waterstof en helium). Het is daarom van groot belang dat we ook het gas in de schijf waarnemen, wat een stuk gecompliceerder blijkt te zijn dan voor het stof (zie Sectie 3.3). Pas vrij recentelijk is het mogelijk geworden om de fysische en chemische evolutie van de gasschijf vast te stellen. Uit deze studies blijkt dat schijven opvallende verschillende gas en stof structuren hebben. Aanvullende studies naar het gas, zoals gepresenteerd in het eerste deel van dit proefschrift, kunnen licht werpen op de processen die relevant zijn voor zowel de verspreiding van het stof als het gas, en hoe deze processen met elkaar verbonden zijn.

3 De studie naar proto-planetaire schijven

Omdat de tijdschalen waarmee we hier te maken hebben erg lang zijn (enkele miljoenen jaren), gebruiken we statistische studies van een groot aantal proto-planetaire schijven die zich in verschillende stadia van ontwikkeling bevinden. Op deze manier kunnen we de complete evolutie van deze schijven in kaart brengen. We vinden ze in wolken van gas en stof die een hoge dichtheid hebben en waar op grote schaal stervorming plaats vindt. Hoe dichterbij deze wolken zijn, hoe makkelijker ze in detail zijn waar te nemen. Voorbeelden van zulke dichtbijstaande stervormende wolken zijn het Taurus-Auriga stervormingscomplex, de Orionnevel en ρ Ophiuchus. Een wat verderweg staand voorbeeld is de Adelaarsnevel in het sterrenbeeld Serpens, zie Figuur 3. Als we de schijven in één stervormende wolk bestuderen, hebben we een uniforme selectie van schijven, die allemaal in een zelfde omgeving ontstaan zijn, onder dezelfde omstandigheden. Dit is ideaal voor het bestuderen van evolutionaire effecten op de planeetvorming. In dit proefschrift kijken we daarom naar het stervormingscomplex in Taurus.

3.1 Instrumenten voor millimeter golflengtes

Al de waarnemingen gepresenteerd in dit proefschrift komen uit het millimeter golflengtegebied. In Figuur 4 geven we een overzicht van de verschillende soorten elektromagnetische straling, ook wel ‘licht’ genoemd. Het zichtbare licht is dat gedeelte van het spectrum dat wij met onze ogen kunnen waarnemen,

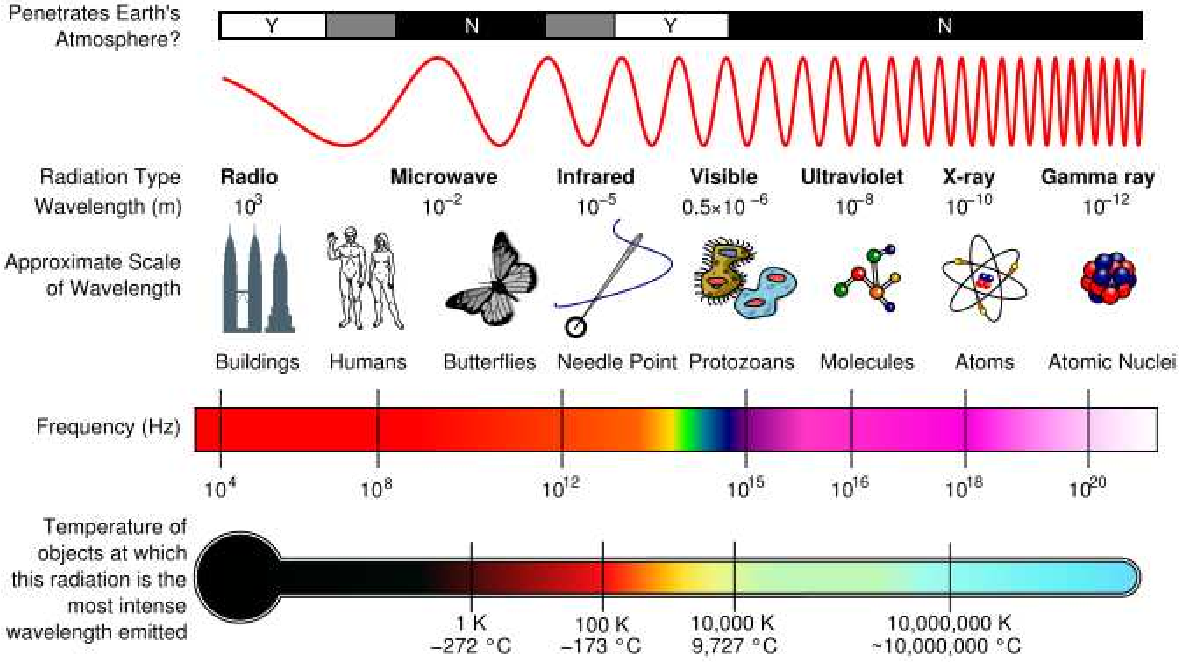

Figuur 4 — Het elektromagnetische spectrum. Zichtbaar licht maakt maar een klein deel uit van het hele spectrum van elektromagnetische straling, ook wel bekend als licht. Merk op dat langere golflengtes koudere objecten in kaart brengen, en hoe dit uiteinde van het spectrum geassocieerd wordt met lage-energie processen.

Figuur 5 — Een kunstenaarsimpressie van de oorspronkelijke visie voor de Atacama Large Millimeter / submillimeter Array (ALMA), gelegen op het Chajnator platform in de Atacama woestijn in Chili. ALMA wordt nu klaar gemaakt voor gebruik en zal eind 2011 haar eerste resultaten prijs geven, als de eerste 16 van de geplande 66 antennes in gebruik worden genomen. (*Credit: ESO*)

terwijl de millimeter golven waar we in dit proefschrift bij stil staan tot de straling behoort met langere golflengtes. Alle voorwerpen zenden zelf straling uit, afhankelijk van hun temperatuur. In Taurus variëren de protoplanetaire schijven in temperatuur van 10 K (−263 °C) in het middenvlak tot 500 K (226 °C) aan het oppervlak. Dit houdt in dat het grootste gedeelte van de straling die de schijf uitzendt in het millimeter gebied zal zijn.

Om straling met langere golflengtes waar te nemen zijn ook grotere telescopen nodig, als we dezelfde resolutie of mate van detaillering willen halen als mogelijk is in het zichtbare licht (zie Figuur 3). Ter vergelijking: de grootste optische telescopen zijn ongeveer 8–10 meter in doorsnee en de Hubble Ruimte Telescoop heeft een spiegel met een diameter van 2,4 meter. De JCMT millimeter telescoop op Mauna Kea in Hawai (zie Hoofdstuk 2) heeft daarentegen een schotel met een doorsnede van 15 meter, terwijl de IRAM telescoop op Pico Veleta in Spanje (Hoofdstuk 6) met zijn 30 meter doorsnee de op een na grootste millimeter schotelantenne ter wereld is. Nog grotere telescopen bouwen die ook nog wendbaar zijn is een grote technologische uitdaging. In zowel Hoofdstuk 2 als 6 zijn de schijven die we met de genoemde schotels bestuderen niet opgelost, wat inhoudt dat we geen spatiële resolutie hebben en niet kunnen onderscheiden waar in de schijf precies de straling vandaan komt. Onze waarnemingen laten dus alleen de totale uitstoot aan straling van de schijf zien, zonder de fijnere details van waar de straling precies vandaan komt. Deze schotels zijn daarom erg geschikt voor grote waarneemprojecten, waarbij heldere schijven kunnen worden geïndentificeerd en onderzocht. Toch gaat een hoop informatie verloren in de data van deze telescopen, die slechts uit één enkele schotel bestaan. Zo kan niets worden gezegd over de verdeling van het stof en gas in de schijf, terwijl we in Sectie 2 juist hebben laten zien dat dit juist belangrijk is om te begrijpen welke processen de schijf kan ondergaan.

Daarom gebruiken we een speciale techniek, interferometrie, om een hogere resolutie te bereiken. Bij

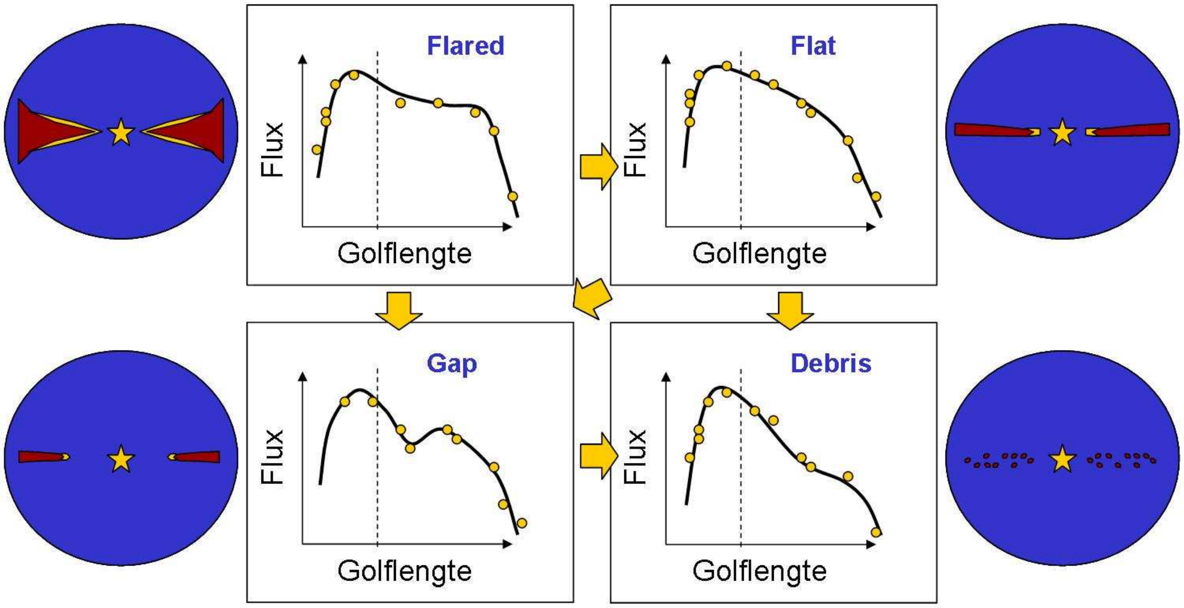

Figuur 6 — Een schematische weergave van de flux (of helderheid) als functie van golflengte voor vier verschillende schijven. Vanaf linksboven en met de klok mee zien we een uitstaande schijf (‘flared’), een afgeplatte schijf (‘flat’), een schijf bestaande uit puin (‘debris’) en een schijf met gat in het centrum (‘gap’). De punten in de grafieken zijn de metingen die we kunnen uitvoeren op een specifieke golflengte en de zwarte lijn is een fit aan deze meetpunten. Metingen links van de verticale stippellijn komen van de ster, en rechts (op langere, koelere golflengtes) van de schijf. Schijven met hogere massa, zoals de uitstaande en afgeplatte schijf zijn het helderst op langere golflengtes, terwijl schijven met een gat in het centrum meer straling op kortere golflengte uitzenden. Met pijlen is aangegeven wat mogelijke routes zijn voor de evolutie van de schijf, over de loop van enkele miljoenen jaren.

deze methode worden meerdere losse telescopen met elkaar verbonden, waardoor een virtuele telescoop ontstaat met een doorsnede van enkele tientallen meters tot soms zelfs honderden kilometers! Behalve hogere resolutie zijn er nog vele andere voordelen, zoals een verbeterde gevoeligheid en de mogelijkheid om compacte, diepgelegen concentraties van materiaal te detecteren. Voorbeelden van zulke interferometers zijn de CARMA array in oost-Californië, IRAM PdBI in de Franse Alpen, de SMA op Mauna Kea in Hawaï en de NMA in Japan. De Atacama Large Millimeter / submillimeter Array (ALMA) is de volgende generatie van interferometers, en zal de enige millimeter interferometer op het zuidelijk halfrond zijn. ALMA is op dit moment in opbouw (zie Figuur 5 voor een kunstenaarsimpressie) en zal een tot 25 keer betere resolutie halen dan de huidige interferometers, in slechts een fractie van de nu nog nodige waarneemtijd.

3.2 Stof

Hoewel het gas het grootste gedeelte van de massa van de schijf voor zijn rekening neemt (zie Sectie 2), levert het stof de belangrijkste bijdrage aan de straling die de schijf uitzendt op millimeter golflengtes. Een stofdeeltje dat straling van de centrale ster opvangt, zendt deze straling weer uit met een karakteristieke golflengte, die bepaald wordt door zijn eigen temperatuur, afmeting en emissievermogen. De totale straling van alle stofdeeltjes vormt een spectrum van flux per golflengte, dat we het stof continuüm noemen (zie Figuur 6). Dit stof continuüm, dat van het nabije infrarood tot radiogolflengtes loopt,

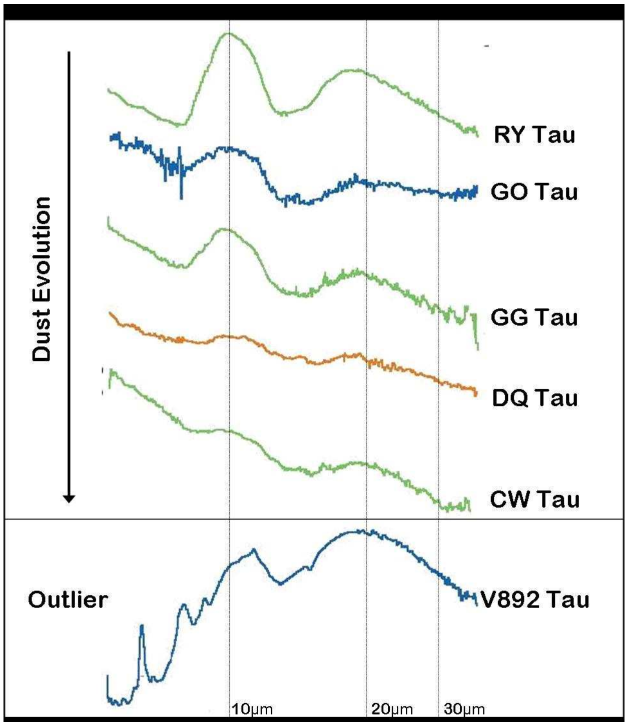

Figuur 7 — De 10μm stralingspiek van silicaat in 6 verschillende schijven in de Taurus stervormende wolk, waargenomen op nabij-infrarood golflengtes door de Spitzer Ruimte Telescoop (*Credit: Kessler-Silacci et al. 2006*). Van boven naar beneden neemt de hoeveelheid kleine stofdeeltjes aan de oppervlakte van deze schijven af, zoals bepaald door de afname in helderheid van de stralingspiek. De minder steile helling van de grafiek suggereert dat dit komt doordat de stofdeeltjes in omvang toenemen en zich in de schijf nestelen, in plaats van vernietigd te worden door verdamping.

is één van de makkelijkst te verkrijgen metingen om een schijf te kunnen classificeren. Daar komt bij dat als we meten hoeveel licht wordt uitgezonden, wat bepaald wordt door de centrale ster, dan kunnen we hieruit opmaken wat de temperatuur en dichtheidsverdeling van het stof in de proto-planetaire schijf zijn. In Figuur 6 zien we dat grotere schijven meer straling uitzenden, wat hen helderder maakt op grotere golflengtes. Dit verband is belangrijk om schijven te kunnen identificeren die grote hoeveelheden circumstellair gas en stof bevatten. Als we corrigeren voor de afstand tot de schijf (objecten die ver weg staan lijken zwakker), dan moeten de helderste schijven het meeste stof bevatten.

Behalve de structuur van de gehele schijf, kunnen we ook uit het stof continuüm opmaken wat de afmetingen van de individuele stofdeeltjes zijn. Dit is belangrijk om te kunnen bepalen in welk stadium van planeetvorming de schijf zich bevindt. Stofdeeltjes beginnen typisch als microdeeltjes (met 1 micrometer = 1 μm = 10^{-6} meters), die gemiddeld zo'n 100 keer kleiner zijn dan de doorsnede van een menselijke haar. Door het stof continuüm op millimeter golflengtes te bestuderen zijn sterrenkundigen tot de ontdekking gekomen dat stofdeeltjes in protoplanetaire schijven afmetingen hebben van enkele centimeters. Als stofdeeltjes nog meer groeien wordt het lastiger om ze te detecteren, omdat ze minder straling uitzenden en alleen op steeds langere golflengtes. Zo weten we dat stofdeeltjes in schijven inderdaad in grootte toenemen, omdat een deel van de straling van de schijf zich naar langere golflengtes heeft verplaatst. Dit kunnen we nauwkeuriger vastleggen door op millimeter golflengtes de helling te meten van het stof continuüm (ofwel, hoe snel valt de zwarte lijn in Figuur 6 af als functie van golflengte).

Behalve het stof continuüm kunnen we ook de stralingspiek van silicaat (SiO) gebruiken, die veroorzaakt wordt door de vibratie van de band die het silicium (S) en zuurstof (O) bij elkaar houdt in het SiO molecuul. De stofdeeltjes die deze piek veroorzaken moeten verhit zijn tot een temperatuur van ongeveer 500 K (226 °C). Deze stofdeeltjes moeten zich dus aan het oppervlak van de schijf bevinden, dicht bij de centrale ster. Dit zijn ook de kleinste stofdeeltjes, aangezien grotere stofdeeltjes niet goed verhit kunnen worden en dus eerder straling op langere golflengtes zullen uitzenden. De 10μm stralingspiek is dus minder prominent aanwezig als de kleinste stofdeeltjes uit de bovenste laag van de schijf verdwenen zijn, ofwel doordat ze in omvang zijn toegenomen, ofwel doordat ze verdampt zijn door de straling van de ster (zie Figuur 7). Om te bepalen welke van deze twee processen domineert (groei of vernietiging), meten we de helling van het mid-infrarode spectrum, net zoals we dat voor het stof continuüm in het millimeter gebied deden. Een kleinere helling geeft aan dat het stof zich in het middenvlak van de schijf heeft genesteld, als gevolg van de groei van de stofdeeltjes. Dit leidt tot het platter worden van de stofschijf. Het gas hoeft het stof hier echter niet in te volgen.

Aangezien er verscheidene modellen voor het gedrag van stof beschikbaar zijn in de literatuur, hebben we in dit proefschrift ons niet toegelegd op het herhalen van de studies naar stof waarnemingen. In plaats daarvan willen we het moleculaire gas in de schijven bestuderen, en zullen alleen in die context de resultaten van het onderzoek naar stof bespreken.

3.3 Gas

Het moleculaire gas in proto-planetaire schijven is een stuk lastiger waar te nemen dan de stof deeltjes. Maar zoals we hierboven al hebben besproken, maakt het gas het grootste deel uit van de schijf en is het een belangrijk ingrediënt voor de vorming van gasplaneten, zoals Jupiter en Saturnus. Het meest voorkomende molecuul in de schijven, en in het hele Heelal, is moleculair waterstof (H_2). Helaas zorgt de symmetrische structuur (twee samengebonden waterstofatomen) van dit molecuul ervoor dat het geen straling produceert door rotatie-energie die we kunnen oppikken in het millimeter gebied. In plaats van H_2 gebruiken we daarom koolstofmono-oxide (CO) als een indicator voor het koude gas. Dit is het op één na meest voorkomende molecuul in het heelal, hoewel er 10.000 keer minder CO moleculen dan H_2 moleculen zijn. Daar staat tegenover dat het wel een groot aantal sterke rotatie lijnen heeft op millimeter golflengtes, wat het één van de geschiktste moleculen maakt om koud gas in schijven waar te nemen.

In tegenstelling tot stofdeeltjes zendt gas licht uit op specifieke golflengtes, die we emissielijnen noemen. Iedere emissielijn in het millimeter gebied hoort bij één specifieke rotatie-energie. Ieder molecuul heeft een beperkt aantal energieniveaus, en verschillende types (of soorten) moleculen hebben verschillende energieniveaus en dus verschillende karakteristieke golflengtes. De energie van een molecuul neemt toe door botsingen met andere moleculen of stofdeeltjes in de schijf, waardoor het naar een hoger energieniveau kan worden gebracht. Deze energie raken ze ook snel weer kwijt door terug te vallen naar een lager energieniveau, waarbij ze straling uitzenden op een golflengte die gelijk is aan het

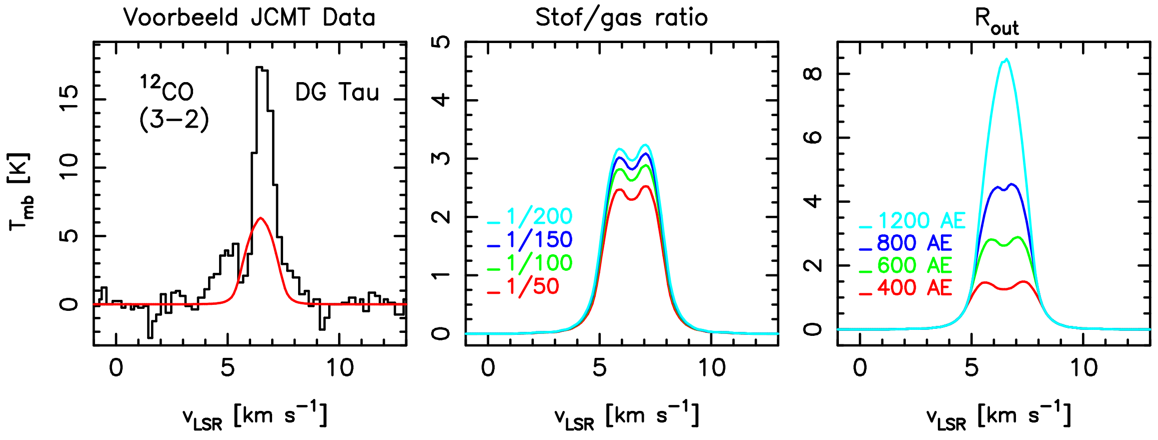

Figuur 8 — Modellen van spectra die laten zien wat voor invloed de verandering van één parameter heeft op het voorspelde lijnprofiel van een onopgeloste schijf. Van links naar rechts zien we (met de oorspronkelijk waarde tussen haakjes): een voorbeeld van een JCMT waarneming met bijdrage van een naburige systeem inclusief onze beste fit aan een theoretisch schijf model; variatie van de stof/gas ratio (1/100); en variatie van de doorsnede van de schijf (600 AE).

energieverschil tussen de twee niveaus. Om een sterke emissielijn te kunnen produceren moeten de moleculen zich in een omgeving bevinden met een geschikte combinatie van dichtheid en temperatuur. Dit houdt in dat we specifieke gebieden in de schijf kunnen bestuderen door naar verschillende moleculen of door naar verschillende emissielijnen van eenzelfde molecuul te kijken. We kunnen ook bepalen hoeveel gas van een bepaald molecuul aanwezig is, door te kijken hoe helder de bijbehorende emissielijnen zijn.

Andere eigenschappen van de schijf kunnen echter ook invloed hebben op de helderheid van een lijn. Daarom hebben we theoretische modellen nodig die voorspellen hoe de lijnprofielen van verschillende schijven eruit zien. In Figuur 8 laten we zien wat de helderheid en de vorm van de emissielijn ons kan vertellen over het moleculaire gas in de schijf. Deze modellen zijn opgesteld voor data van één schotel waardoor de schijf niet opgelost is, maar we kunnen toch informatie over de dichtheidsverdeling, de grootte en de inclinatie van de schijf uit het profiel halen. Maar als we deze parameters afzonderlijk in de modellen aanpassen, zien we dat ze eenzelfde effect op het lijnprofiel kunnen hebben. Hierdoor kunnen we bijvoorbeeld niet gemakkelijk onderscheid maken tussen een grotere schijf (grote $R_{\rm out}$) met een lagere stof/gas verhouding en een kleinere schijf (kleine $R_{\rm out}$) met een hogere stof/gas verhouding. Daarom willen we interferometrie gebruiken om de schijf op te lossen, waarmee we in dit voorbeeld de afmetingen van de schijf direct kunnen bepalen. Opgeloste waarnemingen zijn dus belangrijk, maar zoals al eerder aangegeven, worden ze nu nog begrensd door de gevoeligheid van de instrumenten waarmee we werken. Daarom richten sterrenkundigen zich vooral op de helderste objecten die ze vinden door studies met enkele schotels. Dit proefschrift bevat beide soorten waarnemingen: grote studies met een enkele schotel en gedetailleerde waarnemingen van enkele van de helderste objecten in Taurus.

3.4 Relativistische elektronen

Eén van de belangrijkste eigenschappen van de millimeter straling rond T Tauri sterren is dat deze vrijwel constant is. Dit nemen we aan als we de emissie van het stof continuüm gebruiken om de totale hoeveelheid en de verdeling van het stof rond de ster te bepalen (zie Sectie 3.2 en Figuur 6), aangezien veranderingen in de stof eigenschappen miljoenen jaren in beslag nemen. Het kwam daarom als een complete verrassing toen tijdens één van onze 8 uur durende waarnemingen één van onze bronnen plotseling 27 keer in helderheid toenam in slechts een paar uur tijd (Hoofdstuk 4). Een vergelijkbaar verschijnsel was pas drie keer eerder waargenomen. Deze plotselinge en ongewone toename in helderheid kan worden toegeschreven aan synchrotron straling: straling die uitgezonden wordt door elektronen die langs magnetische veldlijnen spiraliseren met snelheden vergelijkbaar met de lichtsnelheid. Vanwege hun zeer hoge snelheid worden deze elektronen ‘relativistisch’ genoemd.

Alle lage-massa sterren, inclusief onze eigen zon, hebben een magnetisch veld met veldlijnen die van de magnetische noordpool van de ster naar de magnetische zuidpool lopen (zie Figuur 9). In gecompliceerdere gevallen kunnen de veldlijnen ook van een magnetische noordelijke ankerpunt naar een magnetische zuidelijke voetstap leiden. Elektronen die ingevangen worden door deze veldlijnen kunnen heen en weer spiraliseren van de ene pool naar de andere (of van de ene voetstap naar de andere), terwijl ze synchrotron straling uitzenden met een karakteristieke golflengte die omgekeerd evenredig is met hun snelheid. Zo zenden langzamere elektronen straling uit op langere radio-golflengten dan snellere elektronen. Hierdoor is synchrotron straling een veel voorkomend verschijnsel voor radio, maar zeldzamer in het millimeter gebied. De verdeling van snelle en langzame elektronen is een continuüm, wat ervoor zorgt dat de synchrotron straling in een breed spectrum wordt waargenomen, vergelijkbaar met het stof continuüm in Sectie 3.2, in tegenstelling tot de gas emissielijnen van Sectie 3.3.

Door de synchrotron straling van de zon te bestuderen kunnen we de grootte van de magnetische veldlussen afschatten die de elektronen gevangen houden. Deze lussen worden in verband gebracht met zonnevlammen, die optreden als magnetische veldlijnen op het oppervlakte van de zon elkaar snijden en gedwongen worden te hergroeperen. Dit kan alleen gebeuren als de veldlijnen in tegengestelde richting

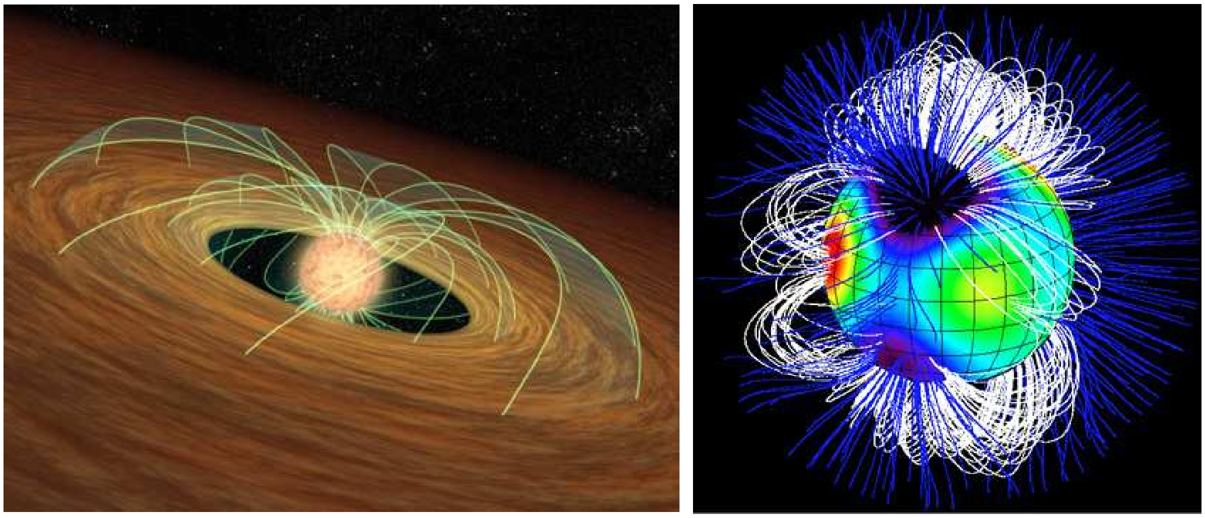

Figuur 9 — Links: kunstenaarsimpressie van stellaire magnetische veldlijnen in interactie met de circumstellaire schijf. (*Credits: NASA / JPL-Caltech / R. Hurt van SSC*). Rechts: een topografische weergave van de magnetische veldlijnen rond de ster τ Scorpio. Open veldlijnen laten toe dat geladen deeltjes, zoals elektronen en geïoniseerde moleculen, uit het systeem ontsnappen met behulp van sterwinden. Dit is ook een manier om een schijf rond een ster te laten verdwijnen. Gesloten veldlijnen geven aan waar geladen deeltjes vastgehouden kunnen worden vlak bij het oppervlak van de ster. (*Credits: ESPaDOnS / CFHT*).

lopen, omdat ze elkaar anders afstoten. Als de veldlijnen hergroeperen komt een grote hoeveelheid magnetische energie vrij, die gebruikt wordt om de elektronen in de buurt van de lus te versnellen. De elektronen verliezen vervolgens snelheid doordat ze energie kwijtraken in de vorm van synchrotron straling, totdat ze geen energie meer over hebben.

Dit proces vindt plaats op de oppervlakken van alle lage-massa sterren, inclusief sterren die zich nog aan het vormen zijn. Grote uitbarstingen van millimeter straling zijn echter zeldzaam, en worden in verband gebracht met reusachtige veldlussen, veel groter dan de typische lussen die we op de zon zien. Door deze uitbarstingen te bestuderen kunnen sterrenkundigen meer leren over de magnetische velden rond andere sterren dan de zon. Voor de studie van proto-planetaire schijven—het onderwerp van dit proefschrift—is het interessant te weten hoe vaak vergelijkbare uitbarstingen met lagere intensiteit, zonder dat we het doorhebben, onze millimeter metingen kunnen beïnvloeden en wat voor effect de bijbehorende hoog-energetische ultraviolette en röntgen stralingspieken op de chemie van de schijf kunnen hebben.

3.5 In het lab

Een andere manier om planeetvorming te bestuderen is door het laboratorium in te duiken. Hier moeten we de eigenschappen en omgeving van een proto-planetaire schijf simuleren, waaronder een hoog vacuüm, extreem lage temperaturen en een verminderd zwaartekrachtveld. Daarnaast moeten de fysische processen die we willen bestuderen kleiner zijn dan het laboratorium zelf. In dit proefschrift bespreken we de fysische uitdaging om stofdeeltjes groter te laten groeien dan enkele centimeters. Tot zover zijn theoretische studies er nog niet in geslaagd te verklaren hoe stofdeeltjes groter kunnen worden. Met een parabolische vlucht manoeuvre kunnen we gewichtsloosheid simuleren voor periodes van 22 seconden (zie Figuur 10), wat de langst mogelijke periode is van verminderde zwaartekracht die we kunnen bereiken zonder de ruimte in te gaan. In plaats daarvan blijven we op een vlieghoogte die door commerciële vliegtuigen wordt gebruikt. In deze 22 seconden van gewichtsloosheid laten we stofdeeltjes met afmetingen van enkele millimeters op elkaar botsen en bestuderen we het resultaat van die botsingen. Een

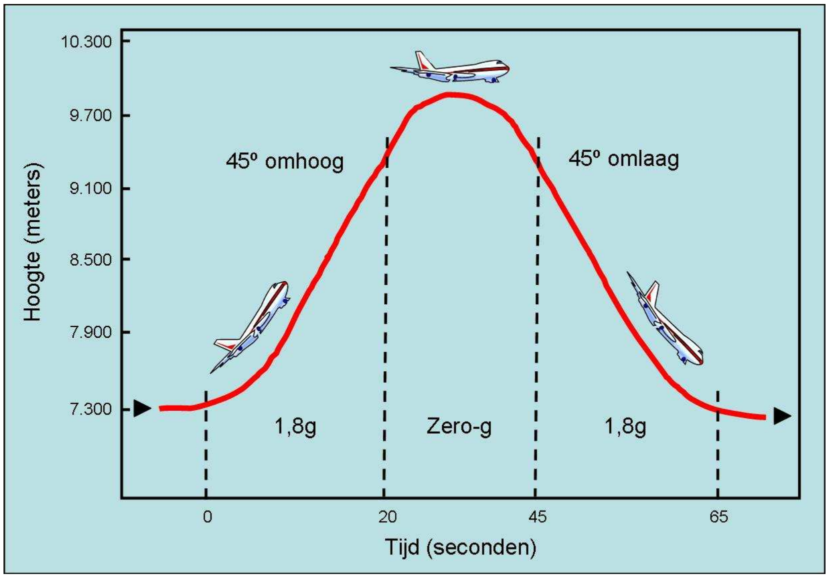

Figuur 10 — Een schematische voorstelling van het verloop van een parabolische vlucht, zoals uitgevoerd door de Europese Ruimtevaart Organisatie (European Space Agency) ESA. Een parabolische vlucht is een methode om de nul-zwaartekracht ('zero-gravity') situatie in proto-planetaire schijven na te bootsen, zodat in intervallen van 22 seconden experimenten uitgevoerd kunnen worden om de processen te testen die stofdeeltjes laten groeien in deze schijven.

dergelijk experiment op de grond uitvoeren is niet mogelijk, omdat de stofdeeltjes met lage snelheiden moeten botsen, zoals ze dat ook in de proto-planetaire schijf doen. Op aarde zouden ze echter door het zwaartekrachtsveld al op de grond zijn gevallen voordat de botsing plaats zou hebben gevonden. Op deze manier kunnen we in onze eigen laboratoria dezelfde processen van planeetvorming bestuderen, die verantwoordelijk kunnen zijn geweest voor de vorming van de aarde en de andere planeten in ons eigen zonnestelsel.

4 Dit proefschrift

Het onderwerp van dit proefschrift is de straling in het millimeter gebied die door proto-planetaire schijven rondom jonge vormende sterren wordt uitgezonden. Dit proefschrift bestaat uit drie delen.

In **deel I** bestuderen we de thermische straling van het stof en het gas in verschillende proto-planetaire schijven in Taurus. We kijken wat er met het gas in de schijven gebeurt als de stofdeeltjes in grootte toenemen en zich dieper in de schijven nestelen. In **Hoofdstuk 2** bespreken we bijvoorbeeld een groot waarneemproject met een enkele schotel, waarmee we het moleculaire gas via HCO^+, HCN en CN bestuderen. Terwijl de stofdeeltjes groeien en zich in het middenvlak van de schijf nestelen, zou het gas aan de oppervlakte van de schijf meer blootgesteld moeten worden aan de hoog-energetische UV en röntgenstraling die uitgezonden wordt door de centrale ster. Daarom verwachten we dat de hoeveelheid HCO^+ en CN toeneemt in de schijf ten koste van HCN, omdat HCN zich onder invloed van UV straling in een waterstofatoom en een CN molecuul splitst. Onze waarnemingen van 21 proto-planetaire schijven in Taurus laten echter geen verband zien tussen de gas moleculen en de eigenschappen van het stof. De eigenschappen en de evolutie van de gebieden in de schijf waar de emissielijnen van het gas vandaan komen ($R \geq 100$ AE) lijken dus niet samen te hangen met de gebieden in de schijf waar we het stof waarnemen ($R \lesssim 30$–100 AE). In **Hoofdstuk 3** presenteren we interferometrie waarnemingen van ^{12}CO van vijf stoffige schijven in Taurus. We vinden CO emissie in drie van de vijf schijven, maar onze waarnemingen kunnen niet alle straling uit de schijf vastleggen. CO is namelijk niet alleen het op één na meest voorkomende molecuul in de schijven, maar ook langs onze gezichtslijn, ofwel in de ruimte tussen ons en de schijven. Hierdoor kan het CO langs de gezichtslijn de straling van de schijven onderscheppen en verstrooien. Dit effect is het grootst voor de lagere-energie niveaus die het makkelijkst te bezetten zijn, zelfs in gebieden met lage dichtheid en temperatuur, zoals in interstellaire moleculaire wolken. We waarschuwen daarom dat de waarnemingen van de lagere rotatie lijnen van CO het gas in de schijven niet volledig traceren, en dus geen goede indicator zijn voor de evolutie van het gas in de schijven. We raden daarom aan voor toekomstige waarnemingen hogere rotatie overgangen van CO te bestuderen.

Deel II van dit proefschrift ontstond terwijl we de waarnemingen voor deel I aan het verzamelen waren en legt zich toe op de ondekking van tijdelijke uitbarstingen in het millimeter gebied, die niet geassocieerd zijn met het stof of het gas, maar met relativistische elektronen die rondom de magnetische veldlijnen van de centrale ster spiraliseren. In **Hoofdstuk 4** bespreken we de ontdekkingen van een uitzonderlijke uitbarsting bij de dubbelster DQ Tau. In **Hoofdstuk 5** bevestigen we vervolgens de zich herhalende eigenschappen van deze uitbarstingen bij DQ Tau en verklaren we deze als de botsing van de stellaire magnetische velden, wanneer de twee sterren elkaar naderen in hun baan. De uitbarstingen treden op omdat de sterren elkaar erg dicht naderen, maar ook omdat ze vervolgens weer op grote afstand van elkaar komen te staan. Dit houdt in dat hun magnetische velden gecombineerd moeten worden op het punt van dichtste nadering, maar ook weer gesplitst moeten worden als de twee sterren weer van elkaar weg bewegen. Iedere keer dat de velden zichzelf moeten reorganiseren, eerst door te combineren en daarna door te splitsen, treedt een uitbarsting op die sterk genoeg is om op millimeter golflengtes te worden waargenomen. In **Hoofdstuk 6** bestuderen we daarom het optreden van deze millimeter uitbarstingen voor een groter aantal jonge dubbelsterren met vergelijkbare banen als DQ Tau. We vinden dat een andere dubbelster, UZ Tau E, tekenen laat zien van een vergelijkbare activiteit. Onze statistieken waarschuwen tegen het traditionele idee van een constant millimeter spectrum en laten zien dat we de millimeter variëteit van jonge sterren beter moeten vastleggen, zeker als we afhankelijk zijn van een enkele fluxmeting in het millimeter gebied om de eigenschappen van het stof en de schijf te bepalen, zoals vaak het geval is voor proto-planetaire schijven.

In **deel III** van dit proefschrift bespreken we een laboratorium opstelling om de aangroei van stofdeeltjes in proto-planetaire schijven op een directe manier te bestuderen. De huidige theorieën voor de vorming van planeten laten stofdeeltjes groeien door botsingen, wat in theoretische modellen en in experimenten in het lab goed en snel werkt voor de kleinste stofdeeltjes. Wat grotere stofdeeltjes zorgen echter voor problemen. Om een rotsachtige planeet zoals de aarde te vormen, of de kern van een gasplaneet zoals Jupiter, moet het stof in de schijf aangroeien tot deeltjes groter dan enkele centimeters. We bevestigen echter met onze experimenten de voorspellingen van theoretische modellen, dat stof- en ijsdeeltjes met afmetingen van enkele centimeters bij snelheden van 1 m/s niet effectief in grootte toenemen door aan elkaar te plakken na botsingen. We vonden dat bij onze experimenten ongeveer 90% van de botsingen gevolgd werd door het terugstuiteren van de deeltjes, terwijl bij 10% versplintering optrad. Deze laboratorium resultaten suggereren samen met recentelijk vervolgexperimenten en aanvullende theoretische modellen, dat een alternatieve methode moet worden gebruikt om keien van enkele meters doorsnee te krijgen, die vervolgens kunnen doorgroeien tot grotere afmetingen door de aantrekkende werking van de zwaartekracht.

In de drie delen van dit proefschrift komen drie belangrijke onderwerpen in de studie naar proto-planetaire schijven aan bod: 1. De evolutie van stof en gas in de schijven en hoe deze met elkaar verband houden, zoals we kunnen opmaken uit waarnemingen van hun thermische straling; 2. De eigenschappen en het voorkomen van tijdelijke niet-thermische uitbarstingen op millimeter golflengtes van relativistische elektronen, en wat deze uitbarstingen ons kunnen vertellen over de eigenschappen van de magnetische velden rondom jonge sterren; 3. Het aangroeien van stofdeeltjes door botsingen in proto-planetaire schijven. Dit werk is van belang voor toekomstig onderzoek met ALMA, de nieuwste revolutie op het gebied van astronomische instrumentatie en één van de ambitieuste projecten ooit ondernomen binnen de sterrenkunde. Deze nieuwe schotels zullen de variaties van radiële snelheden van het gas en de chemische samenstellingen van de schijven beter in kaart brengen, waardoor we betere en volledigere modellen van de schijven zullen kunnen opstellen voor zowel het stof als het gas, voortbordurend op ons werk in deel I van dit proefschrift. De hogere gevoeligheid van ALMA zal ons ook in staat stellen hogere rotatie overgangen in moleculen waar te nemen, die weliswaar minder helder zijn, maar ook betere indicatoren zijn voor de totale gasinhoud van de schijf. ALMA zal bovendien de benodigde waarneemtijd verminderen voor grote waarneemstudies over meerdere tijdperiodes, waardoor we een beter overzicht zullen krijgen van de variabiliteit in de millimeter straling van jonge sterren, zoals we in deel II hebben besproken. Tenslotte gaven we in deel III van dit proefschrift aan dat een model voor planeetvorming waarin stofdeeltjes door botsingen uitgroeien tot deeltjes van enkele meters in doorsnee zowel in theorie als in de praktijk voor uitdagingen staat. Er is goede hoop dat we met ALMA de effecten van getijdenwerking door proto-planeten in de schijf kunnen waarnemen, wat ons meer aanwijzingen zal leveren voor de huidige theorieën voor planeetvorming.

Publication List

REFEREED PAPERS

1. *Hunting for Millimeter Flares from Magnetic Re-connection in Pre-main-sequence Spectroscopic Binaries* (Chapter 6)
   Á. Kóspál, **D. M. Salter**, M. R. Hogerheijde, A. Moór, and G. A. Blake, 2010, Astronomy & Astrophysics, submitted

2. *The Young Binary DQ Tau: A Hunt for X-ray Emission from Colliding Magnetospheres*
   K. V. Getman, P. S. Broos, **D. M. Salter**, G. P. Garmire, and M. R. Hogerheijde, 2010, Astrophysical Journal, submitted

3. *A Single-Dish Survey of the HCO^+, HCN, and CN Emission Toward the T Tauri Disk Population in Taurus* (Chapter 2)
   D. M. Salter, M. R. Hogerheijde, R. F. J. van der Burg, L. E. Kristensen, and C. Brinch, 2010, Astronomy & Astrophysics, submitted

4. *Recurring Millimeter Flares as Evidence for Star-Star Magnetic Re-connection Events in the DQ Tau PMS Binary System* (Chapter 5)
   D. M. Salter, Á. Kóspál, K. V. Getman, M. R. Hogerheijde, T. A. van Kempen, J. M. Carpenter, G. A. Blake, and D. Wilner, 2010, Astronomy & Astrophysics, 521, 32

5. *Grain Growth Across Protoplanetay Discs: 10μm Silicate Feature Versus Millimetre Slope*
   D. J. P. Lommen, E. F. van Dishoeck, C. M. Wright, S. T. Maddison, M. Min, D. J. Wilner, **D. M. Salter**, H. J. van Langevelde, T. L. Bourke, R. F. J. van der Burg, and G. A. Blake, 2010, Astronomy & Astrophysics, 515, 77

6. *A Zero-Gravity Instrument to Study Low Velocity Collisions of Fragile Particles at Low Temperatures* (Chapter 7)
   D. M. Salter, D. Heißelmann, G. Chaparro, G. van der Wolk, P. Reißaus, A. G. Borst, R. W. Dawson, E. de Kuyper, G. Drinkwater, K. Gebauer, M. Hutcheon, H. Linnartz, F. J. Molster, B. Stoll, P. C. van der Tuijn, H. J. Fraser, and J. Blum, 2009, Review of Scientific Instruments, 80, 74501

7. *The Nature of the Class I Population in Ophiuchus as Revealed Through Gas and Dust Mapping*
   T. A. van Kempen, E. F. van Dishoeck, **D. M. Salter**, M. R. Hogerheijde, J. K. Jórgensen, A. C. A. Boogert, 2009, Astronomy & Astrophysics, 498, 167

8. *Captured at Millimeter Wavelengths: a Flare from the Classical T Tauri Star DQ Tau* (Chapter 4)
   D. M. Salter, M. R. Hogerheijde, and G. A. Blake, 2008, Astronomy & Astrophysics Letters, 492, L21

9. *GSC 2137:3085 – A Suspected New Variable*
   P. J. Benson and **D. M. Salter**, 1999, International Bulletin on Variable Stars, 4728

POPULAR ARTICLES

1. *Gewichtloos in een Vliegtuig*
   D. M. Salter and F. J. Molster, 2007, Eureka!, February, Number 16

2. *A Foreign Student's Perspective on Leiden*
   D. M. Salter, 2004, Eureka!, March, Number 5

Curriculum Vitae

Acknowledgements